5-2011

A Multi-wavelength study on gamma-ray bursts and their afterglows

Binbin Zhang
University of Nevada, Las Vegas

A MULTI-WAVELENGTH STUDY ON GAMMA-RAY BURSTS AND THEIR AFTERGLOWS

by

Binbin Zhang

Bachelor of Science
Hebei Normal University, China
2003

A dissertation submitted in partial fulfillment
of the requirements for the

Doctor of Philosophy in Astronomy
Department of Physics and Astronomy
College of Science

Graduate College
University of Nevada, Las Vegas
May 2011

UNLV
UNIVERSITY OF NEVADA LAS VEGAS

THE GRADUATE COLLEGE

We recommend the dissertation prepared under our supervision by

Binbin Zhang

entitled

A Multi-wavelength Study on Gamma-ray Bursts and Their Afterglows

be accepted in partial fulfillment of the requirements for the degree of

Doctor of Philosophy in Astronomy

Bing Zhang, Committee Chair

Kentaro Nagamine, Committee Member

Daniel Proga, Committee Member

David Burrows, Committee Member

Paul O'Brien, Committee Member

Pengtao Sun, Graduate Faculty Representative

Ronald Smith, Ph. D., Vice President for Research and Graduate Studies
and Dean of the Graduate College

May 2011

ABSTRACT

A Multi-wavelength Study on Gamma-ray Bursts and Their Afterglows

by

Binbin Zhang

Dr. Bing Zhang, Examination Committee Chair
Professor of Physics
University of Nevada, Las Vegas

During the prompt emission and afterglow phases, GRBs(Gamma-Ray Bursts) release their huge amount of energy not limited in gamma-ray, but in a wide range of muti-wavelengths, from radio band to GeV gamma-rays. Thanks to the recent missions of Swift and Fermi, I was able to use their multi-wavelength observation data of GRBs and study their physical natures. I have processed all the Swift BAT/XRT and Fermi GBM/LAT GRB observation data. Based on the Swift data, I have studied the following comprehensive topics: (1) high-latitude "curvature effect" of early X-ray tails of GRBs Swift XRT afterglow (2) diverse physical origins of shallow decay phase of Swift XRT afterglow. (3) Jet break (in-)consistency in both X-Ray and Optical observations. Based on the Fermi observation data, I focused on the 17 GRBs with Fermi/LAT high-energy emission and found there are three elemental spectral components, namely, a classical "Band" function component, a quasi-thermal component and an extra non-thermal power law component extending to high energies. The detailed behaviors of these three components are extensively studied and their physical origins and corresponding jet properties and emission mechanisms are also discussed.

ACKNOWLEDGMENTS

It is a great pleasure to thank many people who made my dissertation possible.

Firstly I'd like to express my gratitude to my Ph.D. supervisor, Dr. Bing Zhang. Bing has influenced me significantly both in research and in daily life. With his enthusiasm, his inspiration, and his great efforts to explain things clearly and simply, he always help make research fun during my study. Bing focuses on his research and works with high efficiency, which set an excellent example for me. Throughout the five years when I am staying in UNLV, he provided encouragement, sound advice, good teaching and lots of good ideas. I have also benefited from his policy of providing students with the opportunity to attend conferences to meet a wide variety of people in GRB field, which has definitely been a great help in my career. Bing also generously invited me to his home in Chinese holidays. My sincere thanks go to all his family members: Zhaohui, Rachel and Raymond.

My sincerely thanks also goes to Dr.En-Wei Liang for his excellent advices and suggestion both on my research and life. Being acquaintance for more than eight years, we have been great productive collaborator and best friends.

UNLV GRB group is becoming one of the most active GRB research group in the world. All the members including professors, postdocs, students, long-term and short-term visitors have been making this group in a friendly family-like atmosphere. I'd like to thank all of you for great discussion, comments, suggestions, collaborations and even my English language, in particular Bing Zhang, En-Wei Liang, Xue-Feng Wu, Zi-Gao Dai, Nayantara Gupta, Yi-Zhong Fan, Francisco Virgili, Amanda Maxham, Wei Deng, He Gao, Hou-Jun Lv, Tesla Birnbaum, Robert Gex, Qiang Yuan and Bo Zhang.

I would like to thank many people in Physics & Astronomy Department. I would like to thank Dr. Daniel Proga and Dr. Kentaro Nagamine for their excellent advices and suggestion on my research and career. I would like to thank Dr. Stephen Lepp and Dr. George Rhee for their fun classes in which I learned a lot. I would like to thank my classmates Stefan Luketic, Timothy Water, Robert Thompson and Tae Son Lee for their help and discussion.

My special thanks goes to Dr. Robert D. Preece for his important instructions on *Fermi* data analysis, which made my third research project go smoothly and successfully.

There are many people who have helped me on the research projects during my Ph.D. I'd like to thank my industrial collaborators, in particular, Asaf Pe'er, Felix Ryde, Craig Swenson, Dong Xu, Xiao-Hong Cui, Judith Racusin, Jochen Greiner, Shu-Jin Hou, Xiang-Yu Wang, Jin Zhang, and Fu-Wen Zhang.

My thanks also go to Dr. David Burrows and Dr. Paul O'Brien for serving in my committee and their great suggestions and discussion. In particular I'd like to thank Dr. David Burrows for his critical comments which improved this dissertation significantly. I would also like to thank my committee member and graduate faculty representative, Dr. Pengtao Sun for his patient and suggestions.

Moreover, I should express my earnest thanks to my former advisors Yi-Ping Qin and Wei-Ming Yuan. Their valuable ideas, suggestions and comments are extremely helpful for me to improve my work and learn new knowledge.

I would like to thank my wife, Yanxia Li, for her understanding and love during the past few years. Her support and encouragement was in the end what made this dissertation possible.

This work is dedicated to :

My parents who have always supported me and appreciated the value of education, and,

My wife and daughter who have sacrificed so much.

TABLE OF CONTENTS

LIST OF FIGURES

LIST OF TABLES

PART I

INTRODUCTION

CHAPTER 1

HISTORY OF GRB RESEARCH

Gamma-ray bursts, or GRBs, as indicated by the name itself, are typically "bursts" of MeV photons in cosmological distances. Since later 1960s more than forty years has passed and our understanding of GRBs has also been like a "burst" of all kinds of colors and flavors in both observational and theoretical sides. Like objects in other astronomical fields, progress of understanding GRBs are also mainly led by more and more observational facts. Since the Gamma-ray photons are extinguished by the Earth's atmosphere, the Gamma-ray emission of the GRBs can not be directly observed by ground telescopes. Instead, there are several space satellites launched with Gamma-ray detectors, which are particularly designed to observe GRBs. Prompted by the instrumental progress, the history of GRB research during the last forty years can be divided into the following eras:

"Dark" era (1967−1990) The first GRB was accidentally discovered US Vela satellites which are designed during the 'Cold War' for detecting Gamma-ray emission from the nuclear weapons testing in late 1960s (Klebesadel et al. 1973, Strong et al. 1974). The earliest observation of GRBs only consists several "spikes" in Gamma-ray band and there was no way to identify their localization (however we know they originate outside from the solar system by the offset information got from several "Vela" satellites). The main questions of GRB research during this era is "Where are they from" ? Among more than one hundred models that have been proposed to explain GRBs, only a few assume GRBs occur at cosmological distances. On the other hand, the majority of those models assume GRBs happened closer to the Earth to apparently overcome the energy output issue.

BATSE era (1991-1996) The Burst And Transient Source Experiment (BATSE) which was on-board the Compton Gamma-Ray Observatory (CGRO) was capable to detect Gamma-ray sources from almost the entire sky in 20 keV -2 MeV energy range. From April 1991 to June 2000 it had detected about 3000 GRBs, which provided a large sample for GRBs statistical work. The 1B-4B BATSE catalogs confirmed the apparent

isotropic spatial distribution of GRBs (Meegan et al 1992). Then the cosmological origin of GRBs began to be accepted by most astronomers although the debate between galactic and cosmological origin still continued until BeppoSAX. On the theoretical side, by assuming GRBs occur at cosmological distance, the fireball model has been proposed to explain the huge amount energy (derived from observed flux) and fast time variability. However a baryonic fireball will predict quasi-thermal spectrum , which is different from the observed "Band" function-like non-thermal spectrum. In order to solve this problem, the fireball shock scenario has been proposed (Rees & Meszaros 1992). During the internal and external shock process, the fireball kinetic energy was converted into non-thermal energy. The prompt Gamma-ray light curves and spectra can be understood in terms of the internal shocks due to the collision of two shells with different Lorentz factors. Another contribution from BATSE is that "short" vs "long" classification of GRBs is proposed (Kouveliotou et al 1993, see also Part IV for more discussion on the scheme of classifications).

Beppo-SAX era (1996−2004) The fireball model predict the existence of GRB afterglow, which is the "delay" long time emission in longer energy bands (e.g, optical and X-Ray) after the prompt phase of GRBs. On February 28, 1997, after 30 years of the discovery of GRBs, the Italian X-ray satellite BeppoSAX, detected and localized the first X-ray "afterglow" from a gamma-ray burst (GRB). This afterglow is X-ray counterparts emitted after the initial burst of gamma-rays. The discovery, along with its much-improved localized positions, led to follow-up observation of GRBs at optical and radio wavelengths (van Paradijs et al. 1997). The discovery also led the determination of the cosmological distances and the identification of host galaxies (Djorgovski et al. 1998; Kulkarni et al. 1998a). Another satellite contributed in this era is HETE-2, which was launched in October 2001 and had similar capability with BeppoSAX. HETE-2 discovered GRB 030329 (Hjorth et al. 2003), which resulted in one the solid case of association between GRB and a supernova, SN 2003dh and implied that typical long-duration GRBs

are associated with the deaths of massive stars. Another important progress in this era was the discovery of a new class of sources called X-ray Flashes (Heise et al. 2001), which are less-luminous and lower-redshift population than the traditional GRBs.

Swift era (2004−2008) The Swift Gamma-Ray Burst Explorer (Gehrels et al. 2004) was launched in Novenmber 2004, it is a multi-wavelength satellite with both burst-detection (the Burst Alert Telescope, BAT; Barthelmy et al. 2005a) and afterglow observation capabilities (the X-ray (Burrows, et al 2005a) and UV/optical telescopes (Roming et al. 2005), XRT and UVOT). Swift was designed to accurately localize the burst, slew XRT/UVOT to observe the afterglow within minutes, and provide more-accurate positions during the first ten minutes after each burst. Swift has been a great success. Its observations revealed unusual yet "canonical X-ray afterglow behaviors, including bright X-ray flaring activity during the afterglow phase and enabled detailed studies of the transition from prompt to afterglow emission. For more details on the Swift X-ray afterglow, please see Part II. Swift also detected the first afterglow of a short GRB, a milestone for short burst research. Finally, it detected high-z GRBs 050904, 080913 and 090423, the most distant cosmic explosions and the first GRBs during the epoch of re-ionization.

Fermi era (2008−now) The *Fermi* satellite ushered in a new era of studying GRB prompt emission. The two instruments on board *Fermi*, the Gamma-ray Burst Monitor (GBM; Meegan et al. 2009) and the Large Area Telescope (LAT; Atwood et al. 2009), provide an unprecedented spectral coverage for 7 orders of magnitude in energy (from ∼8 keV to ∼300 GeV). As we will discuss in Part III (Zhang, B.-B. et al 2011), Fermi has made several significant progress on understanding the physical origin of GRBs including (1) Three elemental spectral components (Band function-like, thermal and extra non-thermal power-law components) exist in GRB spectra. (2) In most cases, the featureless Band function spectra extended from ∼ keV to Gev suggest a Poynting-flux-dominated flow. (3) However, one special case that the existence of a thermal component in GRB

090902B (Ryde et al. 2010; Pe'er et al. 2010) suggests that the composition of this GRB is likely a hot fireball without strong magnetization. (4) The delayed onset of GeV emission in some LAT GRBs suggests that there likely be a change of either particle acceleration condition or the opacity of the fireball during the early prompt emission epoch. (5) The long lived GeV emission is like of likely of external origins. The GeV emission during the prompt phase, on the other hand is likely of internal origin.

CHAPTER 2

OVERVIEW OF GRB MULTI-WAVELENGTH OBSERVATION

Prompt Gamma-Ray Emission

Temporal Properties

Duration The duration of GRB, T_{90} or T_{50}, is defined by the time interval within which 90% or 50% of the burst fluence is detected. The typical duration of a GRBs is $\sim 20-30$ seconds for long bursts and $\sim 0.2-1.3$ seconds for short bursts. Observationally the durations of GRBs can be in a range of 5 orders of magnitude, i.e, from $\sim 10^{-2}s$ to $\sim 10^{3}s$. The bimodal distribution of T_{90} has been used to identify the two categories of GRBs, namely, "long" ($T_{90} \geq 2s$) and "short"($T_{90} \leq 2s$) (Kouveliotou et al 1993, Fig. 1).

Instrumentally T_{90} (or T_{50}) also depends on the energy band and the sensitivity limit of the detector. Theoretically, there are three time scales which may be related to the observed GRB duration (Zhang, B et al 2009) : (1) central engine activity time t_{engine} (2) relativistic jet launching time scale t_{jet} (3) energy dissipation time scale t_{dis}. In general, the observed GRB duration T_{90} should satisfy (Zhang, B. et al. 2009)

$$T_{90} \leq t_{dis} \leq t_{jet} \leq t_{engine} \ . \tag{2.1}$$

Light Curves and Variability. Fig. 2 depicts typical GRB prompt light curves from the BATSE sample. As shown in this figure, GRBs can vary from very simple light curves with only a single smooth pulse (FRED-shape) to complex light curves with many erratic pulses of different durations, amplitudes and shapes. In most cases, one can infer at least two different variability in a typical burst (Figure 3). Based on temporal information, GRBs are difficult to categorized.

Several mechanism candidates have been proposed in literature to interpret the temporal variability of GRBs including (1) irregular activity of the central engine in form of

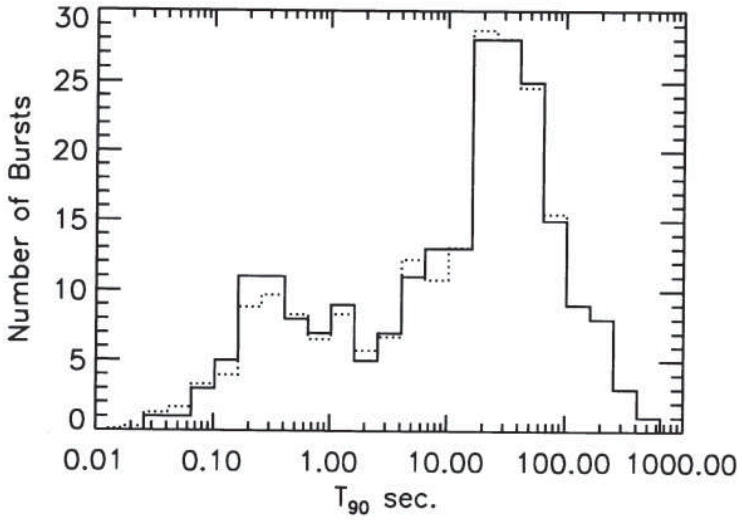

Figure 1 Distribution of T_{90} for GRBs of the first BATSE catalog, from Kouveliotou et al 1993.

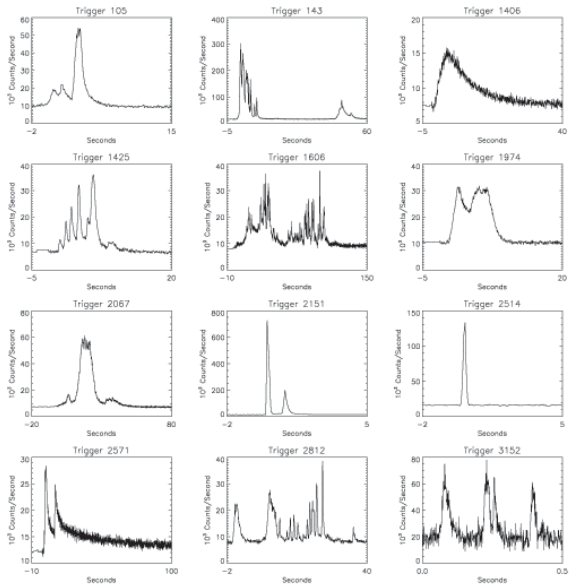

Figure 2 Typical shapes of Gamma-ray burst light curves,credit: J.T. Bonnell (NASA/GSFC)

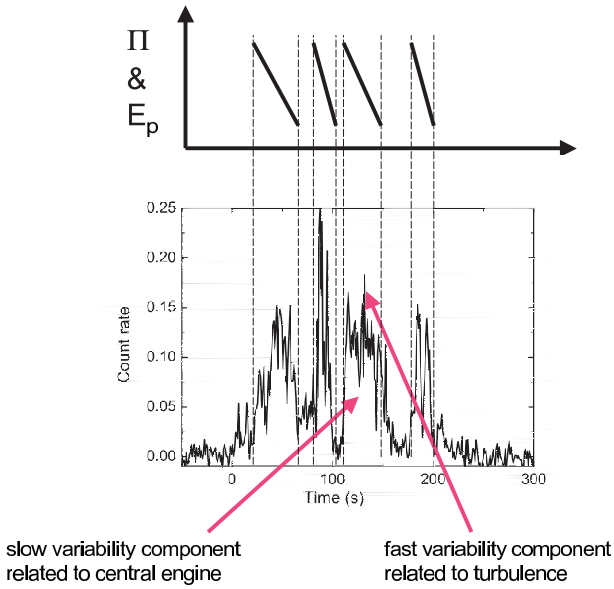

Figure 3 Example of GRB light curve that shows two variability timescales. Picture from Zhang & Yan 2011.

internal shock (Rees & Meszaros 1994; Sari & Piran 1997; Daigne & Mochkovitch 2003; Kobayashi et al. 1997; Maxham & Zhang 2009) or the photosphere emission (Lazzati et al. 2009; Wu & Zhang 2011) (2) locally Lorentz boosted emission regions, such as mini-jets (Lyutikov & Blandford 2003) or relativistic turbulence (Narayan & Kumar 2009; Kumar & Narayan 2009) (3) ICMART (Internal-Collisioninduced MAgnetic Reconnection and Turbulence, Zhang & Yan 2010) event. Interestingly, the last candidate, namely, ICMART model that has two variability components: a broad (slow) component related to the central engine activity, and a narrow (fast) component associated with relativistic magnetic turbulence, which seems consistent with observations (Zhang & Yan 2010, Gao et al 2011,see Figure 3 for illustration.)

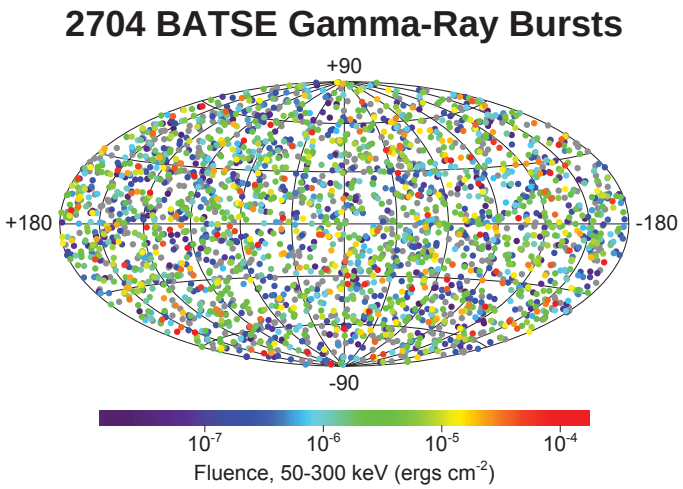

Figure 4 Sky distribution of 2704 GRBs recorded with BATSE during the nine-year mission. The projection is in galactic coordinates. Figure from `http://www.batse.msfc.nasa.gov/batse/grb/skymap/`

Spatial Distribution

The large BATSE GRB samples revealed an isotropic sky distribution (Meegan et al. 1992,see also Fig. 4). The peak count and peak variability distribution follow $logN/logS \propto S^{0.8}$ and $V/V_{max} \simeq 0.35$ which are not consistent with Galactic source populations. The cosmological origin of GRBs was favored by above facts and was confirmed by the detection of first X-Ray afterglow in Beppo-SAX era (Metzger et al. 1997).

Spectral Properties

Band Function-like Spectra In most cases, GRB spectra are "Band" function-like, which is a smoothly joint broken power-law described by the following function (Band et al. 1993):

$$\begin{aligned} n(E) &= A(\tfrac{E}{100\,\mathrm{keV}})^{\alpha}\exp\left(-\tfrac{E}{E_c}\right) && E < E_c, \\ &= A[\tfrac{(\alpha-\beta)E_c}{100\,\mathrm{keV}}]^{\alpha-\beta}\exp(\beta-\alpha)\left(\tfrac{E}{100\,\mathrm{keV}}\right)^{\beta} && E \geq E_c \end{aligned}$$

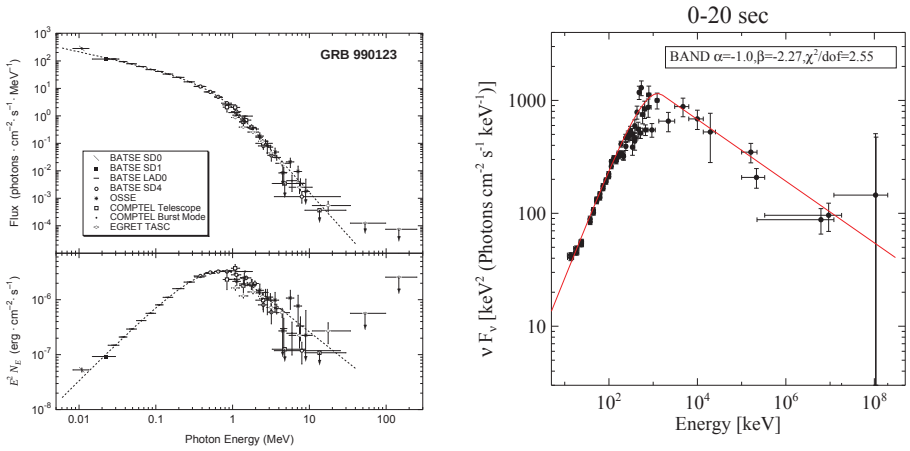

Figure 5 Examples of Band function-like spectrum during GRB prompt emission. *left:* GRB 990123, from Briggs et al 1999. *right:* 080916C, from Zhang, B.-B et al. 2011.

where $E_c = (\alpha - \beta)E_p/(2 + \alpha)$. Three independent spectral parameters are involved, i.e., a low energy photon spectral index α (typical value is -1), a high energy photon spectral index β (typical value is -2.2), and the transition energy E_0 (typical value is $200keV \sim MeV$). Fig. 5 shows two typical observed GRB spectra that can be fitted by Band function extremely well. Note that the featureless Band function spectrum in GRB 080916C extend from $\sim 10keV$ to $\sim 10GeV$. This already challenge the thermal fireball model (Zhang & Pe'er 2009) and strongly suggests that a certain non-thermal emission mechanism is in operation. This demands the existence of a population of power-law-distributed relativistic electrons, possibly accelerated in internal shocks or in regions with significant electron heating, e.g. magnetic dissipation. See Chapter 7 for more discussion.

Thermal Spectra A thermal component (or Blackbody like) spectrum is predicted by the standard fireball model, i.e., when relativistic outflow turn optically thin, it will naturally produce thermal emission from fireball photosphere (Paczynski 1986; Goodman 1986; Rees & Meszaros, 2005; Pe'er et al. 2006a; Thompson et al. 07; Pe'er & Ryde 2010; Beloborodov, 2010; Lazzati et al 2009, 2011; Toma et al 2010 ; Ioka 2010, Ryde et al 2011). There are a few cases (e.g., GRB 911031, left panel of Fig. 6) in BATSE era that the GRB spectra can be fitted with a blackbody component. The most prominent

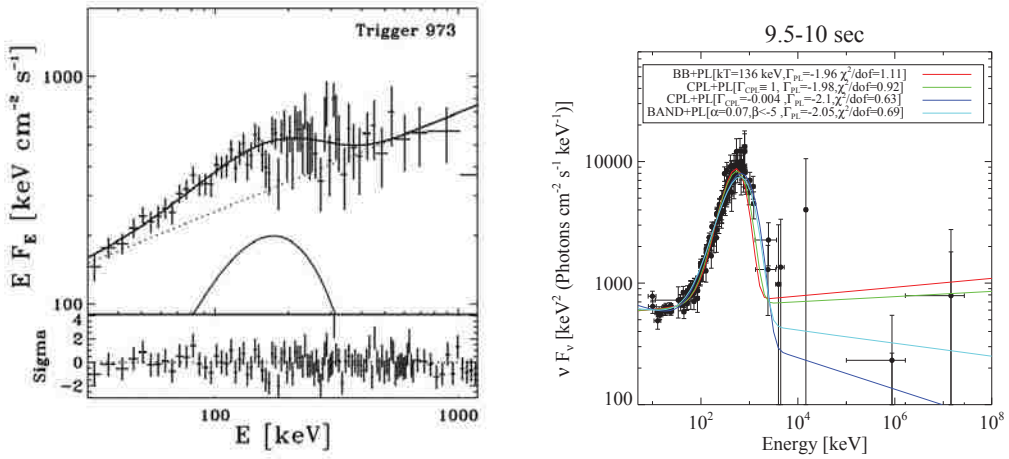

Figure 6 Example of thermal component in GRB spectra. *Left panel:* A spectrum from GRB911031 (#973; 3 s after the trigger) fitted with the photosphere model ryde04, with a power-law slope of $s = -1.53 \pm 0.04$ and $kT = 56 \pm 7$ keV ()from Ryde et al 2006) . *Right Panel: The case of GRB 090902B fitted by a BB+PL model (red line). From Zhang, B.-B et al. 2011.*

case, however, is the recent Fermi/LAT burst, GRB 090902B (right panel of Fig. 6). As shown in Chapter 7, we divided this burst into several slices and the spectrum in each slice can be well fitted by a spectral model containing a blackbody component and an extra non-thermal power-law component. Notice that observationally speaking, the "thermal" spectra during prompt GRBs is not necessarily a pure Planck function. Some superposition effects may modify the thermal spectrum and lead it to be a multi-color blackbody (Ryde et al 2011, see in Chapter 7 for more discussion).

Extra Non-Thermal Power-Law Component As shown in right panel of Fig. 6, two cases of recent Fermi GRBs (i.e, GRBs 090510 & 090902B) reveal the existence of an extra non-thermal power-law spectral component. Several noticeable properties of this component are (Zhang, B.-B, et al 2011): (1) this component is always accompanied by a low energy MeV component (likely the BB component). Its origin may be related to this low energy component; (2) It is demanded in both the low energy end and the high energy end, and amazingly the same spectral index can accommodate the demanded excesses in both ends. This suggests that either this PL component extends for 6-7

orders of magnitude in energy, or that multiple emission components that contribute to the excesses in both the low and high energy regimes have to coincide to mimic a single PL; (3) The spectral slope is positive in the νF_ν space, so that the main energy power output of this component is at even higher energies (possibly near or above the upper bound of the LAT band). Theoretically speaking, Non-thermal GRB spectra are expected to be curved (Mészáros et al. 1994; Pilla & Loeb 1998; Pe'er & Waxman 2004a; Razzaque et al. 2004; Pe'er et al. 2006; Gupta & Zhang 2007; Asano & Terasawa 2009), the existence of the PL component is not straightforwardly expected. See more discussion about understanding this component in Chapter 7

Afterglows

X-Ray Afterglows : A Canonical X-ray Light Curve

Prior to Swift, most X-ray (and optical) afterglow were only detected after several hours of the GRB trigger time. Thanks to its fast-slewing capability, Swift can observe X-Ray emission as early as hundreds seconds after the BAT triggered a burst. The large Swift/XRT light curve sample led the striking discovery of a "canonical" X-Ray light curve (Nousek et al. 2006; Zhang et al. 2006; OBrien et al. 2006; Chincarini et al. 2005). As shown in the cartoon Fig. 7 (Zhang, B et al 2006), a canonical XRT light curve typically consists 4-5 typical segments:

- **I. Steep decay** This segment is observed right after the prompt emission. As discussed in Chapter 3, this segment is tail of the prompt emission and the steep decay slope and strong spectral evolution are due to the curvature (high-latitude) effect.

- **II. Shallow decay** This segment is new and not expected before Swift. With a typical decay slope ~ -0.5, shallow decay phase usually extends from $\sim (10^3)$s to $\sim (10^4)$s, then followed by a temporal break (e.g. Campana et al.2005; De Pasquale et al. 2006). Unlike the early steep decay phase, the shallow decay

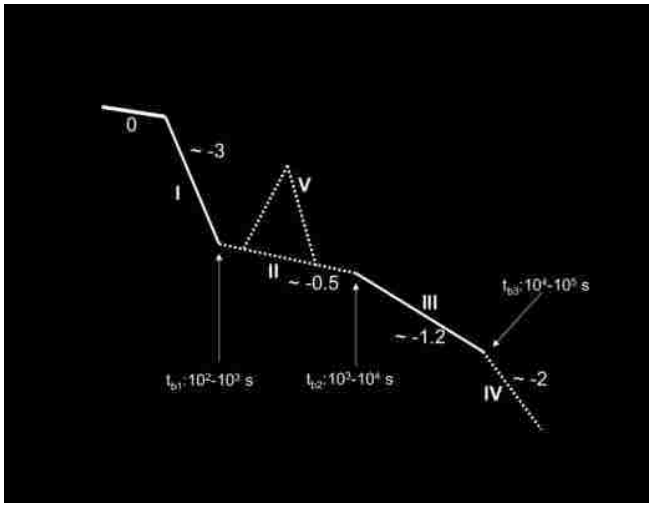

Figure 7 A cartoon picture showing the cannonicial X-ray light curve(from Zhang et al. 2006).

segment has diverse physical origins. In Chapter 5, we analyze the properties of this segment with a sample of 53 long Swift GRBs detected before Feb., 2007. We show that although most of them are usually consistent with the external shock models, the optical observations, however, challenge the energy injection scenario. More interestingly, there are 4 significant outliers in the sample: GRBs 060413, 060522, 060607A and 070110. The shallow decay phase in these bursts is immediately followed by a very steep decay after t_{break}, which is inconsistent with any external shock model. The optical data of these bursts evolve independently of the X-ray data. These X-ray plateaus likely have an internal origin and demand continuous operation of a long-term GRB central engine.

- **III. Normal decay** Following the shallow decay segment, this normal decay segment is not a surprise sine the decay slope (~ -1.2) is normally consistent of predictions of the standard afterglow model (Mészáros & Rees 1997; Sari et al. 1998; Chevalier & Li 2000) .

- **IV. Post Jet break phase :** With a decay slope ~ -2 , this segment satisfies the predictions of the jet model. An achromatic break is expected to be observed in multi-wavelength afterglow light curves at a time when the ejecta are decelerated by the ambient medium down to a bulk Lorentz factor $1/\theta_j$, where θ_j is the jet opening angle. However as shown in Chapter 6, there were only few cases that could be identified as jet-break candidates and there was no "Platinum" case.

- **V. X-ray flares** X-ray flares can be quite frequently observed in long-duration (Falcone et al. 2006), short-duration GRBs (Barthelmy et al. 2005b; Campana et al. 2006a) and XRFs (Romano et al. 2006, 2009). They have variety of "occurring time" (X-ray flares can occur on top of the phases of I-IV that were mentioned above) and amplitudes (up to 6 orders of magnitude) yet normally have similar quite narrow shapes with $\delta t/t \ll 1$. Theoretically, X-ray flares are believed to related to late central engine activities.

In Chapters 3 - 6, I will present the detailed analysis on the segments I,II and III-IV.

External Origin Of The Long-Term GeV Emission

The LAT telescope on-board Fermi satellite have observed long-term > 100 MeV LAT emission in some bright Fermi bursts (e.g. GRBs 080916C, 090510, 090902B and 090926A). An example is shown in Figure 8. For more details of the LAT observations please refer to Part III and Zhang, B.- B. et al. 2011.

Since LAT photons have been detected both in prompt emission and afterglow phase, one question is that whether they are from the same physical origin or not. As shown in Chapter 7, our data analysis suggests a "dilemma" picture regarding the origin of the GeV afterglow. Spectroscopically, the LAT-band emission is usually an extension of the GBM-band emission and forms a single Band-function component, suggesting a common physical origin with the GBM-band emission. In the time domain, the simple temporal behavior (a broken power-law light curve) of LAT emission led to the suggestion that

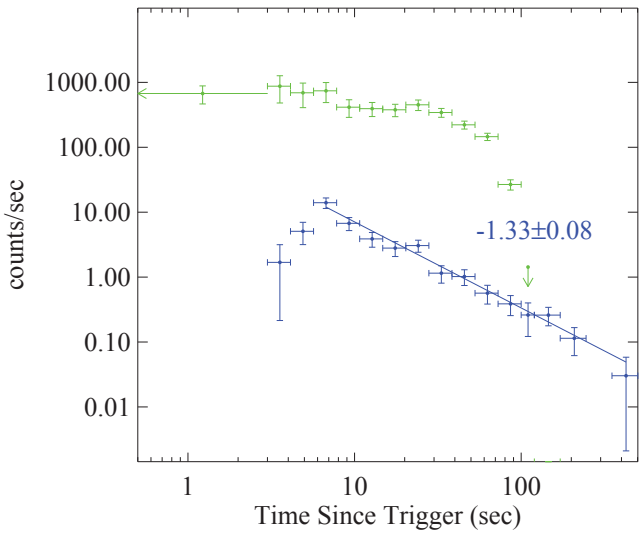

Figure 8 The comparison between the GBM (green) and LAT (blue) count rate lightcurves in log-scale for GRB 080916C

entire GRB GeV emission is of an external forward shock origin (Kumar & Barniol Duran 2009, 2010; Ghisellini et al. 2010), possibly from a highly radiative blastwave.

We tried to solve this dilemma with simulation methods (Maxham et al. 2011). By tracking the energy output from the central engine and modeling the early blastwave evolution of four bright LAT GRBs, we find that the predicted > 100 MeV lightcurve is unable to account for the observed LAT prompt emission (see Figure 9 as an example). Our results suggest that at least during the prompt emission phase, the LAT band emission is not of external forward shock origin.

Optical/Radio Afterglow

Prior to Swift, most of the afterglow observations were in the optical and radio bands. They typically consist two late-time segments: normal decay phase and the jet break phase. Broadband modeling was carried out for some well observed afterglows, and the data were generally consistent with the standard external shock afterglow model. After the launch of Swift the on-board UVOT telescope has been pushed hard to collect the

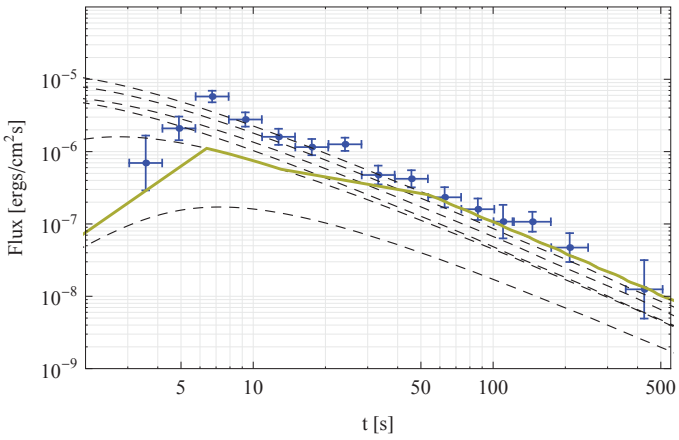

Figure 9 The predicted external shock > 100 MeV lightcurve of GRB 080916C for a radiative blastwave solution (yellow line) as compared with the data (blue points). Successive lightcurves that correspond to different total blastwave kinetic energy are shown as dashed lines, from Maxham et al 2011.

optical photons $\sim$ 100 seconds after the bursts. However, most bursts were too dim or undetectable in UVOT band (Roming et al. 2006). Using the available co-observed UVOT data and XRT data , we have performed a comprehensive study on the achromatic jet problem (Liang et al. 2007, see also Chapter 6)

In some cases, early-time flares were observed in optical and radio bands (e.g. GRB 990123, Akerlof et al. 1999; GRB 021004, Fox et al. 2003; GRB 021211, Fox et al. 2003a), which were explained as the emission from the reverse shock (Sari & Meszaros 2000; Meszaros & Rees 1999; Kobayashi & Zhang 2003).

One of the interesting findings during Swift era is the different intrinsic optical luminosities between long (or type II) and short (or type I) GRBs. It is found that type I GRBs typically have a lower average luminosity than type II GRBs do (Kann et al. 2008, see also Part IV for some discussion).

PART II

Swift X-RAY OBSERVATIONS AND THEIR PHYSICAL IMPLICATIONS

CHAPTER 3

SPECTRAL EVOLUTION OF GRB X-RAY TAILS

This chapter is partially based on the following published paper :

Zhang, B.-B., Liang, E.-W.,& Zhang, B. 2007, The Astrophysical Journal, 666, 1002.

Observation

The extensive observations of Gamma-Ray Bursts (GRBs) suggest that most of the broadband, power-law decaying afterglows are from external shocks as the fireball is decelerated by the ambient medium (Mészáros & Rees 1997a; Sari et al. 1998). The prompt gamma rays and the erratic X-ray flares after the GRB phase (Burrows et al. 2005b), are instead of internal origin, likely from internal shocks (Rees & Mészáros 1994, see Zhang et al. 2006 for detailed discussion)[1]. The direct evidence for the distinct internal origin of prompt gamma-rays and X-ray flares is the steep decay tails following the prompt emission and the flares (Tagliaferri et al. 2005; Nousek et al. 2006; O'Brien et al. 2006), which could be generally interpreted as the so-called "curvature effect" due to the delay of propagation of photons from high latitudes with respect to the line of sight (Fenimore et al. 1996; Kumar & Panaitescu 2000a; Qin et al. 2004; Dermer 2004; Zhang et al. 2006; Liang et al. 2006a). This clean picture is somewhat "ruined" by some recent observations with *Swift*. A strong spectral evolution has been observed in the tails of two peculiar GRBs: 060218 (Campana et al. 2006a; Ghisellini et al. 2006) and 060614 (Gehrels et al. 2006; Zhang et al. 2007b; Mangano et al. 2007), which is not directly expected from the curvature effect model. This suggests that there might be unrevealed emission components in the early afterglow phase. This motivates us to perform a systematic data analysis for both light curves and their spectral evolution of

[1]Ghisellini et al. (2007a) suggested that most power-law decaying X-ray afterglows that show a shallow-to-normal decay transition are "late prompt emission" that is also of internal origin. The fact that most of the X-ray afterglows in the "normal" decay phase satisfy the well-known "closure relation" for the external shocks (Zhang et al. 2007a), however, suggests that this is not demanded for most bursts. GRB 0070110, on the other hand, displays a flat X-ray emission episode followed by a rapid decay. This likely suggests an internal origin of the flat X-ray emission episode at least for some bursts (Troja et al. 2007).

the GRB tails observed by *Swift*/XRT.

Data Reduction and Sample Selection

The X-ray data are taken from the Swift data archive. We develop a script to automatically download and maintain all the Swift X-Ray Telescope (XRT) data. The Heasoft packages, including *Xspec*, *Xselect*, *Ximage*, and Swift data analysis tools, are used for the data reduction. We develop a set of IDL codes to automatically process the XRT data. The procedure is described as follows.

First, run the XRT tool *xrtpipeline* (Version 0.10.6) to reproduce the XRT clean event data, which have been screened with some correction effects (e.g. bad or hot pixels identifications, correct Housekeeping exposure times, etc.). The latest calibration data files (CALDB) are used.

Second, a time filter for the time-resolved spectral analysis is automatically performed. We initially divide the time series of XRT data into n (normally 30) equal segments in log-scale. Generally, these segments are not the real time intervals to perform the spectral analysis because they may not have enough spectral bins to perform spectral fitting. A real time interval for our spectral analysis should satisfy two criteria, i.e., the spectral bins[2] in the time interval should be greater than 10, and the reduced χ^2 should be around unity. If one temporal segment does not satisfy our criteria, we combine the next time segment until the merged segment meets our criteria. With this procedure, we create a time filter array to perform time-resolved spectral analyses.

Third, make pile-up correction and exposure correction for each time interval. The pile-up correction is performed with the same methods as discussed in Romano et al. (2006) (for the Window Timing [WT] mode data) and Vaughan et al. (2006) (for the Photon Counting [PC] mode data). Both the source and the background regions are annuli (for PC) or rectangular annuli (for WT) . For different time intervals, the inner radius of the (rectangular) annulus are dynamically determined by adjusting the inner

[2]We re-group the spectra using *grppha* in order to ensure a minimum of 20 counts per spectral bin

radius of the annulus through fitting the source brightness profiles with the King's point source function (for PC) or determined by the photo flux using the method described in Romano et al. (2006) (for WT). If the pile-up effect is not significant, the source regions are in shape of a circle with radius $R = 20$ pixels (for PC) or of a 40×20 pixel^2 rectangle (for WT) centered at the bursts' positions. The background region has the same size as the source region, but is 20 pixels away from the source region. The exposure correction is made with an exposure map created by the XRT tools *xrtexpomap* for this given time interval.

Fourth, derive the corrected and background-subtracted spectrum and light curve for each time interval. The signal-to-noise ratio is normally 3, but we do not rigidly fix it to this value. Instead we adjust it if needed according to the source brightness at a given time interval.

Fifth, fit the spectrum in each time interval and convert the light curve in count rate to energy flux. The spectral fitting model is a simple power-law combined with the absorptions of both our Galaxy and the GRB host galaxy, $wabs^{\rm Gal} \times zwabs^{\rm host} \times powerlaw$ (for bursts with known redshifts) or $wabs^{\rm Gal} \times wabs^{\rm host} \times powerlaw$ (for bursts whose redshifts are unknown), except for GRB060218, for which a black body component is added to the fitting model, $wabs^{\rm Gal} \times wabs^{\rm host} \times (powerlaw + bbodyrad)$ (Campana et al. 2006a) [3]. The $nH^{\rm Gal}$ value is taken from Dickey & Lockman (1990), while the $nH^{\rm host}$ is taken as a free parameter. We do not consider the variation of $nH^{\rm host}$ within a burst and fix this value to that derived from the time-integrated spectral fitting. With the spectrum in this time interval, we convert the photon flux to the energy flux.

We perform time-resolved spectral analyses with our code for all the Swift GRBs detected from Feb. 2005 to Jan. 2007, if their XRT data are available. We find that the X-rays of most GRBs are not bright enough to make time-resolved spectral analyses,

[3]We fix the parameters of the black body component to the same values as in Campana et al. (2006a). Please note that the XRT light curve of the first orbit is dominated by the black body component 2000 seconds since the GRB trigger. Therefore, the non-thermal emission in the first orbit is considered only for those before 2000 seconds since the GRB trigger.

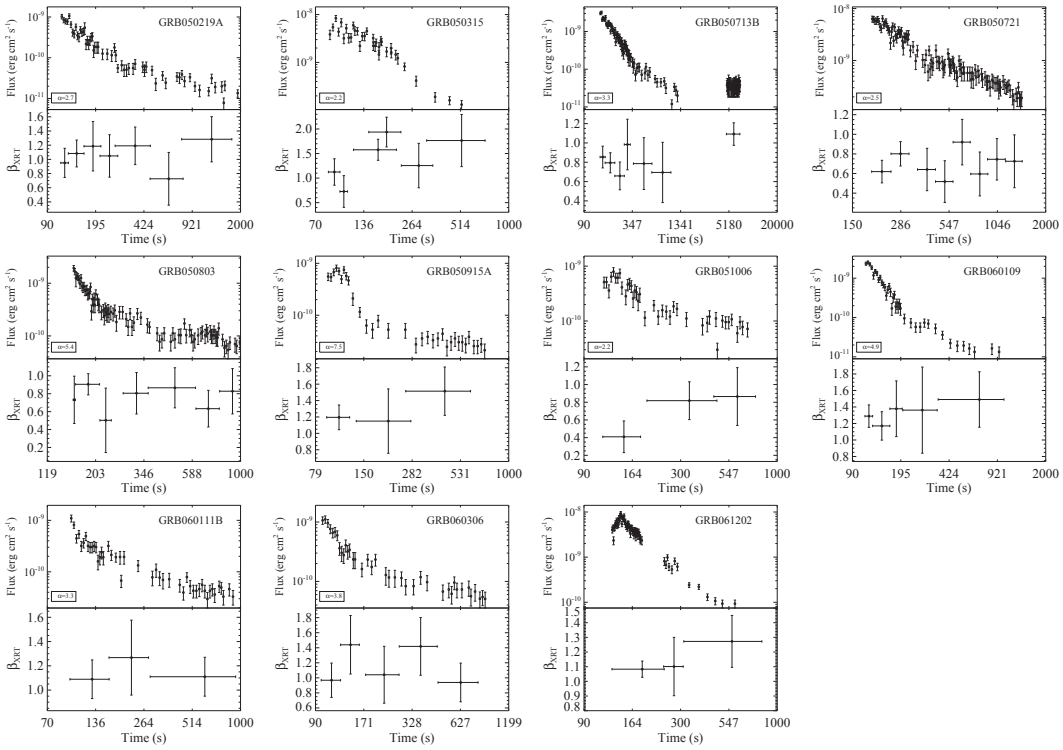

Figure 10 XRT light curve (upper panel of each plot) and spectral index as a function of time (lower panel of each plot) for those tails without significant spectral evolution (Group A). The horizontal error bars in the lower panels mark the time interval for the spectral analyses. Whenever available, the shallow decay segments following the tails and their spectral indices are also shown.

i.e., only time-integrated spectra are derived. Here we focus on the spectral evolution of GRB tails. Therefore, our sample includes only those bursts that have bright GRB tails. All the tails studied have decay slopes $\alpha < -2$, and the peak energy fluxes in the tails are generally greater than 10^{-9} erg cm^{-2} s^{-1}. Some GRB tails are superimposed with significant flares. Although it is difficult to remove the contamination of the flares, we nonetheless include these bursts as well in the sample. Our sample include 44 bursts altogether. Their lightcurves and time-dependent spectral indices are displayed in Figs. 10-12

Results of the Time-Resolved Spectral Analyses

The light curves and spectral index evolutions of the GRB tails in our sample are shown in Figs. 10-12. For each burst, the upper panel shows the light curve and the lower panel shows the evolution of the spectral index β ($\beta = \Gamma - 1$, where Γ is the photon index in the simple power-law model $N(E) \propto \nu^{-\Gamma}$). The horizontal error bars in the lower panel mark the time intervals. For the purpose of studying tails in detail, we zoom in the time intervals that enclose the tails. In order to compare the spectral behaviors of the shallow decay phase following the GRB tail, we also show the light curves and spectral indices of the shallow decay phase, if they were detected.

Shown in Fig.10 are those tails (Group A) whose light curves are smooth and free of significant flare contamination, and whose spectra show no significant evolution. The spectral indices of the shallow decay segment following these tails are roughly consistent with those of the tails. Figure 11 displays those tails (Group B) that have clear hard-to-soft spectral evolution[4], but without significant flares (although some flickering has been seen in some of these tails). The spectral evolution of these tails should be dominated by the properties of the tails themselves. In contract to the tails shown in Fig. 10, the spectra of the shallow decay components following these tails are dramatically harder than the spectra at the end of the tails. This indicates that the tails and the shallow decay components of these bursts have different physical origin.

The rest of the GRBs (about 1/3) in our sample show those tails (Group C) that are superimposed with significant X-ray flares. In most of these tails, strong spectral evolutions are also observed. These bursts are shown in Fig. 12. Since the spectral behaviors may be complicated by the contributions from both the tails and the flares, modeling these tails is no longer straightforward, and we only present the data in Fig.12.

[4]We measure the spectral evolution of these bursts with $\beta_{\rm XRT} \propto \kappa \log t$, and the κ values of these bursts are greater than 1.

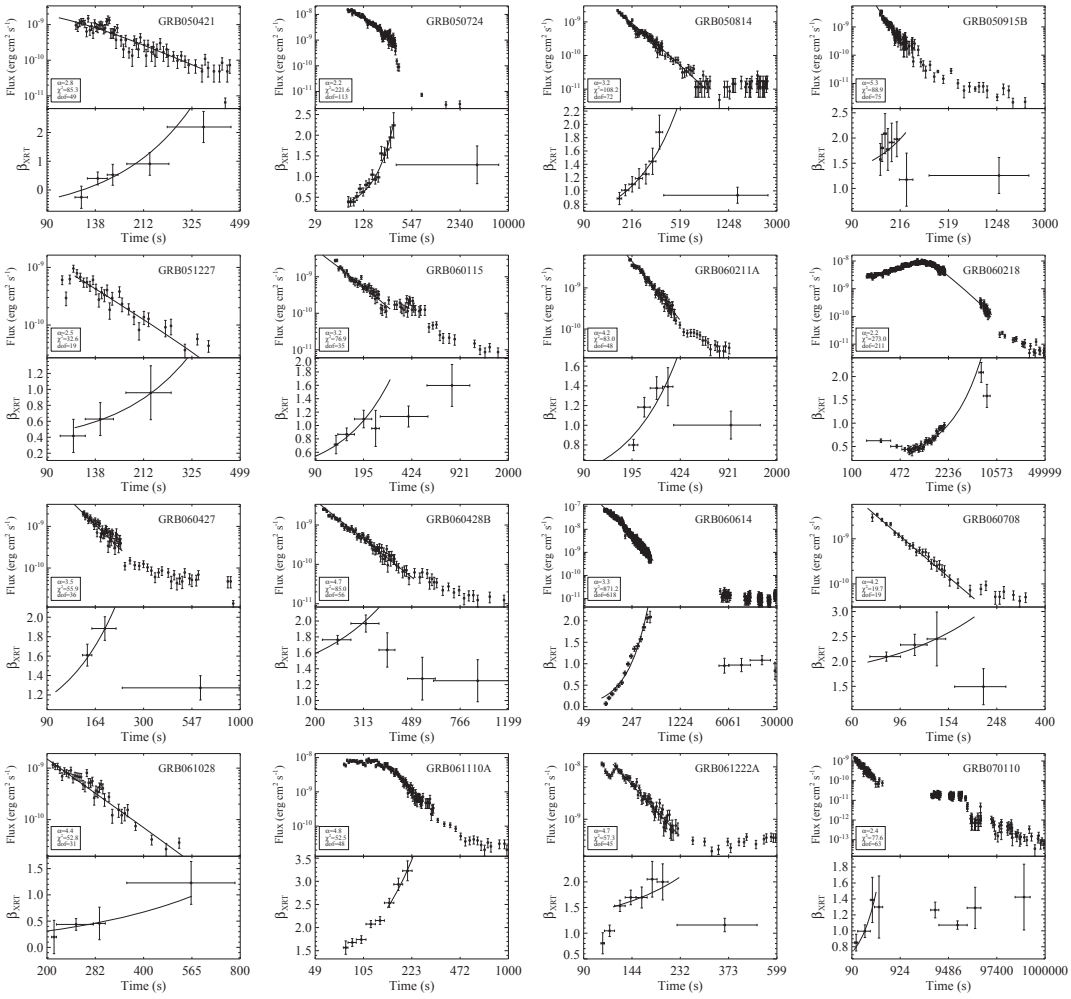

Figure 11 Same as Figure 10 but for those tails with significant spectral evolution but without superposing strong flares (Group B). The solid lines show the results of our proposed modeling.

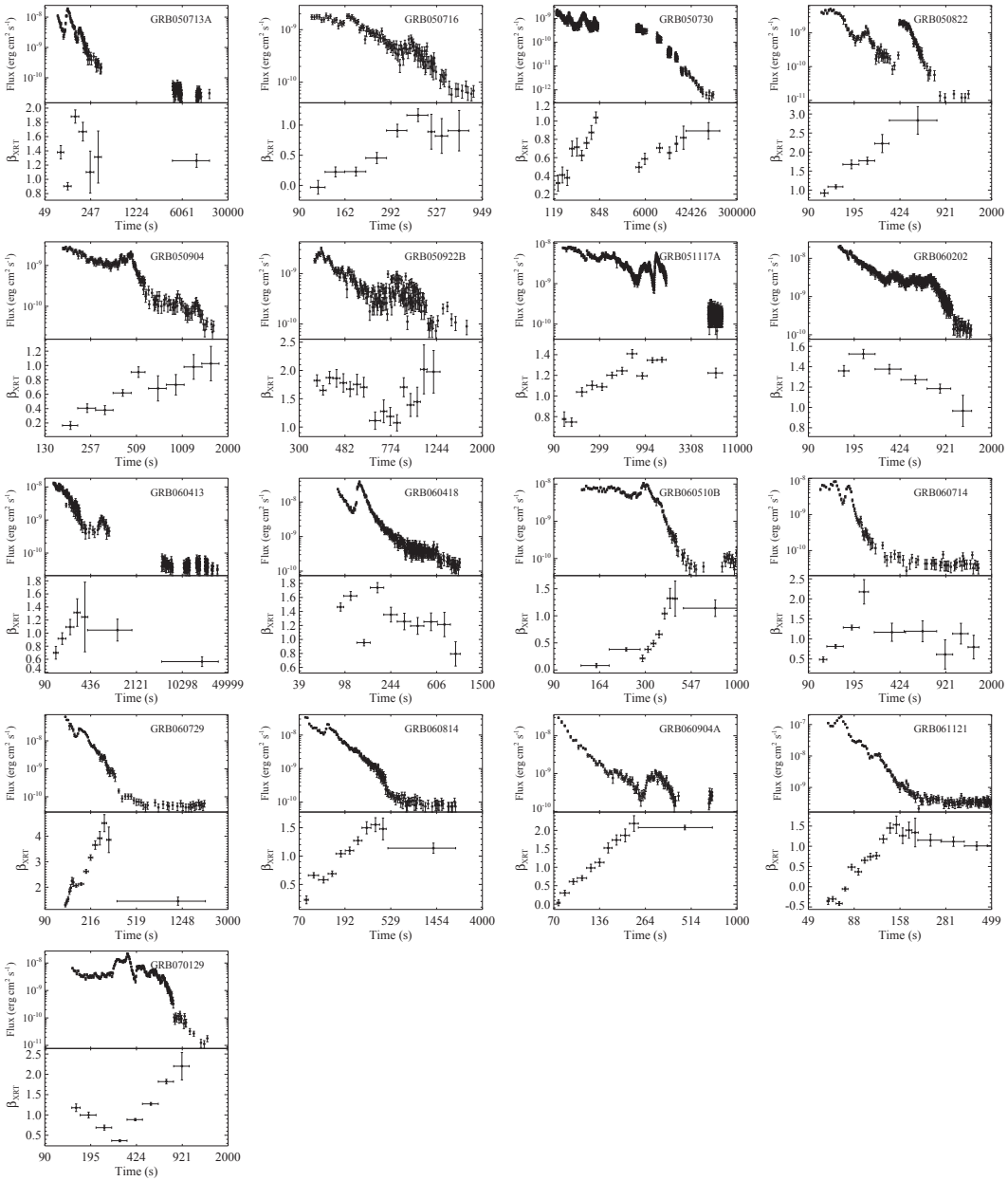

Figure 12 Same as Figure 10 but for those tails with significant flare contamination (Group C).

A Toy Model

The physical origin of the GRB tails is still uncertain. In our sample, one-fourth of the tails do not show significant spectral evolution (Fig. 10). The most straightforward interpretation for these tails is the curvature effect due to delay of propagation of photons from large angles with respect to the line of sight (Fenimore et al. 1996; Kumar & Painaitescu 2000a; Wu et al. 2006). In this scenario, the decay is strictly a power law with a slope $\alpha = -(2+\beta)$ if the time zero point is set to the beginning of the rising segment of the lightcurve (Zhang et al. 2006, see Huang et al. 2002 for the discussion of time zero point in a different context). This model has been successfully tested with previous data (Liang et al. 2006a).

We show here that most of the tails in our sample have significant hard-to-soft spectral evolution (see Figs.11 and 12). The simplest curvature effect alone cannot explain this feature. We speculate three scenarios that may result in a spectral evolution feature and test them in turn with the data.

The first scenario is under the scheme of the curvature effect of a structure jet model. Different from the previous structured jet models (Mészáros, Rees & Wijers 1998; Zhang & Mészáro 2002a; Rossi et al. 2002) that invoke an angular structure of both energy and Lorentz factor, one needs to assume that the spectral index β is also angle-dependent in order to explain the spectral evolution. Furthermore, in order to make the model work, one needs to invoke a more-or-less on axis viewing geometry. Nonetheless, this model makes a clear connection between the spectral evolution and the lightcurve, so that $f^c(\nu,t) \propto [(t-t_p)/\Delta t+1]^{-[2+\beta_c(t)]}\nu^{-\beta_c(t)}$, where $\beta_c(t)$ is the observed spectral evolution fitting with $\beta_c(t) = a + \kappa \log t$. We test this model with GRBs 060218 and 060614, the two typical GRBs with strong spectral evolution, and find that it fails to reproduce the observed light curves.

The second scenario is the superimposition of the curvature effect with a putative underlying power-law decay emission component. This scenario is motivated by the

discovery of an afterglow-like soft component during $10^4 - 10^5$ seconds in the nearby GRB 060218 (Campana et al. 2006a). We process the XRT data of this component, and derive a decay slope -1.15 ± 0.15 and the power law photon spectral index 4.32 ± 0.18. This soft component cannot be interpreted within the external shock afterglow model (see also Willingale et al. 2007), and its origin is unknown. A speculation is that it might be related to the GRB central engine (e.g. Fan et al. 2006), whose nature is a great mystery. The most widely discussed GRB central engine is a black hole - torus system or a millisecond magnetar. In either model, there are in principle two emission components (e.g. Zhang & Mészáros 2004 and references therein). One is the "hot" fireball related to neutrino annihilation. This component tends to be erratic, leading to significant internal irregularity and strong internal shocks. This may be responsible for the erratic prompt gamma-ray emission we see. The second component may be related to extracting the spin energy of the central black hole (e.g. Blandford & Znajek 1977; Mészáros & Rees 1997b; Li 2000a) or the spin energy of the central millisecond pulsar (through magnetic dipolar radiation, e.g. Usov 1992; Dai & Lu 1998a; Zhang & Mészáros 2001a). This gives rise to a "cold", probably steady Poynting flux dominated flow. This component provides one possible reason to refresh the forward shock to sustain a shallow decay plateau in early X-ray afterglows (Zhang et al. 2006; Nousek et al. 2006), and it has been invoked to interpret the peculiar X-ray plateau afterglow of GRB 070110 (Troja et al. 2007). These fact make us suspect that at least some of the observed spectrally evolving tails may be due to the superposition of a curvature effect tail and an underlying soft central engine afterglow[5]. In order to explain the observed hard-to-soft spectral evolution the central engine afterglow component should be much softer than the curvature effect component and it gradually dominates the observed tails. Analogous to forward shock afterglows,

[5]O'Brien et al. (2006) and Willingale et al. (2007) interpret the XRT lightcurves as the superpositions between a prompt component and the afterglow component. The putative central engine afterglow component discussed here is a third component that is usually undetectable but makes noticeable contribution to the tails.

we describe the central engine afterglow component with

$$f^u(\nu, t) \propto t^{-\alpha_u} \nu^{-\beta_u}, \tag{3.1}$$

so that the total flux density can be modelled as

$$f(\nu, t) = f^c(\nu, t) + f^u(\nu, t), \tag{3.2}$$

where $f^c(\nu, t)$ is the normal curvature effect component. The spectral index in the XRT band at a given time thus is derived through fitting the spectrum of $\nu f_\nu(t)$ versus ν with a power law, and the observed XRT light curve can be modeled by

$$F_{\rm XRT}(t) = \int_{\rm XRT} [f^c(\nu, t) + f^u(\nu, t)] d\nu. \tag{3.3}$$

We try to search for parameters to fit tails in our Group (B). Although the model can marginally fit some of the tails, we cannot find a parameter regime to reproduce both the lightcurves and observed spectral index evolutions for GRBs 060218 and 060614. We therefore disfavor this model, and suggest that the central engine afterglow emission, if any, is not significant in the GRB tails.

The third scenario is motivated by the fact that the broad-band data of GRB 060218 could be fitted by a cutoff power law spectrum with the cutoff energy moving from high to low energy bands (Campana et al. 2006a; Liang et al. 2006b). We suspect that our Group B tails could be of the similar origin. As a spectral break gradually passes the XRT band, one can detect a strong spectral evolution. We introduce an empirical model to fit the data. The time dependent flux density could be modeled as

$$F_\nu(E, t) = F_{\nu,m}(t) \left[\frac{E}{E_c(t)}\right]^{-\beta} e^{-E/E_c(t)} \tag{3.4}$$

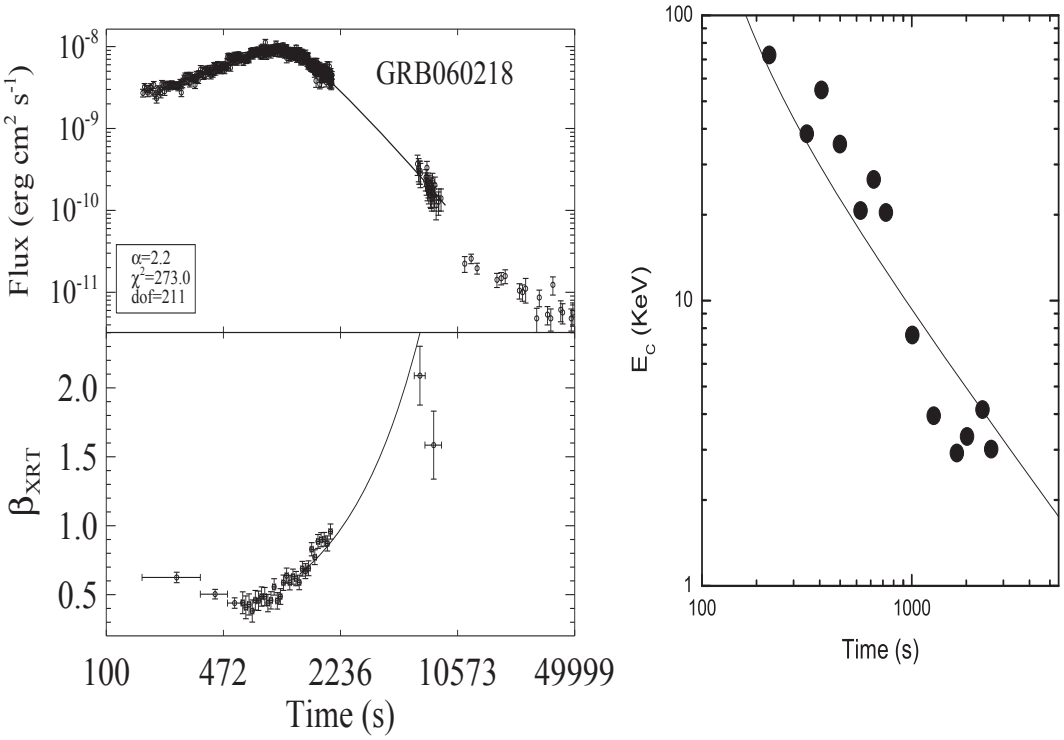

Figure 13 Testing the third empirical model with the broad band data of GRB 060218. *Left*: Comparing the third empirical model prediction (solid lines) with the XRT lightcurve and the spectral evolution derived with the XRT data; *Right*: Comparing the third empirical model prediction (solid line) with the BAT/XRT joint-fit E_c evolution (circles, from Ghisellini et al. 2006, following Campana et al. 2006a).

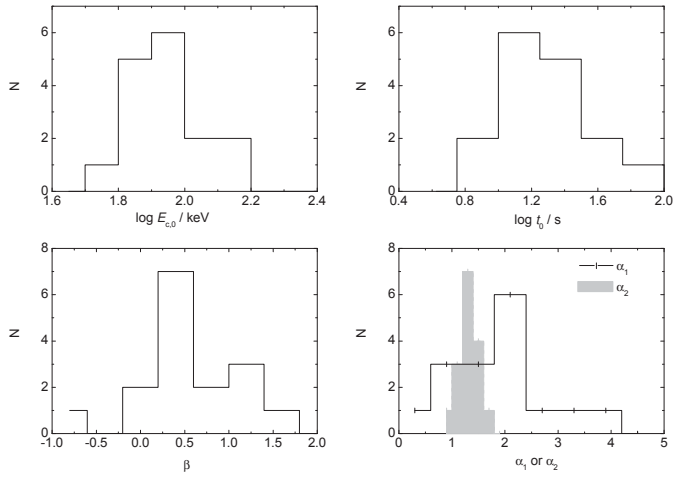

Figure 14 Distributions of the model fitting parameters.

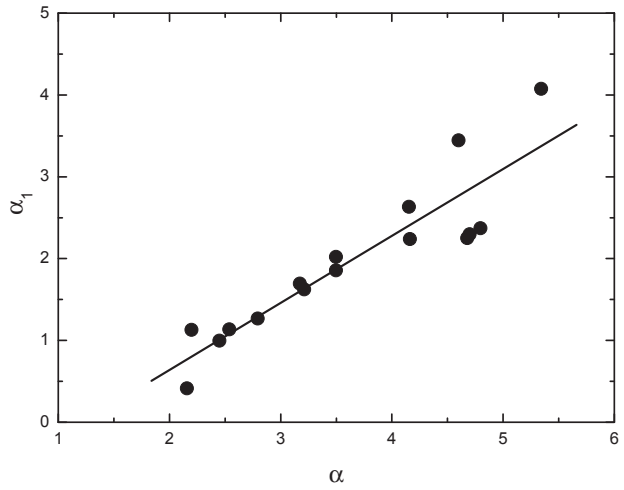

Figure 15 A correlation between the observed tail decay slope α and the decay slope (α_1) of the "spectral amplitude" for the 16 Group B bursts presented in Figure 11. The solid line is the regression line.

where

$$F_{\nu,m}(t) = F_{\nu,m,0}\left(\frac{t-t_0}{t_0}\right)^{-\alpha_1} \tag{3.5}$$

and

$$E_c(t) = E_{c,0}\left(\frac{t-t_0}{t_0}\right)^{-\alpha_2} \tag{3.6}$$

are the temporal evolutions of the peak spectral density and the cutoff energy of the exponential cutoff power law spectrum, respectively. In the model, $t > t_0$ is required, and t_0 is taken as a free parameter. Physically it should roughly correspond to the beginning of the internal shock emission phase, which is near the GRB trigger time. Our fitted t_0 values (Table 1) are typically 10-20 seconds, usually much earlier than the starting time of the steep decay tails, which are consistent with the theoretical expectation. The evolution of E_c has been measured for GRB 060218 (Camapana et al. 2006; Ghisellini et al. 2006; Liang et al. 2006b; Toma et al. 2007). We first test this model with this burst. Our fitting results are shown in Fig. 13. We find that this model well explains the light curve and the spectral evolution of combined BAT-XRT data of GRB 060218. We therefore apply the model to both the light curves and spectral evolution curves of other Group B tails as well (Fig. 11). We do not fit Group C tails (Fig. 12) because of the flare contamination. Our fitting results[6] are displayed in Fig. 11 and are tabulated in Table 1 . The χ^2 and the degrees of the freedom of the fitting to the light curves are also marked in Fig. 11 Although the flickering features in some light curves make the reduced χ^2 much larger than unity, the fittings are generally acceptable, indicating that this model is a good candidate to interpret the data. The distributions of the fitting parameters are shown in Fig. 14. The typical $E_{c,0}$ is about 90 keV at $t_0 \sim 16$ seconds. The distribution of the peak spectral density decay index α_1 has more scatter than the

[6]In principle one should derive the parameters with the combined best fits to both the light curves and β evolutions. This approach is however impractical since the degrees of freedom of the two fits are significantly different. We therefore fit the light curves first, and then refine the model parameters to match the spectral evolution behaviors . The χ^2 reported in Table 1 are calculated with the refined model parameters for the light curves. We cannot constrain the uncertainties and uniqueness of the model parameters with this method

E_c decay index α_2. Interestingly it is found that α_1 is strongly correlated with α, say, $\alpha_1 = (0.82 \pm 0.10)\alpha - (1.00 \pm 0.38)$ (see Fig. 15; the quoted errors are at 1σ confidence level.), with a Spearman correlation coefficient $r = 0.90$ and a chance probability $p < 10^{-4}$ ($N = 16$). This is the simple manifestation of the effect that the faster a burst cool (with a steeper α_1), the more rapidly the tail drops (with a steeper α). The α_2 parameter is around 1.4 as small scatter. This indicates that the evolution behaviors of E_c are similar among bursts, and may suggest a common cooling process among different bursts.

Comparing the three scenarios discussed above, the third empirical model of the prompt emission region is the best candidate to interpret the spectral evolution of the Group B tails. The Group C tails may include additional (but weaker) heating processes during the decay phase (Fan & Wei 2005; Zhang et al. 2006), as have been suggested by the fluctuations and flares on the decaying tails. The steep decay component has been also interpreted as cooling of a hot cocoon around the jet (Pe'er et al. 2006b). This model may be relevant to some tails of the long GRBs, but does not apply to the tails from the bursts of compact star merger origin (such as GRB 050724 and probably also GRB 060614, Zhang et al. 2007b). Another scenario to interpret the tails is a highly radiative blast wave that discharges the hadronic energy in the form of ultra-high energy cosmic ray neutrals and escaping cosmic-ray ions (Dermer 2007). It is unclear, however, whether the model can simultaneously interpret both the observed lightcurves and the spectral evolution curves of these tails. In addition, dust scattering may explain some features of the tails, including the spectral evolution, for some bursts (Shao & Dai 2007).

Butler & Kocevski (2007) used the evolution of the hardness ratio as an indicator to discriminate the GRB tail emission and the forward shock emission. As shown in Fig. 11, the spectra of the tails are significantly different from those of the shallow decay component. Spectral behaviors, including evolution of the hardness ratio, are indeed a good indicator to separate the two emission components. However, no significant difference was observed between the spectra of the tails and the following shallow decay

component for the Group A bursts that show no significant spectral evolution (Fig. 10).

With the observation by CGRO/BATSE, it was found that the prompt GRBs tend to show a spectral softening and a rapid decay (Giblin et al. 2002; Connaughton 2002). Ryde & Svensson (2002) found that about half of the GRB pulses for the BATSE data decay approximately as t^{-3}, and their E_p's also decay as a power law. These results are consistent with the study of X-ray tails in this paper, suggesting a possible common origin of the spectral evolution of GRB emission.

CHAPTER 4

CURVATURE EFFECT OF A NON-POWER-LAW SPECTRUM

This chapter is partially based on the following published paper :

Zhang, B.-B., Zhang, B., Liang, E.-W., & Wang, X.-Y. 2009, The Astrophysical Journal, 690, L10

Introduction

The so called "curvature effect", which accounts for the delayed photon emission from high latitudes with respect to the line of sight upon the abrupt cessation of emission in the prompt emission region (Fenimore et al. 1996; Kumar & Panaitescu 2000a; Dermer 2004; Dyks et al. 2005; Qin 2008), has been suggested to play an important role in shaping the sharp flux decline in GRB tails (Zhang et al. 2006; Liang et al. 2006a; Wu et al. 2006; Yamazaki et al. 2006). In the simplest model, it is assumed that the instantaneous spectrum at the end of the prompt emission is a simple power law with a spectral index β. The predicted temporal decay index of the emission is (with the convention $F_\nu \propto t^{-\alpha}\nu^{-\beta}$)

$$\alpha = 2 + \beta \ , \tag{4.1}$$

if the time origin to define the $\log - \log$ light curve, t_0, is taken as the beginning of the last emission episode before the cessation of emission. Adopting a time-averaged β in the tails, Liang et al. (2006a) found that Eq.(4.1) is generally valid. The strong spectral evolution identified in a group of GRB tails. apparently violates Eq.(4.1), which is valid only for a constant β. These facts, however, do not rule out the curvature effect interpretation of GRB tails. This is because the instantaneous spectrum upon the cessation of prompt emission may not be a simple power law. If the spectrum has a curvature, as the emission from progressively higher latitudes reach the observer, the XRT band is sampling different segments of the intrinsic curved spectrum (Fig.16). This would introduce an apparent spectral evolution in the decaying tail.

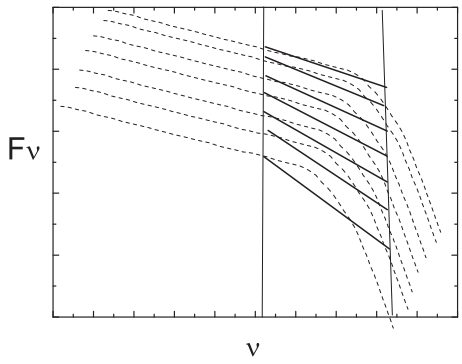

Figure 16 A schematic picture showing that shifting a set of non-power-law spectra in time can equivalently give an apparent spectral evolution in a fixed band. The dashed lines represent a set of exponential-like spectra, whose $F_{\nu_p}(t)$ and $\nu_p(t)$ drop down with time according to Eqs. (4.3) and (4.4). The two vertical solid lines bracket the observed energy band. The thick solid lines denote the effective power law fits to the time-dependent spectra at each time step.

Curvature Effect of a Non-Power-Law Spectrum

We consider a general non-power-law spectrum in the form of

$$F_\nu(\nu) = F_{\nu,c} G(\nu) \ , \tag{4.2}$$

where $G(\nu)$ is the function form of the spectrum with a characteristic frequency ν_c so that $G(\nu_c)$=1, and $F_{\nu,c} = F_\nu(\nu_c)$ is the normalization of the spectrum at $\nu = \nu_c$.

The curvature effect states that given a same spectrum at different latitudes with respect to the line of sight, one has $F_{\nu,c} \propto \mathcal{D}^2$ and $\nu_c \propto \mathcal{D}$, where $\mathcal{D}$ is the Doppler factor. If the high-latitude angle $\theta \gg \Gamma$, the Dopper factor $\mathcal{D} \propto t^{-1}$, so that $F_{\nu,c} \propto t^{-2}$, $\nu_c \propto t^{-1}$ (Kumar & Panaitescu 2000a). Considering the t_0 effect (Zhang et al. 2006; Liang et al. 2006a), this can be written as

$$F_{\nu,c}(t) = F_{\nu,c,p} \left(\frac{t - t_0}{t_p - t_0} \right)^{-2} \tag{4.3}$$

and

$$\nu_c(t) = \nu_{c,p} \left(\frac{t - t_0}{t_p - t_0} \right)^{-1} \tag{4.4}$$

for $t \gg t_p$, where t_0 refers to the time origin of the last pulse in the prompt emission and t_p is the epoch when the curvature-effect decay starts (or the "peak" time of the lightcurve), $F_{\nu,c,p} = F_{\nu,c}(t_p)$ and $\nu_{c,p} = \nu_c(t_p)$. Notice that in the case of $G(\nu) = (\nu/\nu_c)^{-\beta}$ (a pure power law spectrum), one derives $F_\nu \propto (t - t_0)^{-\beta-2}$. This is the relation Eq.(4.1).

We consider several physically motivated non-powerlaw spectra with a characteristic frequency ν_c, including the cut-off power law spectrum and the Band-function (Band et al. 1993). To explore the compatibility with the data, we also investigate different forms of the cutoffs with varying sharpness. In all cases, the $F_{\nu_p}(t)$ and $\nu_p(t)$ follow Eqs.(4.3) and (4.4). When $\nu_c(t)$ drops across an observational narrow energy band, e.g. the Swift/XRT band, it introduces an apparent spectral softening with time, which, if fitted by a power law, shows an increase of photon index with time. In the meantime, the flux within the observing band drops down rapidly, leading to an apparent steep decay phase in the lightcurve (Fig.16).

Simulation Method

We consider a time-dependent cutoff power law photon spectrum taking the form of

$$N(E,t) = N_0(t) \left(\frac{E}{1\ \mathrm{keV}} \right)^{-\Gamma} \exp\left[- \left(\frac{E}{E_c(t)} \right)^k \right] \tag{4.5}$$

where $\Gamma = \beta + 1$ is the power law photon index, and k is a parameter to define the sharpness of the high energy cutoff in the spectrum, $E_c(t)$ is the time-dependent characteristic photon energy, and $N_0(t)$ is a time-dependent photon flux (in units of photons $\cdot\ \mathrm{keV}^{-1}\mathrm{cm}^{-2}\mathrm{s}^{-1}$) at 1 keV (Arnaud 1996). The choice of this function was encouraged by the fact that the spectral evolution of some GRB tails can be fitted by such an empirical model (Campana et al. 2006a; Yonetoku et al. 2008). According to

Eqs.(4.3) and (4.4), and noticing the conversion between the photon flux and the emission flux density, i.e. $F_\nu \propto EN(E)$, we get

$$E_c(t) = E_{c,p}\left(\frac{t-t_0}{t_p-t_0}\right)^{-1} \tag{4.6}$$

and $N(E_c,t) = N_{c,p}\left[(t-t_0)/(t_p-t_0)\right]^{-1}$, where $N_{c,p} = N(E_c,t_p)$, and $E_{c,p} = E_c(t_p)$. This gives

$$N_0(t) = N_{0,p}\left(\frac{t-t_0}{t_p-t_0}\right)^{-(1+\Gamma)} . \tag{4.7}$$

Notice that t_p is the beginning of the steep decay, which is a parameter that can be directly constrained by the data. For a complete lightcurve, we read t_p off from the lightcurve. In the case of an observational gap, usually t_p can be reasonably fixed to the end of the prompt emission. We therefore do not include this parameter into the fits, and derive the other five parameters, namely, $N_{0,p}$, $E_{c,p}$, Γ, t_0, and k from the data. At any time t, the model spectrum can be determined once these parameters are given. One can then confront the model with the real GRB data.

The procedure includes the following steps. (1) For a given burst, we extract its Swift/XRT light curve and n slices of time-dependent spectra using the standard HEASoft/Swift Package. (2) Given a trial set of parameters in the theoretical spectra[1] $\{N_{0,p}$, $E_{c,p}$, Γ, $t_0\}$, using Eqs.(4.5-4.6) we model n time-dependent *theoretical spectra* that correspond to the time bins that are used to derive the time-dependent observed spectra. (3) Based on the theoretical spectra of each time slice, we simulate the corresponding *model spectra* by taking account of the observational effects, including the Swift/XRT response matrix, the absorption column densities (N_H) of both the Milky Way (extracted from the observations from step 1) and the host galaxy of the burst (a free parameter), the redshift (if applicable), and a Poisson noise background. Notice that $n_{H,host}$ is another parameter introduced in the model spectra (besides the other parameters introduced in

[1]Notice that k is fixed to a certain value for a particular model, and is varied when different models are explored.

the theoretical spectra). All these faked spectra can be obtained using HEASoft (Version 6.4) and Xspec (Version 12.4) (4) We fit the faked model spectra with a simple power law model, i.e. $wabs*wabs*powerlaw$ (or $wabs*zwabs*powerlaw$ if the redshift is available) in XSPEC and get the simulated fluxes and spectral indices of the n slices. Here the column densities of both the Milk Way and the host galaxy are fixed to the observed values as in Step 1. (5) We compare the simulated fluxes and spectral indices with the observed ones and access the goodness of the fits using χ^2 statistics. (6) We refine the trial set of parameters based on the comparison and repeat steps (2)-(5) when necessary. We test whether we can reach a set of best-fitting parameters that can reproduce both the light curve and the apparent spectral evolution as observed.

An Example: GRB 050814

We apply the method to GRB050814, a typical burst with well-observed X-ray tail with strong spectral evolution. As seen in Fig.17, the tail has a steep decay index of ~ 3.2, and a strong spectral evolution is apparent at[2] $t < 600$ s. These features are common in most of the GRB X-ray tails. We first fix $k = 1$ in Eq. 4.5, which corresponds to the simplest cutoff powerlaw model. The initial trial parameters we choose are (Γ, $N_{0,p}$, t_0, $E_{p,0}$, $n_{H,host}$) $= (1.2, 0.4, 72.0, 30.0, 0.05)$. The peak time t_p is fixed to 143.6 s, which corresponds to the end of the prompt emission. Some IDL scripts are developed to follow the procedure described above to automatically search for the best-fit parameters to match both the observed light curve and the time-dependent spectral index. The final best-fitting parameters are shown in Table 1. The corresponding simulated light curve (black curve) and spectral indices (green curve) are shown in Fig.17. Figure 17 suggests that the sharp decay and the spectral evolution in the tail of GRB 050814 can be indeed explained by the curvature effect with a cutoff power law spectrum. In Fig.18 we present the comparison between the simulated and observed spectra in the time steps 1 and 6

[2]The PC mode spectra become harder at the end of this tail, which might be due to the contamination of the harder shallow decay component. For simplification, we focus on the WT mode data only.

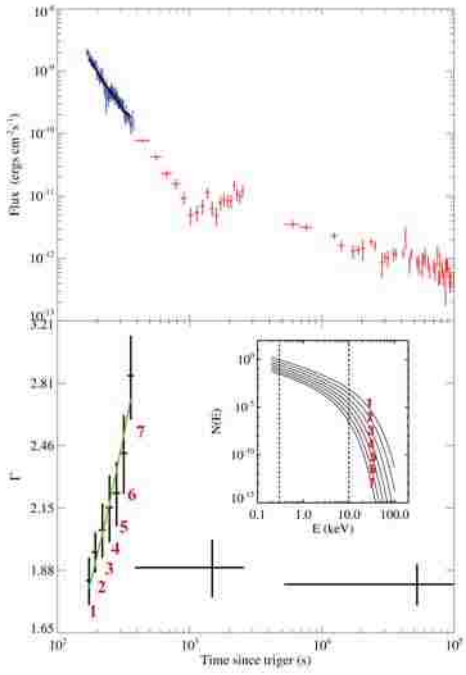

Figure 17 The lightcurve (upper panel) and spectral evolution (lower panel) of the X-ray tail of GRB 050814 with the best-fit theoretical model (black curve in upper panel and green curve in lower panel). The blue and red data points are the window timing and photon counting data, respectively. The inset shows time-dependent theoretical spectra with the XRT band (0.3-10 keV) bracketed by two vertical lines. The integers denote the time segments for the time-resolved spectral analysis.

(as examples), which show reasonable consistency.

Our model predicts that the prompt emission spectrum at $t_p \sim 144$ s should be a cut-off power law with the parameters in Table 1. In order to confirm this, we extract the BAT-band spectrum in the time interval $(141.5 - 146.5)$ s, and compare the data with the model prediction. As shown in Fig.II, the BAT data is roughly consistent with the model prediction, suggesting the validity of the model.

Some physical parameters can be constrained according to our model. The time interval from t_p to the beginning of the steep decay phase $t_{tail,0}$ may be related to the angular spreading time scale $\tau_{ang} = (t_{tail,0} - t_p)/(1+z)$. Noticing $z \sim 5.3$ for GRB050814 (Jakobsson et al. 2005), we can estimate the Lorentz factor of the fireball as $\Gamma =$

Table 1 Best-fitting parameters and their 1-sigma errors for the cutoff power curvature effect model for GRB050814.

$N_{0,p}$	$E_{c,p}$(keV)	Γ	t_0(s)	nH$_{host}$	k	χ^2/dof
0.67(0.12)	10.2(1.3)	1.56(0.25)	103.5(3.4)	0.002(0.04)	1 (fixed)	10.7/9

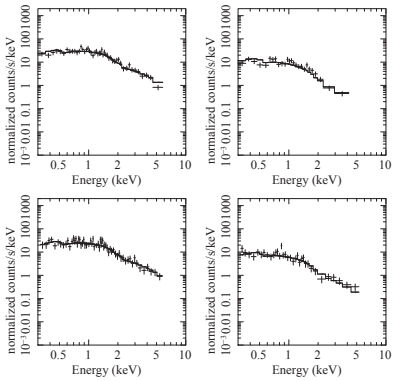

Figure 18 *Upper panel*: Examples of simulated time-dependent spectra of GRB050814 with the best-fit parameters. The time intervals are 1,6 respectively as denoted in Fig.17. In each panel, the data histogram displays the simulated spectrum, and the solid line displays the best-fit ($\chi^2/dof = 39.0/61, 25.2/25$) power law model ($wabs*zwabs*powerlaw$ in XSPEC) that is used to derive the time-dependent photon index Γ. *Lower pabel*: The corresponding observed spectrum in the three time intervals and their power law fits ($\chi^2/dof = 47.1/46, 22.0/19$).

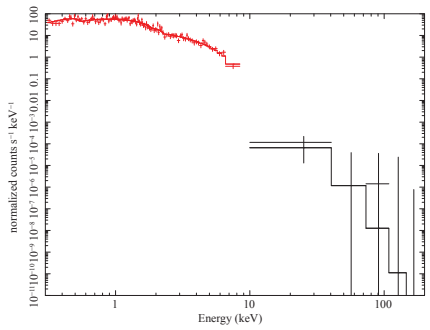

Figure 19 The simulated cut-off power law spectrum at $t_p = 144$ s based on the best fit model confronted by the BAT data in the time interval $(141.5 - 146.5)$ s. The reduced χ^2 of the fitting is 1.2 with dof= 197.

$(R/2c\tau_{ang})^{1/2} \simeq 69 R_{15}^{1/2}$, where $R_{15} = R/(10^{15}$ cm) is the normalized emission radius. Since we know the spectral peak energy E_p at t_p, we can also estimate the corresponding electrons' Lorentz factor for synchrotron emission by $\gamma_{e,p} = \left[E_p/(\hbar\Gamma\frac{eB}{mc})\right]^{1/2} \sim 2.4 \times 10^3 R_{15}^{-1/4} B_3^{-1/2}$. From the rest frame duration of the X-ray tail we are analyzing $\tau_{tail} = (t_{tail,e} - t_{tail,0})/(1+z) \sim (378 - 165)/6.3 = 33.8$ s, one can constrain the minimum jet opening angle as $\theta_j > (2c\tau_{tail}/R)^{1/2} = 2.6^{\rm o} \times R_{15}^{-1/2}$. These values are generally consistent with those derived from various other methods.

We find that the abruptness parameter k cannot be very different from unity. A Band-function spectrum introduces a less significant spectral evolution and it cannot reproduce the data.

Summary

We have successfully modeled the light curve and spectral evolution of the X-ray tail of GRB050814 using the curvature effect model of a cutoff power law spectrum with an exponential cutoff ($k = 1$). It has been discussed in the literature (e.g. Fan & Wei 2005; Barniol-Duran & Kumar 2009) that the GRB central engine may not die abruptly, and that the observed X-ray tails may reflect the dying history of the central engine. If this is indeed the case, the strong spectral evolution in the X-ray tails would demand a

time-dependent particle acceleration mechanism that gives a progressively soft particle spectrum. Such a behavior has not been predicted by particle acceleration theories. Our results suggest that at least for some tails, the spectral evolution is simply a consequence of the curvature effect: the observer views emission from the progressively higher latitudes from the line of sight, so that the XRT band is sampling the different segments of a curved spectrum. This is a simpler interpretation.

The phenomenology of the X-ray tails are different from case to case. We have applied our model to some other clean X-Ray tails, such as GRB050724, GRB080523, and find that they can be also interpreted by this model. Some other tails have superposed X-ray flares, making a robust test of the model difficult. A systematic survey of all the data sample is needed to address what fraction of the bursts can be interpreted in this way or they demand other physically distinct models (e.g. Barniol-Duran & Kumar 2009; Dado et al. 2008).

CHAPTER 5

PHYSICAL ORIGINS OF THE SHALLOW DECAY SEGMENT

This chapter is partially based on the following published paper :

Liang, E.-W., Zhang, B.-B., & Zhang, B. 2007, The Astrophysical Journal, 670, 565.

Statement of coauthorship: This work was led by E.-W. Liang. I processed all the Swift/XRT data, provided the XRT light curves and spectral fitting results that were essentially needed by this work. Based on my data output, our discussion and my frequent feedback, En-Wei led the rest parts of this work which included fitting the light curves, deriving the physical parameters and comparing the results with different theoretical models.

Introduction

Shallow decay phase is generally believed to be related to the energy injection models (Zhang et al. 2006; Nousek et al. 2006; Panaitescu et al. 2006a). Besides that, there are several other models have been proposed to interpret the shallow decay phase (e.g. Zhang 2007 for a review), which include the combination of the GRB tail with the delayed onset of the afterglow emission (Kobayashi & Zhang 2007); off-beam jet model (Toma et al. 2006; Eichler & Granot 2006); pre-cursor model (Ioka et al. 2006); two-component jet (Granot et al. 2006; Jin et al. 2007), varying microphysics parameter model (Ioka et al. 2006; Panaitescu et al. 2006b; Fan & Piran 2006; Granot et al. 2006), etc. The chromaticity of some X-ray shallow-to-normal breaks drives several ideas that go beyond the traditional external forward shock model. For example, Shao & Dai (2007) interpret the X-ray lightcurve as due to dust scattering of some prompt X-rays, so that it has nothing to do with the external shock. Uhm & Beloborodov (2007) and Genet, Daigne & Mochkovitch (2007) interpret both X-ray and optical afterglow as emission from a long-lived reverse shock. Ghisellini et al. (2007a) even suggested that the shallow-to-normal transition X-ray afterglows may be produced by late internal shocks, and the end of this

phase is due to the jet effect in the prompt ejecta (see also Nava et al. 2007).

In this work we systematically analyzed the shallow decay phase data for a large sample of GRBs. In particular, it is desirable to find out how bad the standard external forward shock model is when confronted with the data, e.g. what fraction of bursts actually call for models beyond the standard external forward shock model.

Data Reduction and Sample Selection

We process all the XRT data observed between Feb., 2005 and Jan., 2007. We inspect all the light curves to identify the beginning (t_1) of the shallow decay segment and the end (t_2) of the decay phase following the shallow phase (which usually is the normal decay phase, but in some cases the decay slope could be much steeper). Generally, t_1 is taken as the end of the steep decay segment or the beginning of the observation time, unless significant flares or high level emission bumps following the GRB tails were observed. The ending time t_2 is generally taken as the end of the observation time.

We use a smoothed broken power law to fit the light curve in the time interval $[t_1, t_2]$,

$$F = F_0 \left[\left(\frac{t}{t_{\rm b}} \right)^{\omega\alpha_1} + \left(\frac{t}{t_{\rm b}} \right)^{\omega\alpha_2} \right]^{-1/\omega}, \tag{5.1}$$

where ω describes the sharpness of the break. The larger the ω, the sharper the break. In order to constrain ω it is required that the time interval covers a range from $t_1 \ll t_b$ to $t_2 \gg t_b$, and that the light curve around t_b is well-sampled. The parameter t_b is not significantly affected by ω, but both α_1 and α_2 are.

The $t_{\rm b}$ is roughly considered as the duration of the shallow decay phase. As suggested by Lazzati & Begelman (2006) and Kobayashi & Zhang (2007), the zero time of the external-origin power-law segments should be roughly the BAT trigger time. In our calculation, in order to account for the onset of the afterglow we take a t_0 as 10 seconds after the GRB trigger. The X-ray fluence (S_X) of the shallow decay phase is derived by integrating the fitting light curve from 10 seconds post the GRB trigger to $t_{\rm b}$ without

considering the contributions of both early X-ray flares and the GRB tail emissions. Since the shallow decay phase has a temporal decay index shallower than -1, the results are not sensitive to the choice of t_0. We estimate the uncertainty of S_X with a boostrap method based on the errors of the fitting parameters, assuming that the errors of the fitting parameters, $\sigma_{\log F_0}$, $\sigma_{\log t_{\rm b}}$, σ_{α_1}, and σ_{α_2}, are of Gaussian distributions. We generate 5×10^3 parameter sets of (F_0, $t_{\rm b}$, α_1, α_2) from the distributions of these parameters for each burst, and then calculate $S_{\rm X}$ for each parameter set. We make a Gaussian fit to the distribution of $\log S_{\rm X}$ and derive the central value of $\log S_{\rm X}$ and its error $\sigma_{\log S_{\rm X}}$. In our fittings, α_1 and/or t_b are fixed for GRBs 050801 and 060607A. We do not calculate the errors for the two bursts.

We use the following criteria to select our sample. (1) The XRT light curves have a shallow decay segment following the GRB tails.We require that the so-called shallow decay segment has a slope $\alpha_{\rm X,1} < 0.75$ at 1σ error. (2) Both the shallow decay segment and the follow-up segment are bright enough to perform spectral analysis.

Systematically going through all the *Swift* XRT data before Feb. 2007 we use the above criteria to compile a sample of 53 bursts. Some example of the XRT light curves and the fitting results are shown in Fig. 20, and the data are summarized in Table 2. We also collect the BAT observations of these bursts from GCN circular reports. We search the optical afterglow data of these bursts from published papers and GCN circular reports. We identify a burst as optically bright, if three or more detections in the UV-optical bands were made. We find that 30 out of the 53 bursts are optically bright, but only 15 bursts have an optical light curve with good temporal coverage. We make the Galactic extinction correction and convert the observed magnitudes to energy fluxes. We fit these light curves with a simple power law or the smooth broken power law (ω is also fixed as 3). The fitting results are summarized in Table 3. We directly compare the optical data with the XRT data in Fig. 20 in order to perform a quick visual check of achromaticity of these light curves. If multi-wavelength optical light curves are available,

we show only the one that was observed around the X-ray shallow decay phase with the best sampling.

Table 2 XRT observations and the fitting results of our sample

GRB	t_1(ks)[a]	t_2(ks)[a]	t_b(ks)[b]	$\alpha_{X,1}$ [b]	$\alpha_{,2}$ [b]	χ^2(dof)[b]	S_X[c]	$\Gamma_{X,1}$[d]	$\Gamma_{X,2}$[d]
050128	0.25	70.72	2.76(0.62)	0.49(0.07)	1.26(0.03)	40(48)	3.70(1.07)	1.87(0.14)	1.95(0.06)
050315	5.40	450.87	224.64(38.68)	0.66(0.03)	1.90(0.28)	42(52)	10.88(2.56)	2.06(0.11)	2.18(0.08)
050318	3.34	45.19	10.64(4.97)	0.90(0.23)	1.84(0.19)	27(20)	5.92(6.32)	2.09(0.08)	2.02(0.06)
050319	6.11	84.79	11.20(13.26)	0.23(0.59)	0.99(0.25)	9(9)	1.26(1.42)	2.00(0.06)	2.04(0.07)
050401	0.14	801.04	5.86(0.78)	0.57(0.02)	1.37(0.06)	106(92)	9.32(1.31)	1.91(0.05)	1.99(0.11)
050416A	0.25	261.69	1.74(1.12)	0.43(0.12)	0.90(0.04)	36(38)	0.62(0.38)	2.18(0.31)	2.15(0.10)
050505	3.07	97.19	7.87(1.57)	0.15(0.19)	1.30(0.06)	26(45)	2.34(0.68)	2.00(0.07)	2.03(0.04)
050713B	0.79	478.50	10.80(1.59)	-0.00(0.07)	0.94(0.04)	40(63)	3.28(0.35)	1.85(0.10)	1.94(0.09)
050726	0.42	17.05	1.17(0.33)	0.08(0.33)	1.31(0.09)	13(21)	1.17(0.53)	2.25(0.07)	2.07(0.06)
050801	0.07	46.10	0.25(fixed)	0.00(fixed)	1.10(0.03)	44(45)	0.16(0.01)	1.70(0.19)	1.91(0.12)
050802	0.51	83.83	4.09(0.61)	0.32(0.10)	1.61(0.04)	58(72)	3.66(0.94)	1.91(0.06)	1.89(0.07)
050803	0.50	368.89	13.71(0.90)	0.25(0.03)	2.01(0.07)	94(57)	5.96(0.51)	1.76(0.14)	2.00(0.08)
050822	6.41	523.32	66.99(44.38)	0.60(0.10)	1.25(0.19)	29(44)	4.05(3.12)	2.29(0.13)	2.36(0.11)
051008	3.09	43.77	14.67(3.82)	0.78(0.11)	1.96(0.21)	17(19)	6.87(3.43)	2.00(0.11)	2.06(0.07)
051016B	4.78	150.47	66.40(23.09)	0.71(0.08)	1.84(0.46)	15(16)	2.18(1.10)	2.15(0.13)	2.19(0.13)
051109A	3.73	639.16	27.28(7.90)	0.79(0.07)	1.53(0.08)	39(48)	10.59(4.71)	1.91(0.07)	1.90(0.07)
060105	0.10	360.83	2.31(0.14)	0.84(0.01)	1.72(0.02)	653(754)	42.98(3.84)	2.23(0.05)	2.15(0.03)
060108	0.77	165.26	22.08(7.38)	0.26(0.09)	1.43(0.17)	7(7)	0.53(0.17)	2.17(0.32)	1.75(0.15)
060109	0.74	48.01	4.89(1.10)	-0.17(0.14)	1.32(0.09)	19(13)	0.91(0.20)	2.32(0.15)	2.34(0.14)
060124	13.30	664.01	52.65(10.33)	0.78(0.10)	1.65(0.05)	165(132)	29.65(12.09)	2.10(0.03)	2.08(0.06)
060204B	4.06	98.80	5.55(0.66)	-0.59(0.72)	1.45(0.07)	21(34)	0.87(0.36)	2.54(0.14)	2.77(0.18)
060210	3.90	861.94	24.24(5.01)	0.63(0.05)	1.38(0.05)	144(133)	10.41(2.90)	2.06(0.03)	2.12(0.09)
060306	0.25	124.39	4.67(2.91)	0.40(0.11)	1.05(0.07)	30(32)	1.58(0.98)	2.09(0.16)	2.21(0.10)
060323	0.33	16.28	1.29(0.32)	-0.11(0.23)	1.55(0.16)	4(7)	0.27(0.08)	1.99(0.16)	2.02(0.13)

Table 2 - continued

GRB	t_1(ks)[a]	t_2(ks)[a]	t_b(ks)[b]	$\alpha_{X,1}$ [b]	$\alpha_{,2}$ [b]	χ^2(dof)[b]	S_X[c]	$\Gamma_{X,1}$[d]	$\Gamma_{X,2}$[d]
060413	1.20	253.52	26.43(1.12)	0.18(0.03)	3.42(0.21)	78(71)	13.77(0.82)	1.60(0.08)	1.50(0.10)
060428A	0.23	271.10	11.04(6.58)	0.27(0.09)	0.88(0.08)	25(21)	3.79(1.74)	2.11(0.24)	2.05(0.14)
060502A	0.24	593.06	72.57(15.05)	0.53(0.03)	1.68(0.15)	11(26)	5.09(1.19)	2.20(0.12)	2.15(0.13)
060507	3.00	86.09	6.95(1.68)	-0.37(0.48)	1.25(0.09)	2(8)	0.40(0.16)	2.15(0.19)	2.13(0.12)
060510A	0.16	343.41	9.18(0.67)	0.10(0.03)	1.51(0.03)	93(142)	17.28(1.65)	1.91(0.09)	1.96(0.06)
060522	0.20	0.90	0.53(0.06)	0.14(0.36)	3.15(0.79)	11(11)	0.26(0.12)	2.03(0.16)	2.13(0.30)
060526	1.09	322.75	10.02(4.55)	0.30(0.12)	1.50(0.23)	34(48)	0.79(0.32)	2.08(0.09)	2.08(0.16)
060604	3.52	403.81	11.37(6.80)	0.19(0.48)	1.17(0.08)	34(41)	0.79(0.67)	2.44(0.15)	2.43(0.17)
060607A	1.52	39.52	12.34(0.19)	0.00(fixed)	3.35(0.09)	132(139)	8.45(0.17)	1.44(0.06)	1.64(0.05)
060614	5.03	451.71	49.84(3.62)	0.18(0.06)	1.90(0.07)	70(54)	4.35(0.49)	2.02(0.02)	1.93(0.06)
060707	5.32	813.53	22.21(54.08)	0.37(0.96)	1.09(0.17)	8(11)	0.64(2.01)	1.88(0.09)	2.06(0.20)
060708	3.81	439.09	6.66(3.84)	0.49(0.54)	1.30(0.09)	39(34)	0.96(1.06)	2.41(0.17)	2.28(0.12)
060714	0.32	331.97	3.70(0.97)	0.34(0.10)	1.27(0.05)	53(73)	1.48(0.46)	2.15(0.08)	2.04(0.11)
060719	0.28	182.15	9.57(2.70)	0.40(0.06)	1.31(0.10)	19(26)	1.30(0.37)	2.35(0.13)	2.38(0.26)
060729	0.42	2221.24	72.97(3.02)	0.21(0.01)	1.42(0.02)	459(459)	19.58(0.83)	3.35(0.04)	2.26(0.05)
060804	0.18	122.07	0.86(0.22)	-0.09(0.15)	1.12(0.07)	18(24)	0.97(0.18)	2.04(0.23)	2.14(0.15)
060805A	0.23	75.91	1.30(0.70)	-0.17(0.41)	0.97(0.13)	11(17)	0.06(0.03)	2.10(0.10)	1.97(0.37)
060807	0.28	166.22	8.04(0.35)	0.06(0.03)	1.73(0.05)	67(36)*	1.94(0.11)	2.30(0.28)	2.22(0.08)
060813	0.09	74.25	1.77(0.27)	0.55(0.03)	1.25(0.03)	86(75)	7.31(1.36)	2.09(0.16)	2.04(0.04)

Table 2 - continued

GRB	t_1(ks)[a]	t_2(ks)[a]	t_b(ks)[b]	$\alpha_{\rm X,1}$ [b]	$\alpha_{,2}$ [b]	χ^2(dof)[b]	S_X[c]	$\Gamma_{\rm X,1}$[d]	$\Gamma_{\rm X,2}$[d]
060814	0.57	399.37	17.45(1.71)	0.54(0.02)	1.59(0.05)	81(57)	6.93(0.87)	2.11(0.09)	2.30(0.05)
060906	1.32	36.69	13.66(3.29)	0.35(0.10)	1.97(0.36)	3(7)	0.96(0.29)	2.28(0.37)	2.12(0.17)
060908	0.08	363.07	0.95(0.34)	0.70(0.07)	1.49(0.09)	98(59)*	1.28(0.61)	2.41(0.21)	2.00(0.08)
060912	0.42	86.80	1.13(0.31)	0.13(0.30)	1.19(0.08)	8(26)	0.37(0.15)	2.08(0.11)	1.95(0.13)
061021	0.30	594.16	9.59(2.17)	0.52(0.03)	1.08(0.03)	94(87)	3.59(0.87)	1.81(0.04)	1.70(0.13)
061121	4.89	353.10	24.32(4.38)	0.75(0.06)	1.63(0.05)	121(147)	19.89(6.14)	2.00(0.04)	1.93(0.05)
061202	0.93	357.04	41.65(5.36)	0.10(0.04)	2.20(0.18)	55(49)	13.80(1.12)	2.15(0.09)	3.55(0.44)
061222A	22.78	724.64	32.73(2.17)	-0.61(0.45)	1.75(0.04)	102(59)*	6.62(1.89)	2.46(0.07)	2.22(0.12)
070110	4.10	28.72	20.40(0.44)	0.11(0.05)	8.70(0.88)	43(66)	3.59(0.23)	2.16(0.11)	2.21(0.09)
070129	1.32	546.36	20.12(3.14)	0.15(0.07)	1.31(0.06)	42(70)	1.47(0.24)	2.25(0.07)	2.30(0.10)

[a]The starting and ending time of our lightcurve fitting

[b]The break time and the decay slopes before and after the break, and the fitting χ^2 (degrees of freedom).

[c]The X-ray fluence (in units of 10^{-7} erg cm^{-2}) of the shallow decay phase calculated by integrating the fitting light curve from 10 seconds post the GRB trigger to t_b.

[d]The X-ray photon indices before and after t_b.

*The fitting results of these bursts have an unaccepted reduced χ^2 due to significant flicking.

Table 3 The optical observations and our fitting results

GRB	t_1(ks)[a]	t_2(ks)[a]	$t_{b,O}$(ks)[b]	$\alpha_{O,1}$[b]	$\alpha_{O,2}$[b]	χ^2/(dof) [b]	ref
050318	3.23	22.83	-	0.84(0.22)	-	0.5(1)	(1)
050319	2.00	204.74	-	0.42(0.02)	-	11(16)	(2)-(4)
050401	0.06	1231.18	-	0.80(0.01)	-	43(12)	(5)-(7)
050801	0.02	9.49	0.19(0.02)	-0.02(0.07)	1.10(0.02)	26(42)	(8)
050802	0.34	127.68	-	0.85(0.02)	-	50(10)	(9)-(11)
051109A	0.04	20170.00	21.80(10.95)	0.66(0.02)	1.10(0.08)	106(42)	(12)
060124	3.34	1979.30	-	0.85(0.02)	-	11(19)	(13)-(14)
060210	0.09	7.19	0.70(0.18)	0.01(0.24)	1.23(0.08)	5(12)	(15)-(16)
060526	0.06	893.55	84.45(5.88)	0.67(0.02)	1.80(0.04)	116(56)	(17)
060607A	0.07	13.73	0.16(fixed)	-3.07(0.25)	1.18(0.02)	92(35)	(18)
060614	1.54	934.36	39.09(1.71)	-0.40(0.05)	2.16(0.03)	114(24)	(19)-(21)
060714	3.86	285.87	1.00	0.01(fixed)	1.41(0.03)	35(11)	(22)-(26)
060729	20.00	662.39	43.29(5.15)	-0.37(0.34)	1.34(0.06)	36(27)	(27)
061121	0.26	334.65	1.70(0.73)	0.17(fixed)	0.99(0.05)	18(23)	(28)
070110	0.66	34.76	-	0.43(0.08)		1(4)	29

[a]The time interval concerned in our fitting

[b]For a smooth broken power law fit, $t_{b,O}$, $\alpha_{O,1}$, $\alpha_{O,2}$ are the break time and the decay slopes before and after the break. For a simple power law fit, the decay index and its error are shown in column $\alpha_{O,1}$. In order to make the fittings more reasonable, we assume an error of 0.1 mag for those data points without observational error available.

Twenty-seven out of the 53 GRBs in our sample have redshift measurements. Table 4 reports the properties of these bursts in the burst rest frame, including the durations ($T_{90}^{'}$ and $t_{\rm b}^{'}$) and the equivalent-isotropic radiation energies ($E_{\rm iso,\gamma}$ and $E_{\rm iso,X}$) in the prompt phase and in the shallow decay phase, and the peak energy of the νf_ν spectrum ($E_{\rm p}^{'}$). The $E_{\rm iso,\gamma}$ and $E_{\rm iso,X}$ are calculated by

$$E_{\rm iso,(\gamma,X)} = \frac{4\pi D_L^2 S_{(\gamma,X)}}{1+z}, \tag{5.2}$$

where S_γ is the gamma-ray fluence in the BAT band and S_X is the X-ray fluence in the shallow decay phase in the XRT band, and D_L is the luminosity distance of the source. Due to the narrowness of the BAT band, the BAT data cannot well constrain the spectral parameters of GRBs (Zhang et al. 2007a). Generally the BAT spectrum can be fitted by a simple power law, and the power law index Γ is correlated with $E_{\rm p}$ (Zhang et al. 2007b; see also Sakamoto et al. 2008; Cabrera et al.2007)[1], i.e.,

$$\log E_p = (2.76 \pm 0.07) - (3.61 \pm 0.26) \log \Gamma. \tag{5.3}$$

We estimate $E_{\rm p}$ with this relation if it is not constrained by the BAT data. We then calculate the *bolometric* energy $E_{\rm iso,\gamma}^b$ in the $1 - 10^4$ keV band with the k-correction method used by Bloom et al. (2001), assuming that the photon indices are -1 and -2.3 before and after $E_{\rm p}$, respectively (Preece et al. 2000). Both $E_{\rm p}^{'}$ and $E_{\rm iso,\gamma}^b$ are listed in Table 5.

[1]We should point out that this empirical relation is for BAT observations only. The origin of this relation is due to the narrowness of the BAT instrument. It can be robustly used for those bursts whose $E_{\rm p}$ are roughly within the BAT band.

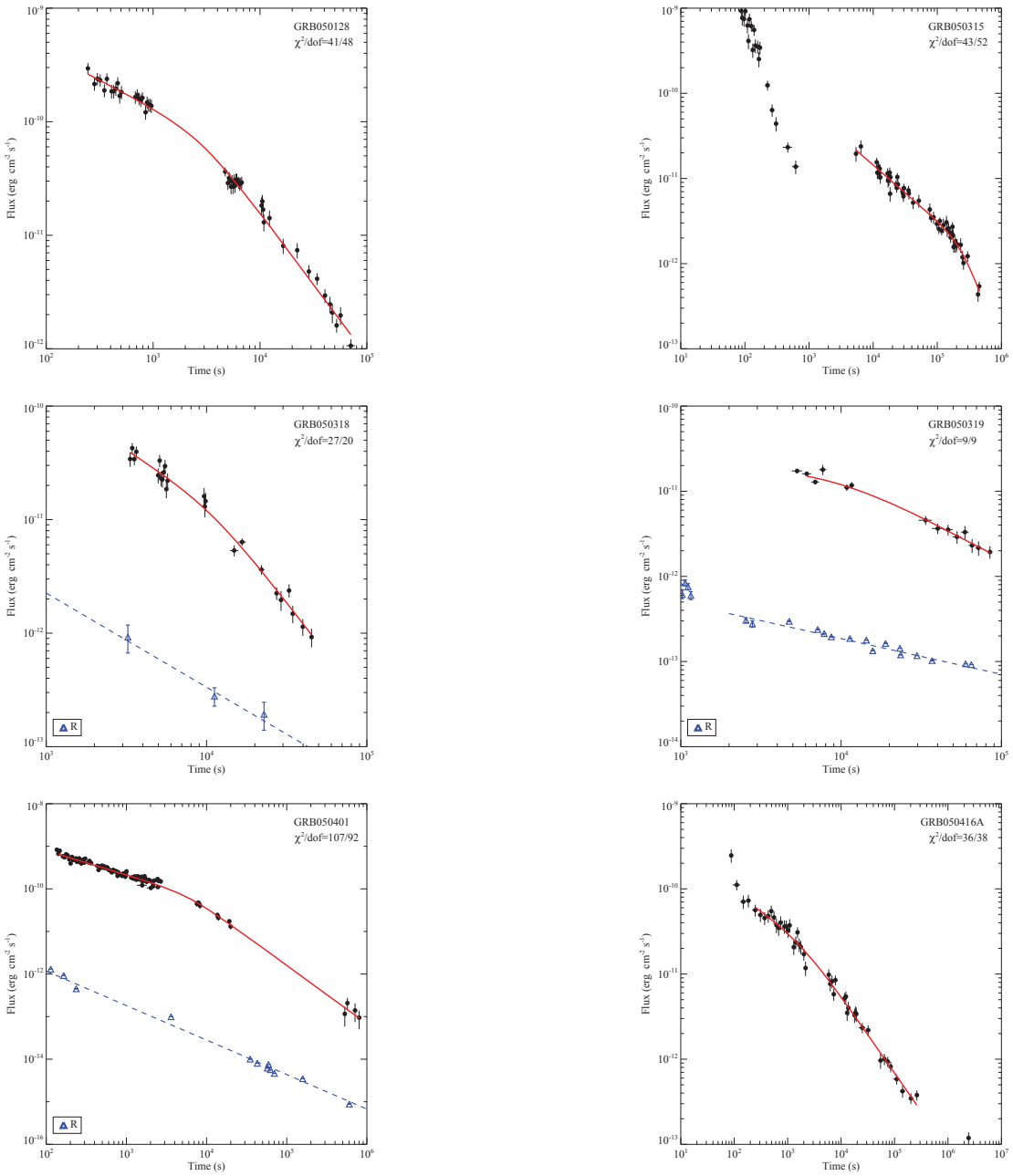

Figure 20 Examples of the XRT light curves (dots) for the bursts in our sample. The *solid* lines are the best fits with the smooth broken power law for the shallow decay phase and its follow-up decay phase (usually the "normal" decay phase). The fitting χ^2 and degrees of freedom are shown in each plot. The optical light curves are shown by opened triangles, if they are available. They are fitted by a smooth broken power law or a simple power law as displayed by dashed lines.

Table 4 Rest-frame properties of the bursts with known redshifts in our sample.

GRB	$\log T_{90}^{'}$(s)	$\log E_{\rm p}^{'}$(keV)	$\log E_{\rm iso,\gamma}$(erg)	$\log E_{\rm iso,\gamma}^{p}$(erg)	$\log E_{\rm iso,X}$(erg)	$\log t_{\rm b}^{'}$(s)
050315	1.51(0.05)	2.0(0.1)	52.41(0.05)	52.84	51.94(0.10)	4.83(0.07)
050318	1.12(0.03)	2.0(0.1)	52.04(0.04)	52.38	51.88(0.46)	4.03(0.20)
050319	0.37(0.09)	2.1(0.1)	52.24(0.04)	52.69	52.03(0.49)	4.01(0.51)
050401	0.93(0.03)	2.7(0.1)	53.41(0.04)	53.69	52.82(0.06)	3.77(0.06)
050416A	0.16(0.04)	1.4(0.1)	50.62(0.05)	51.00	49.69(0.26)	2.88(0.28)
050505	1.06(0.01)	2.8(0.1)	53.14(0.04)	53.51	52.62(0.13)	3.90(0.09)
050802	0.68(0.07)	2.5(0.3)	52.31(0.05)	52.62	51.86(0.11)	3.61(0.06)
050803	1.89(0.04)	2.3(0.2)	51.24(0.03)	51.67	50.29(0.04)	3.85(0.03)
051016B	0.32(0.01)	1.7(0.2)	50.59(0.05)	50.95	50.99(0.22)	4.82(0.15)
051109A	1.03(0.02)	2.6(0.2)	52.43(0.06)	52.82	52.65(0.19)	4.44(0.13)
060108	0.68(0.03)	2.1(0.2)	51.56(0.05)	51.89	51.20(0.14)	4.34(0.15)
060124	2.38(0.01)	3.0(0.4)	53.13(0.04)	53.72	53.08(0.18)	4.72(0.09)
060210	1.72(0.02)	2.8(0.1)	53.36(0.02)	53.72	53.18(0.12)	4.38(0.09)
060502A	1.12(0.07)	2.6(0.1)	52.10(0.02)	52.54	51.82(0.10)	4.81(0.09)
060522	1.05(0.03)	2.8(0.2)	52.69(0.04)	53.03	51.29(0.19)	2.16(0.05)
060526	0.52(0.06)	2.6(0.2)	52.02(0.05)	52.36	51.21(0.26)	3.38(0.25)
060604	0.43(0.13)	2.3(0.4)	51.32(0.10)	51.64	50.88(0.37)	3.27(0.26)
060607A	1.39(0.02)	2.8(0.1)	52.72(0.02)	53.12	52.84(0.01)	4.09(0.01)
060614	1.96(0.02)	1.6(0.1)	50.90(0.01)	51.24	49.25(0.05)	4.70(0.03)
060707	1.19(0.03)	2.5(0.2)	52.61(0.05)	52.98	51.44(1.36)	3.95(1.06)
060714	1.49(0.02)	2.3(0.1)	52.69(0.03)	53.01	51.95(0.14)	3.57(0.11)
060729	1.88(0.04)	2.0(0.2)	51.31(0.03)	51.65	51.35(0.02)	4.86(0.02)
060906	0.97(0.01)	2.3(0.1)	52.78(0.03)	53.09	51.57(0.13)	3.62(0.10)
060908	0.75(0.01)	2.8(0.1)	52.59(0.01)	53.07	51.12(0.21)	2.32(0.16)
060912	0.41(0.04)	2.2(0.1)	51.47(0.03)	51.83	50.21(0.17)	3.05(0.12)
061121	1.54(0.03)	2.6(0.1)	52.78(0.01)	53.23	51.83(0.13)	3.90(0.08)
070110	1.40(0.03)	2.6(0.1)	52.31(0.03)	52.68	52.19(0.03)	4.31(0.01)

The Characteristics of the Shallow Decay Phase and its Relations to the Prompt Gamma-ray Phase

We display the distributions of the characteristics of the shallow decay phase in Fig. 21. It is found that these distributions are consistent with being normal/lognormal, i.e. $\log t_{\rm b}/s = 4.09 \pm 0.61$, $\log S_X/{\rm erg\ cm^{-2}} = -6.52 \pm 0.69$, $\Gamma_{\rm X,1} = 2.09 \pm 0.21$, and $\alpha_1 = 0.35 \pm 0.35$. Quoted errors are at 1σ confidence level.

We investigate the relation of the shallow decay phase to the prompt gamma-ray phase. Figure 22 shows $t_{\rm b}$, S_X, $\Gamma_{\rm X,1}$, and $E_{\rm iso,X}$ as functions of T_{90}, S_γ, Γ_γ, and $E_{\rm iso,\gamma}$, respectively. No correlation between Γ_γ and $\Gamma_{\rm X,1}$ is observed. However, $\Gamma_{\rm X,1}$ is larger than Γ_γ, except for some X-ray flashes (XRFs), indicating that the photon spectrum of the shallow decay phase is generally steeper than that of the prompt gamma-ray phase for typical GRBs.

From Fig. 22 we find tentative correlations of durations, energy fluences, and isotropic energies between the gamma-ray and X-ray phases. The best fits yield $\log t_{\rm b} = (0.61 \pm 0.16) \log T_{90} + (3.00 \pm 0.27)$ ($r = 0.48$ and $p = 0.003$ for $N = 53$), $\log S_X = (0.76 \pm 0.11) \log S_\gamma + (-2.33 \pm 0.60)$ ($r = 0.70$ and $p < 10^{-4}$ for $N = 53$), and $\log E_{\rm iso,X} = (1.00 \pm 0.16) \log E_{\rm iso,\gamma} + (-0.50 \pm 8.10)$ ($r = 0.79$ and $p < 10^{-4}$ for $N = 27$). It is found that $t_{\rm b}$ weakly depends on T_{90}. However, X-ray fluence and isotropic energy are almost linearly correlated with gamma-ray fluence and gamma-ray energy, respectively. $E_{iso,\gamma}$ is greater than $E_{X,iso}$ for most of the bursts, but for a few cases $E_{iso,X}$ is even larger than $E_{\gamma,iso}$.

Testing the Physical Origin of the Shallow Decay Segment

Without broadband afterglow modeling, the "closure relations" between the observed spectral index β and temporal decay index α present a simple test to the models. Although the mechanism of energy injection into the forward shock could vary (e.g. Rees & Mészáros 1998; Dai & Lu 1998a,b; Zhang & Mészáros et al. 2001a; Yu & Dai 2007), the

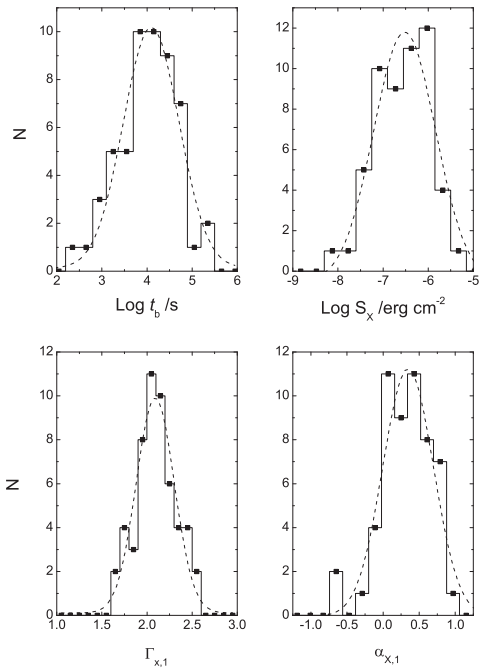

Figure 21 Distributions of the characteristics of the shallow decay segment for the bursts in our sample. The dashed lines are the fitting results with Gaussian functions.

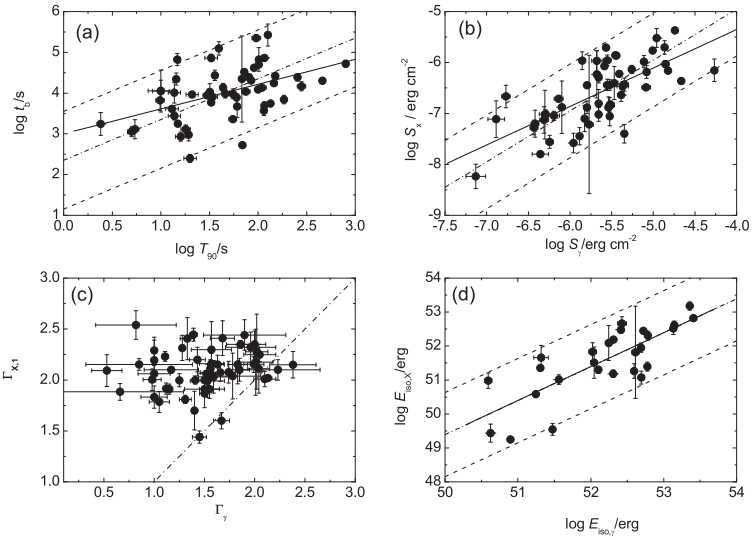

Figure 22 The correlations between the data of the shallow decay phase and the prompt gamma-ray phase. The *solid* line in each panel is the best fit. The *dashed* lines mark a 2σ region defined as $y = x + (A \pm 2 \times \sigma_A)$, where y and x are the quantities in the y and x-axes, respectively, and A and σ_A are the mean and its 1σ standard error of $y - x$, respectively. The *dash-dotted* line is $y = x$.

kinetic energy of the fireball after the energy injection is over should be constant and this "normal" decay phase should be explained with the standard external shock models. In Fig. 23, we present $\alpha_{\rm X,2}$ as a function of spectral index $\beta_{\rm X,2}$, where $\beta_{\rm X,2} = \Gamma_{\rm X,2} - 1$. The closure correlations of the external shock afterglow models for different spectral regimes, different cooling schemes, different ambient medium properties, and different electron distributions (the spectral index $p > 2$ and $p < 2$) are shown in Fig. 23. The fact that the observed $\beta_{X,2}$ is greater than 0.5 for the bursts in our sample suggests that these X-rays are in the spectral regime $\nu_X > \max(\nu_m, \nu_c)$ (Regime I) or $\nu_m < \nu_X < \nu_c$ (Regime II), where ν_m and ν_c are the characteristic frequency and cooling frequency of synchrotron radiation. The relation between α and β for the spectral Regime I is $\alpha = (3\beta - 1)/2$ regardless of the type of the medium (ISM or wind medium). If the X-ray band is in the Regime II, we have $\alpha = 3\beta/2$ (for ISM) and $\alpha = (3\beta + 1)/2$ (for wind).

The spectral index and temporal decay slope of the normal decay phase for most bursts in our sample (49 out of 53 bursts) are roughly consistent with the closure relations of the external shock models. This further favors the idea that the shallow decay segment is also of external shock origin, and probably is related to a long-term energy injection effect.

GRBs 060413, 060522, 060607A, and 070110 have a plateau with a step-like sharp drop ($\omega = 10$ is required in our data fitting). Those sharp drop segment and its prior plateau in these bursts are very likely not of external shock origin. A common signature of these internal-origin plateaus is that the flux almost keeps constant on the plateau but with significant flickering. Although it may not be unreasonable to interpret it as late internal shocks (which usually give rise to erratic collisions within the ejecta and may power X-ray flares), another possibility is that the plateau is powered by tapping the spindown energy of the central engine, as suggested by Troja et al. (2007).

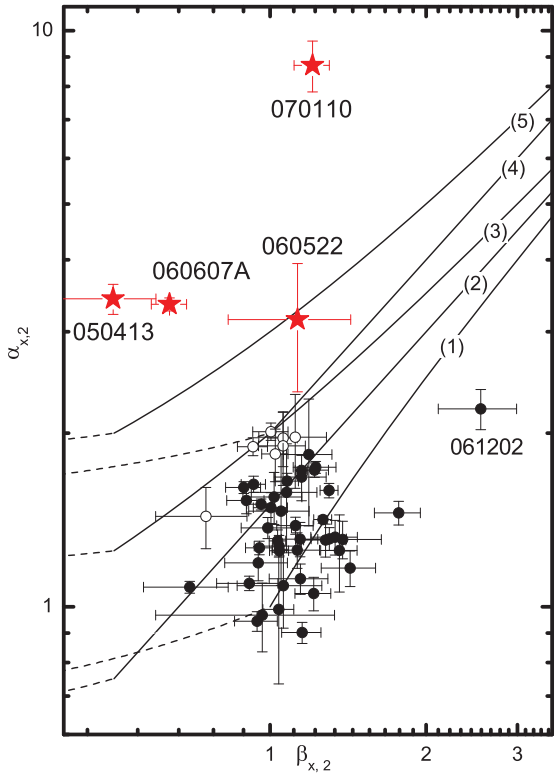

Figure 23 The temporal decay index $\alpha_{\rm X,2}$ as a function of the spectral index $\beta_{\rm X,2}$ for the post-break segment as compared with the closure correlations of various external shock afterglow models: (1) $\nu > \max(\nu_c, \nu_m)$; (2) $\nu_m < \nu < \nu_c$ (ISM, slow cooling); (3) $\nu_m < \nu < \nu_c$ (Wind, slow cooling) (4) $\nu > \nu_c$ (Jet, slow cooling) (5) $\nu_m < \nu < \nu_c$ (Jet, slow cooling). The solid lines are those for electron distribution index $p > 2$, and the dashed lines are for $p < 2$. The *solid* dots represent the bursts whose $\alpha_{\rm X,2}$ and $\beta_{\rm X,2}$ satisfy the models (1) and (2), and the open dots represent those bursts can be explained with the model (3). The stars are those bursts that significantly deviate from the external shock afterglow models including 060522 (see discussion in the text).

.

Summary

We have presented a comprehensive analysis of the *Swift* XRT light curves of long GRBs, focusing on the properties of the shallow decay phase and its relation with the follow-up decay phase. Our sample includes 53 bursts whose X-ray emissions are bright enough to perform spectral and temporal analyses for both phases. We summarize our results as follows.

(1) We find that the distributions of the characteristic properties of the shallow decay phase are log-normal or normal, i.e., $\log t_{\rm b}/s = 4.09 \pm 0.61$, $\log S_X/{\rm erg\ cm^{-2}} = -6.52 \pm 0.69$, $\Gamma_{\rm X,1} = 2.09 \pm 0.21$, and $\alpha_1 = 0.35 \pm 0.35$.

(2) The $E_{\rm iso,X}$ of the shallow decay phase is linearly correlated with the prompt gamma-ray phase, i.e., $\log E_{X,iso} = (1.00 \pm 0.16) \log E_{iso,\gamma} - (0.5 \pm 8.12)$ (with a Spearman correlation coefficient $r = 0.79$ and a chance probability $p < 10^{-4}$). The spectrum of the shallow decay phase is softer than the prompt gamma-ray phases, except for some typical XRFs.

(3) Except for GRB 061202, no spectral evolution is observed during the transition from the shallow decay to the follow-up decay phases. The post break phase in most bursts is consistent with the closure relations of the external shock models. Six out of the 13 bursts with well-sampled optical light curves show an achromatic break in both X-ray and optical bands, but the other 7 cases either do not show any break or have a break at a different epoch in the optical band. This poses an issue to explain t_b of these bursts as the end of the energy injection phase.

(4) With a sub-sample of 27 bursts with known redshifts that satisfy the closure relations of the standard external fireball models, we discover an empirical multi-variable relation among $E_{\rm iso,X}$, $E_{\rm p}^{'}$, and $t_{\rm b}^{\prime}$ (Eq.[7]), which is distinctly different from the $E_{\rm iso,\gamma} - E_{\rm p}^{'} - t_{\rm b,opt}^{\prime}$ relation discussed by Liang & Zhang (2005).

These results suggest that the shallow decay segment observed in most bursts is consistent with having an external forward shock origin, probably due to a continuous

energy injection into the forward shock from a long-lived central engine.

One interesting conclusion from this study is that at least for a small fraction of bursts (e.g. GRBs 060413, 060522, 060607A, and 070110), the observed shallow decay phase is likely of internal origin. A possible energy source for such a component would be the spin energy from the central engine, and an internal dissipation of the spindown power may be the origin (e.g. Troja et al. 2007).

CHAPTER 6

UNDERSTANDING THE JET BREAK

This chapter is partially based on the following published paper :

Liang, E.-W., Racusin, J. L., Zhang, B., Zhang, B.-B., & Burrows, D. N. 2008, The Astrophysical Journal, 675, 528

Statement of coauthorship: This work was led by E.-W. Liang. I processed all the Swift/XRT data, provided the XRT light curves and spectral fitting results that were essentially needed by this work. En-Wei collected the optical data from literature. Based on my X-ray data output and the optical data he collected, our discussion, comments, frequent feedback from me and other co-authors, En-Wei led the rest parts of this work which included fitting the light curves, rating the jet break candidates, deriving the physical parameters and comparing the results with different theoretical models.

Introduction

As one part of a cannonical X-Ray light curve, the jet-like decay segment, however, has occasionally been observed, but only for a small fraction of bursts (Burrows & Racusin 2007; Covino et al. 2006).

The jet models had been extensively studied in the pre-*Swift* era (e.g., Rhoads 1999, Sari et al. 1999; Huang et al. 2000; see reviews by Mészáros 2002; Zhang & Mészáros 2004; Piran 2005). An achromatic break is expected to be observed in multi-wavelength afterglow lightcurves at a time when the ejecta are decelerated by the ambient medium down to a bulk Lorentz factor $\sim 1/\theta_j$, where θ_j is the jet opening angle (Rhoads 1999; Sari et al. 1999). Most GRBs localized in the pre-*Swift* era with deep and long optical monitoring have a jet-like break in their optical afterglow lightcurves (see Frail et al. 2001; Bloom, Frail, & Kulkarni 2003; Liang & Zhang 2005 and the references therein), but the achromaticity of these breaks was not confirmed outside of the optical band. Panaitescu (2007a) and Kocevski & Butler (2008) studied the jet breaks and the jet energy with the

XRT data. However, the lack of detection of a jet-like break in most XRT lightcurves challenges the jet models, if both the optical and X-ray afterglows are radiated by the forward shocks. Multiwavelength observational campaigns raise the concerns that some jet-break candidates may not be achromatic (Burrows & Racusin 2007; Covino et al. 2006). Issues regarding the nature of previous "jet breaks" have been raised (e.g. Zhang 2007). The observational puzzles require a systematical analysis on both the X-ray and the optical data. In this work, we analyze the *Swift*/XRT data of 179 GRBs (from 050124 to 070129) and the optical afterglow data of 57 pre-*Swift* and *Swift* GRBs, in order to systematically investigate the jet-like breaks in the X-ray and optical afterglow lightcurves. We measure a jet break candidate from the data with a uniform method and grade the consistency of these breaks with the forward shock models, then compare these breaks observed in the X-ray and optical lightcurves . Assuming that these breaks are real jet breaks, we revisit the GRB jet energy budget (Frail et al. 2001; Bloom et al. 2003; Berger et al. 2003) with the conventional jet models.

Data

Use the same technique as in Chapter 3 and 5, we process all the XRT data (179 bursts) observed between 2005 January and 2007 January. We are only concerned with the power-law afterglow segments 2, 3, & 4 without considering the steep decay segment and the flares in the lightcurves. First, we inspect the XRT lightcurve of each burst and specify the time interval(s) that we use to derive the spectral and temporal properties. Then, we fit the lightcurve in this time interval with a power-law-like model as presented below. We regard that a lightcurve in the specified time interval does not have significant flares, if the reduced χ^2 of the power law fits is less than 2. We obtain a sample of 103 XRT lightcurves that have a good temporal coverage without significant flares.

We fit the lightcurve using three different models, namely, a single power law (PL) :

$$f = f_0 \left(\frac{t}{t_b}\right) \tag{6.1}$$

a smoothly broken power law (SBPL) :

$$f = f_0 \left[\left(\frac{t}{t_{\rm b,1}}\right)^{\omega_1\alpha_2} + \left(\frac{t}{t_{\rm b,1}}\right)^{\omega_1\alpha_3}\right]^{-1/\omega_1}, \tag{6.2}$$

and a smoothed triple power law (STPL) model:

$$F = (f_{SBPL}^{-\omega_2} + f_j^{-\omega_2})^{-1/\omega_2} \tag{6.3}$$

where

$$f_j = f_0 \left[\left(\frac{t_j}{t_{\rm b,1}}\right)^{\omega_1\alpha_2} + \left(\frac{t_j}{t_{\rm b,1}}\right)^{\omega_1\alpha_3}\right]^{-1/\omega_1} \left(\frac{t}{t_{b,2}}\right)^{-\alpha_4}. \tag{6.4}$$

In the sense of Occam's Razor, the simplest model should be adopted. On ther other hand, in order to avoid missing a jet break in the lightcurves, we accept a fit model as the best one when the derived breaks are sufficiently constrained by the data (i.e. $\delta t_b < t_b$, where δt_b is the fitting error of t_b, even if the χ^2 is not significantly improved when compared to a simpler model). We thus first fit the lightcurves with the STPL model (Eq. [6.3]). This model is a reasonable fit to all of the lightcurves. In case of $\delta t_b < t_b$, we suggest that such a lightcurve has three segments and we adopt the STPL model fit. We find that only 6 lightcurves satisfy this criterion (see Table 5). We fit the remaining lightcurves with the SBPL model (Eq. [6.2]), and similarly we examine whether or not $t_{b,1}$ is sufficiently constrained. The SBPL fits are adopted for 78 lightcurves. We fit the remaining lightcurves (26 bursts) with the SPL model. Our full resulting fits are summarized in Table 5. Using the time intervals defined by the fitting results, we extract the spectrum of each segment, and fit it with a simple power law model with absorption by both our Galaxy and the host galaxy. The spectral fitting results are also reported in

Table 5.

Table 5. XRT observations and the Fitting results

GRB	t_1(ks)[a]	t_2(ks)[a]	$t_{b,1}(\delta t_{b,1})$(ks)[b]	$t_{b,2}(\delta t_{b,2})$(ks)[b]	$\alpha_2(\delta\alpha_2)$[b]	$\alpha_3(\delta\alpha_3)$[b]	$\alpha_4(\delta\alpha_4)$[b]	χ^2(dof)	$\Gamma_2(\delta\Gamma_2)$	$\Gamma_3(\delta\Gamma_3)$	$\Gamma_4(\delta\Gamma_4)$
					STPL						
050128	0.25	70.72	1.13(0.74)	30.67(14.19)	0.34(0.15)	1.00(0.13)	1.98(0.39)	27(46)	1.76(0.07)	2.05(0.08)	1.95(0.15)
060210	3.90	861.94	5.51(0.86)	186.65(76.48)	-0.20(0.39)	1.00(0.05)	1.85(0.27)	134(131)	–	2.12(0.08)	2.11(0.33)
060510A	0.16	343.41	2.89(1.87)	47.65(16.75)	0.01(0.09)	0.87(0.17)	1.74(0.12)	84(140)	1.91(0.07)	2.04(0.14)	2.06(0.14)
060807	0.28	166.22	3.80(1.15)	14.89(5.88)	-0.22(0.13)	0.96(0.24)	1.92(0.12)	42(34)	2.19(0.16)	2.18(0.09)	2.40(0.20)
060813	0.09	74.25	0.19(0.04)	15.24(3.88)	-0.01(0.19)	0.87(0.03)	1.63(0.13)	56(73)	2.05(0.09)	1.99(0.05)	2.10(0.07)
060814	0.87	203.31	5.92(2.88)	68.58(23.27)	0.32(0.13)	1.06(0.12)	2.38(0.40)	44(48)	2.21(0.05)	–	2.30(0.05)
					SBPL						
050124	11.37	58.66	–	29.37(12.61)	–	0.62(0.56)	2.53(0.78)	6(11)	–	2.05(0.29)	1.93(0.21)
050315	5.40	450.87	–	224.64(38.68)	–	0.66(0.03)	1.90(0.28)	42(52)	–	2.31(0.12)	2.17(0.07)
050318	3.34	45.19	–	10.64(4.97)	–	0.90(0.23)	1.84(0.19)	27(20)	–	2.01(0.08)	2.02(0.06)
050319	6.11	84.79	11.20(13.26)	–	0.23(0.59)	0.99(0.25)	–	9(9)	2.00(0.06)	2.04(0.07)	–
050401	0.14	801.04	5.86(0.78)		0.58(0.02)	1.39(0.06)	–	107(92)	2.06(0.06)	2.03(0.04)	–
050416A	0.25	261.69	1.74(1.12)		0.43(0.12)	0.90(0.04)	–	36(38)	2.19(0.20)	2.15(0.10)	–
050505	3.07	97.19	7.87(1.57)		0.15(0.19)	1.30(0.06)	–	26(45)	2.00(0.07)	2.03(0.04)	–
050713A	4.61	1600.08	5.86(1.24)		-0.27(1.05)	1.16(0.03)	–	28(17)	2.25(0.05)	2.21(0.17)	–
050713B	0.79	478.50	10.80(1.59)		-0.00(0.07)	0.94(0.04)	–	40(63)	1.83(0.11)	1.94(0.09)	–
050716	0.64	74.40	7.53(9.02)		0.76(0.16)	1.35(0.24)	–	31(36)	1.60(0.08)	2.01(0.13)	–
050717	0.32	11.23	–	1.84(0.95)	–	0.57(0.21)	1.65(0.12)	28(56)	–	1.61(0.08)	1.89(0.12)
050726	0.42	17.05	–	1.17(0.33)	–	0.80(0.03)	2.32(0.22)	27(34)	–	2.06(0.08)	2.14(0.09)
050730	3.93	108.75	–	6.66(0.29)	–	-0.37(0.25)	2.49(0.04)	203(215)	–	1.65(0.03)	1.70(0.03)
050801	0.07	46.10	0.25(fixed)		0(fixed)	1.10(0.03)	–	44(45)	–	1.91(0.12)	–
050802	0.51	83.83	–	4.09(0.61)	–	0.32(0.10)	1.61(0.04)	58(72)	–	1.92(0.05)	1.89(0.07)
050803	0.50	368.89	–	13.71(0.90)	–	0.25(0.03)	2.01(0.07)	94(57)	–	1.78(0.10)	2.00(0.08)
050820A	4.92	1510.14	–	420.78(179.33)	–	1.11(0.02)	1.68(0.21)	246(292)	–	1.63(0.05)	1.87(0.04)
050822	6.41	523.32	66.99(44.38)		0.60(0.10)	1.25(0.19)	–	29(44)	2.29(0.23)	2.36(0.11)	–
050824	6.31	330.49	11.52(4.25)		-0.40(0.52)	0.61(0.06)	–	45(41)	2.00(0.16)	2.01(0.09)	–
050908	3.97	33.36	–	7.81(5.33)	–	0.13(0.96)	1.58(0.46)	0(1)	–	–	2.09(0.25)
050915A	0.32	88.77	1.94(1.11)		0.39(0.27)	1.24(0.09)	–	7(6)	2.32(0.17)	2.42(0.20)	–
051006	0.23	13.13		0.93(0.71)	–	0.57(0.26)	2.23(0.56)	15(19)	–	1.61(0.14)	1.84(0.20)
051008	3.09	43.77	14.67(3.82)		–	0.86(0.09)	2.01(0.19)	52(49)	–	2.15(0.32)	2.11(0.10)
051016A	0.37	37.41	0.63(0.40)		-0.41(1.18)	0.91(0.12)	–	0(7)	2.40(0.26)	–	–

Table 5 (continued)

GRB	t_1(ks)[a]	t_2(ks)[a]	$t_{b,1}(\delta t_{b,1})$(ks)[b]	$t_{b,2}(\delta t_{b,2})$(ks)[b]	$\alpha_2(\delta\alpha_2)$[b]	$\alpha_3(\delta\alpha_3)$[b]	$\alpha_4(\delta\alpha_4)$[b]	χ^2(dof)	$\Gamma_2(\delta\Gamma_2)$	$\Gamma_3(\delta\Gamma_3)$	$\Gamma_4(\delta\Gamma_4)$
051016B	4.78	150.47	–	66.40(23.09)	–	0.71(0.08)	1.84(0.46)	15(16)	–	-	2.19(0.13)
051109A	3.73	639.16	–	27.28(7.90)	–	0.79(0.07)	1.53(0.08)	39(48)	–	1.91(0.07)	1.90(0.07)
051109B	0.39	87.63	5.11(4.73)		0.56(0.17)	1.22(0.17)	–	15(17)	2.73(0.44)	2.35(0.24)	–
051117A	18.19	970.14	104.23(151.17)		0.51(0.25)	1.07(0.24)	–	21(19)	2.25(0.04)	2.39(0.15)	–
051221A	6.87	118.64	–	40.74(15.89)	–	0.46(0.16)	1.75(0.41)	11(14)	–	2.08(0.09)	2.02(0.19)
060105	0.10	360.83	–	2.31(0.14)	–	0.84(0.01)	1.72(0.02)	653(754)	–	2.23(0.05)	2.15(0.03)
060108	0.77	165.26	–	22.08(7.38)	–	0.26(0.09)	1.43(0.17)	7(7)	–	2.17(0.32)	1.75(0.15)
060109	0.74	48.01	4.89(1.10)		-0.17(0.14)	1.32(0.09)	–	19(13)	2.32(0.15)	2.34(0.14)	–
060124	13.30	664.01	–	52.65(10.33)	–	0.78(0.10)	1.65(0.05)	165(132)	–	2.10(0.06)	2.06(0.08)
060202	1.03	96.23	3.50(6.95)		0.68(0.37)	1.14(0.13)	–	51(31)	2.96(0.19)	3.41(0.14)	–
060203	3.80	32.95	–	12.95(6.69)	–	0.40(0.30)	1.65(0.47)	4(7)	–	2.08(0.19)	2.25(0.13)
060204B	4.06	98.80	–	5.55(0.66)	–	-0.49(0.65)	1.47(0.07)	21(34)	–	2.54(0.14)	2.64(0.16)
060206	0.11	621.77	8.06(1.46)		0.40(0.05)	1.26(0.04)	–	43(44)	2.31(0.12)	2.33(0.32)	–
060211A	5.40	527.10	–	267.24(165.67)	–	0.38(0.08)	1.63(1.27)	10(9)	–	2.15(0.06)	2.11(0.26)
060306	0.25	124.39	4.67(2.91)		0.40(0.11)	1.05(0.07)	–	30(32)	2.10(0.11)	2.21(0.10)	–
060313	0.09	93.22	–	11.18(2.89)	–	0.82(0.03)	1.76(0.18)	95(128)	–	1.84(0.34)	1.78(0.09)
060319	0.33	304.52	–	99.70(26.78)	–	0.84(0.02)	1.92(0.30)	72(93)	–	1.93(0.22)	2.25(0.11)
060323	0.33	16.28	–	1.29(0.32)	–	-0.11(0.23)	1.55(0.16)	4(7)	–	1.99(0.16)	2.02(0.13)
060428A	0.23	271.10	–	125.31(47.19)	–	0.48(0.03)	1.46(0.37)	26(21)	–	2.11(0.24)	1.97(0.10)
060428B	0.96	200.36	3.95(5.55)		0.53(0.41)	1.16(0.13)	–	19(21)	2.41(0.24)	2.10(0.33)	–
060502A	0.24	593.06	–	72.57(15.05)	–	0.53(0.03)	1.68(0.15)	11(26)	–	2.11(0.29)	2.15(0.13)
060507	3.00	86.09	6.95(1.68)		-0.06(0.55)	1.12(0.07)		– 13(24)	2.06(0.23)	2.15(0.14)	–
060510B	4.40	77.71	–	67.90(29.88)	–	0.44(0.18)	2.40(0.00)	4(8)	–	1.71(0.04)	–
060526	1.09	45.20	–	11.60(6.39)	–	0.42(0.12)	1.58(0.34)	5(9)	–	2.07(0.09)	2.08(0.16)
060604	4.14	403.81	11.51(9.81)		0.20(0.77)	1.17(0.09)	–	32(36)	2.44(0.15)	2.43(0.17)	–
060605	0.25	39.85	–	7.14(0.93)	–	0.45(0.04)	1.80(0.13)	22(34)	–	1.62(0.17)	1.83(0.09)
060614	5.03	451.71	–	49.84(3.62)	–	0.18(0.06)	1.90(0.07)	70(54)	–	2.02(0.02)	1.93(0.06)
060707	5.32	813.53	22.21(54.08)		0.37(0.96)	1.09(0.17)	–	8(11)	1.88(0.08)	2.06(0.20)	–
060708	0.25	439.09	7.28(2.34)		0.57(0.08)	1.32(0.07)	–	39(35)	2.30(0.20)	2.36(0.11)	–
060712	0.56	317.56	7.89(2.67)		0.12(0.16)	1.15(0.10)	–	15(14)	3.21(0.38)	2.94(0.28)	–
060714	0.32	331.97	3.70(0.97)		0.34(0.10)	1.27(0.05)	–	53(73)	2.15(0.08)	2.04(0.11)	–
060719	0.28	182.15	9.57(2.70)		0.40(0.06)	1.31(0.10)	–	19(26)	2.35(0.13)	2.28(0.26)	–

Table 5 (continued)

GRB	t_1(ks)[a]	t_2(ks)[a]	$t_{b,1}(\delta t_{b,1})$(ks)[b]	$t_{b,2}(\delta t_{b,2})$(ks)[b]	$\alpha_2(\delta\alpha_2)$[b]	$\alpha_3(\delta\alpha_3)$[b]	$\alpha_4(\delta\alpha_4)$[b]	χ^2(dof)	$\Gamma_2(\delta\Gamma_2)$	$\Gamma_3(\delta\Gamma_3)$	$\Gamma_4(\delta\Gamma_4)$
060729	0.42	2221.24	72.97(3.02)		0.21(0.01)	1.42(0.02)	–	459(459)	2.33(0.08)	2.29(0.07)	–
060804	0.18	122.07	0.86(0.22)		-0.09(0.15)	1.12(0.07)	–	18(24)	2.04(0.23)	2.14(0.15)	–
060805A	0.23	75.91	1.30(0.70)		-0.17(0.41)	0.97(0.13)	–	11(17)	–	1.97(0.37)	–
060906	1.32	36.69	–	13.66(3.29)	–	0.35(0.10)	1.97(0.36)	3(7)	–	2.28(0.37)	2.12(0.17)
060908	0.08	363.07	–	0.95(0.34)	–	0.70(0.07)	1.49(0.09)	98(59)	–	2.01(0.22)	2.00(0.08)
060912	0.12	86.80	2.92(2.77)		0.65(0.12)	1.24(0.11)	–	31(56)	–	2.03(0.12)	–
060923A	0.22	280.62	3.33(1.03)		-0.16(0.22)	1.30(0.06)	–	34(21)	2.05(0.25)	1.86(0.18)	–
060923B	0.16	6.03	0.42(0.64)		-0.73(0.99)	1.08(0.82)	–	2(10)	2.47(0.53)	2.25(0.31)	–
060926	0.09	5.96	1.13(0.92)		0.04(0.14)	1.23(0.52)	–	11(9)	1.93(0.16)	1.88(0.14)	–
060927	0.11	5.64	–	4.24(8.22)	–	0.73(0.32)	1.82(2.60)	4(7)	–	1.65(0.19)	1.92(0.15)
061004	0.39	69.99	1.50(0.52)		-0.08(0.29)	1.04(0.09)	–	13(17)	1.84(0.34)	3.04(0.34)	–
061019	9.07	287.03	10.84(2.15)		-1.38(2.88)	1.15(0.08)	–	6(10)	2.32(0.20)	1.93(0.28)	–
061021	0.30	594.16	9.59(2.17)		0.52(0.03)	1.08(0.03)	–	94(87)	1.90(0.06)	1.72(0.05)	–
061121	4.89	353.10	–	24.32(4.38)	–	0.75(0.06)	1.63(0.05)	121(147)	–	1.71(0.03)	1.96(0.07)
061201	0.10	15.42	–	2.09(0.75)	–	0.57(0.07)	1.61(0.23)	20(29)	–	1.30(0.09)	–
061222A	10.94	724.64	–	60.51(8.89)	–	0.81(0.07)	1.86(0.06)	144(95)	–	2.45(0.06)	2.22(0.12)
070103	0.11	143.98	–	2.88(0.48)	–	0.20(0.10)	1.63(0.08)	43(30)	–	2.32(0.25)	2.52(0.21)
070129	1.32	546.36	20.12(3.14)		0.15(0.07)	1.31(0.06)	–	42(70)	2.25(0.07)	2.30(0.10)	–
					SPL						
050219B	3.21	85.26			–	1.14(0.03)	–	24(32)	–	2.27(0.14)	–
050326	3.34	142.24			–	–	1.63(0.04)	45(34)	–	–	2.15(0.14)
050408	2.60	3223.36			–	0.78(0.01)	–	52(44)	–	2.01(0.18)	–
050525A	5.94	157.85			–	1.40(0.05)	–	11(11)	–	2.17(0.18)	–
050603	39.72	166.22			–	–	1.71(0.10)	8(10)	–	–	1.84(0.09)
050721	0.30	257.24			–	1.18(0.02)	–	80(98)	–	1.77(0.10)	–
050814	2.17	87.85			–	0.65(0.05)	–	21(16)	–	1.91(0.07)	–
050826	0.13	61.93			–	1.02(0.03)	–	23(21)	–	2.19(0.19)	–
050827	65.95	246.35			–	1.24(0.15)	–	12(15)	–	1.88(0.15)	–
051001	6.71	273.86			–	0.70(0.06)	–	30(25)	–	1.93(0.19)	–
051111	10.98	34.24			–	1.09(0.17)	–	1(6)	–	–	–
051117B	0.22	0.62			–	–	1.68(0.27)	0(2)	–	–	–
060115	5.44	326.04			–	0.88(0.04)	–	12(12)	–	2.50(0.38)	–

Table 5 (continued)

GRB	t_1(ks)[a]	t_2(ks)[a]	$t_{b,1}(\delta t_{b,1})$(ks)[b]	$t_{b,2}(\delta t_{b,2})$(ks)[b]	$\alpha_2(\delta\alpha_2)$[b]	$\alpha_3(\delta\alpha_3)$[b]	$\alpha_4(\delta\alpha_4)$[b]	χ^2(dof)	$\Gamma_2(\delta\Gamma_2)$	$\Gamma_3(\delta\Gamma_3)$	$\Gamma_4(\delta\Gamma_4)$
060116	0.21	6.87			–	0.88(0.06)	–	3(6)	–	2.33(0.39)	–
060403	0.05	79.82			–	–	1.67(0.07)	70(57)	–	–	1.58(0.13)
060418	0.20	201.65			–	1.45(0.02)	–	272(283)	–	2.24(0.05)	–
060421	0.12	6.52			–	0.93(0.05)	–	11(7)	–	1.60(0.35)	–
060512	0.11	104.01			–	1.39(0.02)	–	76(58)	–	3.60(0.19)	–
060522	5.50	432.75			–	1.07(0.10)	–	7(13)	–	–	–
060825	0.23	63.15			–	1.08(0.04)	–	4(6)	–	1.64(0.29)	–
061007	0.09	97.82			–		1.68(0.01)	2153(1880)	–	–	2.08(0.05)
061019	2.90	287.03			–	0.95(0.03)	–	28(20)	–	2.12(0.21)	–
070110	43.70	439.51			–	1.05(0.14)	–	9(5)	–	2.36(0.24)	–

[a]The time interval of our fitting.

[b]The fitting results of the two-segment lightcurves with the SBPL model are reported in columns for the jet break candidate (Columns $t_{b,2}$, α_3, α_4, Γ_3, and Γ_4) if their post-break segments are steeper than $\gtrsim 1.5$; otherwise, the results are reported in the columns of the energy injection break(Columns $t_{b,1}$, α_2, α_3, Γ_2, and Γ_3). The results of the fitting results of the one-segment XRT lightcurves with the SPL model are similarly reported in the columns of the energy injection break or of the jet break candidate depending on their temporal decay slopes.

In order to compare the X-ray break candidates with the optical lightcurves, we also perform an extensive analysis of the optical lightcurves for both pre-*Swift* and *Swift* bursts. We search for the optical afterglow data in the literature and compile a sample of 57 optical lightcurves that have a good temporal coverage. These lightcurves are fit with the same strategy as that for the XRT lightcurves. The fitting results are reported in Table 6.

Table 6. Optical Data and the Fitting results

GRB	t_1(ks)[a]	t_2(ks)[a]	$t_{b,O}(\delta t_{b,O})$(ks)	$\alpha_{O,3}(\delta\alpha_{O,3})$	$\alpha_{O,4}(\delta\alpha_{O,4})$	χ^2(dof)[b]
970508	30.00	7421.93	139.67(3.16)	-2.73	1.21(0.02)	29(21)
980703	81.26	343.92	214.92(10.15)	1.11	2.83	7(7)
990123	13.31	1907.45	155.13(78.79)	0.98(0.10)	1.71(0.10)	12(8)
990510	12.44	340.24	101.91(12.48)	0.86(0.03)	1.95(0.14)	17(17)
990712	15.25	2991.47	2000.00(fixed)	0.97	2.32	15(11)
991216	41.17	1100.60	248.71(67.63)	1.22(0.04)	2.17	27(13)
000301	134.00	4198.10	562.87(18.70)	1.04	2.97	25(24)
000926	74.48	591.61	175.18(4.62)	1.48	2.49	35(24)
010222	13.09	2124.75	32.12(3.62)	0.43(0.08)	1.29(0.02)	29(48)
011211	34.40	2755.47	198.66(16.68)	0.85(0.05)	2.36	26(33)
020124	5.77	2787.67	8.47(7.39)	0.76(1.19)	1.85(0.11)	8(9)
020405	85.04	882.60	236.88(15.90)	1.21	2.48	6(10)
020813	14.18	362.83	40.03(0.21)	0.63	1.42	69(43)
021004	21.12	2030.14	300.30(fixed)	0.82(0.02)	1.39(0.05)	82(90)
030226	17.34	609.12	88.83(16.30)	0.88(0.12)	2.41(0.12)	10(12)

Table 6 (continued)

GRB	t_1(ks)[a]	t_2(ks)[a]	$t_{b,O}(\delta t_{b,O})$(ks)	$\alpha_{O,3}(\delta\alpha_{O,3})$	$\alpha_{O,4}(\delta\alpha_{O,4})$	χ^2(dof)[b]
030323	34.68	895.74	400.00(fixed)	1.29	2.11	10(10)
030328	4.90	227.46	18.50(4.32)	0.52(0.09)	1.25(0.05)	52(70)
030329	4.60	100.00	41.00(0.42)	0.84	1.89(0.01)	870(956)
030429	12.53	574.04	158.73(fixed)	0.72(0.03)	2.72	30(10)
030723	15.00	800.00	103.22(5.02)	0.05(0.06)	2.01(0.05)	20(15)
040924	0.95	134.12	1.49(0.96)	0.34(0.64)	1.11(0.06)	19(10)
041006	0.23	550.00	14.24(1.15)	0.44(0.02)	1.27(0.01)	97(69)
050319	0.03	3.00	0.61(0.25)	0.38(0.06)	1.02(0.12)	29(29)
050525	2.83	91.80	40.72(8.18)	1.02(0.12)	3.00(0.57)	28(5)
050730	0.07	358.90	11.61(1.95)	0.26(0.08)	1.67(0.09)	58(16)
050801	0.02	9.49	0.20(0.01)	0.00(0.02)	1.11(0.01)	140(42)
050820A	0.12	663.30	344.98(32.78)	0.88(0.01)	1.48	439(25)
050922C	0.25	69.60	3.13(2.75)	0.63(0.13)	1.14(0.10)	14(17)
051109A	0.04	265.20	36.02(8.28)	0.68(0.01)	1.42(0.12)	116(40)
051111	0.03	20.00	2.61(0.25)	0.79(0.01)	1.70(0.14)	107(84)

Table 6 (continued)

GRB	t_1(ks)[a]	t_2(ks)[a]	$t_{b,O}(\delta t_{b,O})$(ks)	$\alpha_{O,3}(\delta\alpha_{O,3})$	$\alpha_{O,4}(\delta\alpha_{O,4})$	χ^2(dof)[b]
060206	20.00	201.58	71.21(3.65)	1.07(0.02)	1.96	25(50)
060210	0.09	7.19	0.72(0.17)	0.04(0.22)	1.21(0.05)	13(12)
060526	0.06	893.55	84.45(5.88)	0.67(0.02)	1.80(0.04)	116(56)
060605A	0.43	111.96	8.83(1.21)	0.41	2.33(0.16)	2(1)
060607A	0.07	13.73	0.16(fixed)	-3.07(0.25)	1.18(0.02)	92(35)
060614	20.00	934.36	112.35(8.53)	0.77(0.10)	2.70(0.07)	16(16)
060714	3.86	285.87	10.00(fixed)	0.01	1.41(0.03)	35(11)
060729	70.00	662.39	297.49(69.62)	1.09(0.10)	2.13(0.44)	18(19)
061121	0.26	334.65	1.70(0.73)	0.17	0.99(0.05)	18(23)
980326	36.46	117.68		2.14(0.09)		15(6)
991208	179.52	613.24	-	2.30(0.12)		17(9)
000131	357.44	699.06	-	2.55(0.29)	-	0(1)
000418	214.27	2000.00	-	0.81(0.03)	-	13(9)
000911	123.35	1466.26	-	1.36(0.06)	-	9(2)
011121	33.36	1000.00	-	1.98(0.06)	-	7(5)

Table 6 (continued)

GRB	t_1(ks)[a]	t_2(ks)[a]	$t_{b,O}(\delta t_{b,O})$(ks)	$\alpha_{O,3}(\delta\alpha_{O,3})$	$\alpha_{O,4}(\delta\alpha_{O,4})$	χ^2(dof)[b]
021211	0.13	1865.64	-	1.18(0.01)	-	78(50)
050318	3.23	22.83	-	0.84(0.22)	-	0(1)
050401	0.06	1231.18	-	0.80(0.01)	-	43(12)
050408	8.64	434.81	-	0.72(0.04)	-	9(15)
050502	6.12	29.22	-	1.42(0.02)	-	31(19)
050603	34.09	219.71	-	1.75(0.20)	-	16(7)
050802	0.34	127.68	-	0.85(0.02)	-	50(10)
050908	1.32	57.81	-	0.71(0.09)	-	11(10)
060124	3.34	1979.30	-	0.85(0.02)	-	11(19)
060418	3.92	69.53	-	1.36(0.04)	-	8(11)
060904B	0.50	163.13	-	0.86(0.02)	-	60(19)
070110	0.66	34.76	-	0.43(0.08)	-	1(4)

[a]Time interval for temporal analysis.

[b]The fitting χ^2 and degree of freedom. Please note that we take the observed uncertainty as $\sigma_{\log F_O} = 0.05$ for those detection without observed error or with $\sigma_{\log F_O} < 0.05$, in order to properly fit the data. The uncertainties of the fitting parameters of these bursts thus cannot be properly constrained.

Table 7. Definition of Jet Break Candidate Grades

Grade	No Spectral Evolution	$\alpha_4 > 1.5$	Closure Relations	Achromaticity	Number
"Bronze"	Y	Y			42(XRT)+27(Opt.)
"Silver"	Y	Y	Y		27(XRT)+23(Opt.)
"Gold"	Y	Y	Y(1 band)	Y	7
"Platinum"	Y	Y	Y (at least 2 bands)	Y	0

Jet Break Candidates in the X-Ray and Optical Lightcurves

A break with $\Delta\alpha \sim 1$ is predicted by the forward shock jet models. Since it is purely due to dynamic effects, it should be achromatic with no spectral evolution across the break, and both the pre- and post-break segments should also be consistent with the forward shock models. As shown in Table 6, no significant spectral evolution in the segments 3 and 4 is found for most bursts, and the X-ray spectral index is ~ 1 (see also O'Brien et al. 2006). Assuming that both the optical and the X-ray afterglows are produced by the forward shocks, we select jet break candidates from the results shown in Tables 5 and 6, and grade these candidates as "Bronze", "Silver", "Gold", and "Platinum" based on the consistency of data with the models. The definitions of these grades are summarized in Table 7.

"Bronze" Jet Break Candidates

A break with a post-break segment being steeper than 1.5 is selected as "Bronze".. We first select the "Bronze" jet break candidates from both the X-ray and optical data shown in Tables 5 and 6. Without multiple wavelength modelling, the closure relations between the spectral index ($\beta = \Gamma - 1$) and temporal decay slope of the GRB afterglows present an approach to verify whether or not the data satisfy the models (see Table 5 of Zhang & Mészáros 2004 and references therein, in particular Sari et al. 1998; Chevalier & Li 2000; Dai & Cheng 2001). We pick 1.5 as the critical slope to define the "Bronze" jet break sample. As shown in Tables 5 and 6, 42 breaks of the XRT lightcurves and 27 of the optical lightcurves satisfy the "Bronze" jet break candidate criterion. These

lightcurves are shown in Fig.24. We summarize the data of these breaks in Table 8. Our "Bronze" jet break candidate sample is roughly consistent with that reported by Panaitescu (2007a). The jet breaks in the radio afterglow lightcurve of GRBs 970508 (Frail et al.2000) and 000418 (Berger et al. 2001) are also included in our "Bronze" sample.

"Silver" Jet Break Candidates

We promote a "Bronze" jet break candidate to the "Silver" sample if both the pre- and post-break segments are consistent with the models in at least one band. The decay slope of the pre-break segment of a jet break for the bursts in our sample should be steeper than 0.75. Fifty-two out of the 71 "Bronze" jet break candidates in Table 8 agree with the "Silver" candidate criterion (29 in the X-ray lightcurves and 23 in the optical light curves).

"Gold" Jet Break Candidates

A "Gold" jet break candidate requires that the break is achromatic at least in two bands, and that the break should satisfy the criteria of a "Silver" candidate at least in one band. Inspecting the data in Table 8 and the lightcurves in Fig.24, one approximately achromatic break is observed in both X-ray and the optical lightcurves of GRBs 030329, 050730, 050820A, 051109A, and 060605. The optical afterglows of GRBs 050525A, 060206, 060526, and 060614 are bright, and a jet-like break is clearly observed in their optical lightcurves. Guided by the optical breaks, some authors argued for achromatic breaks in the XRT lightcurves of these GRBs. Without the guidance of the optical lightcurves, one cannot convincingly argue a break in the XRT lightcurves of these GRBs, but the data may be still consistent with the existence of an achromatic break. Both the optical and radio data of GRB 990510 are consistent with the jet models. We inspect the data of these bursts case by case, and finally identify 7 "Gold" candidates.

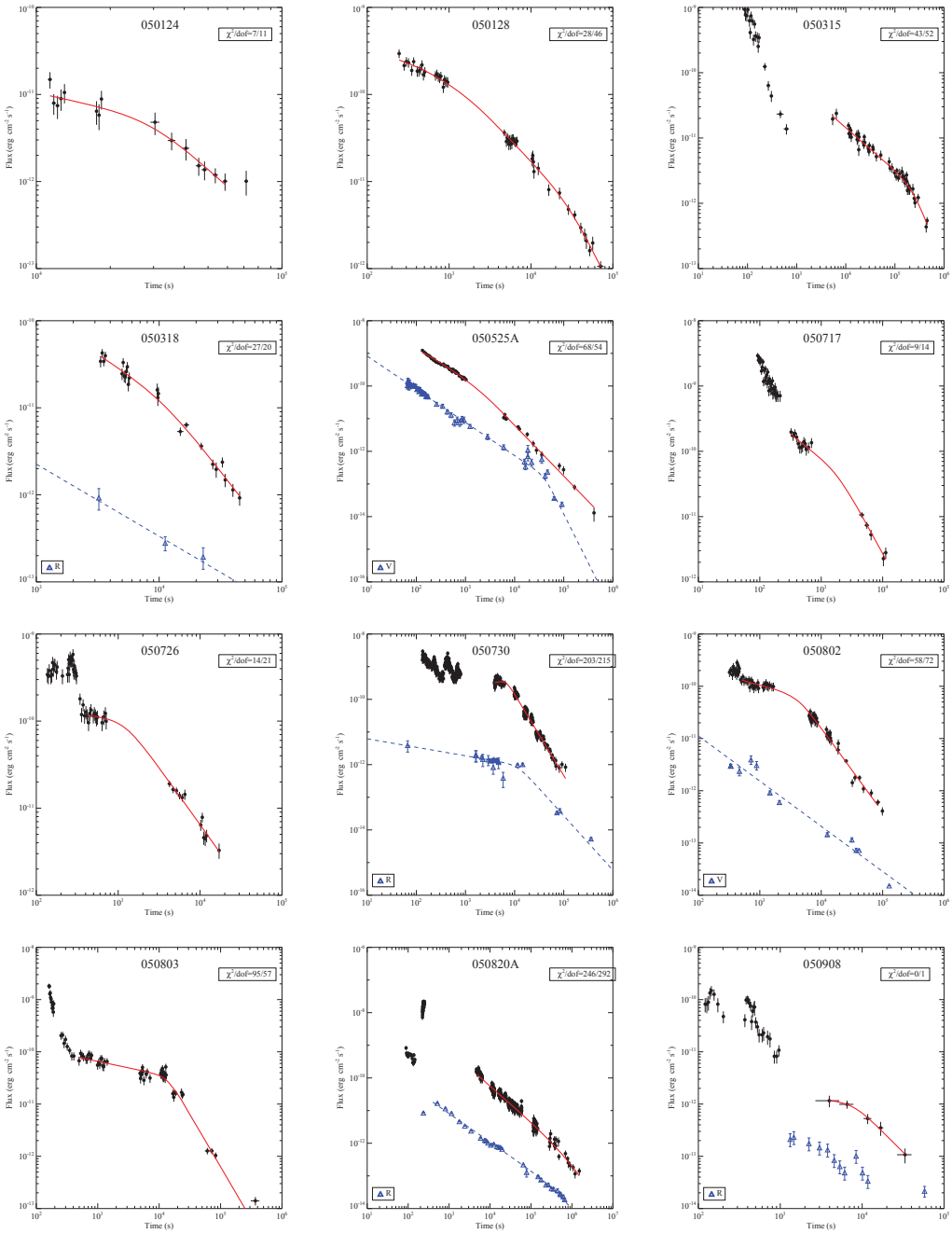

Figure 24 The X-ray (solid dots) and optical (open triangles) lightcurves and their fitting results for derived the jet break candidates .

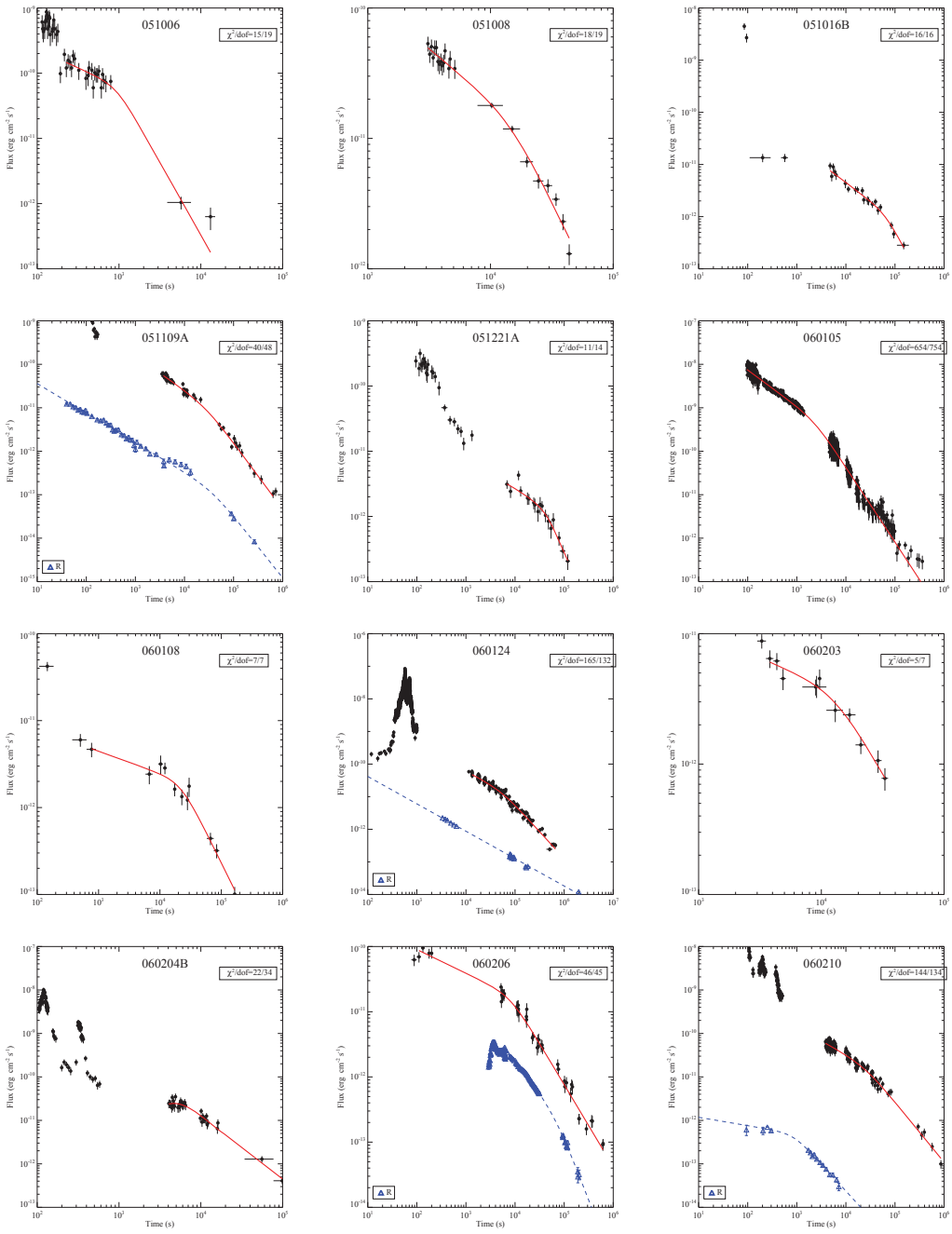

Fig. 24–continued.

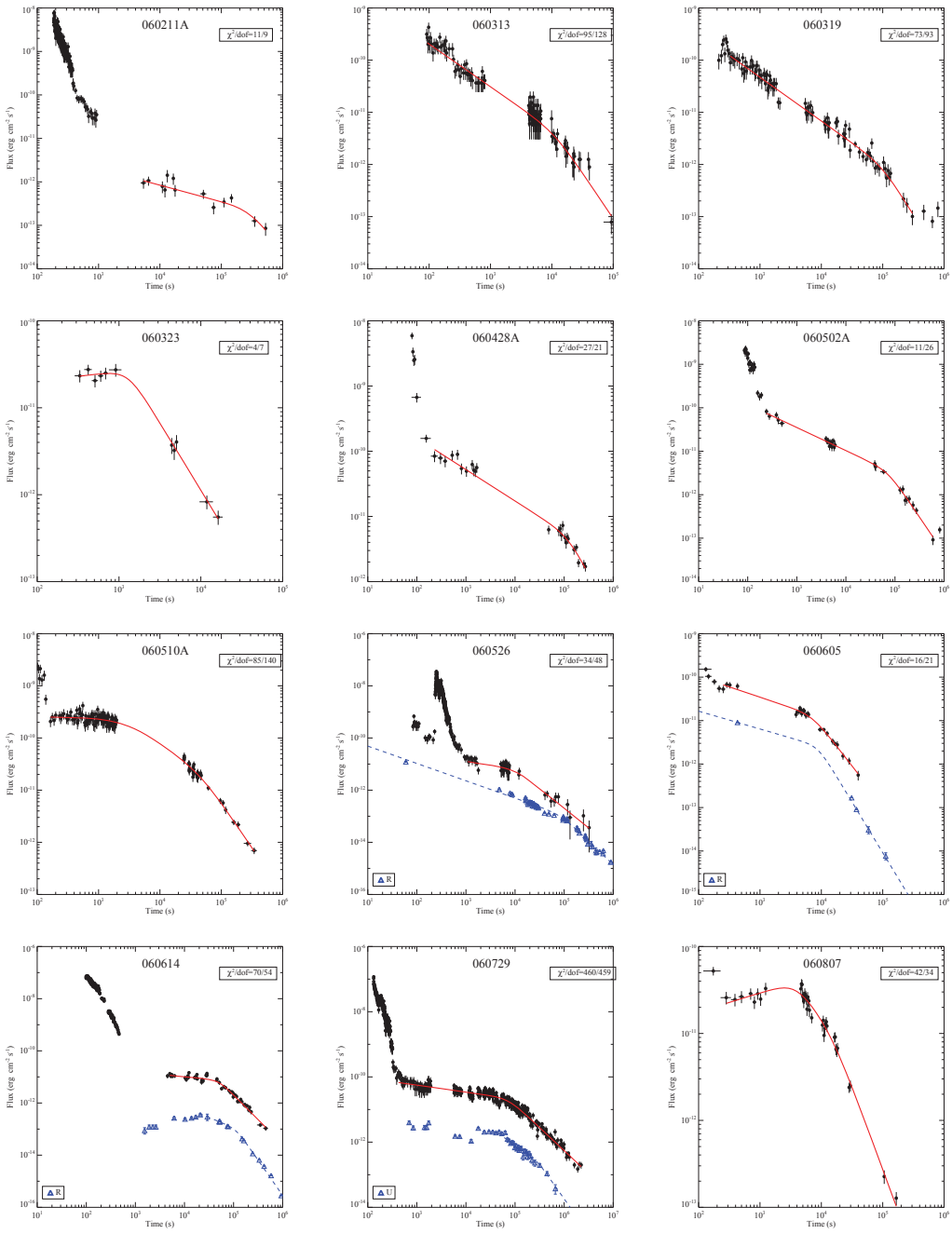

Fig. 24–continued.

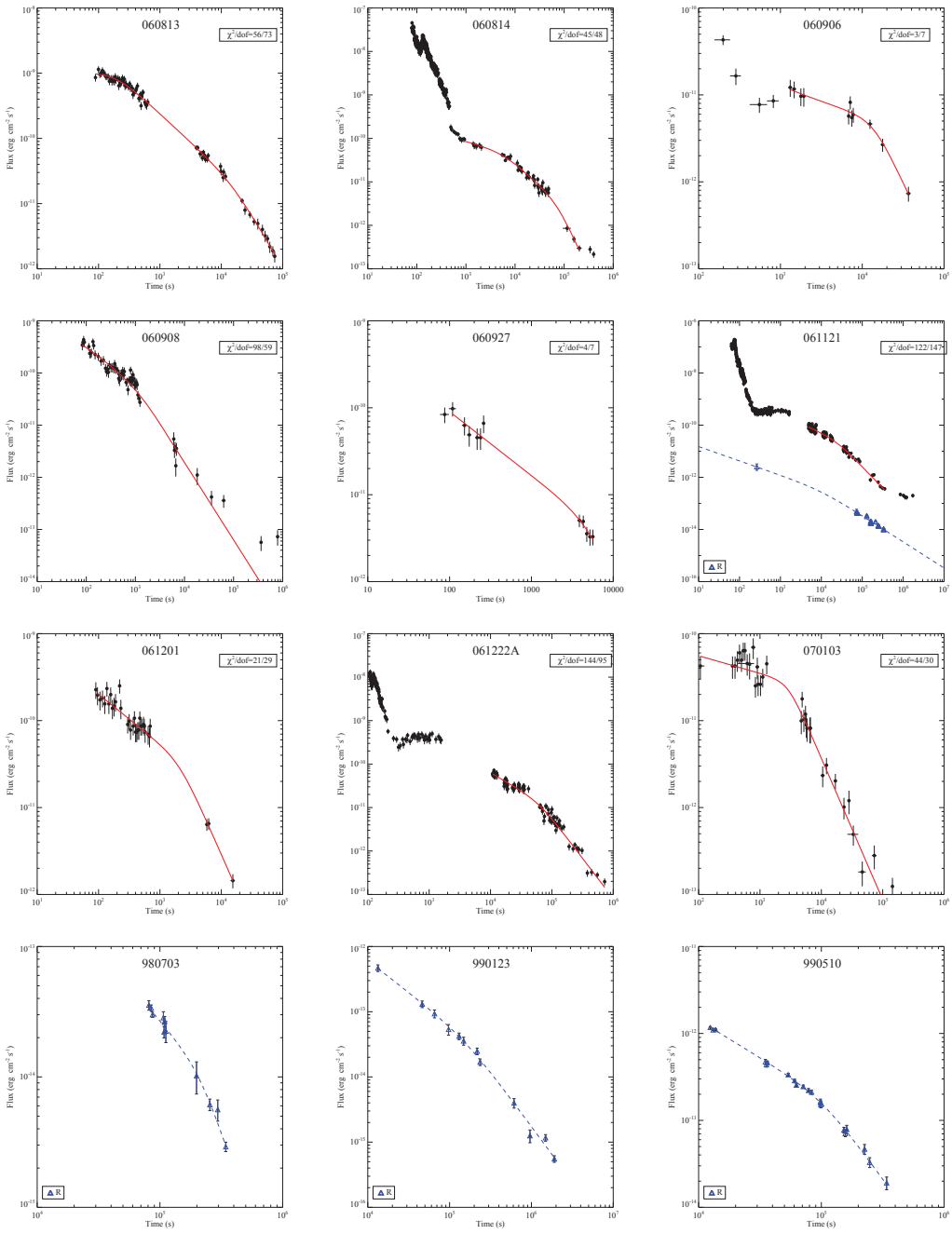

Fig. 24–continued.

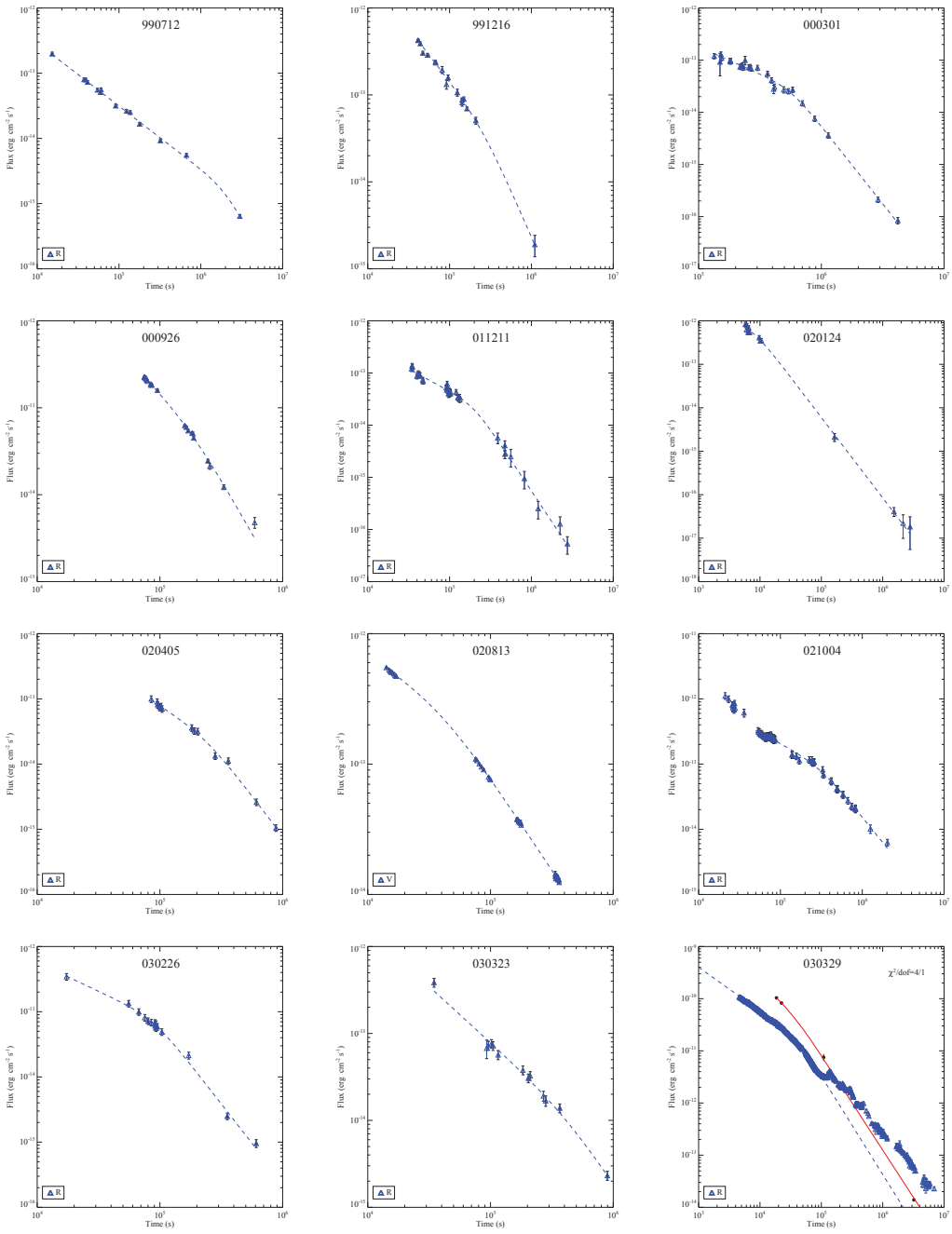

Fig. 24–continued.

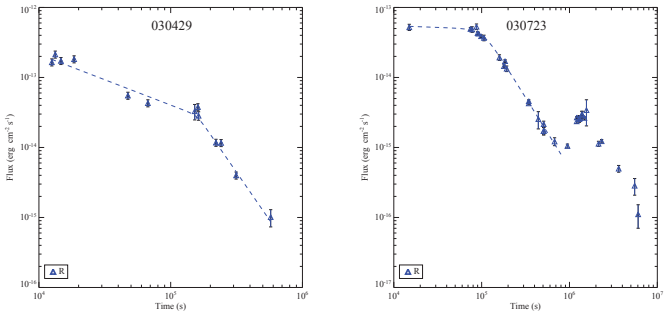

Fig. 24–continued.

Table 8. Jet Break Candidates and Their Grades

GRB	$\beta_2(\delta\beta_2)$	$\beta_4(\delta\beta_4)$	$\alpha_3(\delta\alpha_3)$	$\alpha_4(\delta\alpha_4)$	$t_j(\delta t_j)$(ks)	$\Delta\alpha(\delta\Delta\alpha)$	Grade	Achromaticity*
Radio								
970508[a]					~ 25 (days)		Bronze	?
000418[b]					~ 26 (days)		Bronze	?
Optical								
980703	1.01(0.02)	–	1.11	2.83	214.92(10.15)	1.71	Silver	?
990123	0.80(0.10)	–	0.98(0.10)	1.71(0.10)	155.13(78.79)	0.73(0.14)	Silver	?
990510	0.75(0.07)	–	0.86(0.03)	1.95(0.14)	101.91(12.48)	1.09(0.14)	Gold	$\surd$
990712	0.99(0.02)	–	0.97	2.32	2000	1.35	Silver	?
991216	0.74(0.05)	–	1.22(0.04)	2.17	248.71(67.63)	0.95(0.04)	Silver	?
000301C	0.90(0.02)	–	1.04	2.82	562.87(18.70)	1.78	Silver	?
000926	1.00(0.20)	–	1.48	2.49	175.18(4.62)	1.01	Silver	?
011211	0.74(0.05)	–	0.85(0.05)	2.36	198.66(16.68)	1.52(0.05)	Silver	?
020124	0.91(0.14)	–	0.76(1.19)	1.85(0.11)	8.47(7.39)	1.09(1.19)	Silver	?

Table 8 (continued)

GRB	$\beta_2(\delta\beta_2)$	$\beta_4(\delta\beta_4)$	$\alpha_3(\delta\alpha_3)$	$\alpha_4(\delta\alpha_4)$	$t_j(\delta t_j)$(ks)	$\Delta\alpha(\delta\Delta\alpha)$	Grade	Achromaticity*
020405	1.23(0.12)	–	1.21	2.48	236.88(15.90)	1.27	Silver	?
020813	0.85(0.07)	–	0.63	1.42	40.03(0.21)	0.79	Silver	?
021004	0.39(0.12)	–	0.65(0.02)	1.57(0.05)	300.30	0.92(0.05)	Silver	?
030226	0.70(0.03)	–	0.88(0.12)	2.41(0.12)	88.83(16.30)	1.53(0.17)	Silver	?
030323	0.89(0.04)	–	1.29	2.11	400	0.82	Silver	?
030329	0.66	–	0.84	1.89(0.01)	41.00(0.42)	1.05(0.01)	Gold	$\surd$
030429	1.22(0.04)	–	0.72(0.03)	2.72	158.73	2.00(0.03)	Silver	?
030723	1	–	0.05(0.06)	2.01(0.05)	103.22(5.02)	1.96(0.08)	Bronze	?
050525	0.97(0.10)	–	1.02(0.12)	3.00(0.57)	40.72(8.18)	1.98(0.58)	Gold	$\surd$
050730	0.75	–	0.26(0.08)	3.00(0.57)	1.67(0.09)	2.74(0.58)	Bronze	?
050820A	0.57(0.06)	–	0.88(0.01)	1.48	344.98(32.78)	0.60	Gold	$\surd$
051109A	0.65(0.15)	–	0.68(0.01)	1.42(0.12)	36.02(8.28)	0.74(0.12)	Gold	$\surd$
051111	0.84(0.02)	–	0.79(0.01)	1.70(0.14)	2.61(0.25)	0.91(0.14)	Silver	X

Table 8 (continued)

GRB	$\beta_2(\delta\beta_2)$	$\beta_4(\delta\beta_4)$	$\alpha_3(\delta\alpha_3)$	$\alpha_4(\delta\alpha_4)$	$t_j(\delta t_j)$(ks)	$\Delta\alpha(\delta\Delta\alpha)$	Grade	Achromaticity*
060206	0.70	–	1.07(0.02)	2.00(0.26)	71.21(3.65)	0.93(0.26)	Silver	X
060605	0.8	–	0.41	2.33(0.16)	8.83(1.21)	1.92	Bronze	$\surd$
060526	1.69(0.53)	–	0.67(0.02)	1.80(0.04)	84.45(5.88)	1.13(0.04)	Gold	$\surd$
060614	0.94(0.08)	–	0.77(0.10)	2.70(0.07)	112.35(8.53)	1.93(0.12)	Gold	$\surd$
060729	0.74(0.07)	–	1.09(0.10)	2.13(0.44)	297.49(69.62)	1.03(0.45)	Silver	X
X-Ray								
980828	~ 1		1.44	2.6	190	1.16	Silver	?
030329	1.17	0.8(0.3)	0.87(0.05)	1.84(0.07)	44.93(4.32)	0.97(0.09)	Gold	$\surd$
050124	1.05(0.29)	0.93(0.21)	0.62(0.56)	2.53(0.78)	29.37(12.61)	1.91(0.96)	Silver	?
050128	1.05(0.08)	0.95(0.15)	1.00(0.13)	1.98(0.39)	30.70(14.20)	0.98(0.41)	Silver	?
050315	1.31(0.12)	1.17(0.07)	0.66(0.03)	1.90(0.23)	224.64(38.68)	1.24(0.23)	Silver	?
050318	1.01(0.08)	1.02(0.06)	0.90(0.23)	1.84(0.19)	10.60(4.97)	0.94(0.30)	Silver	X
050525A[c]	1.17(0.18)	1.17(0.18)	1.20(0.03)	1.62(0.16)	13.73(7.47)	0.42(0.16)	Gold	$\surd$

Table 8 (continued)

GRB	$\beta_2(\delta\beta_2)$	$\beta_4(\delta\beta_4)$	$\alpha_3(\delta\alpha_3)$	$\alpha_4(\delta\alpha_4)$	$t_j(\delta t_j)$(ks)	$\Delta\alpha(\delta\Delta\alpha)$	Grade	Achromaticity*
050717	0.61(0.08)	0.89(0.12)	0.57(0.21)	1.65(0.12)	1.84(0.95)	1.08(0.24)	Silver	?
050726	1.06(0.08)	1.14(0.09)	0.79(0.03)	2.32(0.22)	8.78(1.11)	1.53(0.22)	Silver	?
050730	0.65(0.03)	0.70(0.03)	-0.37(0.25)	2.49(0.04)	6.66(0.29)	2.86(0.25)	Bronze	$\surd$
050802	0.92(0.05)	0.89(0.07)	0.32(0.10)	1.61(0.04)	4.09(0.61)	1.29(0.11)	Bronze	X
050803	0.78(0.10)	1.00(0.08)	0.25(0.03)	2.01(0.07)	13.71(0.90)	1.76(0.08)	Bronze	?
050820A	0.63(0.05)	0.87(0.04)	1.11(0.02)	1.68(0.21)	421.00(179.00)	0.57(0.21)	Gold	$\surd$
050908	2.09(0.25)	1.09(0.25)	0.13(0.96)	1.58(0.46)	7.81(5.33)	1.45(1.06)	Bronze	X
051006	0.61(0.14)	0.84(0.20)	0.57(0.26)	2.23(0.56)	0.93(0.71)	1.66(0.62)	Silver	?
051008	1.15(0.32)	1.11(0.10)	0.86(0.09)	2.01(0.19)	14.67(3.82)	1.15(0.21)	Silver	?
051016B	1.19(0.13)	1.19(0.13)	0.71(0.08)	1.84(0.46)	66.40(23.09)	1.13(0.47)	Silver	?
051109A	0.91(0.07)	0.90(0.07)	0.79(0.07)	1.53(0.08)	27.28(7.90)	0.74(0.11)	Gold	$\surd$
051221A[d]	1.07(0.36)	1.02(0.19)	1.20(0.06)	1.92(0.52)	354.00(103.00)	0.72(0.52)	Silver	$\surd$
060105	1.23(0.05)	1.15(0.03)	0.84(0.01)	1.72(0.02)	2.31(0.14)	0.88(0.02)	Silver	?

Table 8 (continued)

GRB	$\beta_2(\delta\beta_2)$	$\beta_4(\delta\beta_4)$	$\alpha_3(\delta\alpha_3)$	$\alpha_4(\delta\alpha_4)$	$t_j(\delta t_j)$(ks)	$\Delta\alpha(\delta\Delta\alpha)$	Grade	Achromaticity*
060108	1.17(0.32)	0.75(0.15)	0.26(0.09)	1.43(0.17)	22.08(7.38)	1.17(0.19)	Bronze	?
060124	1.10(0.06)	1.06(0.08)	0.81(0.09)	1.66(0.05)	52.60(10.30)	0.85(0.10)	Silver	X
060203	1.08(0.19)	1.25(0.13)	0.40(0.30)	1.65(0.47)	12.95(6.69)	1.25(0.56)	Bronze	?
060204B	1.54(0.14)	1.64(0.16)	-0.49(0.65)	1.47(0.07)	5.55(0.66)	1.96(0.65)	Bronze	?
060210	1.12(0.08)	1.11(0.33)	1.00(0.05)	1.85(0.27)	187.00(76.50)	0.85(0.27)	Silver	X
060211A	1.15(0.06)	1.11(0.26)	0.38(0.08)	1.63(1.27)	267.24(165.67)	1.25(1.27)	Bronze	?
060313	0.84(0.34)	0.78(0.09)	0.82(0.03)	1.76(0.18)	11.18(2.89)	0.94(0.18)	Silver	?
060319	0.93(0.22)	1.25(0.11)	0.84(0.02)	1.92(0.30)	99.70(26.78)	1.08(0.30)	Silver	?
060323	0.99(0.16)	1.02(0.13)	-0.11(0.23)	1.55(0.16)	1.29(0.32)	1.66(0.28)	Bronze	?
060428A	1.11(0.24)	0.97(0.10)	0.48(0.03)	1.46(0.37)	125.31(47.19)	0.98(0.37)	Bronze	?
060502A	1.11(0.29)	1.15(0.13)	0.53(0.03)	1.68(0.15)	72.57(15.05)	1.15(0.15)	Bronze	?
060510A	1.04(0.05)	1.06(0.14)	0.93(0.14)	1.77(0.10)	47.70(16.70)	0.84(0.17)	Silver	?
060526 [e]	1.07(0.09)	1.08(0.16)	0.42(0.12)	1.58(0.34)	11.60(6.39)	1.16(0.36)	Gold	$\surd$

Table 8 (continued)

GRB	$\beta_2(\delta\beta_2)$	$\beta_4(\delta\beta_4)$	$\alpha_3(\delta\alpha_3)$	$\alpha_4(\delta\alpha_4)$	$t_j(\delta t_j)$(ks)	$\Delta\alpha(\delta\Delta\alpha)$	Grade	Achromaticity*
060605	0.62(0.17)	0.83(0.09)	0.45(0.04)	1.80(0.13)	7.14(0.93)	1.35(0.14)	Bronze	$\surd$
060614[f]	0.96(0.16)	0.93(0.06)	1.03(0.02)	2.13(0.07)	36.60(2.40)	1.10(0.07)	Gold	$\surd$
060807	1.18(0.09)	1.40(0.20)	0.96(0.24)	1.92(0.12)	14.90(5.88)	0.96(0.27)	Silver	?
060813	0.99(0.05)	1.10(0.07)	0.87(0.03)	1.63(0.13)	15.20(3.88)	0.76(0.13)	Silver	?
060814	1.30(0.05)	1.30(0.05)	1.06(0.12)	2.38(0.40)	68.60(23.30)	1.32(0.42)	Silver	?
060906	1.28(0.37)	1.12(0.17)	0.35(0.10)	1.97(0.36)	13.66(3.29)	1.62(0.37)	Bronze	?
060908	1.01(0.22)	1.00(0.08)	0.70(0.07)	1.49(0.09)	0.95(0.34)	0.79(0.11)	Bronze	?
060927	0.65(0.19)	0.92(0.15)	0.73(0.32)	1.82(2.60)	4.24(8.22)	1.09(2.62)	Silver	?
061121	0.71(0.03)	0.96(0.07)	0.75(0.06)	1.63(0.05)	24.32(4.38)	0.88(0.08)	Silver	?
061201	0.30(0.15)	0.30(0.15)	0.57(0.07)	1.61(0.23)	2.09(0.75)	1.04(0.24)	Bronze	?
061222A	1.45(0.06)	1.22(0.12)	0.81(0.07)	1.86(0.06)	60.50(8.89)	1.05(0.09)	Silver	?
070103	1.32(0.25)	1.52(0.21)	0.20(0.10)	1.63(0.08)	2.88(0.48)	1.43(0.13)	Bronze	?

*If a break is confirmed to be achromatic, we mark the break with a "$\surd$". If a break is clearly chromatic, we mark it with "X". For most of breaks without multi-wavelength observations, we have no information to access to the chromaticity of these breaks, so we mark them with a "?" sign.

"Platinum" Jet Break Candidates

With our definition, a "Platinum" jet break should be independently claimed in at least two bands which should be achromatic. Furthermore, the temporal decay slopes and spectral indices in both bands should satisfy those required in the simplest jet break models. Since the optical and the X-ray afterglows could be in different spectral regimes, their lightcurve behaviors may be different (e.g. Sari et al. 1999). However, none of the seven "Gold" candidates can be promoted to the "Platinum" sample due to the various issues.

Comparison Between The Jet Break Candidates In The X-Ray And Optical Bands

In this section we compare the statistical characteristics of the jet break candidates in the X-ray and optical lightcurves. Our final graded jet break candidates are shown in Table 8. The decay slopes of the pre-break segments of those "Bronze" candidates are much shallower than the prediction of the jet models. We cannot exclude the possibility that some "Bronze" jet break candidates are due to the energy injection effect in the wind medium (Chapter 5). Therefore, for the following analysis, we do not include the "Bronze" jet break candidates.

Detection Fraction

As shown above, within the 103 XRT lightcurves with a good temporal coverage, 27 have "Silver" or "Gold" jet break candidates. This fraction is 23/57 for optical lightcurves. The detection fraction of jet break candidates in the XRT lightcurves is significantly lower than that in the optical lightcurves.

Break Time

Figure 25 shows the distributions of t_j and $\Delta\alpha$ in the X-ray and optical lightcurves. The distributions of $\log t_{\rm j,X}/{\rm s}$ and $\log t_{\rm j,O}/{\rm s}$ peak at 4.5 and ~ 5.5, respectively. The $t_{\rm j,O}$

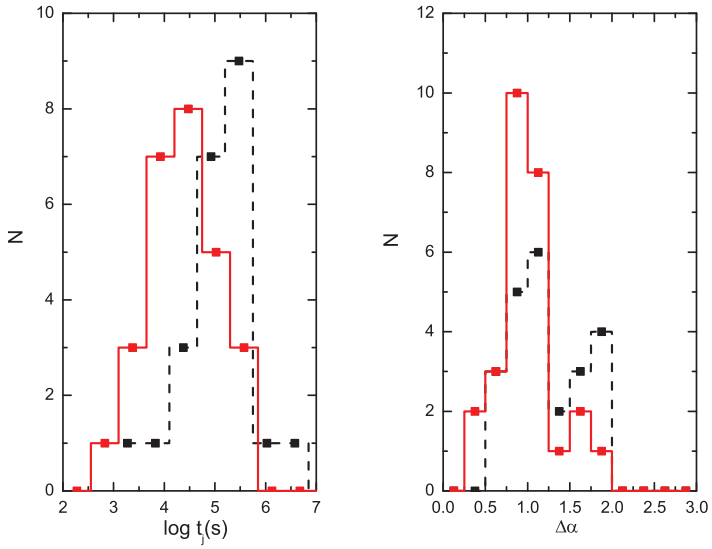

Figure 25 Comparison of the distributions of t_j and $\Delta\alpha$ for the XRT data (solid lines) and the optical data (dashed lines).

distribution has a sharp cutoff right at the high edge of the peak, indicating that the peak is possibly not an intrinsic feature. Since the histogram depends on the bin size selection, we test the normality of the data set with the Shapiro-Wilk normality test. It shows that the probability of a normal distribution for $t_{\rm j,O}$ is $p = 11.5\%$ (at 0.05 confidence level), roughly excluding the normality of the distribution. Therefore, this peak is likely due to an observational selection bias. By contrast, the $t_{\rm j,X}$ distribution is log-normal. The Shapiro-Wilk normality test shows $p = 79.8\%$ (at confidence level 0.05). These results suggest that the $t_{\rm j,X}$ is systematically smaller than $t_{\rm j,O}$ (see also Kocevski & Butler 2008). This raises the possibility that X-ray breaks and optical breaks may not be physically of the same origin.

$\Delta\alpha$

With the closure relations of $p > 2$ and assuming sideways expansion, we derive $\Delta\alpha = (\beta+1)/2$ for the regime-I ISM model and all the wind models, and $\Delta\alpha = \beta/2+1$ for the regime II ISM model. The observed β_X is ~ 1, hence $\Delta\alpha_X \sim 1$ or $\Delta\alpha_X \sim 1.5$. Figure 25 (right) shows that the $\Delta\alpha_X$ distribution peaks at ~ 1, which suggests that most X-ray afterglows are consistent with the regime II models (i.e. X-ray is above both ν_m and ν_c)[1]. The $\Delta\alpha_O$ show a tentative bimodal distribution, with two peaks at ~ 1 and ~ 1.7, roughly corresponding to the regime I ($\nu_O > \max(\nu_{\rm m}, \nu_{\rm c})$) and regime II ($\nu_m < \nu_O < \nu_c$) ISM models, respectively.

Chromaticity

Being achromatic is the critical criterion to claim a break as a jet break. As shown above, the distribution of $t_{\rm j,X}$ is systematically smaller than $t_{\rm j,O}$, which raises the concern of achromaticity of some of these breaks. Monfardini et al. (2006) have raised the concern that some jet-like breaks may not be achromatic. We further check the chromaticity for the jet candidates case by case. We find 13 bursts that have good temporal coverage in both X-ray and optical bands, with a jet break candidate at least in one band. The results are the following.

- The breaks in the X-ray and optical bands are consistent with being achromatic: GRBs 030329, 050525A, 050820A, 051109A, 060526, and 060614.
- The X-ray and optical breaks are at different epochs: GRBs 060206 and 060210
- A "Silver" jet break candidate in the optical band, but no break in the X-ray band: GRBs 051111 and 060729.
- A "Silver" or "Bronze" jet break candidate in the X-ray band, but no break in the optical band: GRBs 050318 ("Silver"), 050802 ("Bronze"), and 060124 ("Silver").

[1]Two GRBs have a $\Delta\alpha_X$ greater than 1.5— GRB 050124 ($\Delta\alpha_X = 1.91 \pm 0.96$) and GRB 051006 ($\Delta\alpha_X = 1.66 \pm 0.62$), but they have large errors.

The ratio of achromatic to chromatic breaks is 6:7, indicating that the achromaticity is not a common feature of these breaks. It is a great issue to claim the chromatic breaks as a jet break. If both the X-ray and optical emissions are from the forward shocks, one can rule out a large fraction (7/13) of these jet break candidates (many are "Silver" candidates) as a jet break! We indicate the achromaticity of the jet break candidates in Table 8. If the above achromatic-to-chromatic ratio is a common value, most of the breaks without multi-wavelength observations (marked with a "?" in Table 8) should be also chromatic. A possible way out to still consider these breaks as jet breaks is to *assume* that the band (either X-ray or optical) in which the break is detected is from the forward shock, while emission from the other band is either not from the forward shock or some unknown processes have smeared the jet break feature from the forward shock in that band. Such a model does not explicitly exist yet. We therefore suggest that *one should be very cautious to claim a jet break, and further infer the GRB energetics from a jet break candidate*. We are probably still a long way from understanding GRB collimation and energetics.

Constraints on GRB Jet Collimation and Kinetic Energetics

As shown above, the observed chromatic feature is not consistent with the forward shock models, and it is risky to infer GRB collimation and energetics from these data. In this section, we *assume* that those "Silver" or "Gold" jet break candidates are jet breaks, and follow the standard forward shock model to constrain jet collimation and kinetic energy of the GRB jets.

Models

In the standard afterglow models, the isotropic kinetic energy ($E_{\rm K,iso}$) can be derived from the data in the normal decay phase, and the jet kinetic energy E_K can be obtained from the jet break information (e.g. Rhoads 1999; Sari et al. 1999; Frail et al. 2001). The models depend on the power law index p of the electron distribution, the spectral

regime, and the medium stratification surrounding the bursts (Mészáros & Rees 1993; Sari et al. 1998; Dai & Lu 1998b; Chevalier & Li 2000; Dai & Cheng 2001). Most bursts in our sample (25 out of 29) are consistent with $p > 2$. We therefore only consider $p > 2$ in this analysis. Essentially all the data are consistent with the ISM model.

We use the X-ray afterglow data to calculate $E_{\rm K,iso}$, following the same procedure presented in our previous work (Zhang et al. 2007), which gives

$$\begin{aligned} E_{\rm K,iso,52} &= \left[\frac{\nu F_\nu(\nu=10^{18}\ {\rm Hz})}{5.2\times10^{-14}\ {\rm ergs\ s^{-1}\ cm^{-2}}}\right]^{4/(p+2)} D_{28}^{8/(p+2)}(1+z)^{-1}t_d^{(3p-2)/(p+2)} \\ &\times (1+Y)^{4/(p+2)} f_p^{-4/(p+2)}\epsilon_{B,-2}^{(2-p)/(p+2)}\epsilon_{e,-1}^{4(1-p)/(p+2)}\nu_{18}{}^{2(p-2)/(p+2)} \\ &\quad \text{(Spectral regime I)} \end{aligned} \tag{6.5}$$

$$\begin{aligned} E_{\rm K,iso,52} &= \left[\frac{\nu F_\nu(\nu=10^{18}\ {\rm Hz})}{6.5\times10^{-13}\ {\rm ergs\ s^{-1}\ cm^{-2}}}\right]^{4/(p+3)} D_{28}^{8/(p+3)}(1+z)^{-1}t_d^{3(p-1)/(p+3)} \\ &\times f_p^{-4/(p+3)}\epsilon_{B,-2}^{-(p+1)/(p+3)}\epsilon_{e,-1}^{4(1-p)/(p+3)} n^{-2/(p+3)}\nu_{18}{}^{2(p-3)/(p+3)} \\ &\quad \text{(Spectral regime II)} \end{aligned} \tag{6.6}$$

where $\nu f_\nu(\nu = 10^{18}{\rm Hz})$ is the energy flux at 10^{18} Hz (in units of ergs s^{-1} cm^{-2}) , z the redshift, D the luminosity distance, f_p a function of the power law distribution index p (Zhang et al. 2007a), n the density of the ambient medium, t_d the time in the observers frame in days, Y the inverse Compton parameter. The convention $Q_n = Q({\rm in\ cgs\ units})/10^{\rm n}$ has been adopted.

If the ejecta are conical, the lightcurve shows a break when the bulk Lorentz factor declines down to $\sim \theta^{-1}$ at a time (Rhoads 1999; Sari et al. 1999)

$$t_j \sim 0.5\ {\rm days}(\frac{E_{\rm K,iso,52}}{n})^{1/3}(\frac{1+z}{2})(\frac{\theta_j}{0.1})^{8/3}. \tag{6.7}$$

The jet opening angle can be derived as

$$\theta_j \sim 0.17\left(\frac{t_j}{1+z}\right)^{3/8}\left(\frac{E_{\rm K,iso,52}}{n}\right)^{-1/8}. \tag{6.8}$$

The geometrically corrected kinetic energy is then given by

$$E_{\rm K,52} = E_{\rm K,iso,52}(1 - \cos\theta_j) \ . \tag{6.9}$$

Results

The results are shown in Table 9 and 10. The distributions of $E_{\rm K,iso}$ and p are displayed in Fig. 26. No significant differences between the pre-*Swift* and the *Swift* samples are found for these parameters. The Kolmogorov-Smirnov test shows that $p_{K-S} = 0.61$ for the $E_{\rm K,iso}$ distribution and $p_{K-S} = 0.81$ for the p distribution. The $E_{\rm K,iso}$ distribution spans almost 3 orders of magnitude, ranging from 2×10^{52} to 1×10^{55} ergs with a log-normal peak at 7×10^{53} ergs. The probability of the normality is 73% at 0.05 confidence level.

Table 9. Derivation of Jet Opening Angles and Kinetic Energies

GRB	z	Reg.[a]	p	$\epsilon_{B,-4}$	Y	$\theta_j(^o)$	$\log E_{\rm K,iso}$[b]	$\log E_{\rm K}$[b]	$\log \nu_m$[c]	$\log \nu_c$[c]	ref.[d]
050315	1.95	I	2.76	1.00	2.45	2.9	55.06	52.17(0.05)	11.71	16.61	1
050318	1.44	I	2.08	1.01	6.91	1.6	53.30	49.91(0.16)	11.86	18.00	2
050319	3.24	I	2.16	1.00	4.93	>2.5	53.76	>50.75	11.69	17.70	3
050401	2.9	II	2.98	0.20	2.59	>4.2	54.97	>52.40	12.51	>18.00	4
050416A	0.65	I	2.32	10.78	0.72	>9.3	51.94	>50.06	11.80	>18.00	5
050505	4.27	I	2.1	1.00	6.28	>2.5	54.03	>51.00	11.56	17.53	6
050525A	0.606	II	3.34	0.99	0.10	2.6	53.98	50.99(0.06)	12.79	>18.69	7
050820A	2.61	I	2.01	1.00	11.05	3.6	54.88	52.17(0.14)	9.65	17.08	8
050922C	2.2	II	2.44	1.49	3.16	>2.9	53.24	>50.35	13.15	>18.00	9
051016B	0.94	I	2.18	3.30	1.31	4.82	52.24	49.79(0.12)	10.31	18.00	10
051221A	0.5465	I	2.14	9.76	0.79	12.06	51.53	49.87(0.10)	10.19	18	11
060124	2.3	II	3.12	0.23	1.06	1.5	55.41	51.91(0.06)	12.11	>18.00	12
060206	4.05	I	2.62	1.00	2.65	1.8	54.48	51.18(0.02)	11.74	16.90	13

Table 9 (continued)

GRB	z	Reg.[a]	p	$\epsilon_{B,-4}$	Y	$\theta_j(^o)$	$\log E_{\rm K,iso}$[b]	$\log E_{\rm K}$[b]	$\log \nu_m$[c]	$\log \nu_c$[c]	ref.[d]
060210	3.91	I	2.24	1.00	5.75	2.7	54.33	51.39(0.14)	12.25	17.37	14
060502A	1.51	II	3.3	0.79	0.15	2.1	54.88	51.71(0.07)	12.04	18.00	15
060512	0.44	II	3.36	1.00	0.12	>6.1	52.38	>50.14	13.41	>19.09	16
060522	5.11	I	2.26	1.00	2.91	>4.8	53.17	>50.73	11.50	17.81	17
060526	3.21	I	2.14	1.01	5.26	2.82	53.41	50.49(0.02)	11.58	17.65	18
060604	2.68	I	2.54	1.00	2.38	>4.6	53.75	>51.26	12.02	17.59	19
060605	3.7	II	2.98	0.60	2.38	>1.6	54.21	>50.81	13.32	>18.00	20
060614	0.13	II	2.72	1.00	0.43	6.8	52.45	50.30(0.02)	10.74	>18.32	21
060714	2.71	I	2.12	1.00	4.26	>5.1	53.32	>50.91	11.17	17.94	22
060729	0.54	I	2.26	1.00	2.42	6.6	53.39	51.21(0.08)	9.93	17.54	23
060814	0.84	I	2.60	2.33	1.41	3.63	53.34	50.64(0.12)	12.6	18 0	24
060908	2.43	II	2.5	1.00	1.62	>8.4	52.78	>50.81	11.99	>18.26	25
060912	0.94	I	2.01	1.02	7.06	>4.4	52.88	>50.35	9.46	17.98	26

Table 9 (continued)

GRB	z	Reg.[a]	p	$\epsilon_{B,-4}$	Y	$\theta_j(^o)$	$\log E_{\rm K,iso}$[b]	$\log E_{\rm K}$[b]	$\log \nu_m$[c]	$\log \nu_c$[c]	ref.[d]
060926	3.2	I	2.01	1.01	15.71	>0.9	54.21	>50.26	11.21	17.21	27
061007	1.26	II	3.16	1.00	1.93	>7.6	53.99	>51.94	14.35	>18.22	28
061121	1.31	II	2.7	0.95	1.01	1.93	53.88	50.63(0.06)	11.57	18.01	29
070110	2.35	I	2.72	1.00	1.70	>7.8	54.31	>52.27	11.38	16.98	30

[a]The spectral regime of the X-rays: I—$\nu_X > \max(\nu_m, \nu_c)$; II—$\nu_m < \nu_X < \nu_c$.

[b]The kinetic energies are in units of ergs. The calculation of the error of $E_{\rm K}$ for those bursts with detection of a jet break takes only the uncertainty of the jet break time into account.

[c]The frequencies are in units of Hz. The ν_c for those X-rays in the spectral regime II is a lower limit.

[d]The reference of redshift.

References. — 1: Kelson & Berger(2005); 2: Berger & Mulchaey(2005); 3: Fynbo et al.(2005a); 4: Fynbo et al.(2005b); 5: Cenko et al.(2005; 6: Berger et al.(2005c); 7: Fynbo et al.(2005c); 8: Ledoux et al.(2005); 9: D'Elia et al.(2005); 10: Soderberg et al.(2005); 11: Berger & Soderberg(2005); 12: Cenko et al.(2006a); 13: Aoki et al.(2006); 14: Cucchiara et al.(2006a); 15: Cucchiara et al.(2006b); 16: Bloom et al.(2006a); 17: Cenko et al.(2006b); 18: Berger & Gladders(2006); 19: Castro-Tirado et al.(2006); 20: Still et al.(2006); 21: Fugazza et al.(2006); 22: Jakobsson et al.(2006a); 23: Thoene et al.(2006) ; 24:Thoene (2007); 25:Rol et al.(2006); 26: Jakobsson et al.(2006b); 27: D'Elia et al.(2006); 28: Jakobsson et al.(2006c); 29: Bloom et al.(2006b); 30: Jaunsen et al.(2006)

The θ_j and E_K distributions are shown in Fig. 27. A sharp cutoff at $\theta_j \sim 1.5^{\rm o}$ is observed. The θ_j of the *Swift* GRBs derived from XRT observations tends to be smaller than that of the pre-*Swift* GRBs. The E_K of the pre-*Swift* GRBs log-normally distribute around 1.5×10^{51} with a dispersion of 0.44 dex (at 1σ confidence level). However, the E_K of the *Swift* GRBs randomly distribute in the range of $10^{50} \sim 10^{52}$ ergs (see also Kocevski & Butler 2008). We examine the correlation between $E_{\rm K,iso}$ and θ_j in Fig. 28. A tentative anti-correlation is found, but it has a large scatter. The best fit yields $E_{\rm K,iso} \propto \theta_j^{-2.35\pm0.52}$, with a linear correlation coefficient $r = -0.66$ and a chance probability of $p \sim 10^{-4}$ (N=28). This suggests that although E_K has a much larger scatter than the pre-*Swift* sample, it is still quasi-universal among bursts.

Conclusions and Discussion

We have presented a systematic analysis on the *Swift*/XRT data of 179 GRBs observed between Jan., 2005 and Jan., 2007 and the optical afterglow lightcurves of 57 GRBs detected before Jan. 2007, in order to systematically investigate the jet-like breaks in the X-ray and optical afterglow lightcurves. Among the 179 XRT lightcurves, 103 have good temporal coverage and have no significant flares in the afterglow phase. The 103 XRT lightcurves are fitted with the STPL, SBPL, or SPL model, and the spectral index of each segment of the lightcurves is derived by fitting the spectrum with a simple absorbed power law model. The same fitting is also made for the 57 optical light curves. We grade the jet break candidates through examining the data with the forward shock models with "Bronze", "Silver", "Gold", or "Platinum". We show that among the 103 well-sampled XRT lightcurves with a break, 42 are "Bronze", and 27 are "Silver". Twenty-seven out of 57 optical breaks are "Bronze", and 23 "Silver". Thirteen bursts have well-sampled lightcurves of both the X-ray and optical bands, but only 6 cases are consistent with being achromatic. Together with the GRB 990510 (in which an achromatic break in optical and radio bands can be claimed, Harrison et al. 1999), we have 7 "Gold" jet break candidates.

Table 10. Observations of pre-*Swift* GRBs derived parameters

GRB	z[a]	Reg.	time (s)[a]	$F_x(\delta F_X)$[a]	$\alpha(\delta\alpha)$[a]	β[b]	t_j(ks)	θ^o	θ_j (rad)[a]	p	$\epsilon_{B,-4}$	Y	$E_{\rm K,iso}$	$E_{\rm K}$	$\log\nu_m$	$\log\nu_c$
970508	0.835	I	47160	7.13	1.1	$1.14^{+0.51}_{-0.36}$	2160.00(432.00)	16.7	0.391	2.28	3.4	1.34	52.53	51.15(0.07)	11.26	18.00
970828	0.958	II	14400	118	1.44(0.07)	$1.1^{+0.3}_{-0.3}$	190.08(34.56)	3.9	0.128	3.2	0.99	0.80	54.31	51.68(0.06)	13.46	18.20
980703	0.966	I	122400	4(1)	1.24(0.18)	$1.77^{+0.6}_{0.47}$	214.92(10.15)	6.1	0.2	2.1	1.01	3.52	52.91	50.67(0.02)	9.81	17.87
990123	1.6	I	84240	19.11(2.2)	1.41(0.05)	$0.99^{0.07}_{-0.08}$	155.13(787.86)	2.9	0.089	2.98	0.40	1.51	54.77	51.87(0.18)	12.32	18.00
990510	1.619	I	42120	32.8(1.4)	1.41(0.18)	$1.19^{+0.14}_{-0.14}$	101.91(124.81)	3.1	0.054	2.38	1.00	3.63	53.98	51.14(0.04)	12.07	17.62
990705	0.84	II	52200	1.9(0.6)	–	1.05	86.40(17.28)	3.8	0.096	3.1	0.99	0.22	53.52	50.85(0.06)	12.18	18.67
991216	1.02	II	39240	250(10)	1.61(0.07)	$0.7^{+0.1}_{-0.1}$	248.71(67.63)	3.7	0.051	2.01	1.0	11/11	54.79	52.12(0.11)	9.57	17.29
000926	2.307	I	197640	2.23(0.77)	–	$0.9^{+0.3}_{-0.2}$	175.18(4.62)	3.3	0.14	2.01	1.00	7.11	54.12	51.34(0.01)	8.29	17.16
010222	1.477	I	117720	1.87(0.18)	1.33(0.04)	$1^{+0.1}_{-0.1}$	80.35(12.96)	2.7	0.08	2.02	1.00	7.59	54.21	51.25(0.05)	9.21	17.29
011211	2.14	II	29600	0.248	0.95(0.02)	$1.16^{+0.03}_{0.03}$	198.66(16.68)	3.5	-	3.32	0.99	0.21	54.11	51.39(0.02)	12.84	18.31
020405	0.689	I	147600	13.6(2.5)	1.15(0.95)	$1^{+0.2}_{-0.1}$	236.88(15.90)	5.7	0.285	2.02	1.00	5.55	53.53	51.21(0.02)	8.63	17.67
020813	1.254	II	114840	22	1.42(0.05)	$0.8^{+0.1}_{-0.1}$	397.44(0.864)	2.2	0.066	2.6	0.55	1.86	54.08	50.95(0.01)	11.57	18.00
021004	2.323	I	113040	4.3(0.7)	1(0.2)	$1.1^{+0.1}_{-0.1}$	300.30(8.64)	4.7	0.24	2.2	1.00	3.69	53.61	51.13(0.01)	10.85	17.54
030329[c]	0.1678	I	22377	157.0(8.7)	1.2(0.1)	1.17 ± 0.04	40.95(0.43)	3.8	0.052	2.34	2.15	2.23	53.09	50.43(0.01)	11.95	18.00

[a]Taken from Berger et al. (2003) and Bloom et al. (2003).

[b]Taken from Sako et al. 2005.

[c]Taken from Willingale et al. (2004).

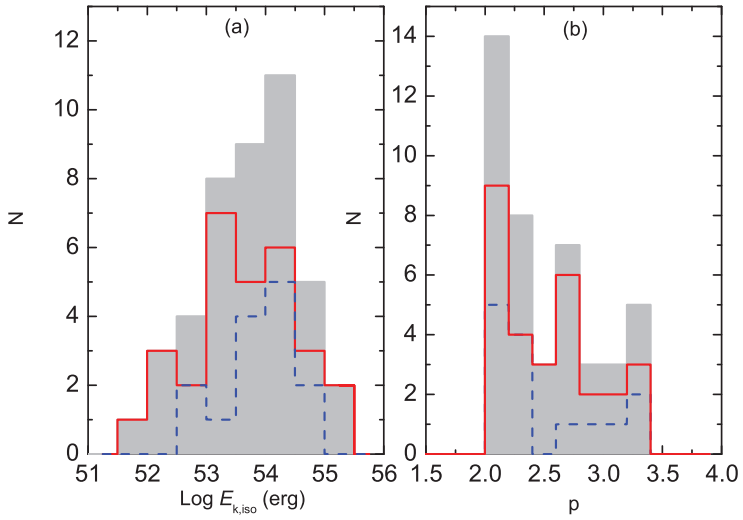

Figure 26 Comparisons of the distributions of $E_{\rm K,iso}$ (panel a) and p (panel b) for *Swift* GRBs (solid lines) with that of the pre-*Swift* GRBs (dashed lines). The shaded columns are for both pre-*Swift* and *Swift* GRBs combined.

However, none of them can be classified as "Platinum", i.e. a textbook version of a jet break. Curiously, 7 out of the 13 jet-break candidates with multi-wavelength data suggest a chromatic break at the "jet break", in contrary to the expectation of the jet models. The detection fraction of a jet break candidate in the XRT lightcurves is lower than that of the optical lightcurves, and the break time is also statistically earlier. These facts suggest that one should be very cautious in claiming a jet break and using the break information to infer GRB collimation and energetics.

We cautiously assume that the breaks in discussion are indeed jet breaks and proceed to constrain the θ_j and E_K by using the X-ray afterglow data using the conventional jet models. We show that the geometrically corrected afterglow kinetic energy E_K has a broader distribution than the pre-*Swift* sample, disfavoring the standard energy reservoir argument. On the other hand, a tentative anti-correlation between θ_j and $E_{\rm K,iso}$ is found for both the pre-*Swift* and *Swift* GRBs, indicating that the E_K could still be quasi-

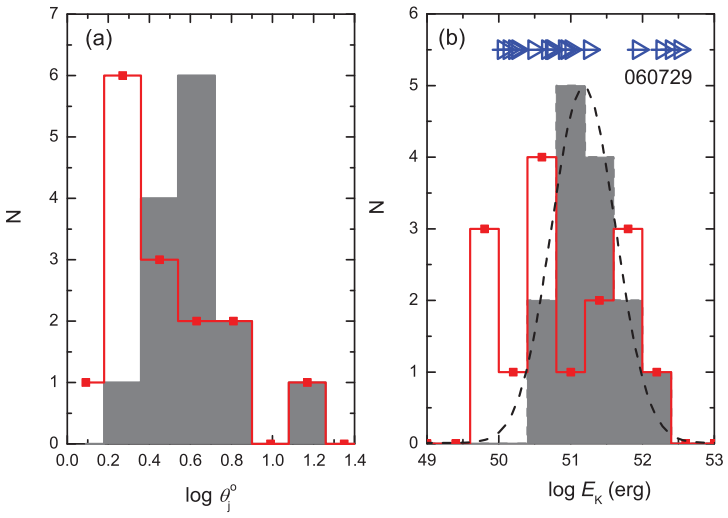

Figure 27 Comparison of the $E_{\rm K}$ distribution of *Swift* GRBs with that of the pre-*Swift* GRBs (shaded columns). The lower limits of $E_{\rm K}$ derived from the XRT observations are marked as open triangles. The dashed line is the Gaussian fit to the distribution of E_K of pre-*Swift* GRBs.

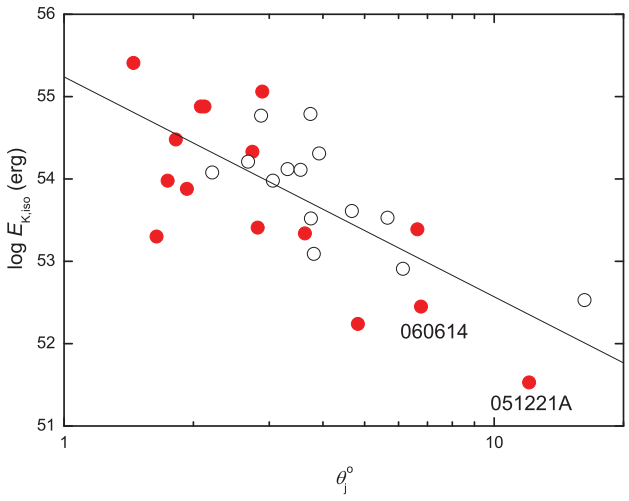

Figure 28 The $E_{\rm K,iso}$ as a function of θ_j for both the pre-*Swift* (open circles) and *Swift* GRBs (solid circles). The solid line is the best fit for both the pre-*Swift* and *Swift* GRBs.

universal.

PART III

Fermi OBSERVATIONS AND THEIR PHYSICAL IMPLICATIONS

CHAPTER 7

A COMPREHENSIVE ANALYSIS ON *FERMI*/LAT GRBS

This chapter is partially based on the following published paper:

Zhang, B.-B., et al. 2011, The Astrophysical Journal, 730, 141

Fermi/LAT Observation and Data Reduction

The *Fermi* satellite ushered in a new era of studying GRB prompt emission. The two instruments on board *Fermi*, the Gamma-ray Burst Monitor (GBM; Meegan et al. 2009) and the Large Area Telescope (LAT; Atwood et al. 2009), provide an unprecedented spectral coverage for 7 orders of magnitude in energy (from ∼8 keV to ∼300 GeV). Since the beginning of GBM/LAT science operation in August 2008 to May 2010, there have been 17 GRBs co-detected by LAT and GBM, with a detection rate comparable to the expectation assuming that the LAT-band emission is the simple extrapolation of the Band spectrum to the GeV range (Ando et al. 2008). As will be shown below, the Band-function fits apply to most LAT GRBs, although some outliers do exist. Broad band spectral analyses have been published by the *Fermi* team for several individual GRBs, e.g. GRB 080916C (Abdo et al. 2009a), GRB 090510 (Abdo et al. 2009b, Ackermann et al. 2010), GRB 090902B (Abdo et al. 2009c, Ryde et al. 2010), GRB 080825C (Abdo et al. 2009d), and GRB 081024B (Abdo et al. 2010a), which revealed several interesting features, such as the nearly featureless Band spectra covering 6 orders of magnitude in all epochs for GRB 080916C, the existence of an extra power law component extending to high energies in GRB 090510 and GRB 090902B, the existence of a quasi-thermal emission component in GRB 090902B, the delayed onset of the LAT-band emission with respect to the GBM-band emission, as well as an extended rapidly decaying GeV afterglow for most GRBs.

These discoveries have triggered a burst of theoretical investigations of GRB prompt emission. Zhang & Pe'er (2009) argued that the lack of a thermal component in the nearly featureless spectra of GRB 080916C suggests a Poynting flux dominated flow for

this burst. The conclusion was strengthened by a follow up study of Fan (2010, see also Gao et al. 2009). On the other hand, the quasi-thermal component in GRB 090902B (Ryde et al. 2010) is well-consistent with the photosphere emission of a hot fireball (Pe'er et al. 2010, Mizuta et al. 2010), suggesting that the burst is not highly magnetized. The possibility that the entire Band function spectrum is photosphere emission was discussed by several authors (Fan 2009; Toma et al. 2010; Beloborodov 2010; Lazzati & Begelman 2010; Ioka 2010). These models have specific predictions that can be tested by the available data. In the high energy regime, Kumar & Barniol Duran (2009, 2010), Ghisellini et al. (2010) and Wang et al. (2010) suggested that the GeV afterglow is of external shock origin, which requires some unconventional parameters (Li 2010a; Piran & Nakar 2010). On the other hand, the fact that LAT emission is the natural spectral extension of GBM emission in some GRBs suggests that the GeV emission may be of an internal origin similar to MeV emission (Zhang & Pe'er 2009). Finally, the delayed onset of the GeV emission has been interpreted as emergence of the upscattered cocoon emission (Toma et al. 2009), synchrotron emission from shock accelerated protons (Razzaque et al. 2010), as well as delayed residual internal shock emission (Li 2010b). Again these models have specific predictions that may be tested by a detailed analysis of the data.

This work is to systematically analyze the GRB data collected by the *Fermi* mission, aiming at addressing some of the above mentioned problems in prompt GRB emission physics. This sample of GRBs were co-detected by LAT and GBM. This sample has a much broader spectral coverage than the GBM-only GRBs, and therefore carries much more information about GRB prompt emission.

Sample and Data Reduction

As of May 2010, 17 GRBs have been co-detected by *Fermi* LAT and GBM. Our sample includes all 17 GRBs (Table 11). We downloaded the GBM and LAT data for these GRBs from the public science support center at the official *Fermi* web site

http://fermi.gsfc.nasa.gov/ssc/data/. An IDL code was developed to extract the energy-dependent lightcurves and time-dependent spectra for each GRB. This code was based on the *Fermi* RMFIT package (V3.3), the *Fermi* Science Tools (v9r15p2) and the HEASOFT tools, which allows a computer to extract lightcurves and spectra automatically. The human involvement is introduced later to refine the analysis when needed. The code automatically performs the following tasks.

1. Extract the background spectrum and lightcurve of the GBM data. *Fermi* records GBM data in several formats. For background reduction we use the CSPEC format data because it has a wider temporal coverage than the event data (time-tagged event, TTE, format). The background spectrum and lightcurve are extracted from some appropriate time intervals before and after the burst[1], and the energy-dependent background lightcurves are modeled with a polynomial function $B(E_{\rm ch}, t)$, where $E_{\rm ch}$ is a specified energy band.

2. Extract the source spectrum and lightcurve of the GBM data. This is done with the event (TTE) data. GBM has 12 NaI detectors (8 keV–1 MeV) and 2 BGO detectors (200 keV–40 MeV). The overall signal-to-noise ratio (SNR) and peak count rate are calculated for each detector. The brightest NaI and BGO detectors are usually used for the analyses. If several detectors have comparable brightnesses, all of them (usually 2-4 detectors) are taken for the analyses. By subtracting the background spectrum and lightcurve obtained in the previous step, the time-dependent spectra and energy-dependent lightcurves of the source in the GBM band are then obtained.

3. Estimate the LAT-band background. Since only a small number of photons are detected by LAT for most GRBs, the background estimation should be performed

[1] An appropriate background time interval is typically when the lightcurve is "flat" with Poisson noise photons. For each burst, we select background time intervals as [-$t_{b,1}$,-$t_{b,1}$] before the burst and [$t_{b,3}$,$t_{b,4}$] after the burst, where t_b's are typically in the order of tens to hundreds of seconds. The exact values vary for different bursts due to their different brightnesses and the corresponding orbit slewing phases.

cautiously. It is not straightforward to estimate an accurate LAT background using off-source regions around the trigger time. In our analyses, the LAT background is extracted using on-source region data long after the GBM trigger when the photon counts merge into a Poisson noise.

Table 11 The GRBs co-detected by *Fermi* LAT and GBM until May, 2010

GRB	z	dur. [sec]	E_p [keV]	$E_{\gamma,\mathrm{iso}}$ [erg]	Fluence $(1-10^4$ keV)	Spectral Type	Onset Delay	$E_{\max}$
080825C	-	22	192 ± 15	-	$4.84^{+0.59}_{-0.57} \times 10^{-5}$	BAND	Y	~ 600 MeV
080916C	4.35	66	1443^{+433}_{-303}	$5.7^{+0.54}_{-0.41} \times 10^{54}$	$1.55^{+0.15}_{-0.11} \times 10^{-4}$	BAND	Y	~ 13.2 GeV
081024B	-	0.8	1258^{+2405}_{-522}	-	$(1,61 \pm 3.8) \times 10^{-6}$	BAND	Y	~ 3 GeV
081215A	-	7.7	1014^{+140}_{-123}	-	$8.74^{+1.21}_{-0.99} \times 10^{-5}$	BAND	-	-
090217	-	32.8	552^{+85}_{-71}	-	$4.48^{+0.69}_{-0.56} \times 10^{-5}$	BAND	N	~ 1 GeV
090323	3.57	150	812^{+181}_{-143}	$> 2.89^{+6.56}_{-0.69} \times 10^{54}$	$> 1.07^{+0.24}_{-0.26} \times 10^{-5}$	BAND	N	~ 1 GeV
090328	0.736	80	756^{+85}_{-72}	$1.02^{+0.087}_{-0.083} \times 10^{53}$	$7.14^{+0.61}_{-0.58} \times 10^{-5}$	BAND	?	> 100 MeV
090510	0.903	0.3	6010^{+2524}_{-1690}	$4.47^{+4.06}_{-3.77} \times 10^{52}$	$2.06^{+1.88}_{-1.74} \times 10^{-5}$	CPL+PL	Y	~ 31 GeV
090626	-	70	362^{+47}_{-41}	-	$7.81^{+0.44}_{-0.38} \times 10^{-5}$	BAND	?	~ 30 GeV
090902B	1.822	21	207 ± 6 [BB]	$(1.77 \pm 0.01) \times 10^{52}$	$(2.10 \pm 0.02) \pm 10^{-4}$	BB+PL	Y	$33.4^{+2.7}_{-3.5}$ GeV
090926A	2.1062	~ 20	412 ± 20	$2.10^{+0.09}_{-0.08} \times 10^{54}$	$1.93^{+0.08}_{-0.07} \times 10^{-4}$	BAND	Y	$\sim$20 GeV
091003	0.8969	21.1	409^{+34}_{-31}	$7.85^{+0.73}_{-0.57} \times 10^{52}$	$3.68^{+0.34}_{-0.27} \times 10^{-5}$	BAND	N	> 150 MeV
091031	-	~ 40	567^{+197}_{-135}	-	$3.17^{+0.64}_{-0.51} \times 10^{-5}$	BAND	N	1.2 GeV
100116A	-	~ 110	1463^{+163}_{-122}	-	$7.34^{+1.42}_{-1.26} \times 10^{-5}$	BAND	N	~ 2.2 GeV
100225A	-	13 ± 3	540^{+381}_{-204}	-	$1.21^{+1.07}_{-0.57} \times 10^{-5}$	BAND	Y	~ 300 MeV
100325A	-	8.3 ± 1.9	198^{+44}_{-37}	-	$6.15^{+2.85}_{-1.81} \times 10^{-6}$	BAND	N	~ 800 MeV
100414A	1.368	26.4 ± 1.6	520^{+42}_{-39}	$5.88^{+0.69}_{-0.65} \times 10^{53}$	$1.20^{+0.12}_{-0.10} \times 10^{-5}$	BAND	N	~ 2.6 GeV

4. Extract the LAT-band spectrum and lightcurve. Both "diffuse" and "transient" photons (level 0-3) are included. Since the LAT point spread function (PSF) strongly depends on the incident energy and the convention point of the tracker (Ohno et al. 2010), the photons are grouped into FRONT and BACK classes and their spectra are extracted separately based on different detector response files. The region of interest (ROI) that contains significant counts of LAT photons is further refined when necessary (Atwood et al. 2009; Abdo et al. 2009d).

5. Extract the background-subtracted GBM and LAT lightcurves for different energy bands. In our analysis, the lightcurves are extracted in the following energy bands: 8–150 keV, 150–300 keV, 300 keV–MeV, 1–30 MeV, and the LAT band (above 100 MeV).

6. Make dynamically time-dependent spectral fits. Initially, the burst duration is divided in an arbitrary number of slices. The code then automatically refines the number of slices and the time interval for each slice, so that the photon counts in each bin (typically minimum 20 counts for GBM spectra) give adequate statistics for spectral fitting (the reduced χ^2 is typically in the range of 0.75 - 1.5, a special case is GRB 090510, see discussion below). The time slices are defined to be be as small as possible as long as the extracted spectra satisfy these statistical criteria. The GBM spectra of the selected NaI and BGO detectors and the LAT "FRONT" and "BACK" type spectra are all extracted for each slice. These spectra, together with the corresponding response files (using the same one as the CSPEC data for LAT, or generated using gtrsp for GBM) are input into XSPEC (V 12.5.1) simultaneously to perform spectral fitting. The following spectral functions are considered (in order of increasing free parameters): single power law (PL), blackbody (BB, Planck function), power-law with exponential cutoff (CPL), and Band function. The models are tested based on the following principles: (1) If a one-component model can adequately describe the data (giving reasonable reduced χ^2, say, between

0.75 and 1.5), two-component models are not considered; (2) for one-component models, if a function with less free parameters can describe the data adequately, it is favored over the models with more parameters. (3) In addition, the Akaike's Information Criterion[2] (AIC, Akaike 1974) is calculated to evaluate each model by considering both the fitting goodness (χ^2) and the complexity of the model. We confirmed that the model with minimal AIC is the preferred model we choose based on the first two criteria. Nonetheless, since most GRBs have a Band-function spectra (see below), we also apply the Band function to those time bins that do not demand it in order to compare the fitting results between the Band function and other functions with less parameters (e.g. power law, blackbody, or power law with exponential cutoff).

To assess the quality of a spectral fit, we use the traditional χ^2 statistics. Due to the low count rate of LAT photons, we use the Gehrels (1986) weighting method in the high energy regime. We also employed the C-stat method (as used by the *Fermi* team), and found that the two methods usually give consistent results. We chose the χ^2 method since it gives more reliable error estimates. All the model fitting parameters and χ^2 statistics are presented in Table 12. For each burst, we present the time-dependent spectral parameters in the designated time bins defined by the statistics of spectral fitting, as well as the time-integrated spectral fit during the entire burst in the last row.

[2]AIC is defined by $AIC = n \ln\left(\frac{\chi^2}{n}\right) + 2k$, where n is the number of data points, k is the number of free parameters of a particular model, and χ^2 is the residual sum of squares from the estimated model (e.g. Shirasaki et al. 2008).

Table 12: Time-resolved and time-integrated spectral fitting parameters of 17 *Fermi*/LAT GRBs.

080825C Model : Band Function

Seq	Time s	α	β	E_0 keV	K $\frac{photons}{keVcm^2s}$@100keV	χ^2	dof
1	0.00-6.75	$-0.57^{+0.05}_{-0.04}$	-2.29 ± 0.04	135^{+10}_{-9}	$0.114^{+0.008}_{-0.007}$	147.1	154
2	6.75-18.1	-0.75 ± 0.06	$-2.35^{+0.09}_{-0.07}$	141^{+16}_{-14}	$0.051^{+0.005}_{-0.004}$	132.7	154
3	18.1-25.0	$-0.95^{+0.17}_{-0.15}$	$-2.17^{+0.17}_{-0.08}$	131^{+56}_{-35}	$0.027^{+0.009}_{-0.006}$	120.1	154
Total	0.00-25.0	-0.73 ± 0.03	$-2.33^{+0.04}_{-0.03}$	148 ± 9	$0.058^{+0.003}_{-0.003}$	265.6	154

080916C Model : Band Function

Seq	Time s	α	β	E_0 keV	K $\frac{photons}{keVcm^2s}$@100keV	χ^2	dof
1	0.00-3.70	$-0.69^{+0.05}_{-0.04}$	$-2.49^{+0.13}_{-0.08}$	342^{+43}_{-37}	$0.047^{+0.003}_{-0.002}$	99.5	124
2	3.70-9.10	-1.14 ± 0.03	$-2.32^{+0.06}_{-0.05}$	1680^{+500}_{-348}	0.027 ± 0.001	153.0	124
3	9.10-17.0	$-1.15^{+0.05}_{-0.04}$	$-2.29^{+0.07}_{-0.05}$	975^{+361}_{-235}	0.016 ± 0.001	125.9	124
4	17.0-25.0	-0.99 ± 0.04	$-2.27^{+0.06}_{-0.04}$	447^{+75}_{-60}	0.024 ± 0.001	114.3	124
5	25.0-41.0	-1.08 ± 0.03	$-2.49^{+0.10}_{-0.07}$	666^{+111}_{-87}	0.017 ± 0.001	124.2	124
6	41.0-66.0	-1.09 ± 0.04	$-2.36^{+0.06}_{-0.05}$	696^{+186}_{-128}	0.010 ± 0.001	162.8	124
Total	0.00-66.0	-1.05 ± 0.02	-2.30 ± 0.02	664^{+51}_{-46}	0.018 ± 0.001	427.5	124

081024B Model : Band Function

Seq	Time s	α	β	E_0 keV	K $\frac{photons}{keVcm^2s}$@100keV	χ^2	dof
1	-0.300-0.800	$-1.15^{+0.14}_{-0.16}$	$-2.20(fixed)$	1478^{+2810}_{-551}	0.007 ± 0.001	353.9	208

081215A Model : Band Function

Seq	Time s	α	β	E_0 keV	K $\frac{photons}{keVcm^2s}$@100keV	χ^2	dof
1	0.00-1.50	-0.65 ± 0.05	$-2.27^{+0.14}_{-0.11}$	753^{+101}_{-88}	0.059 ± 0.002	80.0	71
2	1.50-2.28	$-0.52^{+0.08}_{-0.07}$	$-2.16^{+0.10}_{-0.08}$	280^{+43}_{-39}	$0.223^{+0.020}_{-0.017}$	63.6	61
3	2.28-4.93	-0.60 ± 0.06	$-2.34^{+0.09}_{-0.08}$	178^{+20}_{-17}	$0.156^{+0.013}_{-0.012}$	66.1	77
4	4.93-5.59	$-0.49^{+0.09}_{-0.08}$	$-2.29^{+0.15}_{-0.11}$	214^{+36}_{-31}	$0.266^{+0.032}_{-0.026}$	45.0	54
5	5.59-8.00	$-0.72^{+0.16}_{-0.14}$	$-2.19^{+0.13}_{-0.10}$	102^{+28}_{-22}	$0.093^{+0.029}_{-0.019}$	47.5	82
Total	0.00-8.00	-0.71 ± 0.03	$-2.16^{+0.04}_{-0.03}$	289^{+22}_{-21}	$0.110^{+0.005}_{-0.004}$	179.9	86

090217 Model : Band Function

Seq	Time s	α	β	E_0 keV	K $\frac{photons}{keVcm^2s}$@100keV	χ^2	dof
1	0.00-7.50	-0.59 ± 0.04	$-2.56^{+0.10}_{-0.07}$	365^{+33}_{-30}	0.027 ± 0.001	165.1	156
2	7.50-13.1	-0.83 ± 0.05	$-2.66^{+0.37}_{-0.14}$	470^{+70}_{-58}	0.021 ± 0.001	135.5	156
3	13.1-19.7	-0.96 ± 0.09	$-2.38^{+0.22}_{-0.10}$	257^{+73}_{-51}	0.015 ± 0.002	131.1	156
4	19.7-30.0	$-0.52^{+0.43}_{-0.25}$	$-2.22^{+0.17}_{-0.09}$	118^{+65}_{-52}	$0.008^{+0.009}_{-0.003}$	175.4	156
Total	0.00-30.0	-0.81 ± 0.03	$-2.54^{+0.06}_{-0.04}$	418^{+33}_{-30}	0.015 ± 0.001	371.6	156

TABLE 12 – continued from previous page

090323 Model : Band Function

Seq	Time s	α	β	E_0 keV	K $\frac{photons}{keVcm^2s}$ @100keV	χ^2	dof
1	5.00-14.0	$-0.97^{+0.05}_{-0.04}$	$-2.58^{+0.25}_{-0.13}$	792^{+172}_{-136}	0.016 ± 0.001	98.4	125
2	14.0-25.0	-1.11 ± 0.04	$-2.54^{+0.18}_{-0.10}$	826^{+198}_{-141}	0.017 ± 0.001	127.2	125
3	35.0-50.0	-1.08 ± 0.03	$-2.64^{+0.39}_{-0.15}$	557^{+84}_{-69}	0.018 ± 0.001	151.5	125
4	50.0-60.0	-0.88 ± 0.04	$-2.81^{+1.13}_{-0.24}$	449^{+52}_{-44}	0.026 ± 0.001	115.2	125
5	60.0-135.	$-1.31^{+0.02}_{-0.01}$	$-2.62^{+0.11}_{-0.07}$	987^{+694}_{-116}	0.010 ± 0.001	496.7	125
6	135.-145.	-1.30 ± 0.06	$-2.34^{+0.32}_{-0.12}$	294^{+74}_{-57}	$0.017^{+0.002}_{-0.001}$	208.3	125
Total	0.00-150.	-1.22 ± 0.01	$-2.68^{+0.06}_{-0.04}$	880^{+64}_{-50}	0.012 ± 0.001	857.3	125

090328 Model : Band Function

Seq	Time s	α	β	E_0 keV	K $\frac{photons}{keVcm^2s}$ @100keV	χ^2	dof
1	3.00-8.00	$-0.92^{+0.04}_{-0.03}$	$-2.38^{+0.16}_{-0.10}$	662^{+99}_{-86}	0.024 ± 0.001	188.0	217
2	12.0-20.0	-0.96 ± 0.02	$-2.38^{+0.09}_{-0.06}$	727^{+80}_{-67}	0.024 ± 0.001	199.3	217
3	20.0-30.0	-1.15 ± 0.03	$-2.30^{+0.09}_{-0.07}$	616^{+81}_{-69}	0.020 ± 0.001	250.7	217
Total	0.00-30.0	-1.05 ± 0.01	$-2.44^{+0.05}_{-0.04}$	791^{+58}_{-50}	0.018 ± 0.001	472.5	217

090510 Model : Cut-off Power-Law+Power Law

Seq	Time s	$\Gamma_{\rm CPL}$	E_0 keV	$K_{\rm CPL}$ $\frac{photons}{keVcm^2s}$ @1keV	$\Gamma_{\rm PL}$	$K_{\rm PL}$ $\frac{photons}{keVcm^2s}$ @1keV	χ^2	dof
1	0.450-0.600	-0.76 ± 0.08	2688^{+1360}_{-765}	$1.85^{+0.85}_{-0.63}$	− − −	− − −	83.7	230
2	0.600-0.800	$-0.60^{+0.14}_{-0.13}$	4286^{+1760}_{-1130}	$0.47^{+0.53}_{-0.26}$	$-1.73^{+0.06}_{-0.07}$	$23.2^{+13.0}_{-12.3}$	154.9	251
3	0.800-0.900	$-0.75^{+0.67}_{-0.31}$	777^{+1900}_{-464}	$0.97^{+3.41}_{-0.93}$	$-1.60^{+0.11}_{-0.07}$	$14.3^{+17.9}_{-11.6}$	52.0	178
4	0.900-1.00	− − −	− − −	− − −	-1.62 ± 0.06	$11.5^{+7.4}_{-5.8}$	38.0	134
Total	0.450-1.00	$-0.76^{+0.08}_{-0.07}$	3624^{+759}_{-612}	$1.06^{+0.54}_{-0.39}$	$-1.66^{+0.05}_{-0.03}$	$11.9^{+6.2}_{-5.6}$	215.0	272

090626 Model : Band Function

Seq	Time s	α	β	E_0 keV	K $\frac{photons}{keVcm^2s}$ @100keV	χ^2	dof
1	0.00-9.00	$-0.99^{+0.03}_{-0.02}$	$-2.47^{+0.04}_{-0.03}$	193^{+12}_{-11}	0.079 ± 0.003	340.3	186
2	15.0-20.0	-1.42 ± 0.03	$-2.47^{+0.13}_{-0.08}$	391^{+60}_{-50}	0.040 ± 0.002	155.6	186
3	20.0-27.0	$-1.28^{+0.03}_{-0.02}$	$-2.58^{+0.13}_{-0.08}$	504^{+63}_{-54}	0.034 ± 0.001	136.5	186
4	30.0-40.0	-1.30 ± 0.03	$-2.49^{+0.10}_{-0.06}$	444^{+63}_{-50}	0.025 ± 0.001	211.7	186
Total	0.00-60.0	-1.40 ± 0.01	$-2.62^{+0.04}_{-0.03}$	482^{+27}_{-25}	0.025 ± 0.001	743.3	186

090902B Model : Black Body+Power Law

Seq	Time s	kT (keV) keV	$K_{\rm BB}$ $\frac{L_{39}}{D_{10}^2}$	$\Gamma_{\rm PL}$	$K_{\rm PL}$ $\frac{photons}{keVcm^2s}$ @1keV	χ^2	dof
1	0.00-1.50	$75.60^{+1.86}_{-1.79}$	$38.84^{+1.02}_{-1.03}$	-1.88 ± 0.02	$43.0^{+3.9}_{-3.8}$	330.6	264
2	1.50-2.25	$98.74^{+3.57}_{-3.41}$	$57.13^{+2.25}_{-2.19}$	$-1.84^{+0.03}_{-0.04}$	$31.1^{+5.3}_{-4.3}$	226.3	237

TABLE 12 – continued from previous page

3	2.25-2.81	$121.20^{+5.00}_{-4.79}$	$84.54^{+3.79}_{-3.72}$	$-1.81^{+0.03}_{-0.04}$	$27.5^{+4.6}_{-4.3}$	217.5	238
4	2.81-3.23	$82.52^{+4.32}_{-3.97}$	$58.00^{+3.05}_{-2.88}$	$-1.80^{+0.03}_{-0.04}$	$33.6^{+6.4}_{-5.3}$	199.0	217
5	3.23-3.83	$100.90^{+3.76}_{-3.57}$	$69.22^{+2.81}_{-2.71}$	$-1.83^{+0.03}_{-0.04}$	$34.7^{+6.3}_{-4.8}$	190.7	240
6	3.83-4.46	$86.81^{+2.92}_{-2.79}$	$60.01^{+2.20}_{-2.14}$	$-1.83^{+0.03}_{-0.04}$	$33.4^{+5.7}_{-4.7}$	218.3	236
7	4.46-4.99	$90.79^{+4.78}_{-4.43}$	$47.82^{+2.65}_{-2.52}$	$-1.83^{+0.03}_{-0.04}$	$38.6^{+6.4}_{-5.2}$	207.4	225
8	4.99-5.45	$109.50^{+4.32}_{-4.11}$	$88.50^{+3.82}_{-3.68}$	$-1.82^{+0.04}_{-0.05}$	$31.5^{+6.6}_{-5.2}$	185.3	228
9	5.45-5.86	$116.20^{+5.20}_{-4.94}$	$85.70^{+4.22}_{-4.13}$	$-1.82^{+0.04}_{-0.05}$	$34.6^{+7.2}_{-5.9}$	180.5	227
10	5.86-6.28	$132.60^{+4.36}_{-4.21}$	$141.20^{+5.27}_{-5.14}$	$-1.81^{+0.04}_{-0.05}$	$32.5^{+6.5}_{-5.3}$	186.5	233
11	6.28-6.61	$157.40^{+6.74}_{-6.50}$	$155.60^{+7.77}_{-7.36}$	$-1.81^{+0.04}_{-0.06}$	$38.0^{+8.8}_{-6.0}$	186.2	228
12	6.61-7.19	$171.10^{+5.01}_{-4.85}$	$174.10^{+5.97}_{-5.80}$	$-1.86^{+0.02}_{-0.03}$	$87.2^{+8.6}_{-7.3}$	229.0	248
13	7.19-7.65	$174.20^{+5.55}_{-5.35}$	$207.90^{+7.57}_{-7.37}$	$-1.87^{+0.02}_{-0.03}$	$124.3^{+12.1}_{-10.3}$	231.3	244
14	7.65-8.00	$217.80^{+7.47}_{-7.29}$	$307.00^{+12.50}_{-12.20}$	-1.87 ± 0.02	$203.5^{+15.0}_{-13.2}$	223.0	243
15	8.00-8.50	$204.80^{+5.62}_{-5.48}$	$288.60^{+9.22}_{-9.01}$	-1.91 ± 0.01	$344.6^{+17.3}_{-15.7}$	319.9	248
16	8.50-9.00	$206.60^{+5.97}_{-5.83}$	$281.00^{+9.35}_{-9.16}$	$-1.93^{+0.01}_{-0.02}$	$375.7^{+21.5}_{-19.3}$	260.2	249
17	9.00-9.50	$206.20^{+5.99}_{-5.83}$	$270.50^{+9.11}_{-8.91}$	-1.92 ± 0.01	$445.6^{+20.5}_{-18.9}$	325.6	248
18	9.50-10.0	$135.90^{+3.26}_{-3.18}$	$209.90^{+5.53}_{-5.45}$	$-1.96^{+0.01}_{-0.02}$	$553.2^{+28.6}_{-26.0}$	271.2	244
19	10.0-10.5	$168.80^{+4.58}_{-4.47}$	$236.40^{+7.18}_{-7.04}$	-1.94 ± 0.02	$378.4^{+23.8}_{-20.9}$	258.3	244
20	10.5-11.0	$195.70^{+6.03}_{-5.89}$	$246.60^{+8.70}_{-8.50}$	-1.90 ± 0.01	$352.5^{+17.7}_{-16.0}$	348.6	247
21	11.0-11.5	$145.20^{+4.50}_{-4.34}$	$179.10^{+5.98}_{-5.81}$	-1.93 ± 0.02	$332.2^{+20.8}_{-18.3}$	278.5	242
22	11.5-12.0	$153.10^{+4.43}_{-4.32}$	$169.30^{+5.68}_{-5.56}$	-1.92 ± 0.02	$253.5^{+18.8}_{-16.2}$	241.9	241
23	12.0-12.4	$61.07^{+3.09}_{-2.90}$	$44.61^{+2.31}_{-2.24}$	-1.90 ± 0.02	$242.6^{+18.4}_{-15.9}$	194.7	214
24	12.4-13.2	$35.36^{+0.92}_{-0.88}$	$31.80^{+0.91}_{-0.90}$	-1.92 ± 0.01	$271.2^{+12.8}_{-11.9}$	324.6	231
25	13.2-13.3	$42.30^{+1.68}_{-1.59}$	$87.55^{+3.92}_{-3.83}$	-1.84 ± 0.03	$213.7^{+27.0}_{-22.7}$	141.4	180
26	13.3-13.6	$45.32^{+2.10}_{-1.97}$	$57.60^{+2.79}_{-2.72}$	-1.87 ± 0.02	$276.6^{+23.4}_{-20.6}$	175.3	192
27	13.6-13.8	$53.27^{+2.02}_{-1.94}$	$69.62^{+2.90}_{-2.85}$	$-1.87^{+0.02}_{-0.03}$	$203.7^{+20.6}_{-17.3}$	169.2	199
28	13.8-14.1	$66.19^{+2.92}_{-2.72}$	$89.79^{+3.93}_{-3.80}$	-1.84 ± 0.02	$187.8^{+15.3}_{-13.8}$	275.3	206
29	14.1-14.2	$105.70^{+5.22}_{-4.91}$	$201.80^{+10.2}_{-9.99}$	-1.82 ± 0.03	$169.6^{+20.2}_{-18.2}$	177.9	204
30	14.2-14.4	$120.40^{+5.93}_{-5.70}$	$199.60^{+10.40}_{-10.00}$	$-1.83^{+0.02}_{-0.03}$	$159.9^{+18.7}_{-15.2}$	180.7	211
31	14.4-14.6	$51.74^{+2.45}_{-2.30}$	$57.16^{+2.86}_{-2.79}$	$-1.86^{+0.02}_{-0.03}$	$186.8^{+18.8}_{-16.2}$	164.6	194
32	14.6-14.8	$99.11^{+4.23}_{-4.00}$	$155.80^{+6.88}_{-6.57}$	-1.85 ± 0.03	$160.5^{+19.3}_{-15.4}$	173.6	211
33	14.8-15.0	$71.48^{+3.30}_{-3.09}$	$115.90^{+5.55}_{-5.38}$	-1.82 ± 0.03	$149.0^{+19.0}_{-15.9}$	165.7	196
34	15.0-15.1	$102.20^{+5.60}_{-5.26}$	$220.80^{+12.2}_{-11.7}$	-1.81 ± 0.03	$159.0^{+21.9}_{-18.3}$	184.4	202
35	15.1-15.2	$102.10^{+4.40}_{-4.22}$	$233.10^{+10.5}_{-10.1}$	-1.81 ± 0.03	$144.6^{+18.9}_{-15.4}$	212.1	199
36	15.2-15.5	$127.0^{+3.85}_{-3.73}$	$223.0^{+7.36}_{-7.18}$	$-1.85^{+0.0201}_{-0.0234}$	$160.7^{+14.3}_{-12.5}$	216.60	215
37	15.5-15.7	$150.70^{+6.16}_{-5.99}$	$254.80^{+11.80}_{-11.30}$	-1.83 ± 0.03	$120.5^{+15.9}_{-12.4}$	168.4	221
38	15.7-16.2	$59.42^{+1.81}_{-1.74}$	$63.99^{+2.15}_{-2.12}$	-1.88 ± 0.02	$169.4^{+14.3}_{-12.4}$	197.2	221
39	16.2-16.3	$84.53^{+3.95}_{-3.69}$	$132.10^{+6.36}_{-6.08}$	-1.84 ± 0.03	$168.9^{+20.3}_{-16.5}$	190.3	203
40	16.3-16.5	$90.82^{+3.67}_{-3.47}$	$160.90^{+6.85}_{-6.63}$	-1.83 ± 0.03	$158.1^{+18.3}_{-15.4}$	177.3	206
41	16.5-16.7	$94.44^{+4.55}_{-4.25}$	$143.00^{+7.11}_{-6.81}$	-1.84 ± 0.03	$160.6^{+19.1}_{-15.8}$	169.6	210
42	16.7-16.9	$78.69^{+4.46}_{-4.10}$	$96.94^{+5.55}_{-5.29}$	$-1.83^{+0.03}_{-0.04}$	$137.2^{+18.4}_{-15.1}$	155.4	198
43	16.9-17.1	$47.97^{+2.65}_{-2.47}$	$40.30^{+2.33}_{-2.26}$	$-1.84^{+0.02}_{-0.03}$	$138.7^{+15.3}_{-13.1}$	144.2	191
44	17.1-17.5	$63.52^{+2.29}_{-2.19}$	$75.35^{+2.93}_{-2.87}$	$-1.86^{+0.02}_{-0.03}$	$148.8^{+15.6}_{-13.1}$	171.4	206
45	17.5-17.8	$68.97^{+3.46}_{-3.26}$	$54.62^{+2.85}_{-2.76}$	$-1.85^{+0.02}_{-0.03}$	$113.7^{+12.6}_{-10.6}$	191.9	209
46	17.8-18.3	$46.21^{+1.56}_{-1.50}$	$38.75^{+1.39}_{-1.36}$	-1.87 ± 0.02	$142.8^{+10.4}_{-9.5}$	248.0	228
47	18.3-18.9	$57.27^{+1.95}_{-1.85}$	$52.36^{+1.80}_{-1.75}$	-1.88 ± 0.02	$166.4^{+10.6}_{-9.8}$	334.0	233
48	18.9-19.4	$57.29^{+1.97}_{-1.87}$	$49.10^{+1.75}_{-1.71}$	-1.88 ± 0.02	$156.0^{+10.7}_{-9.7}$	302.1	220

TABLE 12 – continued from previous page

49	19.4-19.6	$49.44^{+1.96}_{-1.86}$	$81.63^{+3.50}_{-3.39}$	-1.83 ± 0.03	$147.1^{+18.8}_{-15.7}$	167.7	189		
50	19.6-19.7	$54.68^{+2.24}_{-2.14}$	$88.95^{+3.88}_{-3.81}$	$-1.83^{+0.02}_{-0.03}$	$164.9^{+18.9}_{-18.3}$	171.8	192		
51	19.7-19.9	$57.57^{+2.59}_{-2.43}$	$94.89^{+4.29}_{-4.21}$	$-1.83^{+0.02}_{-0.03}$	$178.0^{+18.3}_{-16.0}$	202.2	194		
52	19.9-20.1	$72.81^{+4.16}_{-3.90}$	$91.88^{+5.28}_{-5.08}$	$-1.85^{+0.02}_{-0.03}$	$197.8^{+20.5}_{-17.5}$	170.6	196		
53	20.1-20.3	$43.33^{+3.37}_{-3.07}$	$42.35^{+2.99}_{-2.88}$	$-1.82^{+0.02}_{-0.03}$	$136.6^{+16.6}_{-14.9}$	165.1	189		
54	20.3-20.6	$50.94^{+2.52}_{-2.41}$	$53.85^{+2.64}_{-2.59}$	-1.86 ± 0.02	$193.9^{+17.2}_{-15.3}$	221.4	205		
55	20.6-20.9	$46.04^{+1.79}_{-1.71}$	$51.23^{+2.16}_{-2.12}$	-1.87 ± 0.02	$192.5^{+16.7}_{-14.8}$	192.6	196		
56	20.9-21.0	$42.49^{+2.20}_{-2.04}$	$55.46^{+2.90}_{-2.79}$	-1.84 ± 0.03	$148.9^{+18.6}_{-16.0}$	171.3	183		
57	21.0-21.3	$36.47^{+2.44}_{-2.20}$	$23.88^{+1.59}_{-1.53}$	$-1.87^{+0.02}_{-0.03}$	$152.9^{+17.0}_{-14.5}$	143.5	189		
58	21.3-21.7	$42.84^{+1.23}_{-1.19}$	$50.72^{+1.67}_{-1.63}$	$-1.88^{+0.02}_{-0.03}$	$155.2^{+14.8}_{-12.7}$	186.5	212		
59	21.7-21.9	$47.05^{+2.89}_{-2.70}$	$46.19^{+2.89}_{-2.80}$	$-1.84^{+0.02}_{-0.03}$	$161.9^{+17.8}_{-15.5}$	152.6	195		
60	21.9-22.2	$49.53^{+3.39}_{-3.13}$	$42.03^{+2.94}_{-2.83}$	$-1.84^{+0.02}_{-0.03}$	$153.6^{+17.5}_{-15.1}$	147.1	188		
61	22.2-23.0	$31.13^{+4.08}_{-3.30}$	$5.72^{+0.62}_{-0.60}$	-1.90 ± 0.02	$126.0^{+10.2}_{-9.4}$	187.3	233		
Total	0.00-30.0	$96.71^{+0.461}_{-0.484}$	$71.65^{+0.34}_{-0.36}$	-1.93 ± 0.01	$175.1^{+1.2}_{-1.3}$	14732.0	276		

090902B Model : Band Function + Power Law

	Time s	α	β	E_0 keV	K $\frac{photons}{keVcm^2s}$ @$100keV$	$\Gamma_{\rm PL}$	$K_{\rm PL}$ $\frac{photons}{keVcm^2s}$ @$1keV$	χ^2	dof
Total	0.00-23.0	-0.83 ± 0.01	$-3.68^{+0.12}_{-0.20}$	724^{+13}_{-12}	0.099 ± 0.001	$-1.85^{+1.85}_{-1.85}$	43.4 ± 1.5	2024.3	275

090926A Model : Band Function

Seq	Time s	α	β	E_0 keV	K $\frac{photons}{keVcm^2s}$ @$100keV$	χ^2	dof
1	0.00-2.81	$-0.53^{+0.04}_{-0.03}$	$-2.43^{+0.06}_{-0.05}$	235^{+16}_{-15}	0.106 ± 0.004	189.0	210
2	2.81-3.75	-0.48 ± 0.03	$-2.75^{+0.21}_{-0.13}$	255^{+15}_{-14}	$0.303^{+0.011}_{-0.010}$	168.6	196
3	3.75-5.62	-0.57 ± 0.02	-2.35 ± 0.02	208 ± 8	0.344 ± 0.009	269.1	213
4	5.62-7.50	-0.73 ± 0.02	$-2.50^{+0.13}_{-0.08}$	326 ± 15	0.191 ± 0.004	229.7	210
5	7.50-9.38	-0.63 ± 0.03	$-2.81^{+0.17}_{-0.13}$	183^{+9}_{-8}	$0.255^{+0.009}_{-0.008}$	169.6	209
6	9.38-11.2	-0.75 ± 0.02	$-2.52^{+0.10}_{-0.08}$	193^{+9}_{-8}	$0.327^{+0.010}_{-0.009}$	228.1	213
7	11.2-13.1	-0.80 ± 0.03	$-2.29^{+0.06}_{-0.05}$	154^{+11}_{-10}	$0.242^{+0.014}_{-0.012}$	186.1	212
8	13.1-15.9	-0.99 ± 0.05	$-2.36^{+0.22}_{-0.11}$	161^{+22}_{-19}	$0.081^{+0.008}_{-0.007}$	164.7	213
9	15.9-20.0	-1.26 ± 0.08	$-2.07^{+0.07}_{-0.04}$	216^{+68}_{-48}	$0.025^{+0.004}_{-0.003}$	170.9	214
Total	0.00-20.0	-0.74 ± 0.01	-2.34 ± 0.01	226 ± 4	0.165 ± 0.002	777.1	216

091003 Model : Band Function

Seq	Time s	α	β	E_0 keV	K $\frac{photons}{keVcm^2s}$ @$100keV$	χ^2	dof
1	7.00-15.0	-1.33 ± 0.05	$-2.41^{+0.20}_{-0.10}$	426^{+101}_{-77}	0.012 ± 0.001	234.5	246
2	15.0-18.0	-1.01 ± 0.04	$-2.52^{+0.19}_{-0.10}$	337^{+43}_{-38}	0.040 ± 0.002	152.4	243
3	18.0-20.0	-0.85 ± 0.03	$-2.55^{+0.10}_{-0.07}$	357^{+28}_{-26}	0.094 ± 0.003	218.9	242
4	20.0-26.0	$-1.36^{+0.06}_{-0.05}$	$-2.35^{+0.15}_{-0.08}$	429^{+143}_{-97}	0.014 ± 0.001	189.2	246
Total	0.00-26.0	$-1.09^{+0.02}_{-0.01}$	$-2.58^{+0.05}_{-0.04}$	474^{+27}_{-25}	0.024 ± 0.001	446.2	246

091031 Model : Band Function

Seq	Time s	α	β	E_0 keV	K $\frac{photons}{keVcm^2s}$ @$100keV$	χ^2	dof

TABLE 12 – continued from previous page

1	0.00-8.00	-0.89 ± 0.06	$-2.44^{+0.09}_{-0.07}$	496^{+111}_{-84}	0.013 ± 0.001	177.1	186
2	8.00-15.0	$-0.86^{+0.06}_{-0.05}$	$-2.50^{+0.13}_{-0.08}$	357^{+55}_{-47}	0.020 ± 0.001	173.3	186
3	15.0-25.0	$-0.78^{+0.11}_{-0.10}$	$-2.55^{+0.26}_{-0.12}$	467^{+157}_{-104}	0.006 ± 0.001	187.1	186
Total	0.00-25.0	$-0.87^{+0.04}_{-0.03}$	$-2.55^{+0.06}_{-0.05}$	458^{+51}_{-33}	0.012 ± 0.001	347.2	186

100116A Model : Band Function

Seq	Time s	α	β	E_0 keV	K $\frac{photons}{keV cm^2 s}$ @100keV	χ^2	dof
1	-2.00-5.00	$-1.03^{+0.13}_{-0.11}$	$-2.54^{+2.54}_{-0.24}$	384^{+201}_{-124}	0.006 ± 0.001	104.8	155
2	80.0-90.0	$-1.03^{+0.05}_{-0.04}$	$-2.80^{+0.97}_{-0.21}$	791^{+192}_{-142}	0.010 ± 0.001	127.8	155
3	90.0-95.0	-1.00 ± 0.01	$-3.22^{+1.51}_{-0.25}$	1459^{+161}_{-121}	0.033 ± 0.001	156.9	155
4	95.0-110.	-1.03 ± 0.05	$-2.63^{+0.23}_{-0.11}$	677^{+169}_{-120}	0.009 ± 0.001	127.0	155
Total	0.00-110.	$-1.11^{+0.01}_{-0.02}$	$-3.13^{+0.11}_{-0.09}$	2867^{+430}_{-283}	0.004 ± 0.001	415.6	155

100225A Model : Band Function

Seq	Time s	α	β	E_0 keV	K $\frac{photons}{keV cm^2 s}$ @100keV	χ^2	dof
1	0.00-6.00	$-0.53^{+0.22}_{-0.19}$	$-2.43^{+0.87}_{-0.19}$	263^{+120}_{-74}	0.010 ± 0.002	51.8	94
2	6.00-12.0	$-0.93^{+0.15}_{-0.13}$	$-2.30^{+0.26}_{-0.12}$	507^{+351}_{-181}	$0.009^{+0.002}_{-0.001}$	40.3	93
Total	0.00-12.0	$-0.77^{+0.12}_{-0.11}$	$-2.37^{+0.18}_{-0.10}$	375^{+129}_{-86}	0.010 ± 0.001	64.5	94

100325A Model : Band Function

Seq	Time s	α	β	E_0 keV	K $\frac{photons}{keV cm^2 s}$ @100keV	χ^2	dof
1	-3.00-10.0	$-0.72^{+0.11}_{-0.10}$	$-2.60^{+1.89}_{-0.21}$	155^{+32}_{-26}	0.014 ± 0.002	151.6	125

100414A Model : Band Function

Seq	Time s	α	β	E_0 keV	K $\frac{photons}{keV cm^2 s}$ @100keV	χ^2	dof
1	1.00-7.25	$-0.19^{+0.06}_{-0.05}$	$-2.54^{+0.16}_{-0.10}$	256^{+22}_{-20}	0.036 ± 0.002	124.3	156
2	7.25-14.3	$-0.25^{+0.05}_{-0.04}$	$-2.89^{+0.51}_{-0.24}$	281^{+19}_{-20}	$0.040^{+0.002}_{-0.001}$	124.5	156
3	14.3-19.6	$-0.56^{+0.04}_{-0.03}$	$-2.53^{+0.16}_{-0.10}$	361^{+28}_{-26}	0.047 ± 0.002	135.1	156
4	19.6-25.5	-0.76 ± 0.03	$-2.45^{+0.11}_{-0.07}$	386^{+30}_{-28}	0.052 ± 0.002	131.9	156
Total	1.00-26.0	-0.52 ± 0.02	$-2.62^{+0.07}_{-0.05}$	344^{+12}_{-12}	0.042 ± 0.001	281.7	156

Data Analysis Results

The data analysis results are presented in Figs. 29-45. Each figure corresponds to one burst, and contains 10-11 panels. In the left panels, the lightcurves in 5 energy bands (8–150 keV, 150–300 keV, 300 keV–1 MeV, 1–30 MeV, and > 100 MeV) are presented in linear scale, together with the temporal evolution of the spectral parameters (α, β, E_p for Band function, kT for blackbody function, and Γ for single power law photon index). The top right panel is an example photon spectrum with model fitting, typically taken at the brightest time bin. The time-dependent model spectra are presented in the mid-right panel. The time-slices for the time-resolved spectral fitting are marked with vertical lines in the left panel lightcurves. In the bottom right panel, the GBM and LAT lightcurves are presented and compared in logarithmic scale.

In the following, we discuss the results of several individual bright GRBs, and then discuss other GRBs in general. We then present statistics of spectral parameters and and some possible correlations.

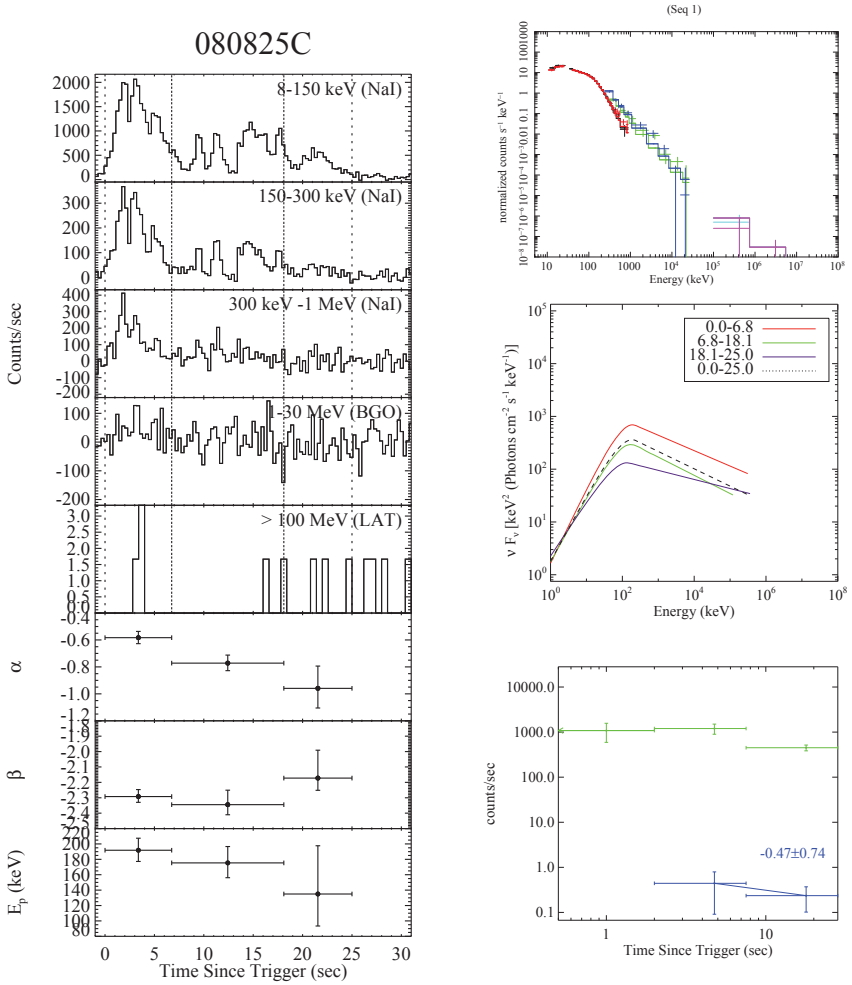

Figure 29 Joint temporal and spectral analysis of GBM and LAT data for GRB 080825C. *Left panels:* the background-subtracted GBM and LAT lightcurves (from top: 8-150 keV, 150-300 keV, 300 keV - 1 MeV, 1-30 MeV, >100 MeV), and evolution of spectra parameters (α, β, E_p). *Right panels:* an example (the brightest episode) of the observed photon spectrum as compared with the spectral model (*top*), the best fit νF_ν spectra of all time bins (*middle*), and the comparison between the GBM (green) and LAT (blue) count rate lightcurves in log-scale (*bottom*).

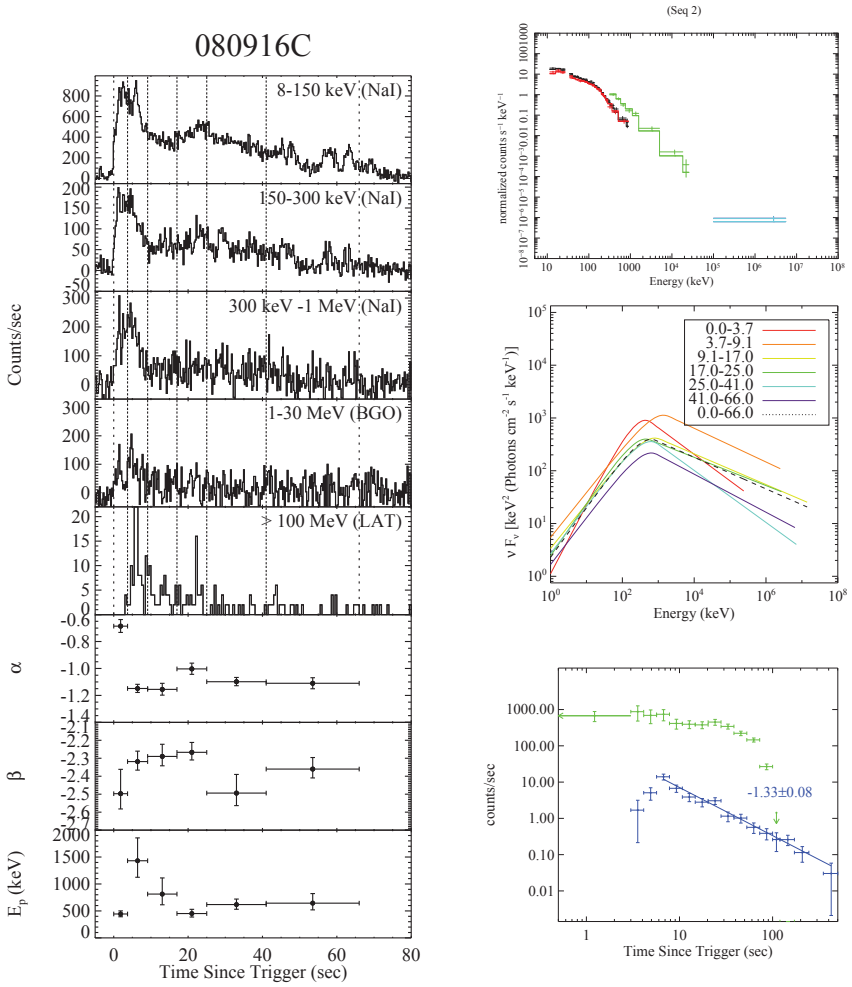

Figure 30 Same as Figure 29, but for GRB 080916C.

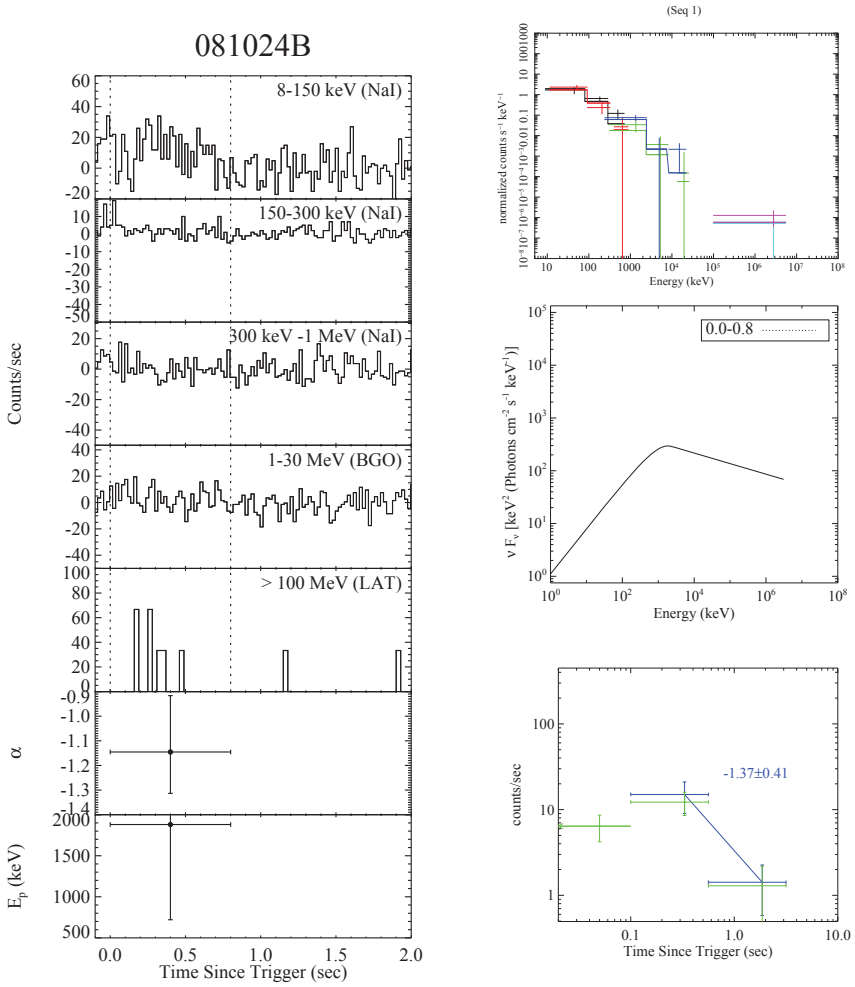

Figure 31 Same as Figure 29, but for GRB 081024B.

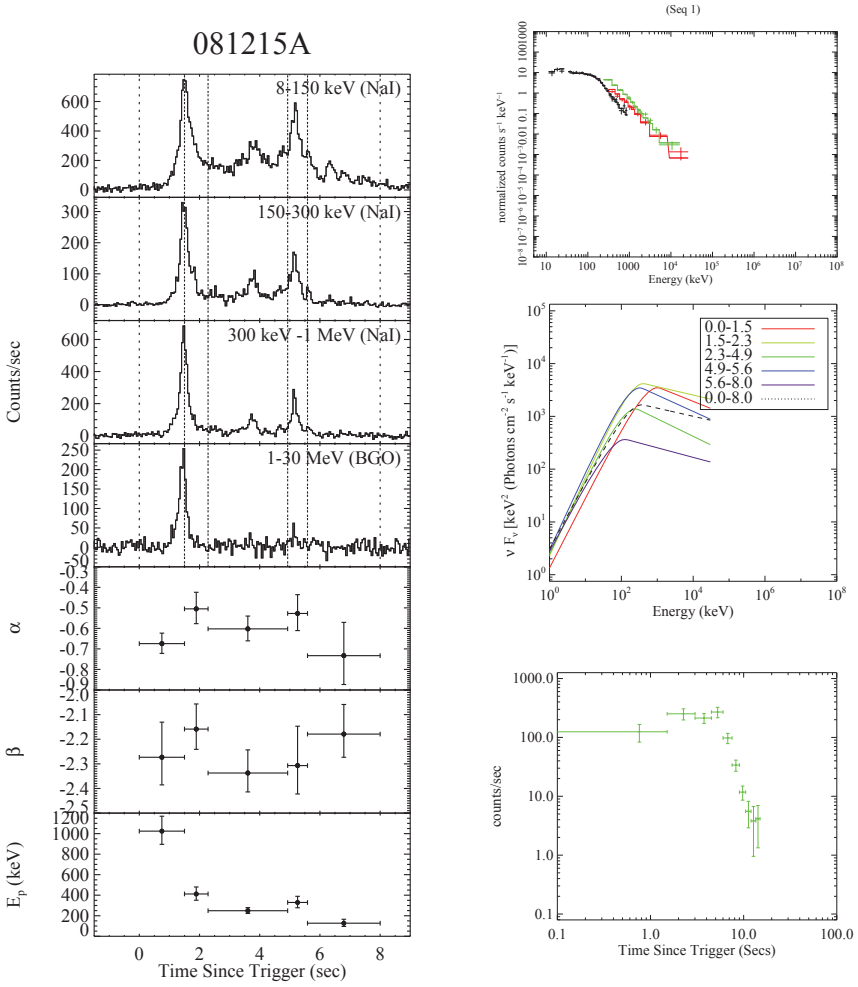

Figure 32 Same as Figure 29, but for GRB 081215A. This burst was at an angle of 86 degrees to the LAT boresight. The data cannot be obtained with the standard analysis procedures. Using a non-standard data selection, over 100 counts above background were detected within a 0.5 s interval in coincidence with the main GBM peak (McEnery et al. 2008). We thus add this GRB in our sample, but do not add its LAT data in our analysis.

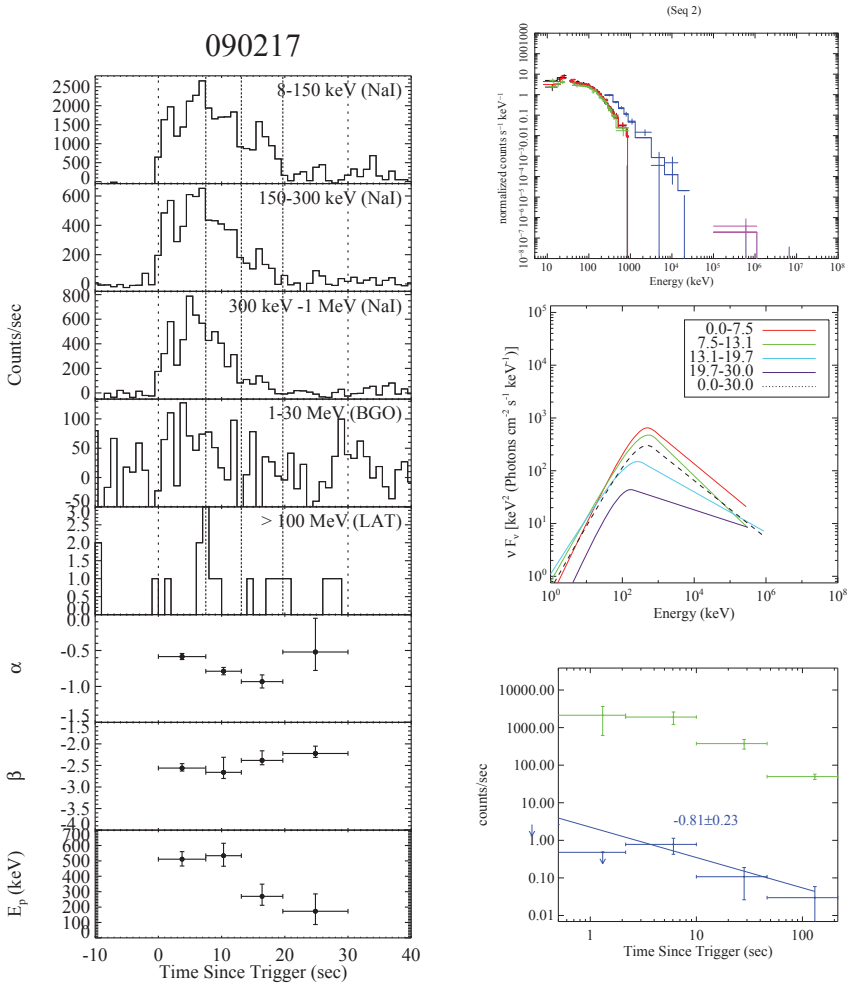

Figure 33 Same as Figure 29, but for GRB 090217.

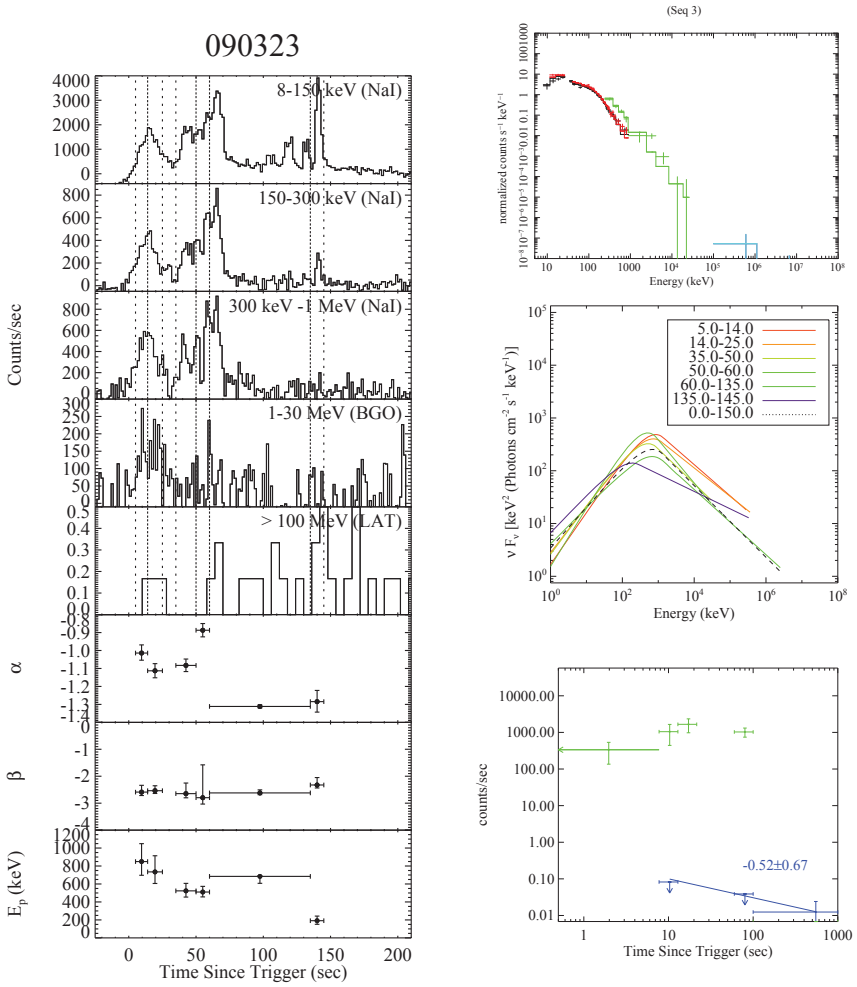

Figure 34 Same as Figure 29, but for GRB 090323.

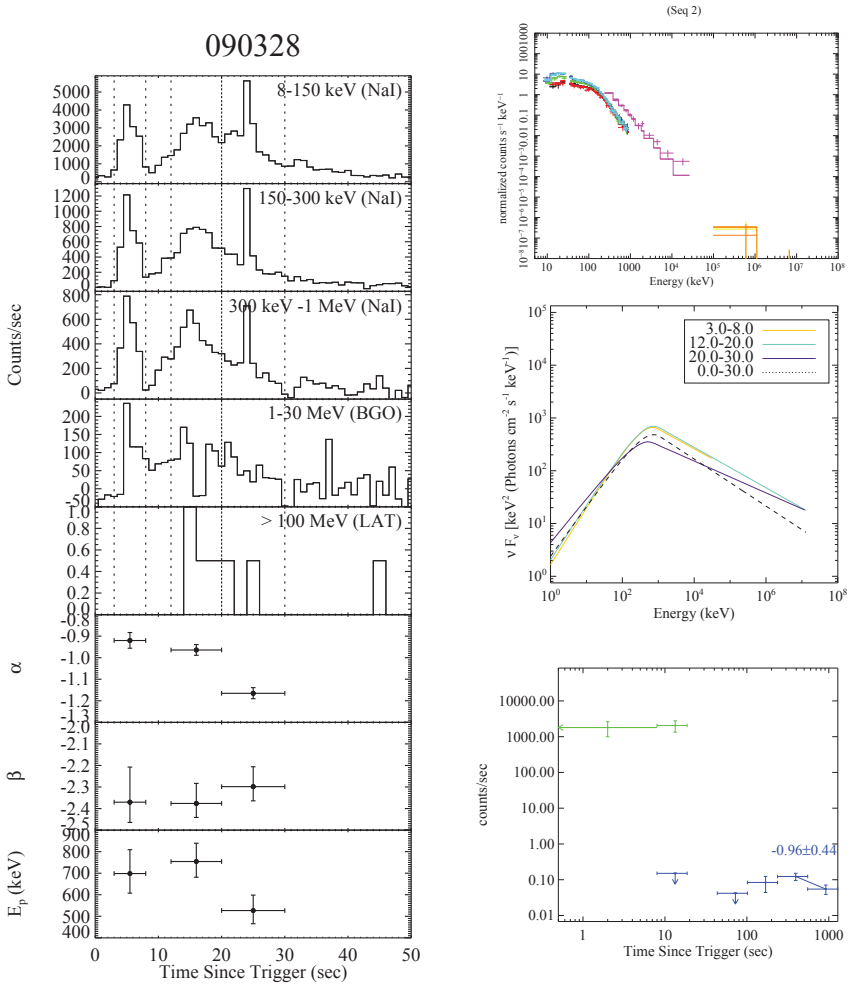

Figure 35 Same as Figure 29, but for GRB 090328.

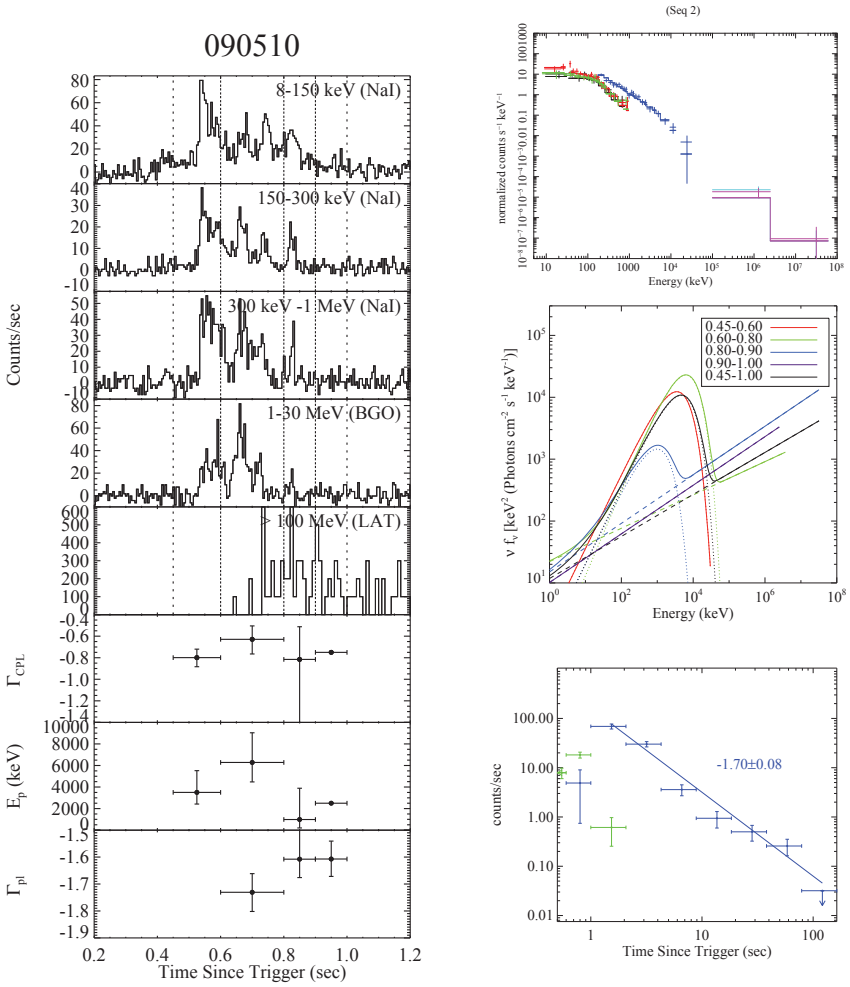

Figure 36 Same as Figure 29, but for GRB 090510. The applied model is cut-off power-law plus power-law (CPL + PL).

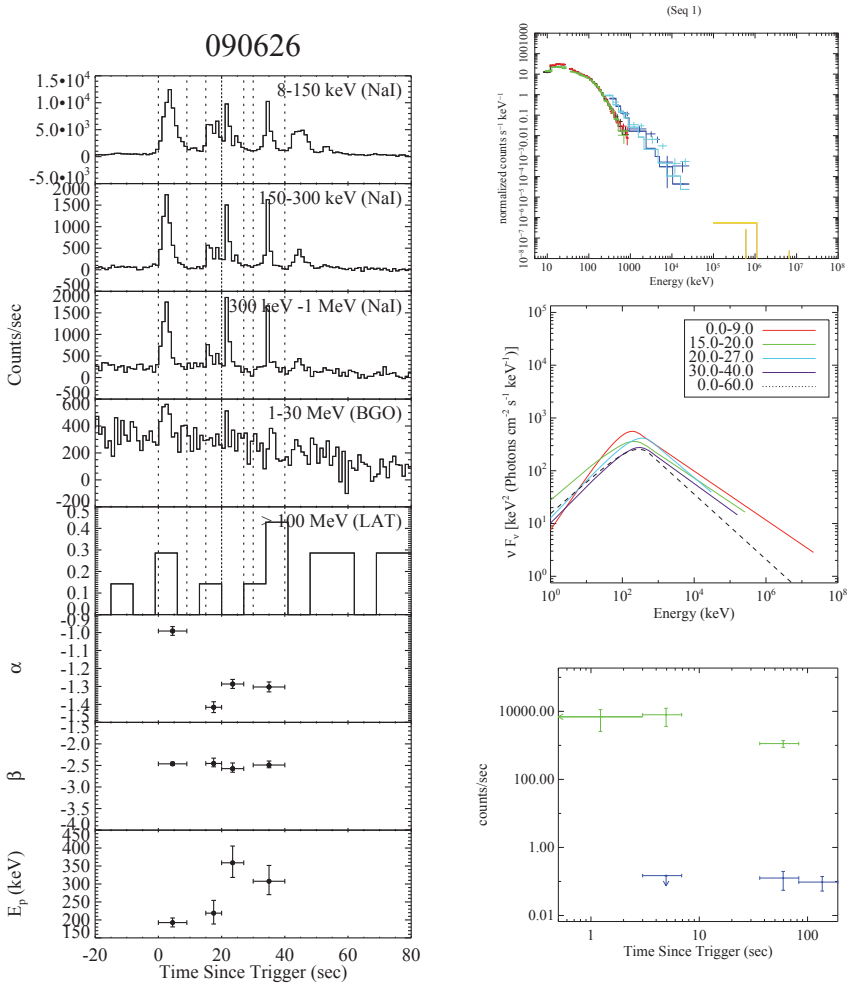

Figure 37 Same as Figure 29, but for GRB 090626.

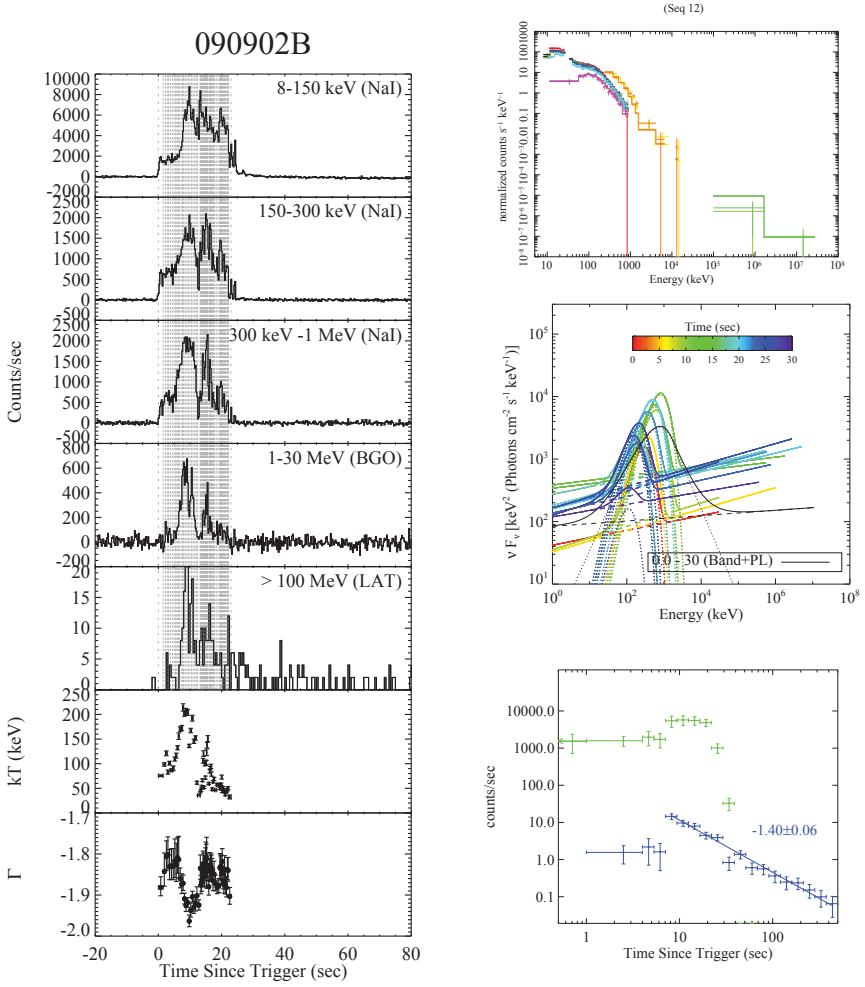

Figure 38 Same as Fig. 1, but for GRB 090902B. The applied model is blackbody plus power law (BB + PL).

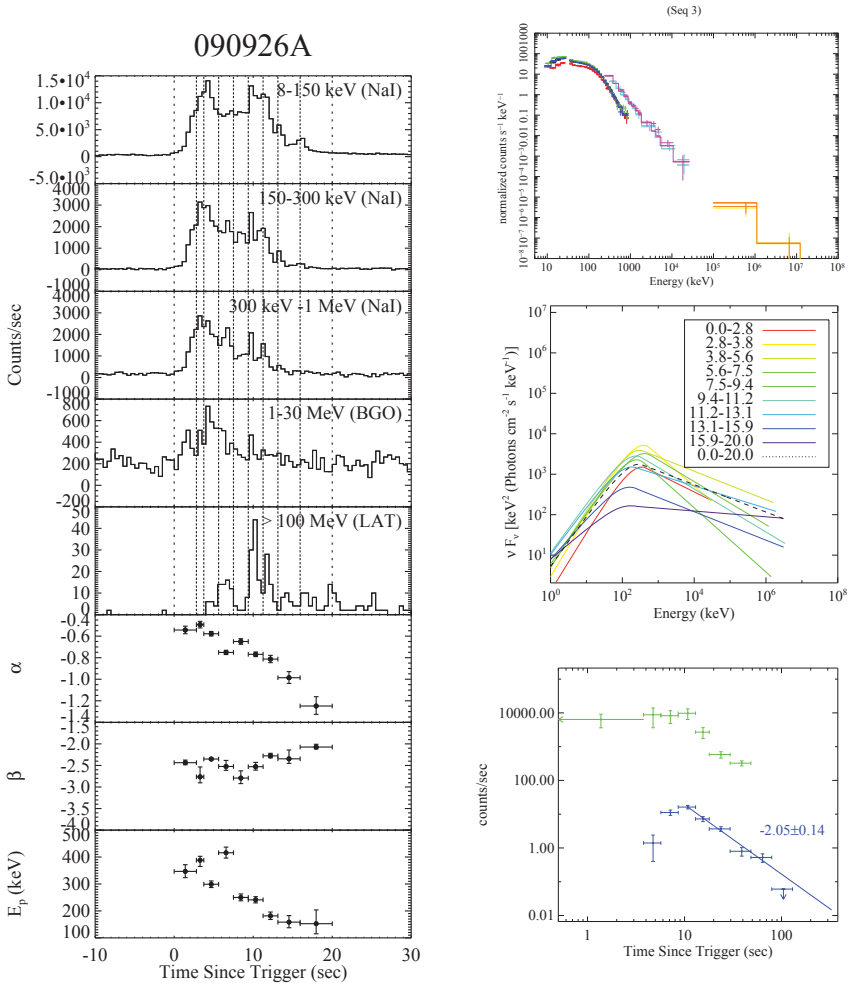

Figure 39 Same as Figure 29, but for GRB 090926A.

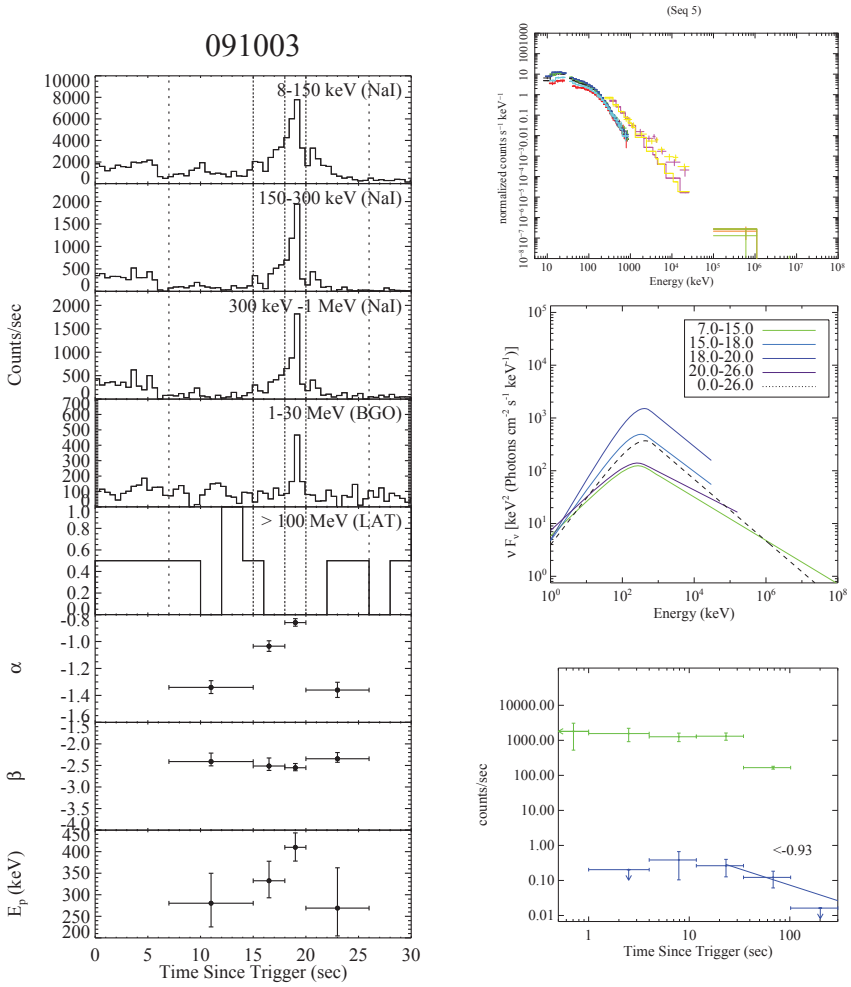

Figure 40 Same as Figure 29, but for GRB 091003.

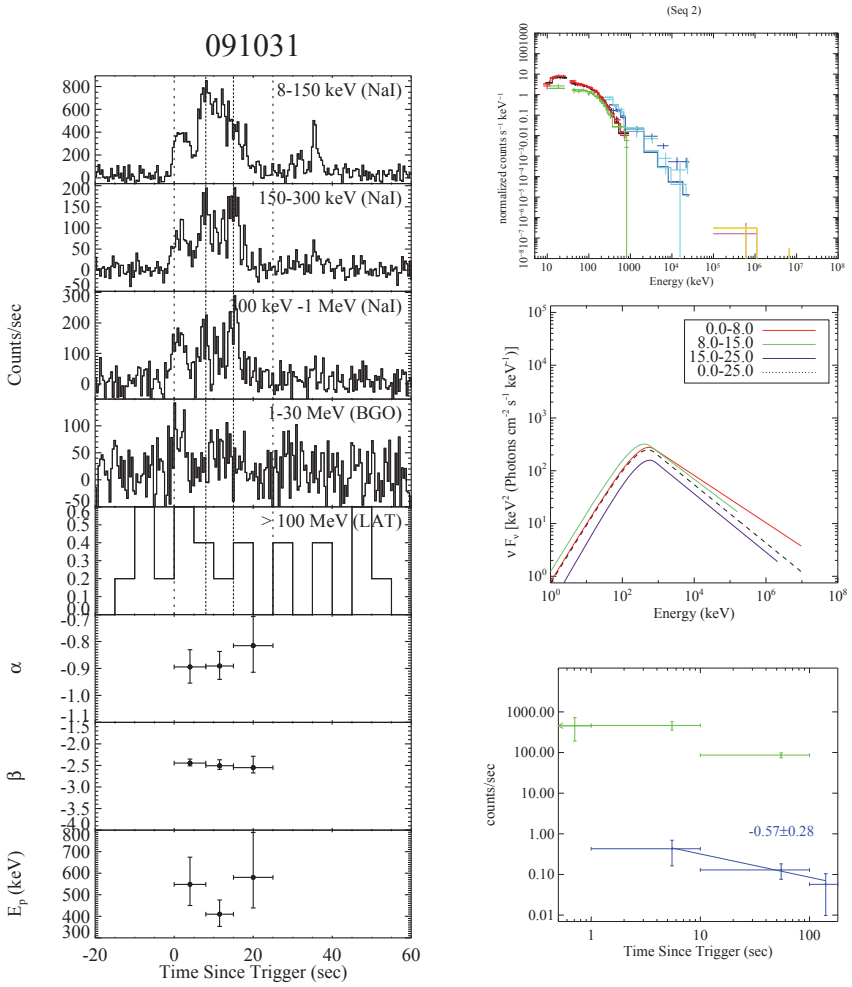

Figure 41 Same as Figure 29, but for GRB 091031.

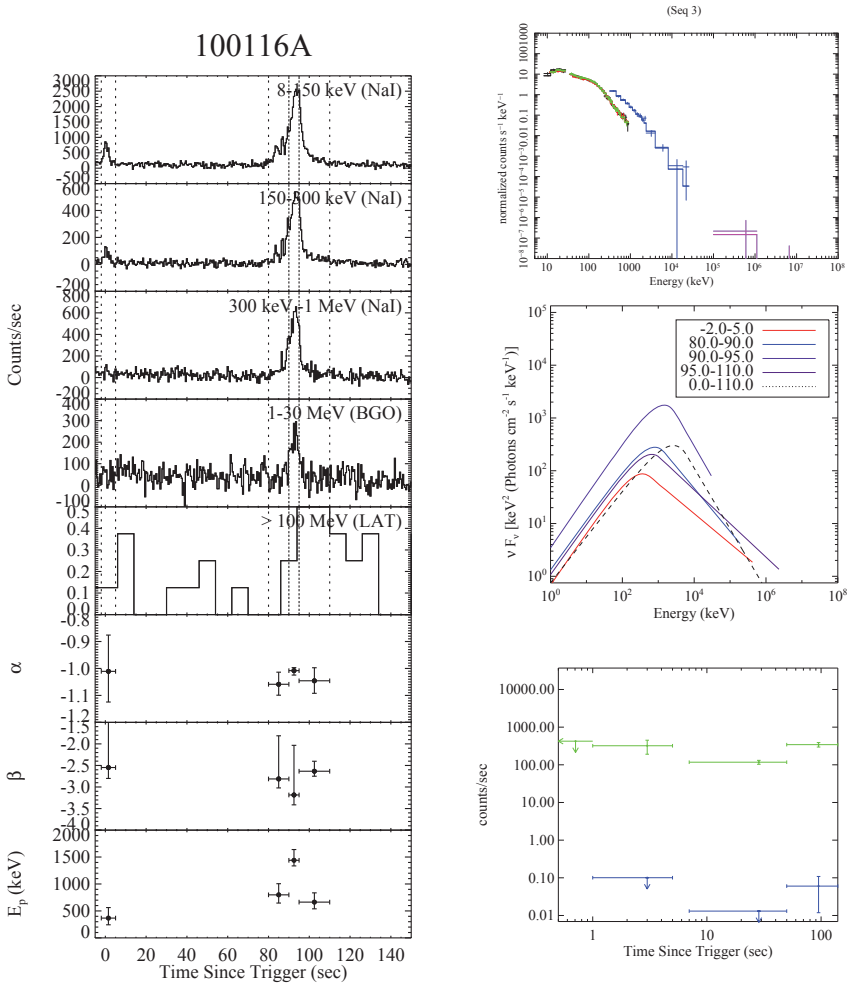

Figure 42 Same as Figure 29, but for GRB 100116A.

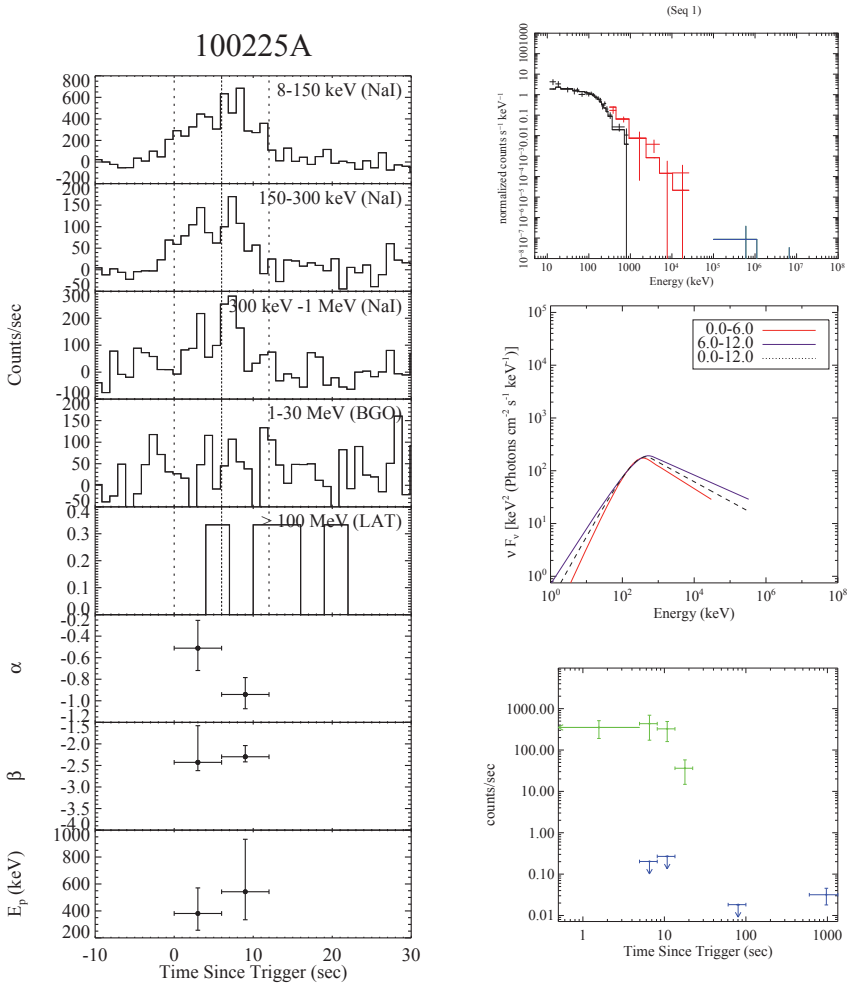

Figure 43 Same as Figure 29, but for GRB 100225A.

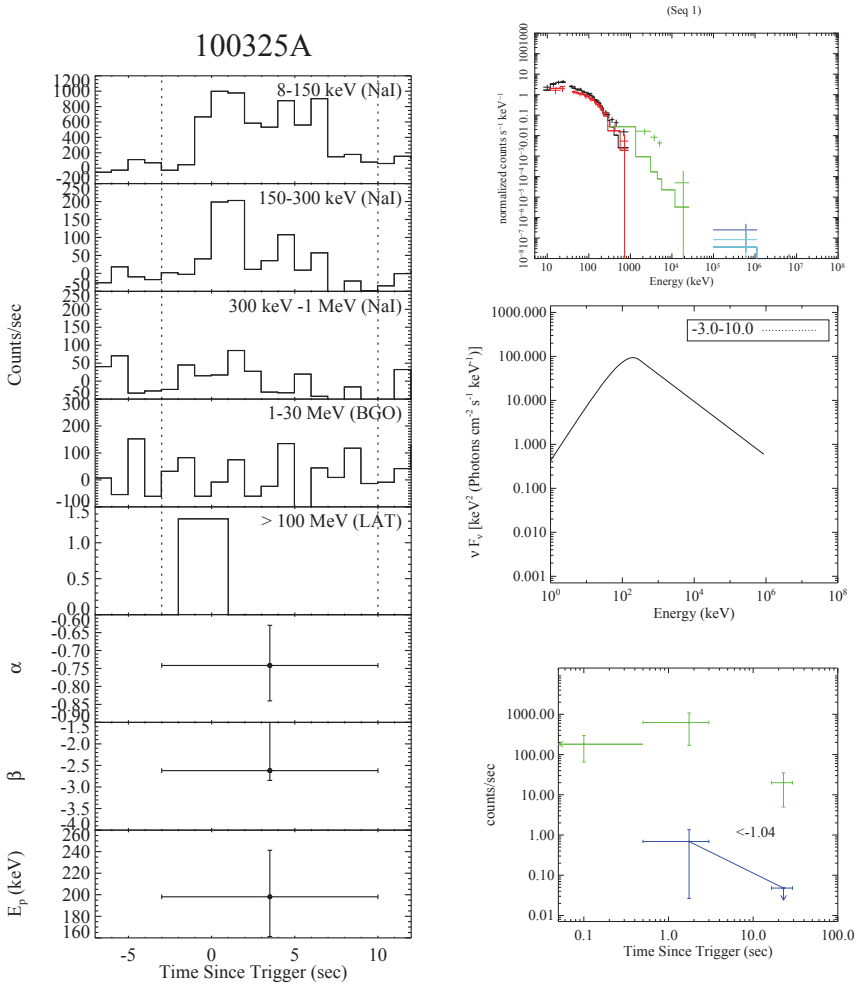

Figure 44 Same as Figure 29, but for GRB 100325A.

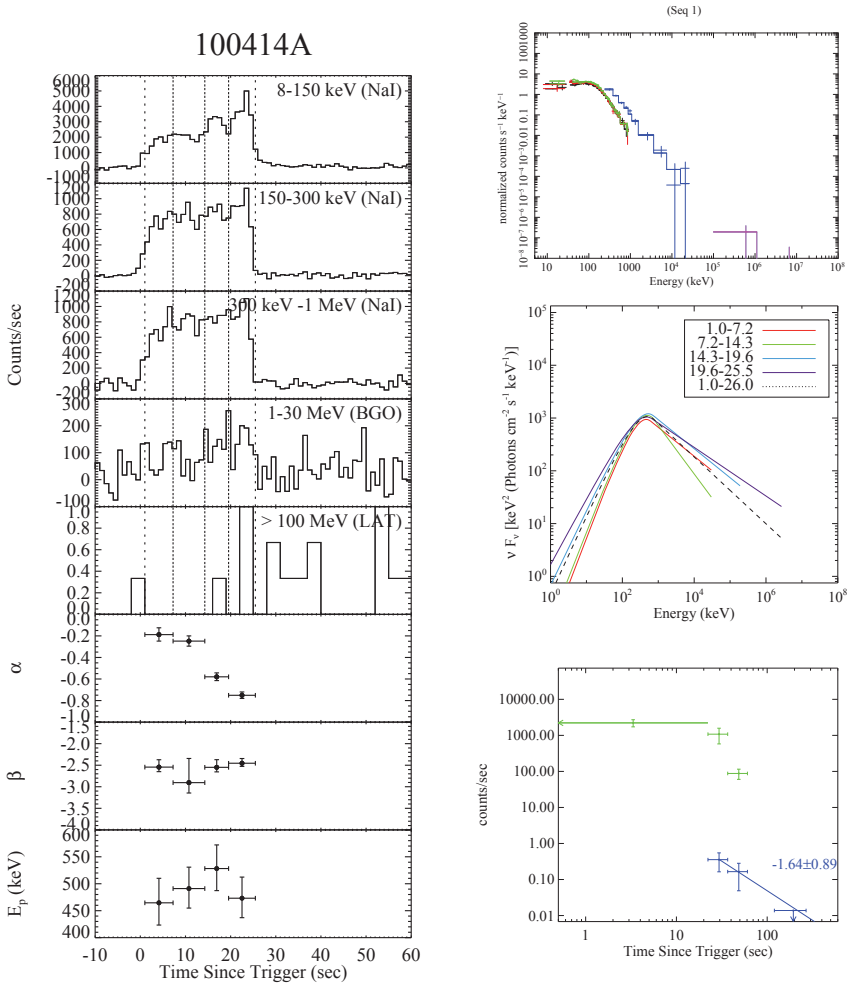

Figure 45 Same as Figure 29, but for GRB 100414A.

GRB 080916C

As shown in Fig.30, GRB 080916C is a long GRB with a duration ~ 66 s. The entire lightcurve can be divided into 6 segments. The smallest time bins during the brightest epochs (first two) are 3.7 s and 5.4 s, respectively. This corresponds to a rest-frame time interval ≤ 1 s (given its redshift 4.35, Greiner et al. 2009a). In all the time intervals, we found that the Band-function gives excellent fits to the data, consistent with Abdo et al. (2009a). Initially there is a spectral evolution where the spectra "widen" with time (α hardening and β softening), but later the spectral parameters essentially do not

evolve any more. We note that the steep β in the first time bin is mostly because of the non-detection in the LAT band. The tight upper limit above 100 MeV constrains the range of β not to be too hard. On the other hand, with GBM data alone, the data in first time bin can be still fit as a Band function, with $\beta \sim -2.12^{+0.158}_{-0.107}$ similar to the values at later epochs. This suggests an alternative interpretation to the data: The high energy spectral index may be similar throughout the burst. The delayed onset of LAT-band emission may be because initially there is a spectral cutoff around 100 MeV, which later moves to much higher energies (e.g. above 13.2 GeV in the second time bin).

It is interesting to note that the time integrated spectrum of GRB 080916C throughout the burst is also well fit with a Band function, where the spectral indices do not vary with time resolution. As an example, we present in Fig.46 the νF_ν spectra of GRB 080916C for three time bins with varying time resolution. Remarkably, the parameters do not vary significantly: $\alpha \sim -1.12$, $\beta \sim -2.25$ for 3.5-8 s; $\alpha \sim -1.0$, $\beta \sim -2.29$ for 2-10 s; $\alpha \sim -1.0$, $\beta \sim -2.27$ for 0-20 s. This is in stark contrast with GRB 090902B discussed below.

GRB 090510

The short GRB 090510 was triggered with a precursor 0.5 s prior to the main burst. Two LAT photons were detected before the main burst. During the first time slice (0.45-0.5 s), no LAT band emission is detected, and the GBM spectrum can be well fit with a PL with an exponential cutoff (CPL hereafter). In the subsequent time slices, an additional PL component shows up, and the time-resolved spectra are best fit by the CPL + PL model. If one uses a Band + PL model to fit the data, the high energy spectral index β of the Band component cannot be constrained. If one fixes β to a particular value, it must be steeper than -3.5 in order to be consistent with the data. The CPL invoked in these fits has a low energy photon index $\Gamma_{\rm CPL} \sim -(0.6-0.8)$, which is very different from the case of a BB (where $\Gamma_{\rm CPL} \sim +1$). On the other hand, the high-energy

regime (exponential cutoff) is very similar to the behavior of a BB.

Since this is a short GRB, we do not have enough photons to perform very detailed time-resolved spectral analysis. However, in order to investigate spectral evolution and the interplay between the MeV component and the extra PL component, we nonetheless make 4 time bins (see also Ackermann et al. 2010). As a result, the reduced χ^2 of each segment is outside the range of $0.75 \leq \chi^2/\mathrm{dof} \leq 1.5$ as is required for other GRBs. Our reduction results are generally consistent with those of the Fermi team (Abdo et al. 2009b; Ackermann et al. 2010).

GRB 090902B

The spectrum of GRB 090902B is peculiar. Abdo et al. (2009c) reported that both the time-integrated and time-resolved spectra of this GRB can be fit with the Band+PL model. Ryde et al. (2010) found that the time-resolved spectra can be fit with a PL plus a multi-color blackbody model. This raises the interesting possibility that a blackbody-like emission component is a fundamental emission unit shaping the observed GRB spectra.

In order to test this possibility, we carried out a series of time-resolved spectral analysis on the data (Fig.46). We first fit the time-integrated data within the time interval 0-20 s, and found that it can be fit with a model invoking a Band function and a power law, but with a poor $\chi^2/\mathrm{dof} \sim 3.52$. Compared with the Band component of other GRBs, this Band component is very narrow, with $\alpha \sim -0.58$, $\beta \sim -3.32$. A CPL + PL model can give comparable fit, with $\Gamma_{\mathrm{CPL}} \sim -0.59$. Next we zoom into the time interval 8.5 - 11.5 s, and perform spectral fits. The Band+PL and CPL+PL models can now both give acceptable fits, with parameters suggesting a narrower spectrum. For the Band+PL model, one has $\alpha \sim -0.07$, $\beta \sim -3.69$ with $\chi^2/\mathrm{dof} = 1.26$. For the CPL+PL model, one has $\Gamma_{\mathrm{CPL}} \sim -0.08$ with $\chi^2/\mathrm{dof} = 1.30$. Finally we zoom into the smallest time bin (9.5 - 10 s) in which the photon counts are just enough to perform adequate spectral fits. We find that the Band + PL model can no longer constrain β. The spectrum becomes

even narrower, with $\alpha \sim 0.07$ and $\beta < -5$. The CPL+PL model can fit the data with a range of allowed $\Gamma_{\rm CPL}$. In particular, if one fixes $\Gamma_{\rm CPL} \sim +1$ (the Rayleigh-Jeans slope of a blackbody), one gets a reasonable fit with $\chi^2/{\rm dof} = 0.92$. This encourages us to suspect that a blackbody (BB) + PL model can also fit the data. We test it and indeed found that the model can fit the data with $\chi^2/{\rm dof} = 1.11$. These different models require different $\Gamma_{\rm PL}$ for the extra PL component, but given the low photon count rate at high energies, all these models are statistically allowed. Since the BB + PL model has less parameters than the CPL + PL and Band + PL models, we take this model as the simplest model for this smallest time interval.

Next, we tried to divide the lightcurve of GRB 090902B into as many as time bins as possible so that the photon numbers in each time bin are large enough for statistically meaningful fits to be performed. Thanks to its high flux, we managed to divide the whole data set (0-30 s) into 62 time bins. We find that the data in each time bin can be well fit by a BB+PL model, and that the BB temperature evolves with time. The fitting results are presented in Table 12 and Fig.38. The time-integrated spectrum, however, cannot be fit with such a model ($\chi^2/{\rm dof} = 14732/276$). A Band+PL model gives a much improved fit, although the fit is still not statistically acceptable ($\chi^2/{\rm dof} = 2024/275$). The best fitting parameters are $\alpha = -0.83$, $\beta = -3.68$, $E_p = 847$ keV, and $\Gamma = -1.85$. Notice that the high energy photon index of the time-integrated Band spectrum is much steeper/softer than that observed in typical GRBs (Fig.48).

In Fig.47, we display the lightcurves of both the thermal and the power-law components. It is found that the two components in general track each other. This suggests that the physical origins of the two components are related to each other.

An important inference from the analysis of GRB 090902B is that a Band-like spectrum can be a result of temporal superposition of many blackbody-like components. This raises the interesting possibility of whether all "Band" function spectra are superposed thermal spectra. From the comparison between GRB 090902B and GRB 080916C

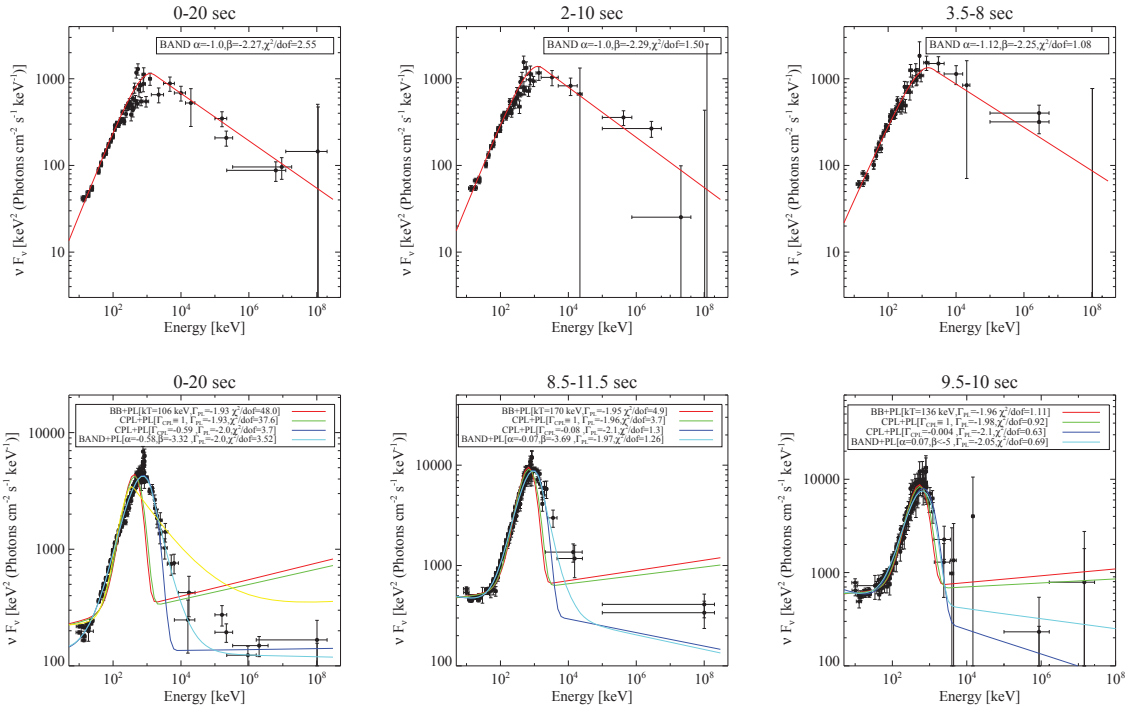

Figure 46 A comparison between GRB 080916C and GRB 090902B. *Upper panel*: The case of GRB 080916C. The Band parameters are $(\alpha, \beta) = (-1.0, -2.27)(-1.0, -2.29), (-1.12, -2.25)$ for 0-20 s, 2-10 s, and 3.5-8 s, respectively. Little spectral parameter variation is seen with reducing time bins. *Lower panel*: The case of GRB 090902B. (1) For 0-20 s, the Band+PL model ($\alpha = -0.58$, $\beta = -3.32$, $\Gamma_{\rm PL} = -2.0$ with $\chi^2/{\rm dof} = 3.52$) and the CPL+PL model ($\Gamma_{\rm CPL} = -0.59$, $\Gamma_{\rm PL} = -2.0$ with $\chi^2{\rm dof} = 3.7$) give marginally acceptable fits to the data. The CPL+PL model with $\Gamma_{\rm CPL} = 1$ (Rayleigh-Jeans) and the BB+PL model give unacceptable fits. (2) For 8.5-11.5 s, the Band+PL model ($\alpha = -0.07$, $\beta = -3.69$, $\Gamma_{\rm PL} = -1.97$ with $\chi^2/{\rm dof} = 1.26$) and the CPL+PL model ($\Gamma_{\rm CPL} = -0.08$, $\Gamma_{\rm PL} = -2.1$ with $\chi^2{\rm dof} = 1.3$) give acceptable fits to the data. The CPL+PL model with $\Gamma_{\rm CPL} = 1$ ($\chi^2/{\rm dof} = 3.7$) and the BB+PL model ($\chi^2/{\rm dof} = 4.9$) give marginally acceptable fits. (3) 9.5-10 s, the Band+PL model ($\alpha = 0.07$, $\beta < -5$, $\Gamma_{\rm PL} = -2.05$ with $\chi^2/{\rm dof} = 0.69$) can only give an upper limit on β. The CPL+PL model ($\Gamma_{\rm CPL} = -0.0004$, $\Gamma_{\rm PL} = -2.1$ with $\chi^2{\rm dof} = 0.63$) give marginally acceptable fit to the data. On the other hand, the CPL+PL model with $\Gamma_{\rm CPL} = 1$ ($\chi^2/{\rm dof} = 0.92$) and the BB+PL model ($\chi^2/{\rm dof} = 1.11$) give acceptable fits. Clear narrowing trend is seen when the time bins get smaller.

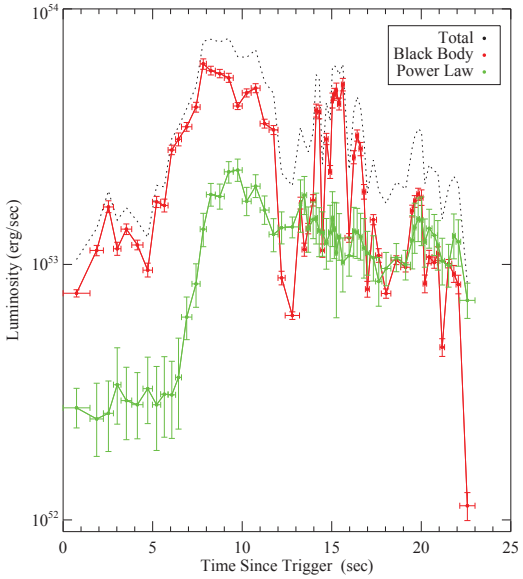

Figure 47 A comparison between the lightcurves of the blackbody component (red) and the power-law component (green) in GRB 090902B. The total lightcurve (the sum of the two components, *dotted* line) is also shown for comparison.

(Fig.46), we find that such speculation is far-fetched. As discussed above, GRB 080916C shows no evidence of "narrowing" as the time bin becomes small ($\sim$ 1 s in the rest frame). In the case of GRB 090902B, a clear "narrowing" feature is seen. For the time integrated spectrum, GRB 080916C has a wide Band function (with $\alpha \sim -1.0$, $\beta \sim -2.27$), while GRB 090902B (0-20 s) has a narrow Band function (with $\alpha = -0.58$, $\beta = -3.32$) with worse reduced χ^2. Another difference between GRB 090902B and GRB 080916C is that the former has a PL component, which leverages the BB spectrum on both the low-energy and the high-energy ends to make a BB spectrum look more similar to a (narrow) Band function. GRB 080916C does not have such a component, and the Band component covers the entire *Fermi* energy range (GBM & LAT). We therefore conclude that GRB 090902B is a special case, whose spectrum may have a different origin from GRB 080916C (and probably most other LAT GRBs as well, see Section below for more discussion).

GRB 090926A

This is another bright long GRB with a duration ~ 20 s. In our analysis, the lightcurve is divided into 9 segments. The Band function gives an acceptable fit to all the time bins (Fig.39). We however notice a flattening of β after ~ 11 s after the trigger. Also the Band function fit gives a worse reduced χ^2 (although still acceptable) after this epoch. Since our data analysis strategy is to go for the simplest models, we do not explore more complicated models that invoke Band + PL or Band + CPL (as is done by the Fermi team, Abdo et al. 2010b). In any case, our analysis does not disfavor the possibility that a new spectral component emerges after ~ 11 s since the trigger (Abdo et al. 2010b).

Other GRBs

The time resolved spectra of other 13 GRBs are all adequately described by the Band function, similar to GRB 080916C. The Band-function spectral parameters are generally similar to GRB 080916C. It is likely that these GRBs join GRB 080916C forming a "Band-only" type GRBs. In the current sample of 17 GRBs, only GRB 090510, GRB 090902B and probably GRB 090926A do not belong to this category and have an extra PL component extending to high energies. One caveat is that some GRBs in the sample are not very bright, so that we only managed to divide the lightcurves into a small number of time bins (e.g. 3 bins for GRB 080825C, 1 bin for GRB 081024B, 3 bins for GRB 090328, 3 bins for GRB 091031, 2 bins for GRB 100225A, and 1 bin for GRB 100325A). So one cannot disfavor the possibility that the observed spectra are superposition of narrower components (similar to GRB 090902B). However, at comparable time resolution, GRB 090902B already shows features that are different from these GRBs: (1) the Band component is "narrower", and (2) there is an extra PL component. These two features are not present in other GRBs. We therefore suggest that most LAT/GBM GRBs are similar to GRB 080916C.

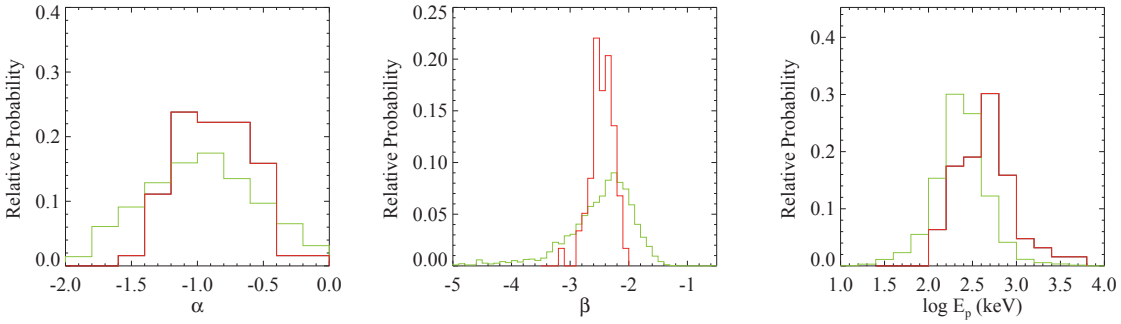

Figure 48 Distributions of the Band-function parameters α, β, and E_p in our sample (red) in comparison with the BATSE bright sources sample (green). The BATSE sample is adopted from Preece et al. (2000).

Spectral Parameter Distributions

Since the time-resolved spectra of most GRBs in our sample can be adequately described as a Band function, we present the distributions of the Band function parameters in this section. Since their MeV component may be of a different origin, GRB 090510 and GRB 090902B are not included in the analysis.

The distributions of the spectral parameters α, β, and E_p are presented in Figure 48, with a comparison with those of the bright BATSE GRB sample (Preece et al. 2000). It is found that the distributions peak at $\alpha = -0.9$, $\beta = -2.6$, and $E_p \sim 781$ keV, respectively. The α and β distributions are roughly consistent with those found in the bright BATSE GRB sample (Preece et al. 2000). The E_p distribution of the current sample has a slightly higher peak than the bright BATSE sample (Preece et al. 2000). This is likely due to a selection effect, namely, a higher E_p would favor GeV detections.

Spectral Parameter Correlations

For time-integrated spectra, it was found that E_p is positively correlated with the isotropic gamma-ray energy and the isotropic peak gamma-ray luminosity (Amati et al. 2002; Wei & Gao 2003; Yonetoku et al. 2004). For time resolved spectra, E_p was also found to be generally correlated with flux (and therefore luminosity, Liang et al. 2004),

although in individual pulses, both a decreasing E_p pattern and a E_p-tracking-flux pattern have been identified (Ford et al. 1995; Liang & Kargatis 1996; Kaneko et al. 2006; Lu et al. 2010).

In Fig.49, we present the E_p-luminosity relations. Fig.49a is for the global $E_p - L^p_{\gamma,\rm iso}$ correlation. Seven GRBs in our sample that have redshift information (and hence, the peak luminosity) are plotted against previous GRBs (a sample presented in Zhang et al. 2009). Since the correlation has a large scatter, all the GBM/LAT GRBs follow the same correlation trend. In particular, GRB 090902B, whose E_p is defined by the BB component, also follows a similar trend. This suggests that even if there may be two different physical mechanisms to define a GRB's E_p, both mechanisms seem to lead to a broad $E_p - L^p_{\gamma,\rm iso}$ relation. It is interesting to note that the short GRB 090510 (the top yellow point), even located at the upper boundary of the correlation, is still not an outlier. This is consistent with the finding (Zhang et al. 2009; Ghirlanda et al. 2009) that long/short GRBs are not clearly distinguished in the $L^p_{\gamma,\rm iso} - E_p$ domain.

In Fig.49b, we present the internal $E_p - L_{\gamma,\rm iso}$ correlation. It is interesting to note that although with scatter, the general positive correlation between E_p and $L_{\gamma,\rm iso}$ as discovered by Liang et al. (2004) clearly stands. More interestingly, the BB-defined E_p (in GRB 090902B) follows a similar trend to the Band-defined E_p (e.g. in GRB 080916C and GRB 090926A), although different bursts occupy a different space region in the $E_p - L_{\gamma,\rm iso}$ plane.

In Fig.50, we present various pairs of spectral parameters in an effort to search for possible new correlations. The GRBs with redshift measurements are marked in colors, while those without redshifts are marked in gray with an assumed redshift $z = 1$. In order to show the trend of evolution, points for same burst are connected, with the beginning of evolution marked as a circle.

No clear correlation pattern is seen in the $E_p - \alpha$ and $E_p - \beta$ plots. Interestingly, a preliminary trend of correlation is found in the following two domains.

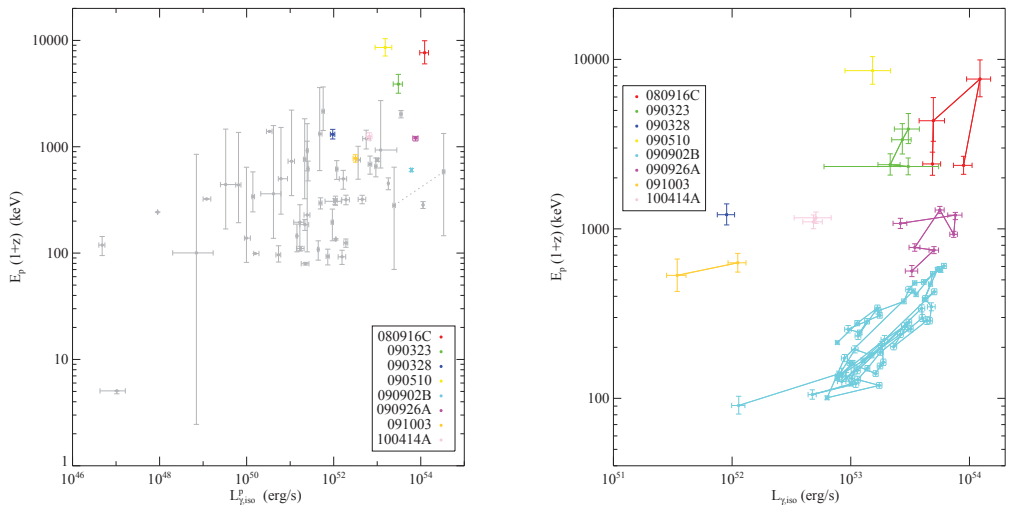

Figure 49 The global $L^p_{\gamma,\rm iso}$ vs. $E_p(1+z)$ correlation (panel a) and internal $L_{\gamma,\rm iso}$ vs. $E_p(1+z)$ correlation (panel b) for the 8 *Fermi*/LAT GRBs with known redshifts. The grey dots in (a) are previous bursts taken from Zhang et al. (2009).

- An $\alpha - \beta$ anti-correlation: Fig.50a shows a rough anti-correlation between α and β in individual GRBs. This suggests that a harder α corresponds to a softer β, suggesting a narrower Band function. In the time domain, there is evidence in some GRBs (e.g. GRB 080916C, GRB 090926A, and GRB 100414A, see Figs.30,39,45) that the Band function "opens up" as time goes by, but the opposite trend is also seen in some GRBs (e.g. GRB 091031, Fig.41). The linear Pearson correlation coefficients for individual bursts are insert in Fig.50a

- A flux-α correlation: Fig.50b shows a rough correlation between flux and α. Within the same burst, there is rough trend that as the flux increases, α becomes harder. The linear Pearson correlation coefficients for individual bursts are presented in Fig.50b inset. One possible observational bias is that when flux is higher, one tends to get a smaller time slice based on the minimum spectral analysis criterion. If the time smearing effect can broaden the spectrum, then a smaller time slice tends to give a narrower spectrum, and hence, a harder α. This would be relevant to bursts similar to GRB 090902B, but not bursts similar to GRB 080916C (which does

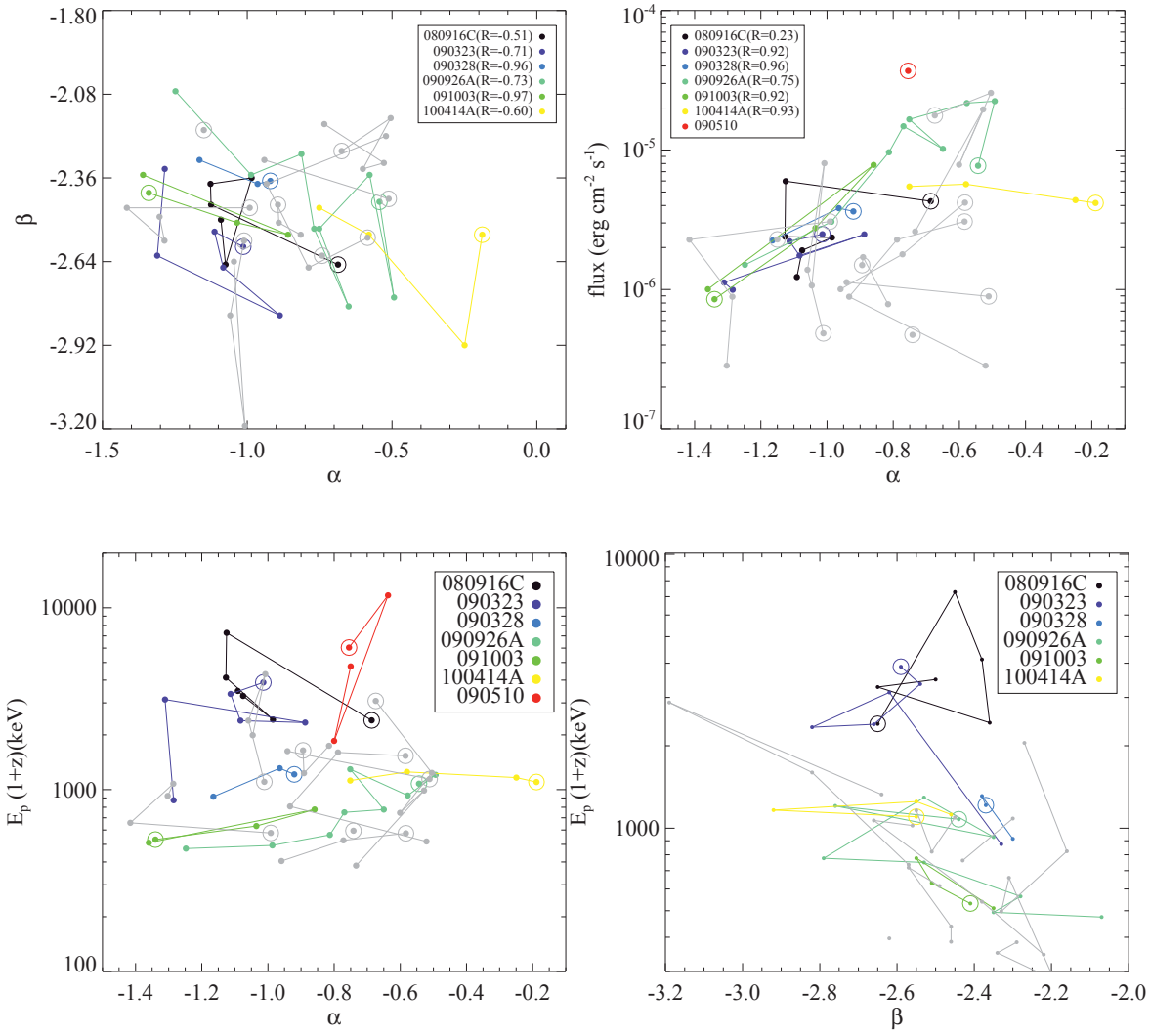

Figure 50 The two dimension plots of various pairs of spectral parameters. (a) $\alpha - \beta$, with linear Pearson correlation coeffcients for individual bursts marked in the inset; (b) $\alpha-$flux, with linear Pearson correlation coeffcients for individual bursts marked in the inset; (c) $E_p - \alpha$; (d) $E_p - \beta$. For those burst without redshift, $z = 2.0$ is assumed (grey symbols and lines).

not show spectral evolution as the time resolution becomes finer). More detailed analyses of bright GRBs can confirm whether such a correlation is intrinsic or due to the time resolution effect discussed above.

Several caveats should be noted for these preliminary correlations: First, some bursts do not obey these correlations, so the correlations, if any, are not universal; Second, the currently chosen time bins are based on the requirement for adequate spectral analyses, so the time resolution varies in different bursts. For some bright bursts, a burst pulse can be divided into several time bins, while in some faint others, a time bin corresponds to the entire pulse; Third, the current sample is still too small. A time-resolved spectral analysis for more bright GBM GRBs may confirm or dispute these correlations.

Three Elemental Spectral Components and Their Physical Origins

Three Phenomenologically Identified Elemental Spectral Components

The goal of our time-resolved spectral analysis is to look for "elemental" emission units that shape the observed GRB prompt gamma-ray emission. In the past it has been known that time-integrated GRB spectra are mostly fit by the Band function (Band et al. 1993). However, whether this function is an elemental unit in the time-resolved spectra is not known. One speculation is that this function is the superposition of many simpler emission units. If such a superposition relies on adding the emission from many time slices, then these more elemental units should show up as the time bins become small enough.

One interesting finding of our time-resolved spectral analyses is that the "Band"-like spectral component seen in GRB 090902B is different from that seen in GRB 080916C and some other Band-only GRBs. While the Band spectral indices of GRB 080916C essentially do not change as the time bins become progressively smaller, that of GRB 090902B indeed show the trend of "narrowing" as the time bin becomes progressively smaller. With the finest spectral resolution, GRB 090902B spectra can be fit by the

superposition of a PL component and a CPL function, including a Planck function. Even for the time-integrated spectrum, the "Band"-like component in GRB 090902B appears "narrower" than that of GRB 080916C. All these suggest that the "Band"-like component of GRB 090902B is fundamentally different from that detected in GRB 080916C and probably also other Band-only GRBs[3]. Similarly, the time-resolved spectra of the short GRB 090510 can be well fit by the superposition of a PL component and a CPL spectrum (although not a Planck function). The PL component extends to high energies with a positive slope in νF_ν. The CPL component may be modeled as a multi-color blackbody spectrum. We therefore speculate that the MeV component of GRB 090510 is analogous to that of GRB 090902B.

Phenomenologically, the power law component detected in GRB 090902B and GRB 090510 is an extra component besides the Band-like component. Such a component may have been also detected in the BATSE-EGRET burst GRB 941017 (González et al. 2003), and may also exist in GRB 090926A at later epochs.

We therefore speculate that phenomenologically there might be three elemental spectral components that shape the prompt gamma-ray spectrum. These include: (I) a *Band function component* ("Band" in abbreviation) that covers a wide energy range (e.g. 6-7 orders of magnitude in GRB 080916C) and persists as the time bins become progressively smaller. It shows up in GRB 080916C and 13 other LAT GRBs; (II) a *quasi-thermal component* ("BB" in abbreviation[4]) which becomes progressively narrower as the time bin becomes smaller, and eventually can be represented as a blackbody (or multi-color blackbody) component as seen in GRB 090902B; (III) a *power law component* ("PL" in abbreviation) that extends to high energy as seen in GRBs 090902B and 090510, which has a positive slope in the νF_ν spectrum and should have an extra peak energy (E_p) at

[3]Our finest time interval is around 1s in the rest frame of the burst. Theoretically, how time-integrated spectra broaden with increasing time bins is subject further study. Our statement is therefore relevant for time resolution longer than 1s.

[4]Notice that the abbreviation "BB" here not only denotes blackbody, but also includes various modifications to the blackbody spectrum such as multi-color blackbody.

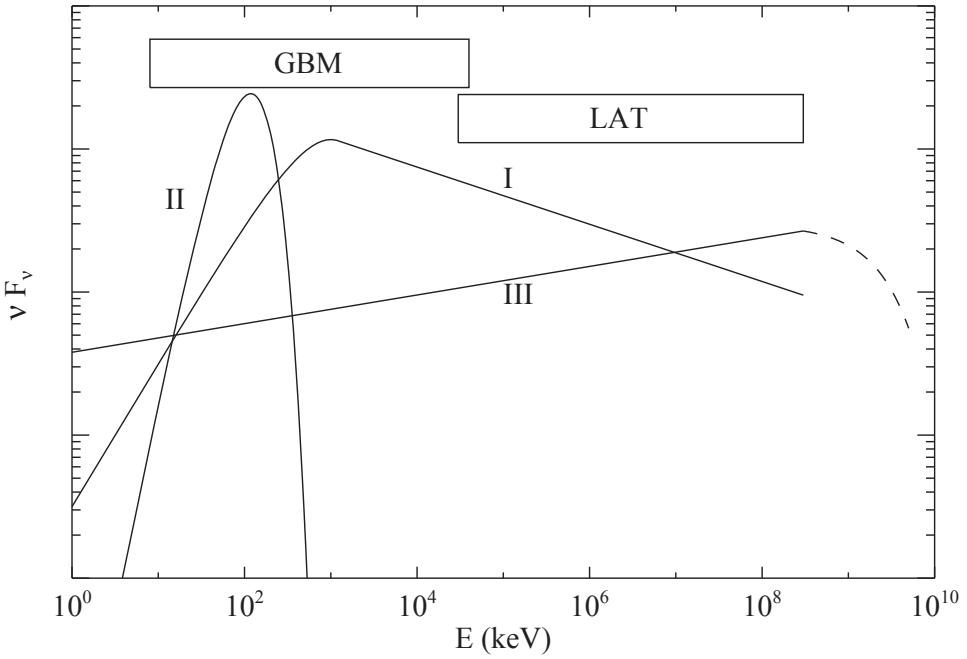

Figure 51 A cartoon picture of three elemental spectral components that shape GRB prompt emission spectra: (I) a Band-function component that is likely of the non-thermal origin; (II) a quasi-thermal component; and (III) an extra power-law component that extends to high energy, which is expected to have a cut-off near or above the high energy end of the LAT energy band.

an even higher energy that is not well constrained by the data.

Figure 51 is a cartoon picture of the νF_ν spectrum that includes all three phenomenologically identified elemental spectral components. The time resolved spectra of the current sample can be understood as being composed of one or more of these components. For example, GRB 080916C and other 13 GRBs have Component I (Band), GRB 090902B and probably GRB 090510 have Components II (BB) and III (PL), and GRB 0900926A has Component I initially, and may have components I and III at later times.

Possible Physical Origins of the Three Spectral Components

Band Component

The fact that the this component extends through a wide energy range (e.g. 6-7 orders of magnitude for GRB 080916C) strongly suggests that a certain non-thermal emission mechanism is in operation. This demands the existence of a population of power-law-distributed relativistic electrons, possibly accelerated in internal shocks or in regions with significant electron heating, e.g. magnetic dissipation. In the past there have been three model candidates for prompt GRB emission: synchrotron emission, synchrotron self-Compton (SSC), and Compton upscattering of a thermal photon source. In all these models the high energy PL component corresponds to emission from a PL-distributed electron population. The spectral peak energy E_p may be related to the minimum energy of the injected electron population, an electron energy distribution break, or the peak of the thermal target photons.

Most prompt emission modeling (Mészáros et al. 1994; Pilla & Loeb 1998; Pe'er & Waxman 2004a; Razzaque et al. 2004; Pe'er et al. 2006a; Gupta & Zhang 2007) suggest that the overall spectrum is curved, including multiple spectral components. Usually a synchrotron component is accompanied by a synchrotron self-Compton (SSC) component. For matter-dominated fireball models, one would expect the superposition of emissions from the photosphere and from the internal shock dissipation regions. As a result, the fact that 14/17 ($\sim 80\%$) of GRBs in our sample have a Band-only spectrum is intriguing. The three theoretically expected spectral features, i.e. the quasi-thermal photosphere emission, the SSC component (if the MeV component is of synchrotron origin), and a pair-production cutoff at high energies, are all not observed. This led to the suggestion that the outflows of these GRBs are Poynting flux dominated (Zhang & Pe'er 2009). Within such a picture, the three missing features can be understood as the following: (1) Since most energy is carried in magnetic fields and not in photons, the photosphere emission (BB component) is greatly suppressed; (2) Since the magnetic

energy density is higher than the photon energy density, the Compton Y parameter is smaller than unity, so that the SSC component is naturally suppressed; (3) A Poynting flux dominated model usually has a larger emission radius than the internal shock model (Lyutikov & Blandford 2003 for current instability and Zhang & Yan 2011 for collision-induced magnetic reconnection/turbulence). This reduces the two-photon annihilation opacity and increases the pair cutoff energy. This allows the Band component extend to very high energy (e.g. 13.2 GeV for GRB 080916C).

Another possibility, advocated by Beloborodov (2010) and Lazzati & Begelman (2010) in view of the *Fermi* data (see also discussion by Thompson 1994; Rees & Mészáros 2005; Pe'er et al. 2006; Giannios & Spruit 2007; Fan 2009; Toma et al. 2010; and Ioka 2010), is that the Band component is the emission from a dissipative photosphere. This model invokes relativistic electrons in the regions where Thomson optical depth is around unity, which upscatter photosphere thermal photons to high energies to produce a power law tail. This model can produce a Band-only spectrum, but has two specific limitations. First, the high energy power law component cannot extend to energies higher than GeV in the cosmological rest frame, since for effective upscattering, the emission region cannot be too far above the photosphere. The highest photon energy detected in GRB 080916C is 13.2 GeV (which has a rest-frame energy ~ 70 GeV for its redshift $z = 4.35$). This disfavors the dissipative photosphere model. This argument applies if the LAT-band photons are from the same emission region as the MeV photons, as suggested by the single Band function spectral fits. It has been suggested that the LAT emission during the prompt phase originates from a different emission region, e.g. the external shock (Kumar & Barniol Duran 2009; Ghisellini et al. 2010). This requires that the two distinct emission components conspire to form a nearly featureless Band spectrum in all temporal epochs, which is contrived. As will be shown in Sect.7 later, there is compelling evidence that the LAT emission during the prompt emission phase is of an internal origin. In particular, the peak of the GeV lightcurve of GRB 080916C coincides with the second

(the brightest) peak of GBM emission, and the 13.2 GeV photon coincides with another GBM lightcurve peak. All these suggest an internal origin of the GeV emission during the prompt phase.

The second limitation of the dissipative photosphere model is that the photon spectral index below E_p is not easy to reproduce. The simplest blackbody model predicts a Rayleigh-Jeans spectrum $\alpha = +1$. By considering slow heating, this index can be modified as $\alpha = +0.4$ (Beloborodov 2010). Both are much harder from the observed $\alpha \sim -1$ value. In order to overcome this difficulty, one may appeal to the superposition effect, i.e. the observed Band spectrum is the superposition of many fundamental blackbody emission units (e.g. Blinnikov et al. 1999; Toma et al. 2010; Mizuta et al. 2010; Pe'er & Ryde 2010). However, no rigorous calculation has been performed to fully reproduce the $\alpha = -1$ spectrum. Pe'er & Ryde (2010) show that when the central engine energy injection is over and the observed emission is dominated by the high-latitude emission, an $\alpha = -1$ can be reproduced with the flux decaying rapidly with $\propto t^{-2}$. During the phase when the central engine is still active, the observed emission is always dominated by the contribution along the line of sight, which should carry the hard low energy spectral index of the blackbody function. Observationally, the Band component spectral indices are not found to vary when the time bins are reduced (in stark contrast to the narrow Band-like component identified in GRB 090902B). This suggests that at least the temporal superposition of many blackbody radiation units is not the right interpretation for this component.

Quasi-Thermal (BB) Component

The MeV component in GRB 090902B narrows with reduced time resolution and eventually turns into being consistent with a blackbody (or multi-color blackbody) as the time bin becomes small enough. This suggests a thermal origin of this component. Within the GRB content, a natural source is the emission from the photosphere where the photons

advected in the expanding relativistic outflow turn optically thin for Compton scattering. In fact, the original fireball model predicts a quasi-thermal spectrum (Paczýnski 1986; Goodman 1986). In the fireball shock model, such a quasi-blackbody component is expected to be associated with the non-thermal emission components (Mészáros & Rees 2000; Mészáros et al. 2002; Daigne & Mochkovitch 2002; Pe'er et al. 2006).

Some superposition effects may modify the thermal spectrum to be different from a pure Planck function. The first is the temporal smearing effect. If the time bin is large enough, one samples photosphere emission from many episodes, and hence, the observed spectrum should be a multi-color blackbody. This effect can be diminished by reducing the time bin for time-resolved spectral analyses. GRB 090902B is such an example. The second effect is inherited in emission physics of relativistic objects. At a certain epoch, the observer detects photons coming from different latitudes from the line of sight, with different Doppler boosting factors. The result is an intrinsic smearing of the Planck function spectrum. Pe'er & Ryde (2010) have shown that after the central engine activity ceases, the high-latitude emission effect would give an $\alpha \sim -1$ at late times, with a rapidly decaying flux $F_\nu \propto t^{-2}$. This second superposition effect is intrinsic, and cannot be removed by reducing the time bins.

The case of the thermal component is most evidenced in GRB 090902B, and probably also in GRB 090510. In both bursts, the MeV component can be well fit with a CPL + PL spectrum. The exponential cutoff at the high energy end is consistent with thermal emission with essentially no extra dissipation. For GRB 090902B, the low energy spectral index $\Gamma_{\rm CPL}$ is typically ~ 0, and can be adjusted to $+1$ (blackbody). For GRB 090510, $\Gamma_{\rm CPL}$ is softer (~ -0.7). Since it is a short GRB, the high-latitude effect may be more important. The softer low energy spectral index may be a result of the intrinsic high-latitude superposition effect (Pe'er & Ryde 2010).

Power-Law (PL) Component

This component is detected in GRB 090902B and GRB 090510. Several noticeable properties of this component are: (1) For our small sample, this component is always accompanied by a low energy MeV component (likely the BB component). Its origin may be related to this low energy component; (2) It is demanded in both the low energy end and the high energy end, and amazingly the same spectral index can accommodate the demanded excesses in both ends. This suggests that either this PL component extends for 6-7 orders of magnitude in energy, or that multiple emission components that contribute to the excesses in both the low and high energy regimes have to coincide to mimic a single PL; (3) The spectral slope is positive in the νF_ν space, so that the main energy power output of this component is at even higher energies (possibly near or above the upper bound of the LAT band).

Since the non-thermal GRB spectra are expected to be curved (Mészáros et al. 1994; Pilla & Loeb 1998; Pe'er & Waxman 2004a; Razzaque et al. 2004; Pe'er et al. 2006a; Gupta & Zhang 2007; Asano & Terasawa 2009), the existence of the PL component is not straightforwardly expected. It demands coincidences of various spectral components to mimic a single PL component in the low and high energy ends. Pe'er et al. (2010) have presented a theoretical model of GRB 090902B. According to this model, the apparent PL observed in this burst is the combination of the synchrotron emission component (dominant at low energies), the SSC and Comptonization of the thermal photons (both dominant at high energies). A similar model was analytically discussed by Gao et al. (2009) within the context of GRB 090510.

One interesting question is how Component III (PL) differs from Component I (Band). Since both components are non-thermal, they may not be fundamentally different. They can be two different manifestations of some non-thermal emission mechanisms (e.g. synchrotron and inverse Compton scattering) under different conditions. On the other hand, since Component III seems to be associated with Component II (BB) (e.g. in GRB

090902B and GRB 090510), its origin may be related to Component II. One possible scenario is that Component III (at least the part above component II) is the Compton-upscattered emission of Component II (e.g. Pe'er & Waxman 2004b for GRB 941017). The fact that the lightcurves of the BB component and the PL component of GRB 090902B roughly track each other (Fig.47) generally supports such a possibility. Within this interpretation, one must attribute the PL part below the thermal peak as due to a different origin (e.g. synchrotron, see Pe'er et al. 2010). Alternatively, Component I and III may be related to non-thermal emission from two different emission sites (e.g. internal vs. external or two different internal locations). Indeed, if the late spectra of GRB 090926A are the superposition of the components I and III, then both components can coexist, which may correspond to two different non-thermal emission processes and/or two different emission sites.

Possible Spectral Combinations of GRB Prompt Emission

Using the combined GBM and LAT data, we have phenomenologically identified three elemental spectral components during the prompt GRB phase (Fig.51). Physically they may have different origins (see above). One may speculate that all the GRB prompt emission spectra may be decomposed into one or more of these spectral components. It is therefore interesting to investigate how many combinations are in principle possible, how many have been discovered, how many should not exist and why, and how many should exist and remain to be discovered. We discuss the following possibilities in turn below (see Fig.52 for illustrations).

1. Component I (Band) only:

   This is the most common situation, which is observed in 14/17 GRBs in our sample exemplified by GRB 080916C. Either the BB and PL components do not exist, or they are too faint to be detected above the Band component. If the BB component is suppressed, these bursts may signify non-thermal emission from an Poynting flux

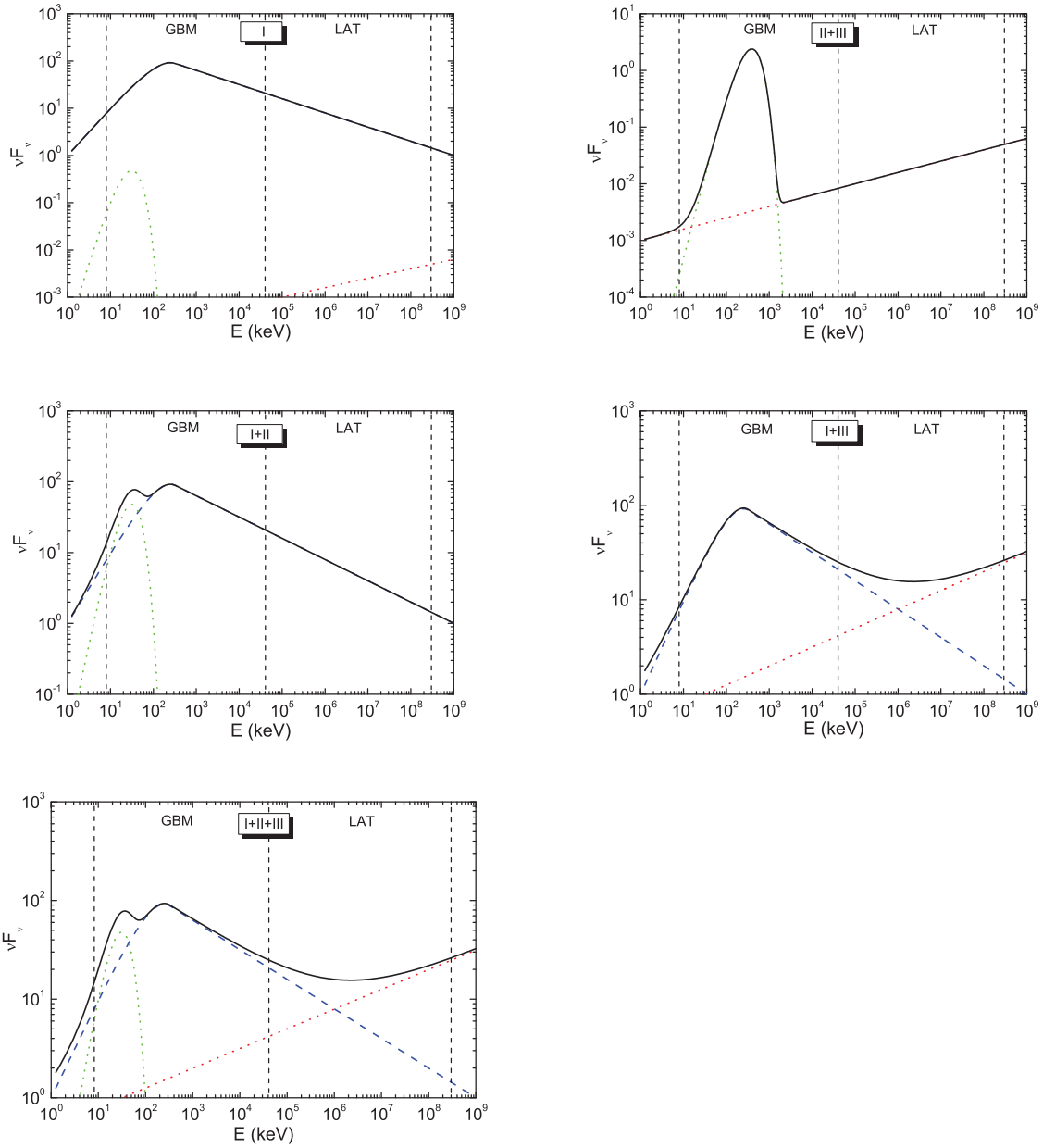

Figure 52 Five possible spectral combinations with the three spectral components.

dominated flow.

2. Component II (BB) only:

   No such case exists in the current sample. GRB 090902B, and probably also GRB 090510, have a BB component, but it is accompanied by a PL component in both GRBs. It remains to be seen whether in the future a BB-only GRB will be detected, or whether a BB component is always accompanied by a PL component. Since the case of GRB 090902B is rare, we suspect that the BB-only GRBs are even rarer, if they exist at all.

3. Component III (PL) only:

   Our PL component stands for the high energy spectral component seen in GRB 090902B and GRB 090510, which likely has a high E_p near or above the boundary of the LAT band. Observationally, there is no solid evidence for such PL-only GRBs[5]. In our current sample which covers the widest energy band, the PL component only exists in 2 out of 17 GRBs, and is found to be associated with the BB component. The luminosity of the PL component is found to roughly track that of the thermal component (Fig.47). If the PL component is the Comptonization of a low energy photon source (e.g. the BB component), then PL-only GRBs may not exist in nature.

4. I + II:

   Such a case is not found in our sample. If the Band component is the emission from the internal shocks and the BB component is the emission from the photosphere, then such a combination should exist and be common for fireball scenarios. An

[5]Most of Swift GRBs can be fit with a PL (Sakamoto et al. 2008). However, this is due to the narrowness of the energy band of the gamma-ray detector BAT on board Swift. The E_p of many Swift GRBs are expected to be located outside the instrument band. In fact, using a Band function model and considering the variation of E_p within and outside the BAT band, one can reproduce the apparent hardness of Swift GRBs, and obtain an effective correlation between the BAT-band photon index and E_p (e.g. Zhang et al. 2007a; Sakamoto et al. 2009). If a GRB is observed in a wider energy band, the spectrum should be invariably curved.

identification of such a case would confirm the non-thermal nature of the Band component (since the thermal component is manifested as the BB component). Observationally, an X-ray excess has been observed in 12 out of 86 ($\sim 14\%$) bright BATSE GRBs (Preece et al. 1996). This could be due to the contamination of a BB component in the X-ray regime. With the excellent spectral coverage of *Fermi*, we expect that such a spectral combination may be identified in some GRBs, even if technically it may be difficult because there are too many spectral parameters to constrain.

5. I + III:

   Such a combination has not been firmly identified in our sample. Nonetheless, the spectral hardening of GRB 090926A after 11 s may be understood as the emergence of the PL component on top of the Band component seen before 11 s. Physically it may be related to two non-thermal spectral components or non-thermal emission from two different regions.

6. II + III:

   Such a case is definitely identified in GRB 090902B, and likely in GRB 090510 as well. From the current sample, it seems that such a combination is not as common as the Band-only type, but nonetheless forms a new type of spectrum that deserves serious theoretical investigations. Physically, the high-energy PL component is likely the Compton up-scattered emission of the BB component, although other non-thermal processes (e.g. synchrotron and SSC) could also contribute to the observed emission (Pe'er et al. 2010).

7. I + II + III:

   The full combination of all three spectral components (e.g. Fig.51) is not seen from the current sample. In any case, in view of the above various combinations (including speculative ones), one may assume that the full combination of the three

spectral components is in principle possible. Physically this may correspond to one photosphere emission component and two more non-thermal components (either two spectral components or non-thermal emission from two different regions). Nonetheless, technically there are too many parameters to constrain, so that identifying such a combination is difficult.

Physical Origin Of The Gev Emission

LAT-Band Emission vs. GBM-Band Emission

Besides the joint GBM/LAT spectral fits, one may also use temporal information to investigate the relationship between the emission detected in the GBM-band and that detected in the LAT band. In this section we discuss three topics: delayed onset of LAT emission, rough tracking behavior between GBM and LAT emissions, and long-lasting LAT afterglow.

Delayed Onset Of Lat Emission

The *Fermi* team has reported the delayed onset of LAT emission in several GRBs (GRBs 080825C, 080916C, 090510, 090902B, Abdo et al. 2009a,b,c,d). Our analysis confirms all these results. In Table 11, we mark all the GRBs in our sample that show the onset delay feature.

There have been several interpretations to the delayed onset of GeV emission discussed in the literature. Toma et al. (2009) suggested that GeV emission is the upscattered cocoon emission by the internal shock electrons. Razzaque et al. (2010) interpreted the GeV emission as the synchrotron emission of protons. Since it takes a longer time for protons to be accelerated and be cooled to emit GeV photons, the high energy emission is delayed. Li (2010b) interpreted GeV emission as the upscattered prompt emission photons by the residual internal shocks.

Although it is difficult to test these models using the available data, our results give

some observational constraints to these models. First, except GRBs 090510 and 090902B whose GeV emission is a distinct spectral component, other GRBs with onset delay still have a simple Band-function spectrum after the delayed onset. This suggests that for those models that invoke two different emission components to interpret the MeV and GeV components, one needs to interpret the coincidence that the GeV emission appears as the natural extension of the MeV emission to the high energy regime.

For such delayed onsets whose GeV and MeV emissions form the same Band component, one may speculate two simpler explanations. One is that there might be a change in the particle acceleration conditions (e.g. magnetic configuration in the particle acceleration region). As shown in Sect.7, the early spectrum during the first time bin (before onset of LAT emission) of GRB 080916C may be simply a consequence of changing the electron spectral index. One may speculate that early on the particle acceleration process may not be efficient, so that the electron energy spectral index is steep. After a while (the observed delay), the particle acceleration mechanism becomes more efficient, so that the particle spectral index reaches the regular value. The second possibility is that there might be a change in opacity. The GBM data alone during the first time bin gives a similar β as later epochs. It is possible that there might be a spectral cutoff slightly above the GBM band early on. A speculated physical picture would be that the particle acceleration conditions are similar throughout the burst duration, but early on the pair production opacity may be large (probably due to a lower Lorentz factor or a smaller emission radius), so that the LAT band emission is attenuated. The opacity later drops (probably due to the increase of Lorentz factor or the emission radius), so that the LAT band emission can escape from the GRB. Within such a scenario, one would expect to see a gradual increase of maximum photon energy as a function of time. Figure 53 shows the LAT photon arrival time distribution of GRB 080916C. Indeed one can see a rough trend of a gradual increase of the maximum energy with time.

One last possibility is that the LAT band emission is dominated by the emission from

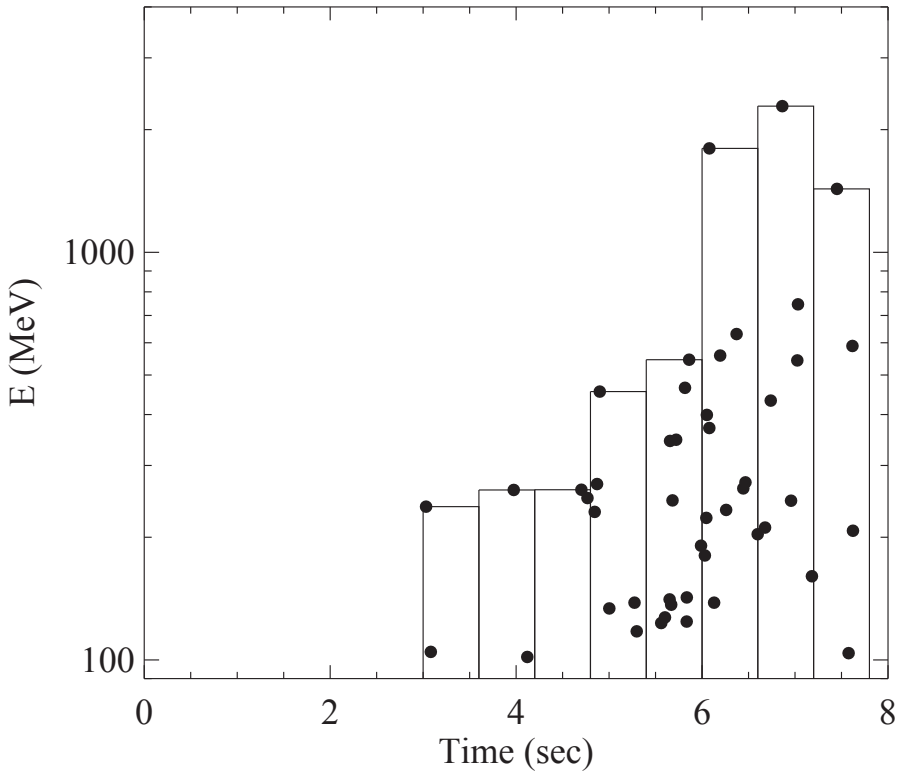

Figure 53 LAT photon arrival time distribution for GRB 080916C. A rough trend of gradual increase of the maximum photon energy with time is seen.

the external shock, which is delayed with respect to the GBM-band prompt emission. This possibility is discussed in more detail below.

Rough Tracking Behavior

Inspecting the multi-band lightcurves (Figs.29-45 left panels), for bright GRBs (e.g. 080916C, 090217, 090323, 090902B) the LAT emission peaks seem to roughly track some peaks of the GBM emission (aside from the delayed onset for some of them). For example, the peak of the LAT lightcurve of GRB 080916C coincides with the second GBM peak. This is consistent with the spectral analysis showing that most time-resolved joint spectra are consistent with being the same (Band-function) spectral component. Even for GRB 090902B whose LAT band emission is from a different emission component from the MeV BB component, the emissions in the two bands also roughly track each other (Fig.47). This suggests that the two physical mechanisms that power the two spectral components are related to each other.

The rough tracking behavior is evidence against the proposal that the entire GeV emission is from the external forward shock. Within the forward shock model, the fluctuation in energy output from the central engine should be greatly smeared, since the observed flux change amplitude is related to $\Delta E/E \ll 1$ (where E is the total energy already in the balstwave, and ΔE is the newly injected energy from the central engine), rather than ΔE itself within the internal models.

Long Term Emission in the LAT Band

In order to study the long-term lightcurve behavior, we extract the GBM-band and LAT-band lightcurves in logarithmic scale and present them in the bottom right panel of Figs.29-45. We unevenly bin the LAT lightcurves with bin sizes defined by the requirement that the signal-to-noise ratio must be > 5. For a close comparison, we correspondingly re-bin the GBM lightcurves using the same bin sizes. Some GRBs (e.g.

080916C, 090510, 090902B, and 090926A) have enough photons to make a well sampled LAT lightcurve.

In several GRBs, LAT emission lasts longer than GBM emission and decays as a single power law (Ghisellini et al. 2010). The decay indices of LAT emission are marked in the last panel of Figs.29-45, which can be also found in Table 13. Due to low photon numbers, it is impossible to carry out a time resolved spectral analysis. In any case, the LAT-band photon indices of long-term LAT emission are estimated and also presented in Table 13. In Table 11, we mark those GRBs with detected LAT emission longer than GBM emission and those without. The most prominent ones with long lasting LAT afterglow are GRBs 080916C, 090510, 090902B, and 090926A. Spectral analyses suggest that the LAT emission in GRBs 090510 and 090902B is a different spectral component from the MeV emission. The GBM lightcurves of these GRBs indeed follow a different trend by turning off sharply as compared with the extended PL decay in the LAT band. GRB 090926A, on the other hand, shows a similar decay trend in both GBM and LAT bands. GRB 080916C is special. Although the spectral analysis shows a single Band function component, the GBM lightcurve turns over sharply around 70-80 seconds, while the LAT emission keeps decaying with a single PL.

One caveat of LAT long-term lightcurves is that they depend on the level of background and time-bin selection. Due to the low count rate at late times, the background uncertainty can enormously change the flux level, and a different way of binning the data may change the shape of the lightcurve considerably. In our analysis, the background model is extracted from the time interval prior to the GBM trigger in the same sky region that contains the GRB. The bin-size is chosen to meet the 5σ statistics to reduce the uncertainty caused by arbitrary binning.

Our data analysis suggests a controversial picture regarding the origin of this GeV afterglow. Spectroscopically, the LAT-band emission is usually an extension of the GBM-band emission and forms a single Band-function component, suggesting a com-

Table 13 Temporal and spectral properties of the long-term LAT emission.

Name	$\alpha_{\rm LAT}$	$\Gamma_{\rm LAT}$
080825C	-0.47 ± 0.74	-1.71
080916C	-1.33 ± 0.08	-1.77
081024B	-1.37 ± 0.41	-1.98
081215A	-	-
090217	-0.81 ± 0.23	-1.97
090323	-0.52 ± 0.67	-1.75
090328	-0.96 ± 0.44	-1.82
090510	-1.70 ± 0.08	-1.94
090626	-	-1.53
090902B	-1.40 ± 0.06	-1.76
090926A	-2.05 ± 0.14	-2.03
091003	< -0.93	-1.74
091031	-0.57 ± 0.28	-1.73
100116A	-	-1.68
100225A	-	-1.77
100325A	< -1.04	-1.53
100414A	-1.64 ± 0.89	-1.85

mon physical origin with the GBM-band emission. If one focuses on the prompt emission lightcurves, the LAT-band activities seem to track the GBM-band activities. Even for GRB 090902B which shows a clear second spectral component, the PL component variability tracks that of the BB component well (Fig.47), suggesting a physical connection between the two spectral components. These facts tentatively suggest that at least during the prompt emission phase, the LAT-band emission is likely connected to the GBM-band emission, and may be of an "internal" origin similar to the GBM-band emission.

It has been suggested that the entire GeV emission originates from the external shock (e.g. Kumar & Barniol Duran 2009a, 2009b; Ghisellini et al. 2010; Corsi et al. 2009). This idea is based on the power law temporal decay law that follows the prompt emission. Such a GeV afterglow scenario is not straightforwardly expected for the following reasons. First, before *Fermi*, afterglow modeling suggests that for typical afterglow parameters, the GeV afterglow is initially dominated by the synchrotron self-Compton component (Mészáros & Rees 1994; Dermer et al. 2000; Zhang & Mészáros 2001b; Wei & Fan 2007; Gou & Mészáros 2007; Galli & Piro 2007; Yu et al. 2007; Fan et al. 2008), or by other

IC processes invoking both forward and reverse shock electrons (Wang et al. 2001). For very energetic GRBs such as GRB 080319B, one may expect a synchrotron-dominated afterglow all the way to an energy ~ 10 GeV (Zou et al. 2009; Fan et al. 2008). Second, the required parameters for the external shock are abnormal to interpret the data. For example, the magnetic field strength at the forward shock needs to be much smaller than equipartition, consistent with simply compressing the ISM magnetic field without shock amplification (Kumar & Barniol Duran 2010). This, in turn, causes a problem in accelerating electrons to a high enough energy to enable emission of GeV photons (Li 2010a; Piran & Nakar 2010). Moreover, the circumburst number density of these long GRBs are required to be much lower than that of a typical ISM (e.g., Kumar & Barniol Duran 2010), which challenges the collapsar model. Finally, observed GeV decay slope is typically steeper than the predictions invoking a standard adiabatic forward shock (e.g. Figs.30,36,38,39,45, see also Ghisellini et al. 2010). One needs to invoke a radiative blastwave (Ghisellini et al. 2010) or a Klein-Nishina cooling-dominated forward shock (Wang et al. 2010) to account for the steepness of the decay slope.

The external shock model to interpret the entire GeV emission is challenged by the following two arguments. First, the GeV lightcurve peak coincides the second peak of the GBM lightcurve for GRB 080916C. This requires a fine-tuned bulk Lorentz factor of the fireball to make the deceleration time coincide the epoch of the second central engine activity. This is highly contrived. Second, the external shock component should not have decayed steeply while the prompt emission is still on going. To examine this last point, we have applied the shell-blastwave code developed by Maxham & Zhang (2009) to model the blastwave evolution of GRB 080916C using the observed data by assuming that the outflow kinetic energy traces the observed gamma-ray lightcurve (assuming a constant radiation efficiency). The resulting LAT-band lightcurve always displays a shallow decay phase caused by refreshing the forward shock by materials ejected after the GeV lightcurve peak time even for a radiative blastwave, in stark contrast to the

data. This casts doubts on the external shock origin of GeV emission during the prompt phase (Maxham et al. 2011). We note that detailed modeling of GRB 090510 (He et al. 2010) and GRB 090902B (Liu & Wang 2011) with the external shock model both suggests that the prompt GeV emission cannot be interpreted as the emission from the external forward shock.

Collecting the observational evidence and the theoretical arguments presented above, we suggest that at least during the prompt emission phase (when GBM-band emission is still on), the LAT-band emission is not of external forward shock origin.

After the GBM-band prompt emission is over, the LAT-band emission usually decays as a PL. We note that the long-term GeV lightcurve can be interpreted in more than one way. (1) If one accepts that the prompt GeV emission is of internal origin, one may argue that the external shock component sets in before the end of the prompt emission and thereafter dominates during the decay phase (Maxham et al. 2011). This requires arguing for coincidence of the same decaying index for the early internal and the late external shock emission. Considering a possible superposition effect (i.e. the observed flux during the transition epoch includes the contributions from both the internal and external shocks), this model is no more contrived than the model that interprets prompt GeV emission as from external shocks, which requires coincidence of internal emission spectrum and the external shock emission spectrum to mimic the same Band spectrum in all time bins (Kumar & Barniol Duran 2009). (2) An alternative possibility is to appeal to an internal origin of the entire GeV long-lasting afterglow, which reflects the gradual "die-off" of the central engine activity. The difficulty of such a suggestion is that it must account for the different decaying behaviors between the GBM-band emission and LAT-band emission in some (but not all) GRBs (e.g. GRB 080916C). To differentiate between these possibilities, one needs a bright GRB co-triggered by *Fermi* LAT/GBM and *Swift* BAT, so that an early *Swift* XRT lightcurve is available along with the early GeV lightcurve. The external-shock-origin GeV afterglow should be accompanied by a PL

decaying early X-ray lightcurve (Liang et al. 2009) instead of the canonical steep-shallow-normal decaying pattern observed in most *Swift* GRBs (Zhang et al. 2006; Nousek et al. 2006; O'Brien et al. 2006). A violation of such a prediction would suggest an internal origin of the GeV afterglow.

Summary and Discussion

I have presented a comprehensive joint analysis of 17 GRBs co-detected by *Fermi* GBM and LAT. A time-resolved spectral analysis of all the bursts with the finest temporal resolution allowed by statistics is carried out in order to reduce temporal smearing of different spectral components. Our data analysis results can be summarized as the following:

- We found that the time-resolved spectra of 14 out of 17 GRBs are best modeled with the classical "Band" function over the entire *Fermi* spectral range, which may suggest a common origin for emissions detected by LAT and GBM. GRB 090902B and GRB 090510 are found to be special in that the data require the superposition between a MeV component and an extra power law component, and that the MeV component has a sharp cutoff above E_p. More interestingly, the MeV component of GRB 090902B becomes progressively narrower as the time bin gets smaller, and can be fit with a Planck function as the time bin becomes small enough. This is in stark contrast to GRB 080916C, which shows no evidence of "narrowing" with the reducing time bin. This suggests that the Band-function component seen in GRB 080916C is physically different from the MeV component seen in GRB 090902B.

- We tentatively propose that phenomenologically there can be three elemental spectral components (Fig.51), namely, (I): a Band-function component (Band) that extends to a wide spectral regime without "narrowing" with reduced time bins, which is likely of non-thermal origin; (II): a quasi-thermal component (BB) that "narrows" with reducing time bins and that can be reduced to a blackbody (or

multi-color blackbody) function; and (III): a power-law component (PL) that has a positive slope in νF_ν space and extends to very high energy beyond the LAT energy band.

- Component I (Band) is the most common spectral component, which appears in 15 of 17 GRBs. Except GRB 090926A (which may have Component III at late times), all these GRBs have a Band-only spectrum in the time-resolved spectral analysis.

- Component II (BB) shows up in the time-resolved spectral analysis of GRB 090902B and possibly also in GRB 090510. The MeV component of these two GRBs can be fit with a power law with exponential cutoff (CPL). Since data demand the superposition with an additional PL component (Component III), the uncertainty in the spectral index of the PL component makes it possible to have a range of low energy photon indices for the CPL component. In particular, the MeV component of GRB 090902B can be adjusted to be consistent with a blackbody (Plank function). This is not possible for GRB 090510, whose low energy photon index is softer. In any case, the MeV component of GRB 090510 may be consistent with a multi-color blackbody.

- Component III (PL) shows up in both GRB 090902B and the short GRB 090510, and probably in the late epochs of GRB 090926A as well. It has a positive slope in νF_ν, which suggests that most energy in this component is released near or above the high energy end of the LAT energy band.

- With the above three elemental emission components, one may imagine 7 possible spectral combinations. Most ($\sim$ 80%) of GRBs in our sample have the Band-only spectra. GRB 090902B has the BB+PL spectra in the time resolved spectral analyses, and GRB 090510 has a CPL + PL spectra. Both can be considered as the superposition between Components II and III. GRB 090926A may have the superposition between I and III at late epochs. Other combinations are not

identified yet with the current analysis, but some combinations (e.g. I+II, I+II+III) may in principle exist.

- LAT-band emission has a delayed onset with respect to GBM-band emission in some (but not all) GRBs and it usually lasts much longer. In most cases (all except GRBs 090902B and 090510), however, the LAT and GBM photons are consistent with belonging to the same spectral component, suggesting a possible common origin. For bright bursts, the LAT-band activities usually roughly track the GBM-band activities. In the long-term, the LAT and GBM lightcurves sometimes (not always) show different decaying behaviors. The LAT lightcurves continuously decay as a power-law up to hundreds of seconds.

- A statistical study of the spectral parameters in our sample generally confirms the previously found correlations between E_p and luminosity, both globally in the whole sample and individually within each burst. We also discover preliminary rough correlations between α and β (negative correlation) and between flux and α (positive correlation). Both correlations need confirmation from a larger sample.

From these results, we can draw the following physical implications regarding the nature of GRBs.

The Band-only spectra are inconsistent with the simplest fireball photosphere-internal-shock model. This is because if the Band component is non-thermal emission from the internal shock, the expected photosphere emission should be very bright. A natural solution is to invoke a Poynting-flux-dominated flow. An alternative possibility is to interpret the Band component as the photosphere emission itself. However, the following results seem to disfavor such a possibility. (1) In some cases (e.g. GRB 080916C), the Band-only spectrum extends to energies as high as 10s of GeV; (2) The low-energy photon indices in the time-resolved spectra are typically -1, much softer than that expected in the photosphere models; (3) There is no evidence that the Band component is the tem-

poral superposition of thermal-like emission components in the Band-only sample. We therefore suggest that GRB 080916C and probably all Band-only GRBs may correspond to those GRBs whose jet composition is dominated by a Poynting flux rather than a baryonic flux (Zhang & Pe'er 2009; Zhang & Yan 2011).

The existence of a bright photosphere component in GRB 090902B (see also Ryde et al. 2010; Pe'er et al. 2010) suggests that the composition of this GRB is likely a hot fireball without strong magnetization. It is rare, but its existence nonetheless suggests that GRB outflow composition may be diverse. Its associated PL component is hard to interpret, but it may be from the contributions of multiple non-thermal spectral components (Pe'er et al. 2010). The case of GRB 090510 may be similar to GRB 090902B. The low-energy spectral index of the MeV component is too shallow to be consistent with a blackbody, but the high-latitude emission from an instantaneously ejected fireball (which is relevant to short GRBs) would result in a multi-color blackbody due to the angular superposition effect (Pe'er & Ryde 2010).

The delayed onset of GeV emission may be simply due to one of the following two reasons: (1) The particle acceleration condition may be different throughout the burst. Initially, the electron spectral index may be steep initially (so that GeV emission is too faint to be detected), but later it turns to a shallower value so that GeV emission emerges above the detector sensitivity; (2) Initially the ejecta may be more opaque so that there was a pair-production spectral cutoff below the LAT band. This cutoff energy later moves to higher energies to allow LAT photons to be detected. Within this picture, the electron spectral index is similar throughout the burst. There are other models discussed in the literature to attribute GeV emission to a different origin from the MeV component. This is reasonable for GRB 090510 and GRB 090902B, but for most other GRBs this model is contrived since the GeV emission appears as the natural extension of the MeV Band-function to high energies.

The GeV emission during the prompt phase is very likely not of external forward shock origin. This is due to the following facts: (1) In most GRBs the entire *Fermi*-band emission is well fit by a single Band component. The GeV emission is consistent with being the extension of MeV to high energies. (2) During the prompt phase and except for the delayed onset in some GRBs, the LAT-band activities in bright GRBs generally track GBM-band activities. The latter property is relevant even for GRB 090902B which shows clearly two components in the spectra. (3) The peak of GeV lightcurve coincides the second peak of GBM lightcurve for GRB 080916C. A more reasonable possibility is that the GeV emission during the prompt phase has an "internal" origin similar to its MeV counterpart.

The origin of the long lasting GeV afterglow after the prompt emission phase (end of the GBM-band emission) is unclear. If it is from the external forward shock, one needs to introduce abnormal shock parameters, and to argue for coincidence to connect with the internal-origin early GeV emission to form a simple PL decay lightcurve. Alternatively, the long lasting GeV emission can be also of the internal origin. Future joint *Fermi*/*Swift* observations of the early GeV/X-ray afterglows of some bright GRBs will help to differentiate between these possibilities.

The two tentative correlations ($\alpha - \beta$ and α-flux) proposed in this work need to be confirmed with a larger data sample, and their physical implications will be discussed then.

PART IV

GRB CLASSFICATION STUDY

CHAPTER 8

MOTIVATIONS

This chapter is partially based part of the following published paper:
Zhang, B., Zhang, B.-B. et al. 2009, The Astrophysical Journal, 703, 1696.

Statement of coauthorship: This chapter and Chapters 10 & 11 are partially based on the published paper mentioned above. This paper (Zhang, B., Zhang, B.-B. et al. 2009, The Astrophysical Journal, 703, 1696) was led by Bing Zhang. This paper was motivated by my data analysis results on the two high-z GRBs 080913 & 090423 (Fig. 57). I then constructed the burst samples and processed, calculated and collected the data of observation properties (e.g, XRT light curves, T_{90}. E_p, E_{iso} etc.) except for the optical band light curves (which were provided by D. A. Kann, Figure 64). I studied the distribution and correlations between those properties. Based on my results, Bing proposed the classification scheme and the recommended judgment procedure. The physical implications and discussion are also led by Bing.

Phenomenologically, gamma-ray bursts (GRBs) have been generally classified into the long-duration, soft-spectrum class and the short-duration, hard-spectrum class in the CGRO/BATSE era based on the bimodal distribution of GRBs in the duration-hardness diagram (Kouveliotou et al. 1993)[1]. There is no clear boundary line in this diagram to separate the two populations. Traditionally, an observer-frame BATSE-band duration $T_{90} \sim 2$ s has been taken as the separation line: bursts with $T_{90} > 2$s are "long" and bursts with $T_{90} < 2$s are "short".

The journey was long to uncover the physical origins of these two phenomenologically different classes of GRBs. The discoveries and the routine observations of the broad band afterglows of long GRBs reveal that their host galaxies are typically irregular (in

[1]Several analyses have suggested the existence of an intermediate duration group (Mukherjee et al. 1998; Horvath 1998; Hakkila et al. 2000). However, as discussed in the bulk of the text below, there is so far no strong indication of the existence of a third, physically distinct category of cosmological GRBs based on multiple observational data. So we will focus on the two main phenomenological categories of GRBs in this work

a few cases spiral) galaxies with intense star formation (Fruchter et al. 2006). In a handful of cases these GRBs are firmly associated with Type Ib/c supernovae (SNe; e.g., Hjorth et al. 2003; Stanek et al. 2003; Campana et al. 2006a; Pian et al. 2006). This strongly suggests that they are likely related to deaths of massive stars. Theoretically, the "collapsar" model of GRBs has been discussed over the years as the standard scenario for long GRBs (Woosley 1993; Paczynski 1998; MacFadyen & Woosley 1999; Woosley & Bloom 2006)

The breakthrough to understand the nature of some short GRBs was made in 2005 after the launch of the Swift satellite (Gehrels et al. 2004). Prompt localizations and deep afterglow searches for a handful of short GRBs (Gehrels et al. 2005; Bloom et al. 2006; Fox et al. 2005; Villasenor et al. 2005; Hjorth et al. 2005a; Barthelmy et al. 2005b; Berger et al. 2005) suggest that some of them are associated with nearby early-type galaxies with little star formation. Deep searches of associated supernovae from these events all led to non-detections (e.g. Kann et al. 2008 and references thereins). These are in stark contrast to the bursts detected in the pre-Swift era (mostly long-duration). On the other hand, the observations are consistent with (although not a direct proof of) the long-sought progenitor models that invoke mergers of two compact stellar objects, leading candidates being NS-NS and NS-BH systems (Paczynski 1986; Eichler et al. 1989; Paczynski 1991; Narayan et al. 1992). Although the sample with secure host galaxies is small, a general trend in the community is to accept that the BATSE short/hard population bursts are of this compact star merger origin[2]

The clean dichotomy of the two populations (both phenomenological and physical) was soon muddled by the detection of a nearby long-duration GRB without SN association (Gehrels et al. 2006; Gal-Yam et al. 2006; Fynbo et al. 2006; Della Valle et al. 2006a). GRB 060614 has $T_{90} \sim 100$s in the Swift BAT (Barthelmy et al. 2005b) band,

[2]It is widely accepted that at least a fraction of short/hard GRBs are the giant flares of soft gamma-ray repeaters in nearby galaxies (Palmer et al. 2005; Tanvir et al. 2005) The observations suggest that the contribution from such a population is not significant (Nakar et al. 2006), but see Chapman et al. (2009). We do not discuss these bursts in this work.

which phenomenologically definitely belongs to the long duration category. On the other hand, the light curve is characterized by a short/hard spike (with a duration $\sim$ 5 s) followed by a series of soft gamma-ray pulses. The spectral lag at the short/hard spike is negligibly small, a common feature of the short/hard GRBs (Gehrels et al. 2006). Very stringent upper limits on the radiation flux from an underlying SN have been established (Gal-Yam et al. 2006; Fynbo et al. 2006; Della Valle et al. 2006a). These facts are consistent with the compact star merger scenario and suggests that duration and hardness are not necessarily reliable indicators of the *physical* nature of a GRB any more.

The two high-z GRBs, GRB 080913 at $z = 6.7$ (Greiner et al. 2009a) and GRB 090423 at $z = 8.3$ (Tanvir et al. 2009; Salvaterra et al. 2009) introduce a further complication to the scheme associating GRBs with particular theoretical models. Being the two GRBs with the highest redshifts as of the time of writing, these two bursts each have a redshift-corrected duration $[T_{90}/(1+z)]$ shorter than 2 seconds, with a hard spectrum typical for short/hard GRBs. This naturally raises the interesting question regarding the progenitor system of the burst (Greiner et al. 2009a; Perez-Ramirez et al. 2010; Belczynski et al. 2010; Tanvir et al. 2009; Salvaterra et al. 2009) More generally, it again raises the difficult question regarding how to use the observed properties to judge the physical origin of a GRB. More generally, it again raises the difficult question regarding how to use the observed properties to judge the physical origin of a GRB. All the above facts motivate use to make some attempts to address the difficult classification problems.

CHAPTER 9

GRB 060614: SHORT OR LONG ?

This chapter is based on the following published paper :

Zhang, B., Zhang, B.-B., Liang, E.-W., Gehrels, N., Burrows, D. N., & Mészáros, P. 2007, The Astrophysical Journal, 655, L25

Statement of coauthorship: This work is led by Bing Zhang. Bing Zhang provided the motivations and basic ideas of this work. I processed the BAT data of GRB 060614, analyzed the time dependent spectra. Based on the observation results I got, we discussed the possible simulation method. I then simulated a pseudo GRB. The implication on GRB classification is led by Bing Zhang.

Obervation

GRB 060614 poses a great puzzle to the above clean bimodal T_{90} scenario. Being a long GRB (Gehrels et al. 2006) at a low redshift $z = 0.125$ (Price et al. 2006), it is surprising that deep searches of an underlying supernova give null results: the limiting magnitude is hundreds of times fainter than SN 1998bw, and fainter than any Type Ic SN ever observed (Gal-Yam et al. 2006; Fynbo et al. 2006; Della Valle et al. 2006). This raises interesting questions regarding whether this is a collapsar-type event without supernova, or is a more energetic merger event, or belongs to a third class of GRBs (e.g. Gal-Yam et al. 2006). From the prompt emission analysis, GRB 060614 has very small spectral lags (Gehrels et al. 2006), being consistent with the property of typical short GRBs (Yi et al. 2005; Norris & Bonnell 2006). However, based on the duration criterion, this event definitely belongs to the long category ($T_{90} \sim 100$s in the BAT band). One interesting feature is that the lightcurve is composed of a short-hard episode followed by an extended soft emission component with strong spectral evolution. A growing trend in the "short" GRB observations has been that they are not necessarily short, as observed by Swift and HETE-2. For example, the lightcurve of GRB 050709 (Villasenor

et al. 2005) consists of a short-hard pulse with $T_{90} \sim 0.2$s and a long-soft pulse with $T_{90} \sim 130$s. GRB 050724 (Barthelmy et al. 2005b) has a prominent emission lasting for ~ 3s followed by a long, soft, less prominent emission peaking at ~ 100s after the trigger, and XRT observations reveal strong flare-like activities within the first hundreds of seconds. All these raise the issue of how to define a short GRB. The consensus is that multi-dimensional criteria (other than duration and hardness alone) are needed.

We notice that GRB 060614 is more energetic (with an isotropic gamma-ray energy $E_{\rm iso} \sim 8.4 \times 10^{50}$ ergs) than typical short GRBs, such as 050709 ($E_{\rm iso} \sim 2.8 \times 10^{49}$ ergs) and 050724 ($E_{\rm iso} \sim 10^{50}$ ergs), though still much less energetic than typical long GRBs (with $E_{\rm iso}$ typically $\sim 10^{52}$ ergs or higher). This raises the interesting possibility that it might be an energetic version of the short GRBs.

Data Analysis

We first proceed with an analysis of the data of GRB 060614. This burst was detected by *Swift*/BAT on 2006 June 14 at 12:43:48 UT. This is a long, bright burst, with $T_{90} \sim 100$s and the gamma-ray fluence $S_\gamma = 2.17 \pm 0.04 \times 10^{-5}$ ergs cm^{-2} in the 15-150 keV band (Gehrels et al. 2006). We reduce the BAT data using the0 standard BAT tools. The time-integrated spectrum is well fitted by a simple power law ($N \propto E^{-\Gamma}$) with $\Gamma = 1.90 \pm 0.04$ and $\chi^2/dof = 60/56$. A cutoff power law or a broken power law does not improve the fitting. The spectrum shows a strong temporal evolution, with $\Gamma \sim 1.5$ at the beginning and $\Gamma \sim 2.2$ near the end. To clearly display this spectral evolution effect, we split the observed light curves into four energy bands, i.e. 15-25, 25-50, 50-100, 100-350 keV, with a time bin of 64 ms. The results are shown in Fig.54(a)-(d) (see also Gehrels et al. 2006). Since the first peak of the light curves starts at 2 seconds before the trigger, we define t_0 as 2 seconds prior to the trigger time for convenience. All the light curves are highly variable, with three bright, sharp peaks between $t_0 \sim t_0 + 5$s, a gap of emission from $t_0 + 5$s to $t_0 + 10$s, and long, softer extended emission up to

$\sim t_0 + 100$s. By comparing the 4 lightcurves, one can clearly see that the contribution of the soft photons increases with time, indicating a clear hard-to-soft spectral evolution. We perform a detailed time-dependent spectral analysis by dividing the light curve into 9 segments, which roughly correspond to the significant peaks in the light curve. We fit the spectra for each time segment with a simple power law model. The results are shown in Fig.54(e). It is seen that Γ steadily increases with time. The Spearman correlation analysis yields a relation between Γ and $\log t$ as

$$\Gamma = (1.50 \pm 0.07) + (0.38 \pm 0.04) \log t \tag{9.1}$$

at 1σ confidence level, with a correlation coefficient $r = 0.97$, a standard deviation 0.06, and a chance probability $p < 10^{-4}$ for $N = 9$.

Generating a Pseudo Burst from GRB 060614

We want to downgrade GRB 060614 by a factor of ~ 8 to match the isotropic energy of GRB 050724. GRB 050724 has a robust association with an elliptical host galaxy (Barthelmy et al. 2005b; Berger et al. 2005), and hence, is a good candidate for a compact star merger progenitor. It also has well detected early to late X-ray afterglows (Barthelmy et al. 2005b; Campana et al. 2006b; Grupe et al 2006) to be directly compared with our pseudo burst.

One technical difficulty is how to derive the spectral parameters of the pseudo burst when $E_{\rm iso}$ is degraded. The spectra of both long and short GRBs can be fitted by the Band function, a smoothly-joint broken power law function characterized by three parameters: the break energy E_0 and the photon indices Γ_1 and Γ_2 before and after the break, respectively (Band et al. 2003; Preece et al. 2000; Cui et al. 2005). The peak energy of the νf_ν spectrum is $E_p = (2 + \Gamma_1)E_0$. It has been discovered that for long duration GRBs and their soft extension X-ray flashes, most bursts satisfy a rough relation $E_p \propto E_{iso}^{1/2}$ (Amati et al. 2002; Lamb et al 2005; Sakamoto et al. 2006). GRB 060614 is

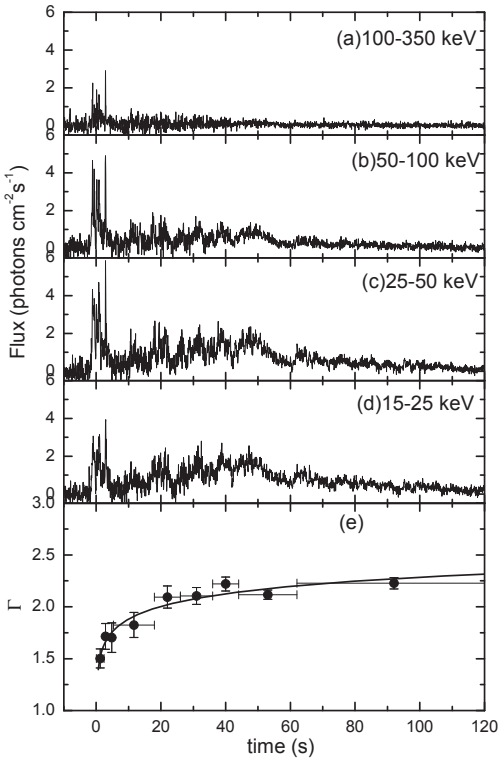

Figure 54 *Panel (a)-(d)*: Light curves of GRB 060614 in different energy bands. *Panel (e)*: Temporal evolution of the photon index.

found to also satisfy the relation (Amati 2006). More intriguingly, within a given burst, a similar relation $E_p \propto L_{\rm iso}^{1/2}$ generally applies (Liang et al. 2004). Such an empirical relation is likely related to the fundamental radiation physics, independent of the progenitors. For example, in the internal shock synchrotron model, such a relation could be roughly reproduced if the Lorentz factors of various bursts do not vary significantly (e.g. Zhang & Mészáros 2002b). Alternatively, a general positive dependence of E_p on $E_{\rm iso}$ is expected if E_p reflects the thermal peak of the fireball photosphere (Mészáros et al. 2002; Rees & Mészáros 2005; Ryde et al. 2006; Thompson et al. 2006). We therefore assume the validity of the Amati-relation to generate the pseudo burst: to generate a pseudo burst with $E_{\rm iso} \sim 8$ times smaller, the time-dependent E_p's of the pseodo burst are systematically degraded by a factor of ~ 3.

A challenging task is to determine E_p for each time segment. The BAT is a narrow band (15-150 keV) instrument, and usually it is difficult to constrain E_p directly from the Band-function spectral fit. About 80% of the GRB spectra observed by BAT can be only fitted by a simple power law. In deriving GRB radiative efficiency of a sample of Swift bursts, we developed a method to derive E_p by combining spectral fits and the information of the hardness ratio (Zhang et al. 2007). The derived E_p's are generally consistent with the joint spectral fits for those bursts co-detected by BAT and Konus-Wind, suggesting that the method is valid. Using the sample of Zhang et al. (2007), we find that the simple power law index Γ is well correlated with E_p (Fig. 55). The Spearman correlation analysis gives

$$\log E_p = (2.76 \pm 0.07) - (3.61 \pm 0.26) \log \Gamma \tag{9.2}$$

at 1σ confidence level, with a correlation coefficient 0.94, a standard deviation 0.17, and a chance probability $p < 10^{-4}$ for $N = 27$. Sakamoto et al. (2008) independently derived a similar relationship using the E_p data of those GRBs simultaneously detected by Swift and Konus-Wind. In Figure 55, we have also plotted the bursts with E_p measured with

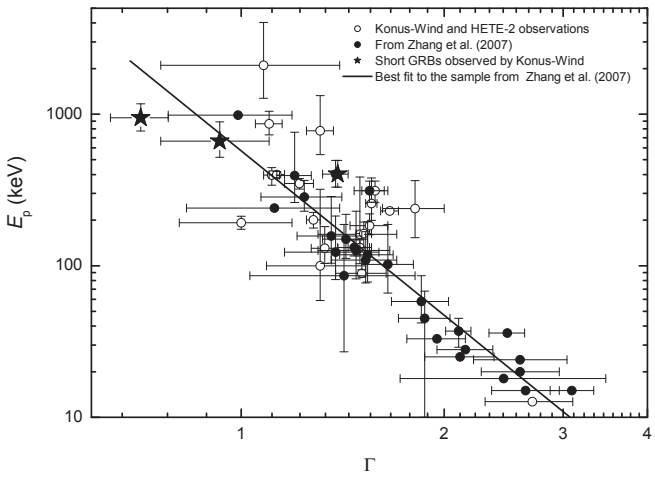

Figure 55 E_p as a function of the photon index Γ in a simple power law model for the sample of GRB presented in Zhang et al. (2007). The measured E_p data from Konus-Wind and HETE-2, including both long (open circles) and short (stars) bursts, are also plotted.

Konus-Wind and HETE-2. They are generally consistent with the correlation (Eq. 9.2). This empirical relation is adopted in our generation of the pseudo burst.

Our procedure is the following. (1) Using the $E_p - \Gamma$ relation (eq.9.2) we estimate E_p as a function of time for GRB 060614; (2) Using the Amati-relation, we derive E_p as a function of time for the pseudo burst, i.e. $E_p^{\rm pseudo} = E_p^{060614}(E_{\rm iso}^{\rm pseudo}/E_{\rm iso}^{060614})^{1/2} = E_p^{060614}(E_{\rm iso}^{050724}/E_{\rm iso}^{060614})^{1/2}$; (3) Assuming photon indices $\Gamma_1 = 1$ and $\Gamma_2 = 2.3$ for the Band-function[1] and keeping the same normalization of the Band function, we calculate the counts in the BAT and XRT bands as a function of time and make the light curves in the BAT and XRT bands with this spectrum. (4) We generate a white noise similar to that of GRB 050724; (5) We adjust the amplitude of the lightcurve in the BAT band to ensure that the gamma-ray fluence above the noise level of the pseudo GRB

[1]Based on the statistics for a large sample of GRB, it is found that $\Gamma_1 \sim 1$ and $\Gamma_2 \sim 2.3$ (Preece et al. 2000). The typical Γ_1 value for a small sample of short GRBs is 0.7. Taking $\Gamma_1 = 1$ or 0.7 does not change our simulation results significantly.

in the BAT band is the same as that of GRB 050724[2]. (6) Using the time-dependent spectral parameters, we extrapolate the BAT lightcurve to the XRT band. We also process the XRT data of GRB 060614, which has a steep decay component following the prompt emission. We adjust the XRT lightcurve to match the tail of the pseudo burst (blue lightcurve in Fig. 56), as has been the case for the majority of Swift bursts (e.g. Tagliaferri et al. 2005; Barthelmy et al. 2005b; Nousek et al. 2006; Zhang et al. 2006; O'Brien et al. 2006; Liang et al. 2006).

The simulated light curves (red) are shown in Fig. 56 as compared with the observed lightcurves of GRB 050724. Very encouraging results are obtained. The BAT-band lightcurve of the pseudo burst is characterized by short, hard spikes (with $E_p \sim 150$ keV at first 2 seconds) followed by very weak and faint emission episodes at later times. The softer components merge with the background. We estimate $T_{90} \sim 53$ s in the BAT band. By extrapolating the lightcurve to the BATSE band (inset of Fig. 56a) and by using the BATSE threshold (0.424 cts cm^{-2} s^{-1}), one gets $T_{90} \sim 4.4$ s. This number marginally places the psuedo burst in the short category, All the previous soft spikes in the BAT band of GRB 060614 are now moved to the XRT band to act as erratic X-ray flares (e.g. Burrows et al. 2005b), which are also present in GRB 050724 (Barthelmy et al. 2005b). It is clear that the pseudo burst is very similar to GRB 050724.

Implicaiton on GRB Classification and Discussion

We have "made" a marginally short hard GRB from the long GRB 060614[3]. The only assumption made is the validity of the $E_p \propto E_{\rm iso}^{1/2}$ relation, which is likely related to the radiation physics only. The results suggest that had GRB 060614 been less energetic (say, as energetic as the more typical short GRB 050724), it would also have been detected

[2]Assuming the same redshift as GRB 050724, this would make $E_{\rm iso}^{\rm pseudo}$ very close to $E_{\rm iso}^{050724}$. A slight difference is expected due to different spectral parameters of the two bursts, but this correction effect would not affect the general conclusion.

[3]Without introducing the Amati-relation, a previous attempt to change long bursts to short ones (Nakar & Piran 2002) led to negative results.

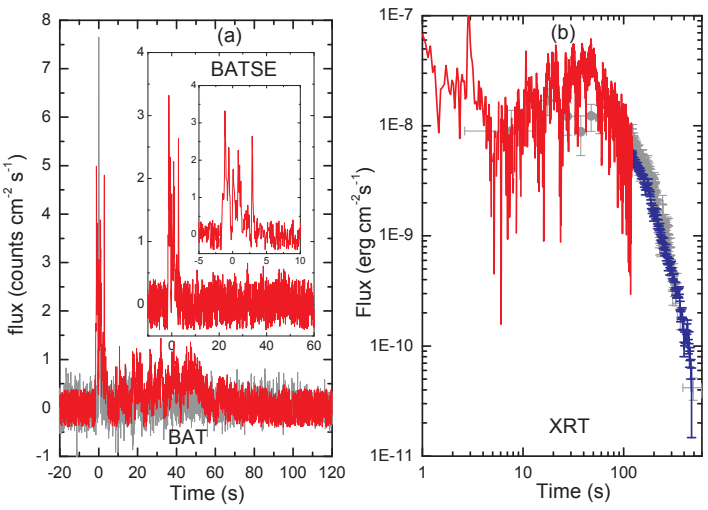

Figure 56 The simulated gamma-ray and X-ray lightcurves of the pseudo burst (red) as compared with those of GRB 050724 (grey). *Panel (a)*: The gamma-ray lightcurves in the BAT (main panel) and BATSE (inset) bands. The zero-level horizontal lines denote the detector thresholds. The innermost inset zooms in on the detail of the short-hard spikes as observed by BATSE. *Panel (b)*: Light curves of the soft extension extrapolated to the XRT band. The blue curve is the XRT lightcurve of GRB 060614, re-scaled to match that of the pseudo burst.

.

as a marginal short GRB by BATSE. Along with the facts that GRB 060614 has very small spectral lags (Gehrels et al. 2006) and that there is no supernova association (Gal-Yam et al. 2006; Fynbo et al. 2006; Della Valle et al. 2006), our finding strengthens the hypothesis that GRB 060614 is a more energetic version of the previously-defined short-hard class of bursts. The lower-than-normal star-forming rate of the host galaxy and its large offset from the bright UV regions (Gal-Yam et al. 2006) is also consistent with such a picture.

By making such a connection, the traditional long-soft vs. short-hard GRB classification dichotomy based primarily on burst duration seems to break down. The total duration of GRB 060614 is far longer than the traditional 2 s separation point based on the bimodal distribution of the BATSE bursts (Kouveliotou et al. 1993), or even the 5 s point identified by Donaghy et al. (2006). Yet, given the evidence cited above, it seems entirely likely that there is no fundamental distinction between GRB 060614 and the other short-hard bursts *except* for the duration. We therefore suggest that the time has come to abandon the terms "short" and "long" in describing GRB classes. Instead, by analogy to supernova classification, we suggest the alternative classes of Type I and Type II GRBs. Type I GRBs are associated with old stellar populations (similar to Type Ia SNe) and the likeliest candidates are compact star mergers. Observationally, Type I GRBs are usually short and relatively hard, but are likely to have softer extended emission tails. They have small spectral lags and low luminosities, falling in a distinct portion of a lag-luminosity plot (Gehrels et al. 2006). They have no associated SNe and can be associated with either early or late type galaxies, but typically are found in regions of low star formation. Type II GRBs are associated with young stellar populations and are likely produced by core collapses of massive stars (similar to Type II and Ib/c SNe). Observationally, they are usually long and relatively soft. They are associated with star forming regions in (usually) irregular galaxies and with SN explosions. According to this classification, we suggest that GRB 060614 is a Type I GRB. It has been noted that a

sample of BATSE and Konus-Wind bursts have properties similar to GRB 060614, and we suggest that they belong to Type I as well. A direct prediction of such a scenario is that *some 060614-like GRBs will be detected in elliptical galaxies in the future.*

The association of GRB 060614 with Type I GRBs exacerbates the problem of how to make extended emission from a merger-type GRB, which arose when extended X-ray flares were detected following GRB 050724. Barthelmy et al. (2005a) and Faber et al. (2006) suggest NS-BH mergers as the possible progenitor to extend the accretion episodes. Dai et al. (2006) argued that the final product of a NS-NS merger may be a heavy, differentially-rotating NS, whose post-merger magnetic activity would give rise to flares following the merger events. Rosswog (2007) suggest that some debris may be launched during the merger process, which would fall back later to power flares at late times. Alternatively, disk fragmentation (Perna et al. 2006) or magnetic field barrier near the accretor (Proga & Zhang 2006) would induce intermittent accretion that power the flares. Finally, King et al. (2007) suggest a WD-NS merger to interpret Type I GRBs (cf. Nayaran et al. 2001). More detailed numerical simulations are needed to verify these suggestions.

CHAPTER 10

IMPLICATIONS FROM GRB 080913 AND GRB 090423

This chapter is based part of the following published paper:

Zhang, B., Zhang, B.-B. et al. 2009, The Astrophysical Journal, 703, 1696.

Statement of coauthorship: see Chapter 8.

The light curve of GRB 080913 as detected by Swift/BAT is shown as the black solid curve in Fig.57a. The burst duration T_{90} (the time interval during which 90% of the fluence is measured) in the BAT (15-150 keV) band is 8 ± 1 s. The average BAT band spectrum can be adequately fit by a power law with exponential cutoff, with the peak energy $E_p = 93 \pm 56$ keV (Greiner et al. 2009a). A combined Swift/BAT and Konus/Wind (20-1300 keV) fit using the Band-function spectrum gives $E_p = 121^{+232}_{-39}$ keV (Palshin et al. 2008). Given the measured redshift $z = 6.7$ (Greiner et al. 2009a), this is translated to a rest frame duration of $T_{90}^{rest} \sim 1$ s, and a best-fit rest frame peak energy $E_p^{rest} \sim 710$ keV and $E_p^{rest} \sim 930$ keV for the cutoff power law and Band-function spectra, respectively. Although being recognized as a long duration burst phenomenologically, this burst has an intrinsically short duration and an intrinsically hard spectrum.

In order to compare this burst with other phenomenologically classified short hard GRBs, we simulate a "pseudo" GRB by placing GRB 080913 at $z = 1$. We consider three factors. First, the specific photon flux $N(E_p)$ at E_p is proportional to $(1+z)^2/D_L^2$, where D_L is the luminosity distance. This can be translated to an increase of a factor of ~ 6.8 of $N(E_p)$ from $z = 6.7$ to $z = 1$. Second, we consider the BAT band (15-150 keV) emission of the pseudo GRB, which corresponds to an energy band lower by a factor of $(1+6.7)/(1+1) \sim 3.85$ in GRB 080913. We therefore extrapolate the observed BAT spectrum to lower energies and assume a similar light curve in that band. Third, we compress the time scale by a factor of ~ 3.85 to account for the cosmological time dilation effect. After applying these transformations, we are able to construct the BAT-band light curve of the pseudo GRB at $z = 1$ as shown in Fig.57a.

GRB 080913 displays a series of early X-ray flares (Greiner et al. 2009a). It is interesting to check whether they would show up in the BAT band for the pseudo GRB to mimic the "extended emission" seen in a subgroup of Swift "short/hard" GRBs (Norris & Bonnell 2006; Troja et al. 2008)[1]. We therefore manipulate the XRT (Burrows et al. 2005b) data of GRB 080913 to simulate the BAT band extended emission of the pseudo burst. We first extrapolate the GRB 080913 XRT data to the BAT band according to the measured XRT photon spectral index. We then follow the three steps mentioned above to shift this BAT-band "virtual" emission to the BAT band emission of the pseudo burst. This is shown as blue data points in Fig.57a. By adding the appropriate noise level for the BAT observation, we show that these extrapolated XRT emission components stick out the background, which would appear as the extended emission in the BAT band for the pseudo burst. We note that our method is based on the assumption of the power law extension of the X-ray flare spectrum ($0.3-10$ keV) to the BAT band of the pseudo burst ($1.3-39$ keV). On the other hand, since X-ray flares are generally believed to be due to GRB late central engine activities (Burrows et al. 2005a; Zhang et al. 2006; Lazzati Perna 2007; Chincarini et al. 2007), they may have a Band-function or cutoff power law spectrum (Falcone et al. 2007). If the E_p's of the X-ray flares are within or not far above the XRT window, the extrapolated extended emission would be degraded. We should therefore regard the level of the extended emission of the pseudo burst as an upper limit. We estimate the BAT-band duration of the pseudo GRB as $T_{90}(\mathrm{pseudo}) \sim 2.0$ s without extended emission or $T_{90}(\mathrm{pseudo, EE}) \sim 140$ s with extended emission. In any case, the observational properties of this pseudo burst are very similar to some "short/hard" GRBs detected in the Swift era. By comparing the flux level of the pseudo GRB with other short/hard GRBs, we find that it belongs to the bright end of the short/hard GRB flux

[1]Rigorously based on the T_{90} criterion, the fraction of Swift bursts that have $T_{90} < 2$ s is much smaller than that of BATSE bursts. Many display extended emission that extends T_{90} up to several 10s to even more than 100 seconds. The current approach in the community is to define a burst "short/hard" if it appears short in the BATSE band. A growing trend is to also include some bursts with extended emission even in the BATSE band to the "short/hard" category.

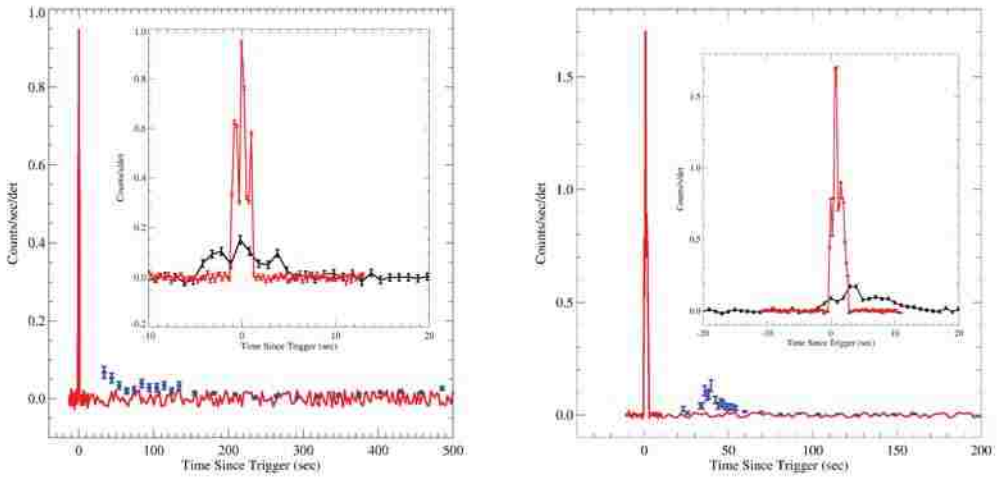

Figure 57 The simulated 15-150 keV light curves of the pseudo GRBs obtained by placing GRB 080913 and GRB 090423 at $z = 1$. The red curves display the extrapolated BAT data, and the blue data points show the extrapolated XRT data. Inset: a comparison of the light curve of the pseudo GRBs (red) and the observed GRBs (black). (a) GRB 080913; (b) GRB 090423.

distribution, similar to, e.g. GRB 051221A (Burrows et al. 2006; Soderberg et al. 2006), GRB 060313 (Roming et al. 2006), GRB 060121 (Donaghy et al. 2006), and the recent GRB 090510 detected by Fermi LAT/GBM and Swift (Hoversten et al. 2009; Ohno et al. 2009; Guiriec et al. 2009; Rau et al. 2009).

GRB 090423 at $z = 8.3$ is amazingly similar to GRB 080913. It was detected by Swift/BAT with a BAT-band $T_{90} \sim 10.3$ s (Tanvir et al. 2009). Given the measured redshift $z = 8.26^{+0.07}_{-0.08}$, the corresponding rest-frame duration is $\sim T_{90}/(1+z) \sim 1.1$ s. The peak energy measured by BAT is $E_p = 48.6 \pm 6.2$ keV, corresponding to a rest-frame value $E_p^{rest} = 451 \pm 58$ keV. We performed a similar analysis on GRB 080913. The results are shown in Fig.57b. Nearly identical conclusions can be drawn from both bursts.

In the above analyses, the intrinsic duration of a burst is defined as $T_{90}/(1+z)$, and the duration of the corresponding pseuodo GRB at $z = 1$ is defined as $2T_{90}/(1+z)$. These calculated durations correspond to different energy bands in the rest frame (the same observed band after redshifting). Strictly speaking, in order to derive the durations of the pseudo GRBs in the observed energy band, one needs to know the time-dependent

spectral information, which is not available for these bursts. Observationally, pulse widths at high energies tend to be narrower than those at low energies (Ford et al. 1995; Romano et al. 2006; Page et al. 2007). An empirical relation $w \propto E^{-a}$ with $a \sim 0.3$ has been suggested (Fenimore et al. 1995; Norris et al. 2005; Liang et al. 2006b). For a given observed energy band, this suggests $w \propto (1+z)^{-a}$, which would correspond to a correction factor of $(1+z)^{a-1}$ rather than $(1+z)^{-1}$ to derive the intrinsic duration. However, GRB prompt emission is usually composed of multiple pulses. The separations between the pulses, which are more relevant for the T_{90} definition, may not follow the same energy-dependence of the pulse widths. We therefore do not introduce this extra correction factor of T_{90} throughout the work. For GRB 080913 and GRB 090423, if one takes the $(1+z)^{a-1}$ correction factor, the derived intrinsic durations are in the marginal regime between the phenomenologically-defined long and short GRBs.

Figure 58 displays the locations of GRB 080913, GRB 090423, their corresponding pseudo GRBs at $z = 1$, and their rest-frame counterparts in the traditional $T_{90}-$HR (hardness ratio) two-dimensional distribution plane. Also plotted are the BATSE GRB sample (orange), the Gold samples of Type II (blue) and Type I (red) GRBs, and the Other SGRB Sample (green) (see Chapter 11 for the details of the sample definitions). It is evident that GRB 080913 and GRB 090423 would have been recognized as phenomenologically short/hard GRBs should they have occurred at $z \leq 1$.

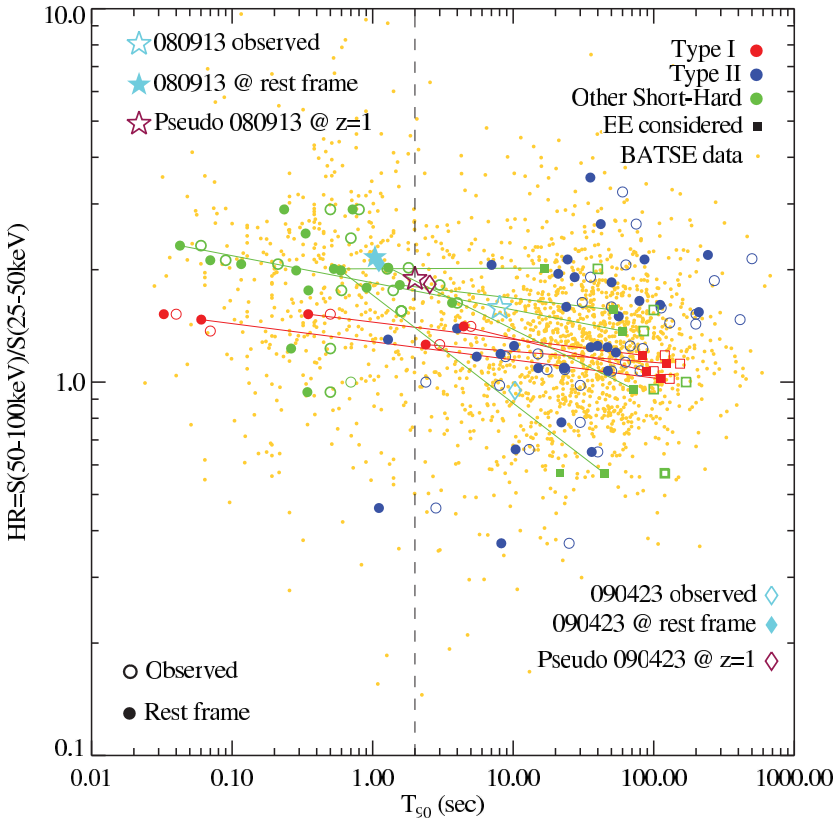

Figure 58 The T_{90} – HR diagram of GRBs. The background orange dots are BATSE GRBs. Overplotted are Type II Gold Sample (blue), Type I Gold Sample (red), and other short/hard GRBs (green), mostly detected by Swift. Open symbols are for the observed values, while the filled symbols are the rest-frame values. For short GRBs with extended emission, those with the short spike only are denoted as circles, while those including the extended emission are denoted as squares. The same bursts (with different T_{90} with or without extended emission) are connected by lines. GRB 080913, GRB 090423, their pseudo counterparts at $z = 1$, and their rest-frame counterparts are marked with special colors/symbols.

CHAPTER 11

A PHYSICAL VIEW OF GRB CLASSIFICATION

This chapter is based part of the following published paper:

Zhang, B., Zhang, B.-B. et al. 2009, The Astrophysical Journal, 703, 1696.

Statement of coauthorship: see Chapter 8.

Phenomenological vs. Physical Classification Schemes: Weaknesses and Strengths

The eventual goal of GRB studies is to identify the physical origins of every observed GRB, including its progenitor system, central engine, energy dissipation mechanism, and radiation mechanism. To achieve this goal, a combination of observations and theoretical modeling is needed. The number of competitive models and the allowed parameter space steadily reduce as more and more observational data are accumulated. This is evident in the history of GRB studies: while more than 100 models were proposed before 1992 (Nemiroff 1994), only two broad categories of progenitor models remain competitive at the time. A group of GRBs are hosted by active star-forming dwarf galaxies (Fruchter et al. 2006), some of which have clear (Type Ic) SN associations (Hjorth et al. 2003; Stanek et al. 2003; Campana et al. 2006b; Pian et al. 2006). This points toward a massive star origin of this group of bursts. At least a few bursts were discovered to be associated with galaxies with a very low star-forming rate (SFR; Gehrels et al. 2005; Bloom et al. 2006; Barthelmy et al. 2005b; Berger et al. 2005b), which point toward a non-massive-star origin of the bursts, likely due to mergers of compact objects. Therefore it is now justified to discuss at least two physically distinct categories of GRB models as well as how to associate a particular burst with either category based on certain observational criteria.

In the literature, some physical classification schemes of GRBs have been discussed (Zhang et al. 2007b; Bloom et al. 2008). Strictly speaking, these are not classifications of GRBs, but are classifications of models that interpret GRB data. A scientific classification scheme is based on statistical formalisms, which make use of a uniform set of

observational data with instrumental biases properly corrected, and classify objects based on statistically significant clustering of some measured properties. Examples include to classify SNe broadly into Type II/I based on whether there are/are not hydrogen lines in the optical spectrum, and to classify GRBs into two (Kouveliotou et al. 1993) or three (Mukherjee et al. 1998; Horvath 1998) classes based on BATSE T_{90} analyses. The classes defined by the phenomenological data do not carry physical meanings, and theoretical modeling is needed to clarify whether different phenomenological classes of objects are of different physical origins. Compared with the SN classification schemes, which are based on the "yes/no" criteria regarding the existence of spectral lines and therefore are relatively insensitive to the instrumental details, the GRB phenomenological classification schemes suffer another major drawback, i.e., every parameter that one can directly measure is strongly instrument dependent. For example, T_{90} is strongly energy dependent, and sensitivity dependent, so that a "short" GRB in a hard energy band would become a "long" GRB in softer bands or if the detector sensitivity is increased. The membership of a particular GRB to a particular category (e.g., long versus short) is not guaranteed. As a result, such classification schemes cannot be compared from one mission to another, and are of limited scientific value.

A physical classification scheme, on the other hand, is on theoretical models that interpret the data. As a result, it suffers the great difficulty of associating a particular burst to a particular model category. In order to achieve the goal, multiple observational criteria are demanded, but always with non-uniform instrumental selection effects. Ideally, with infinitely sensitive detectors in all wavelengths, it may be possible to derive a set of quantitative observational criteria that can be used to rigorously associate a particular GRB to a particular model category based on statistical properties. However, realistically this is essentially impossible since different criteria rely on completely different observational instruments with different observational bands and sensitivities which are quite non-uniform. Also different criteria could carry different weights in judging the

associated model category of a particular burst. The weighting factors of different criteria are also difficult to quantify. Human insights rather than pure statistical analyses are needed. Another drawback of a physical classification scheme is that it depends on the models, which are subject to further development as more data are accumulated. The classification criteria are therefore also subject to modification based on data. This can be diminished by invoking model-independent criteria as much as possible. For example, the Type I/II GRB model classification scheme discussed in this work only appeals to whether the model invokes a degenerate-star or a massive-star, regardless of the concrete progenitor systems or energy dissipation and radiation mechanisms.

Despite of its weaknesses, a physical classification scheme of models and associating a particular object to a particular model class has the strength to achieve a better understanding of the physical origin of astrophysical objects. For example, in the supernova field, there is now a consensus that only a sub-group of Type I SNe (Type Ia) has a distinct physical origin, which is related to explosive disruptions of white dwarfs. The other two sub-types of Type I SNe (Type Ib/Ic) are more closely related to Type II SNe and form together a broad physical category of SN models that invoke massive star core collapses. Such a physical classification scheme of SN models (massive star origin vs. white dwarf origin) and the efforts to associate the observed SNe to them reflect a deeper understanding of the physical origins of SNe. The same applies to GRBs. The statistical classification of long-, short- and probably intermediate-duration GRBs has been established in the BATSE era. However, it took several missions and many years of broad-band observations to reveal that there are at least two physically distinct types of models that are associated with these GRBs. Although data are not abundant enough to unambiguously associate every individual GRB to these model categories, current data already revealed some perplexing observational facts that demand more serious investigations of the observational criteria to judge the physical origin of a particular GRB (i.e. the physical model associated with this GRB).

In the rest of the chapter, we will discuss Type I/II GRBs, which are defined as the GRBs that are associated with two distinct physical models. This is not a new classification scheme of GRBs to replace the existing long/soft vs. short/hard classification scheme, but is a parallel classification of the models that the observed GRBs can be associated with based on multiple criteria data analyses. The two approaches are complementary. As discussed above, T_{90} is energy-band-dependent and sensitivity-dependent, so that the membership of a particular GRB to a particular duration category is not always guaranteed. On the other hand, if adequate information is retrieved in an ideal observational campaign, the association membership of a particular GRB to a particular physical model category is almost certain regardless of the detector energy band and sensitivity. For example, if a SN is detected to be associated with a GRB, one can safely associate this GRB to the Type II model category regardless of its T_{90} detected by different detectors.

Type I/II GRBs: A More Physical Classification

Definition

We reiterate here the definitions of the Type I/II GRBs. Improving upon the descriptions presented in Chapter 9, we hereby more rigorously define the following:

- Type I GRBs (or compact star GRBs) are those GRBs that are associated with the theoretical models invoking destructive explosions in old-population, degenerate, compact stars. The likeliest model candidate is mergers of two compact stars.

- Type II GRBs (or massive star GRBs) are those GRBs that are associated with the theoretical models invoking destructive explosions in young-population massive stars. The likeliest model candidate is core collapses of massive stars.

Here we do not specify the progenitor systems of each model type. In reality, there could be multiple possible progenitor systems within each model category (see also Bloom

et al. 2008). Within the Type I model category, possible progenitor systems include NS-NS mergers (Paczynski 1986; Eichler et al. 1989; Narayan et al. 1992; Rosswog et al. 2003), NS-BH mergers (Paczynski 1991; Faber et al. 2006), and possibly Black Hole-White Dwarf (BH-WD) or Neutron Star-White Dwarf (NS-WD) mergers (Fryer et al. 1999; King et al. 2007) (cf. Narayan et al. 2001), see Nakar (2007); Lee & Ramirez-Ruiz (2007) for reviews. On the other hand, within the Type II model category, one may have collapses of single stars (i.e., collapsars; Woosley 1993; MacFadyen & Woosley 1999), or collapses of massive stars in binary systems (Fryer et al. 2007).

The definitions of Type I/II GRBs are based on the physical models that GRBs can be associated with rather than their observational properties. The scheme is therefore intended to be "operational". The connections between the physical model properties and the observational criteria

How to Associate a Burst with a Physical Model Category?

It is not always easy to associate a particular GRB to a particular physical model category based on observational criteria. We propose to use multiple observational criteria, which are summarized in Table 14. This is an extension of Figure 2 of Zhang (2006). A new column lays out the issues of each criterion. The criteria are sorted by relevant observations. The first six rows (duration, spectrum, spectral lag, $E_{\gamma,iso}$, $E_p - E_{\gamma,iso}$ relation, and $L^p_{\gamma,iso}$-lag relation, are based on the gamma-ray properties only. The next five rows (supernova association, circumburst medium type, $E_{K,iso}$, jet opening angle, and the geometrically corrected energies E_γ and E_K), are based on follow-up broadband observations and afterglow modeling. The next three rows (host galaxy type, specific star forming rate of the host galaxy, and offset of the GRB from the host galaxy) are based on observations of the host galaxies. The next two rows (redshift distribution and luminosity function) are statistical properties. The final row is the gravitational wave criterion. In general, most of these criteria are not "conclusive", i.e., one cannot draw a

firm conclusion based on a single criterion. Nonetheless, there are several criteria which, if satisfied, would unambiguously associate a GRB to a certain physical model category. These are marked in bold in Table 14. In particular, if a GRB is found in an elliptical or an early type galaxy, or if the SSFR of its host galaxy is very low, one would be able to associate it with Type I. On the other hand, a SN association or the identification of a wind-type medium in a GRB would establish its association with Type II.

Table 14 Observational criteria for physically classifying GRBs.

Criterion	Type I	Type II	Issues
Duration	Usually short, but can have extended emission.	Long without short/hard spike, can be shorter than 1s in rest frame.	No clear separation line.
Spectrum	Usually hard (soft tail)	Usually soft	Large dispersion, overlapping
Spectral Lag	Usually short	Usually long, can be short.	Related to variability time scale
$E_{\gamma,iso}$	Low (on average)	High (on average)	Wide distribution in both, overlapping
$E_p - E_{\gamma,iso}$	Usually off the track.	Usually on the track.	Some Type II off the track.
$L^p_{\gamma,iso}$−lag	Usually off the track.	Usually on the track.	Some Type II off the track.
SN association	No.	**Yes.**	Some Type II may be genuinely SNless.
Medium type	Low-n ISM.	**Wind** or High-n ISM.	Large scatter of n distribution.
$E_{K,iso}$	Low (on average)	High (on average)	Large dispersion, overlapping
Jet angle	Wide (on average)	Narrow (on average)	Difficult to identify jet breaks
E_γ and E_K	Low (on average)	High (on average)	Type I BH-NS BZ model $\sim$ Type II.
Host galaxy type	**Elliptical, early** and late	Late	Deep spectroscopy needed.
SSFR	**Low** or high	High (exception GRB 070125)	overlapping
Offset	Outskirt or outside	Well inside	How to claim association if outside?
z-distribution	Low average z	High average z	overlapping
L-function	Unknown	Broken power law, 2-component	overlapping
GW signals	Precisely modeled	Unknown	No data yet

Unfortunately, the above four criteria are usually not satisfied for most GRBs. One is then obliged to use multiple criteria since there are overlapping predicted properties between the two physical model types for each individual criterion. In Fig.59 we cautiously propose an operational procedure to discern the physical origin of a GRB based on the available data.

There are five outcomes in the flowchart. Besides the solid Type I/II identifications, we also define Type I/II "candidates" and the "unknown" category. The Type I/II candidates refer to those with evidence of associating a burst to a particular physical model category, but the evidence is not strong enough to make a firm claim. The unknown category includes the oddball GRBs that do not obviously fit into any criteria discussed in this paper, or the observational data are not adequate for us to make the judgement. They may be associated with Type I, Type II or a completely new type of models. Some qualitative rather than quantitative criteria have been used (e.g. high/low SSFR, large offset, large/small E_γ, E_K). The reason is that it is very difficult to adopt quantitative criteria at the current stage, since the distributions of these quantities predicted by both physical model types and displayed in the statistical analyses of the Type I/II Gold Samples are continuous, without sharp transitions. The "high/low" and "large/small" definitions are based on the statistical properties, and therefore in the relative sense. If confusion occurs (e.g. the quantity is near the boundary and not easy to judge whether it is high/low, large/small, one can follow the "?" sign to go down the flowchart. The flowchart is reasonably operational, i.e. essentially every GRB with reasonable afterglow follow up observations can find a destiny in the chart. For example, the SN-less long-duration GRB 060614 (Gehrels et al. 2006; Gal-Yam et al. 2006; Fynbo et al. 2006; Della Valle et al. 2006a) is associated with Type I (based on low SSFR), and the other SN-less GRB 060505 (Fynbo et al. 2006; Ofek et al. 2007; McBreen et al. 2008) can be associated with a Type I candidate based on its small energetics, or an "unknown" burst if one argues that the $L^p_{\gamma,iso}-$lag relation is satisfied for this burst (McBreen et al.

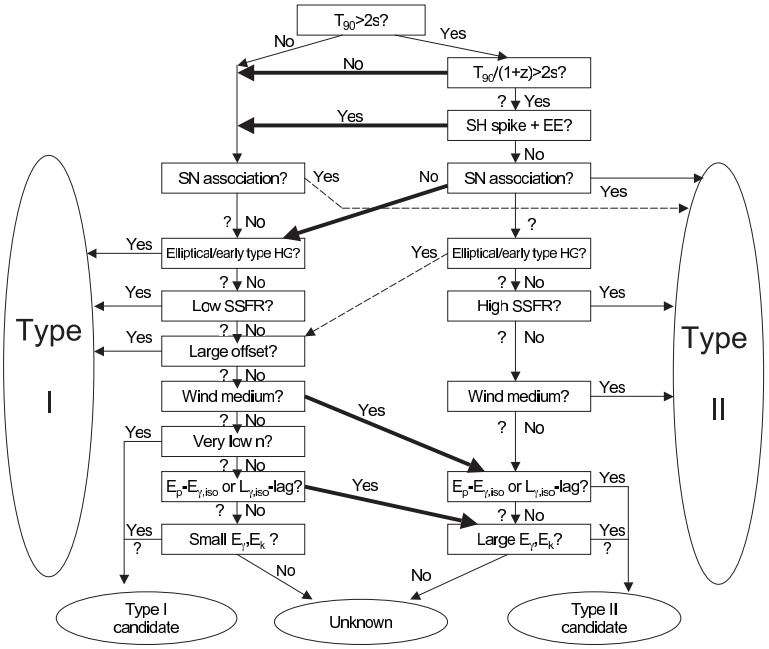

Figure 59 A recommended procedure to judge the association of a particular GRB to a particular physical model category. Multiple observational criteria have been applied. Question marks stand for no information being available to judge the validity of the criterion. The two dotted arrows stand for the possibilities that are in principle possible but have never been observed. Five thick arrows bridge the long-duration and short-duration GRBs, suggesting that the there can be long duration Type I and short duration Type II GRBs.

2008) GRB 080913 and GRB 090423 find their homes as Type II candidates based on the $E_p - E_{\gamma,iso}$ correlation. GRB 060121 (a high-z short GRB) satisfying the $E_p - E_{\gamma,iso}$ is also found to be associated with the "Type II candidate" outcome in the flowchart. It is possible that the procedure and the criteria may be further revised as more data are accumulated. The current procedure only reflects the best knowledge for the time being.

In the flowchart, there are five thick arrows that bridge the short-duration and long-duration GRBs. This suggests that the duration information sometimes is misleading. Some long duration GRBs can be associated with Type I (e.g. GRB 060614 and probably GRB 080503, Peyley et al. 2008), and some short duration GRBs can be associated with Type II (e.g. GRB 060121, GRB 080913 and GRB 090423). We also present two dashed arrows in the flowchart. These two tracks (a short GRB associated with a SN and a long GRB with an elliptical/early type host galaxy) are in principle possible, but such bursts have never been observed so far[1]. The order of the criteria in Fig.8 is based on the "definiteness" of the criteria, with the higher-level ones carrying more weight than the lower-level ones. Notice that "hardness" is generally not regarded as a definitive criterion in the flowchart (except for the relative hardness of the short spike and the extended emission).

Type I And Type II Samples and their Statistical Properties

Sample Selection

We define the following three samples based on the criteria detailed below.

Type II Gold Sample. This sample is defined such that at least one of the following two criteria are satisified.

1. There is a spectrally confirmed SN association with the GRB;

2. The specific star forming rate (SSFR) is very high (to be specific, the SSFR satisfies

[1]The GRB field is full of surprises. If some short/hard GRBs are indeed associated with Type II as argued in this paper, one may someday discover a SN associated with a short/hard GRB. We encourage continuous SN searches for all nearby GRBs, both long and short.

$\log \mathrm{SSFR} > -0.2$ or SSFR> 0.63 Gyr^{-1} in the sample of Savaglio et al. 2009); the GRB location does not have a large offset from the center; and there is no stringent upper limit on the existence of a SN associated with the GRB.

Notice that the GRB properties (duration, hardness and lag) are not the considerations to define the sample. Since not many GRBs have host SSFR information published, this sample is by no means complete, and there should be many more Type II GRBs that are not included. The purpose of selecting this sample is to use the most stringent criteria to investigate how the best Type II GRB candidates look like. As a result, we do not include the GRBs that have a claimed SN bump in the optical light curve but no confirmed SN spectroscopic signature. The threshold of SSFR is arbitrary. This limiting value was chosen because Table 11 of Savaglio et al. 2009 has a mix of long and short GRBs for $\log \mathrm{SSFR(Gpc^{-1}}) < -0.3$, which is the regime where confusion arises. The lower bound $\log \mathrm{SSFR} > -0.2$ can be regarded as a safe line above which GRB hosts have very active star formation. One exception is the short duration GRB 051221A (Soderberg et al. 2006; Burrows et al. 2006). The SSFR value ($\log \mathrm{SSFR} > 0.804$) is way above the threshold. However, since deep searches have ruled out the association of a 1998bw-like SN (Soderberg et al. 2006), we do not include it in the Type II sample, and will include it in the "Other short hard sample". We note that many Swift long GRBs should be associated with Type II. However, since no published SSFRs are available for most of them, we refrain from including them in the Type II Gold Sample. This sample should be expanded significantly later when the host galaxy information of the Swift GRBs is released. Right now the Type II Gold Sample includes 33 GRBs (Table 15 Top Panel). This is already a large enough sample to study the statistical properties of Type II GRBs.

Type I Gold Sample. The Gold Sample of Type I GRBs is defined by at least one of the following two criteria.

1. The host galaxy is elliptical or early type;

2. The GRB location has a relatively low local SSFR, or a large offset from the center of the host galaxy; and deep searches reveal stringent upper limits on the existence of an underlying SN.

Again the GRB properties (duration, hardness, lag) are not considered. Some arguments (Belczynski et al. 2006; Zheng & Ramirez-Ruiz 2007) have suggested that a fraction of Type I GRBs may be located in star forming regions of star forming galaxies. Our criteria do not select those, since we do not demand completeness of sample selection. After systematically checking the archival data, we only identify 5 bursts in the Type I Gold Sample: GRBs 050509B, 050709, 050724, 060614[2], and 061006 (Table 15 Middle Panel). The details of individual GRBs are presented in the Appendix of this chapter.

Other SGRB Sample. Most short/hard GRBs in the Swift era satisfy neither of the two criteria of the Type I Gold Sample. Some of them do not have their host galaxies convincingly identified. Others have host galaxies with active star formation. These GRBs are usually regarded as Type I candidates simply because they are "short/hard". There could be a good fraction of Type I GRBs in this sample, but we are not sure that they can ALL be associated with Type I. Since we define the Gold Samples not based on the GRB properties, we leave these bursts in a separate sample, without specifying whether they are associated with Type I or Type II. There are 20 bursts in this sample (Table 15 Bottom Panel).

[2]In the literature GRB 060614 is usually taken as a controversial candidate for Type I. This was mainly because of its long duration. We do not consider duration as a criterion when selecting the Gold Sample. This burst satisfies the criterion #2 of the Type I Gold Sample.

Table 15. Sample of Type I/II and Other Short-Hard GRBs

GRB name	z redshift	log SSFR Gyr^{-1}	SN?	T_{90} sec	T_{90} w/ EE sec	HR[a] $\frac{S(50-100keV)}{S(25-50keV)}$	lag^b sec	E_p keV	$E_{\gamma,iso}$ 10^{52} erg	$L_{p,iso}$ 10^{50} erg/s
Type II Gold										
970228	0.695	0.082	?	~ 80	n/a	1.07	0[c]	115 ± 38	1.6 ± 0.1	$93.3^{+5.7}_{-6.1}$
970508	0.835	0.534	?	~ 23.1	n/a	1.09	$0.384^{+0.090,b}_{-0.026}$	79±23	0.61 ± 0.13	$14.3^{+0.5}_{-0.6}$
971214	3.418	0.467	?	31.0 ± 1.2	n/a	1.63	$0.066^{+0.026}_{-0.048}$	155±30	21 ± 3	684 ± 65
980425	0.0085	-0.883	Y	23.3 ± 1.4	n/a	1.08	1.46±0.18	119 ± 24	$(6.1 \pm 0.62) \times 10^{-5}$	$4.8^{+7.5}_{-7.8} \times 10^{-4}$
980613	1.0964	1.184	?	50	n/a	1.59	...[d]	93 ± 43	0.59 ± 0.09	$16.7^{+3.9}_{-4.7}$
980703	0.966	0.885	?	411.6±9.3	n/a	1.47	$0.402^{+0.162}_{-0.134}$	254 ± 51	7.2 ± 0.7	166^{+32}_{-31}
990123	1.6	0.340	?	63.4±0.3	n/a	2.06	$0.018^{+0.012}_{-0.012}$	781 ± 62	229 ± 37	3517^{+210}_{-198}
990506	1.30658	-0.081	?	130.0±0.1	n/a	1.44	0.04 ± 0.02	283 ± 57	94 ± 9	930^{+54}_{-52}
990712	0.4331	0.093	?	~ 30	n/a	0.98	0.045±0.014	65 ± 11	0.67 ± 0.13	$73.1^{+5.9}_{-6.4}$
991208	0.707	1.121	?	~ 68	n/a	1.25	...	183 ± 18	22.3 ± 1.8	110 ± 11
000210	0.846	0.049	?	~ 15	n/a	1.19	...	408 ± 14	14.9 ± 1.6	1003^{+80}_{-79}
000418	1.1181	0.757	?	~ 30	n/a	?	...	134 ± 10	9.1 ± 1.7	$11.3^{+4.0}_{-4.1}$
000911	1.0585	-0.124	?	~ 500	n/a	2.14	...	579 ± 116	67 ± 14	558^{+128}_{-95}
000926	2.0379	-0.165	?	~ 25	n/a	0.37	...	101 ± 6.5	27.1 ± 5.9	107 ± 43
011121	0.362	-0.464	Y	~ 30	n/a	0.78	...	217 ± 26	7.8 ± 2.1	49.8 ± 4.0
011211	2.14	-0.084	?	~ 270	n/a	1.87	...	59 ± 7	5.4 ± 0.6	$21.8^{4.8}_{-5.2}$
020405	0.695	-0.174	Y	~ 60	n/a	3.23	...	364 ± 73	10 ± 0.9	$117^{+7.2}_{-6.7}$
020813	1.255	1.167	?	113.0±1.1	n/a	1.58	0.16 ± 0.04	142 ± 13	66 ± 16	450^{+94}_{-86}
020819B	0.41	-0.664	?	~ 50.2	n/a	1.07	...	50 ± 15	0.68 ± 0.17	...
020903	0.25	0.555	Y	~ 13	n/a	0.66	...	3 ± 1	$(24 \pm 6) \times 10^{-4}$	...

Table 15 (continued)

GRB name	z redshift	log SSFR Gyr^{-1}	SN?	T_{90} sec	T_{90} w/ EE sec	HR[a] $\frac{S(50-100keV)}{S(25-50keV)}$	lag^b sec	E_p keV	$E_{\gamma,iso}$ 10^{52} erg	$L_{p,iso}$ 10^{50} erg/s
021211	1.006	-0.841	Y	~ 8	n/a	0.98	0.32 ± 0.04	46 ± 7	1.12 ± 0.13	155^{+33}_{-29}
030328	1.52	0.680	?	~ 199.2	n/a	1.43	0.2 ± 0.2	126 ± 13	47 ± 3	191 ± 38
030329	0.1685	0.304	Y	~ 62.9	n/a	1.13	$0.58^{+0.60}_{-0.36}$	68 ± 2	1.5 ± 0.3	22.5 ± 4.5
030528	0.782	1.355	?	~ 83.6	n/a	1.23	12.5 ± 0.5	62 ± 3	2.5 ± 0.3	$17.3^{+3.6}_{-3.4}$
031203	0.1055	1.287	Y	~ 40	n/a	0.65	0.24±0.12	~ 292	~ 0.01	$0.12^{+0.03}_{-0.02}$
040924	0.858	0.071	?	2.39±0.24	n/a	1.00	0.3 ± 0.04	67 ± 6	0.95 ± 0.09	191 ± 20
041006	0.716	-0.131	?	17.40±0.25	n/a	1.08	...	63 ± 13	3 ± 0.9	$44^{+1.7}_{-1.8}$
050525A	0.606	?	Y	8.830±0.004	n/a	1.17	$0.0865^{+0.0065}_{-0.008}$	84.1 ± 1.7	2.89 ± 0.57	111.8 ± 2.1
050826	0.297	0.172	?	35.5±1.2	n/a	1.91	...	340^{+790}_{-210}	0.03±0.04	$0.33^{+0.32}_{-0.08}$
051022	0.8	0.142	?	~ 200	n/a	1.52	...	418 ± 143	53 ± 5	364^{+48}_{-47}
060218	0.033	-0.061	Y	~ 2000	n/a	0.76	218^{+356}_{-140}	4.9 ± 0.3	$(77 \pm 1.4) \times 10^{-4}$	$1.0 \pm 0.6 \times 10^{-3}$
060602A	0.787	?	?	75.0±0.2	n/a	2.65	...	280^{+570}_{-150}	0.91 ± 0.06	$6.14^{+2.54}_{-0.80}$ ...
080520	1.545	?	?	2.82±0.67	n/a	0.46	...	~ 30	0.073 ± 0.019	...
Type I Gold										
050509B	0.2248	-0.853	N	0.040±0.004	n/a	1.52	0.0043±0.0032	82^{+611}_{-80}	$2.4^{+4.4}_{-1} \times 10^{-4}$	$0.07^{+0.10}_{-0.05}$
050709	0.1606	-0.512	N	0.07±0.01	130 ± 7	1.37/1.02[j]	0 ± 0.002	83^{+18}_{-12}	$(2.7 \pm 1.1) \times 10^{-3}$	$5.4^{+0.67}_{-0.69}$
050724	0.2576	-0.367	N	3±1	154.20 ± 1.12	1.26/1.12	-0.0042 ± 0.0082	110^{+400}_{-45}	$9^{+11}_{-2} \times 10^{-3}$	$0.99^{+0.23}_{-0.10}$
060614	0.1254	-0.863	N	~ 5	106.0 ± 3.3	1.41/1.07	0.003 ± 0.009	302^{+214}_{-85}	0.24 ± 0.04	$1.39^{+0.13}_{-0.07}$
061006	0.4377	-2.189	N	~ 0.5	120.00 ± 0.04	1.52/1.18	...	640^{+144}_{-227}	0.22 ± 0.12	$24.60^{+1.22}_{-0.77}$
Other Short-Hard Bursts										
000607	0.14	?	?	~ 0.008	n/a	2.18	...	...	...	...

Table 15 (continued)

GRB name	z redshift	log SSFR Gyr^{-1}	SN?	T_{90} sec	T_{90} w/ EE sec	HR[a] $\frac{S(50-100keV)}{S(25-50keV)}$	lag^b sec	E_p keV	$E_{\gamma,iso}$ 10^{52} erg	$L_{p,iso}$ 10^{50} erg/s
050813	∼0.72	?	N	0.6±0.1	n/a	1.76	-0.0097 ± 0.014	210^{+710}_{-130}	$(1.5^{+2.5}_{-0.8}) \times 10^{-2}$	4.13 ± 2.02
051210[g]	>1.4	?	?	1.27±0.05	40	2.01	-0.0053 ± 0.024	410^{+650}_{-260}	$> 0.191 \pm 0.032$	...
051221A	0.5464	0.804	?	1.4±0.2	n/a	1.74	0 ± 0.004	402^{+72}_{-93}	$0.28^{+0.21}_{-0.1}$	25.8 ± 0.9
060121	1.7/4.6	?	?	1.60±0.07	∼ 120	1.55/0.57[h]	0.017±0.009[i]	104^{+134}_{-78}	$4.18^{+3.29}_{-0.39}/22.3^{+17.5}_{-2.07}$	$2445 \pm 162/33574 \pm 2226$
060313	≤ 1.1	?	?	0.7±0.1	n/a	2.43	$(3 \pm 7) \times 10^{-4}$	922^{+306}_{-177}	$\leq 6.24^{+0.43}_{-3.66}$	...
060502B	0.287	?	?	0.09±0.02	n/a	2.12	$(-2 \pm 8) \times 10^{-4}$	340^{+720}_{-190}	$3^{+5}_{-2} \times 10^{-3}$	0.65 ± 0.09
060505	0.0889	-0.777	?	4±1	n/a	1.63	0.36±0.05	∼ 223	$(3.39 \pm 0.60) \times 10^{-3}$	~ 0.009[k]
060801	1.131	?	?	0.5±0.1	n/a	2.89	0.008 ± 0.008	620^{+1070}_{-340}	0.17 ± 0.021	$47.6^{+6.2}_{-1.6}$
061201	0.111?	?	?	0.8±0.1	n/a	2.90	$2.7^{+3.3}_{-2.4} \times 10^{-3}$	873^{+458}_{-284}	$0.018^{+0.002}_{-0.015}$	...
061210	0.4095	?	?	≃0.06	85±5	2.32/1.37	...	540^{+760}_{-310}	$0.09^{+0.16}_{-0.05}$	21.5 ± 1.4
061217	0.8270	?	?	0.212±0.041	n/a	2.07	-0.007±0.009[j]	400^{+810}_{-210}	$0.03^{+0.04}_{-0.02}$	10.8 ± 1.8
070429B	0.9023	?	?	0.5±0.1	n/a	1.23	...	120^{+746}_{-66}	0.03 ± 0.01	24.6 ± 3.8
070714B	0.9225	?	?	∼ 3	∼ 100	1.82/1.56	0.014 ± 0.007	1120^{+780}_{-380}	$1.16^{+0.41}_{-0.22}$	57.3 ± 3.6
070724A	0.457	?	?	0.50±0.04	n/a	0.94	...	∼ 68	0.003 ± 0.001	$1.58^{+0.34}_{-0.14}$
071227	0.3940	?	?	1.8±0.4	∼ 100	2.02/0.96	$(0.4 \pm 14) \times 10^{-4}$,[l]	∼ 1000	0.22 ± 0.08	3.34 ± 0.49
080503	...	?	N	∼0.7	170± 40	1.0	-0.013±0.009[m]	...	...	...
080913	6.7	?	?	8 ± 1	n/a	1.58	0 ± 0.42	121^{+232}_{-39}	7 ± 1.81	1200^{+1622}_{-300}
090423	8.3	?	?	10.3 ± 1.1	n/a	1.50	$0.046^{+0.085}_{-0.058}$	48^{+6}_{-5}	10 ± 3	∼ 1880

Duration-Hardness Distribution

Figure 58 presents the traditional T_{90}-hardness ratio (HR) plot of GRBs. Superimposed on the BATSE data (orange small dots) are the three samples defined above: Type II Gold Sample (blue), Type I Gold Sample (red), and other SGRB sample (green). The HR is defined as the fluence ratio between (50-100) keV and (25-50) keV. For BATSE bursts, this corresponds to the fluence ratio between channel 2 and channel 1. For other detectors (HETE-2, Swift/BAT, Konus/Wind, INTEGRAL) with different detector energy bands, we perform spectral fits and use the fitted model to derive the HR. Besides the observed points (open symbols), we also plot the corresponding "rest-frame" points (filled symbols) for each burst. The HR is then defined as the flux ratio between the rest-frame (50-100) keV band and (25-50) keV bands, which is again derived from spectral fitting. For a power law fit, the rest frame HR is the same as the observed one. For a curved spectrum (e.g. a Band function or an exponential cutoff power law), the two can be different. The T_{90} values are energy- and detector-dependent. We do not make efforts to convert all T_{90} to the BATSE-band, since this requires time-dependent spectral analyses and extrapolations, and for many bursts the data quality is not sufficient to perform such an analysis. Instead we simply plot T_{90} measured by different detectors (e.g. Swift and HETE). The correction to the BATSE-band T_{90} is usually not significant for most long GRBs, but could be significant to those GRBs with soft extended emission. Traditionally, the "rest frame" T_{90} are not used to defined long vs. short for a particular GRB. We present them here just to show how the intrinsic distribution may differ from the observed one. To derive the rest-frame T_{90}^{rest}, we simply divide the observed value by $(1 + z)$. More rigorously one needs to again take into account the light curve evolution with energy. This again requires a time-dependent spectral analysis. Since most bursts do not have such detailed information, and since the correction would not be significant for most bursts, we neglect this correction for the sake of simplicity and uniformity.

For short GRBs with extended emission, we use circles to denote the short spikes only (excluding the extended emission), while using squares to denote the full emission with extended emission included. These two locations for the same burst with and without extended emission are connected by lines. Since the mean HR is derived, the HRs including extended emission are usually smaller than those without, as the extended emission is typically softer than the initial short spikes.

From Fig. 58 one can make the following interesting observations. First, the Type II GRBs are generally long, and they well represent the long/soft population of the BATSE GRBs in the T_{90}-HR plane. However, some Type II GRBs have a duration close to the 2-second separation line, and their intrinsic duration can be shorter than 2 s (e.g. GRB 040924 with $T_{90} = 2.39 \pm 0.24$ s at $z = 0.858$, and GRB 080520 with $T_{90} = 2.82 \pm 0.67$ at $z = 1.545$). Levan et al. (2007) also discussed a sample of apparently-long, intrinsically-short GRBs. Secondly, *four out of five Type I Gold Sample GRBs are not strictly "short"*. Except GRB 050509B, all the others have extended emission aside from the initial "short/hard" spike. The spike itself is longer than 2 s for GRB 050724 and GRB 060614. *All 5 Type-I Gold Sample bursts have a moderate HR. None has an extremely hard spectrum.* Thirdly, the Other SGRB Sample fills in the short/hard region in the $T_{90}-$HR diagram more uniformly, suggesting that it represents the BATSE short/hard sample well. Some bursts in the sample also have extended emission.

Empirical Correlations

Figure 60a displays the $E_p - E_{\gamma,iso}$ (Amati) relation of the three samples. The spectral parameters are collected from the published papers or GCN circular reports (see Table 14 for references). For those GRBs with extended emission (including Type I Gold Sample GRBs 050724, 060614, and 061006), we only consider the short hard spikes. For all the bursts, the isotropic gamma-ray energy ($E_{\gamma,iso}$) is calculated in the GRB rest-frame $1 - 10^4$ keV band through extrapolation based on the spectral parameters. We can see

that most GRBs in the Type II Gold Sample indeed follow the $E_p \propto E_{\gamma,iso}^{1/2}$ (Amati) relation. However, there are three noticeable outliers: GRB 980425, GRB 031203, and GRB 050826. The first two are nearby low-luminosity (LL) GRBs, which have been argued to be from a distinct population (e.g., Liang et al. 2007; Virgili et al. 2009). Another nearby LL GRB 060218 is a soft burst (Campana et al. 2006b) and satisfies the Amati relation well. GRB 050826 with $T_{90} \sim 35$ s is an intermediate Type II GRB between the more "classical" Type II and the nearby LL-GRBs (Kann et al. 2007), and deviates from the relation. We also pay special attention to the two intrinsically short Type II GRBs. Although GRB 040924 is right on the Amati-relation track, GRB 080520 seems to be slightly off the track. The Type I Gold Sample and the other SGRB Samples are populated above the conventional Amati-relation track. Since many short/hard GRBs have Ep outside the BAT band, their Ep error bars are large. The values in our analyses are adopted from Butler et al. (2007). In any case, it seems that they follow a separate track with a shallower slope than the Amati-relation. Excluding GRBs 080913, 090423 and 060121 (which are likely Type II, see §6.2), a best fit to the Type I Gold and Other SGRB samples lead to a slope 0.34, with the 3σ limits of the slope as (0.15-0.53) (see Fig.60a). GRB 080913 is marginally within the 3σ regions for the Type II Amati-relation, but is also consistent with this new track defined by Type I and other short/hard GRBs within 3σ. GRB 090423 aligns with the Type II Amati-relation more closely.

A likely reason that the Type I and the Other SGRB Samples deviate from the Amati relation of Type II GRBs is simply because they have shorter durations so that they have smaller $E_{\gamma,iso}$ values than the Type II GRBs with a similar E_p. To test this, we plot the $E_p - L_{\gamma,iso}^p$ relation (Yonetoku relation) in Fig.60b. We can see that the distinction between Type II and Type I GRBs becomes less significant, although the correlation now has a much larger scatter. Noticing the large error bars of the Type I and Other SGRB Samples, one may conclude that there is no distinct difference among the three samples as far as the Yonetoku relation is concerned. A similar conclusion was drawn by

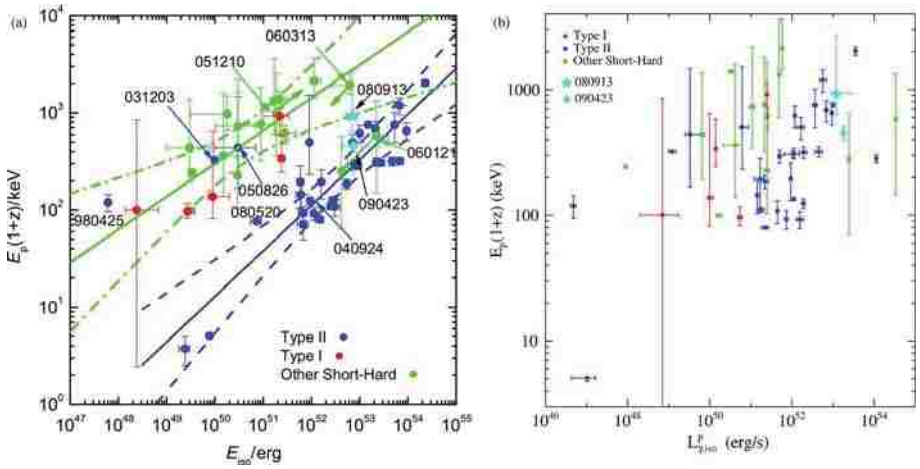

Figure 60 (a) The $E_p - E_{\gamma,iso}$ diagram of the three samples of GRB discussed in the paper: Type II Gold Sample (blue), Type I Gold Sample (red), and other short/hard GRBs (green). Two possible redshifts $z = 4.6, 1.7$ for the short GRB 060121 are adopted, which satisfies the relation well (unlike other short/hard GRBs). GRB 080913 and GRB 090423 (cyan) are also plotted for comparison. The best-fit $E_p - E_{\gamma,iso}$ correlations for both Type II and Type I/Other SGRB samples are plotted (solid lines) with the 3σ boundary (dashed line) marked. (b) The $E_p - L^p_{\gamma,iso}$ diagram. The same convention has been used.

Ghirlanda et al. (2009) in an analysis of the BATSE GRBs.

Figure 61a displays the luminosity-spectral lag diagram of GRBs with the three samples plotted. A group of Gold Sample Type II GRBs indeed define a $L^p_{\gamma,iso} \propto (\Delta t_{rest})^{-\delta}$ correlation track (Norris et al. 2000; Gehrels et al. 2006), although several low-luminosity, long-lag GRBs lie below the extrapolation of the track (see also Gehrels et al. 2006; Liang et al. 2006b). Gold Sample Type I GRBs are clustered at the lower left corner. This is as expected: short durations define short lags, and smaller energy budgets define lower luminosities. About half of the "Other SGRBs" are clustered close to the Type I Gold Sample, suggesting that they may be associated with Type I as well. Some others fill in the gap between the Type I and Type II Gold Samples. In particular, GRB 060121 lies right on the track for both putative redshifts 1.7 and 4.6 (de Ugarte Postigo et al. 2006). GRB 070714B is also close to the track. The SN-less GRB 060505 clusters with other nearby low-luminosity Type II GRBs. Finally, the two high-z GRBs 080913 (notice that

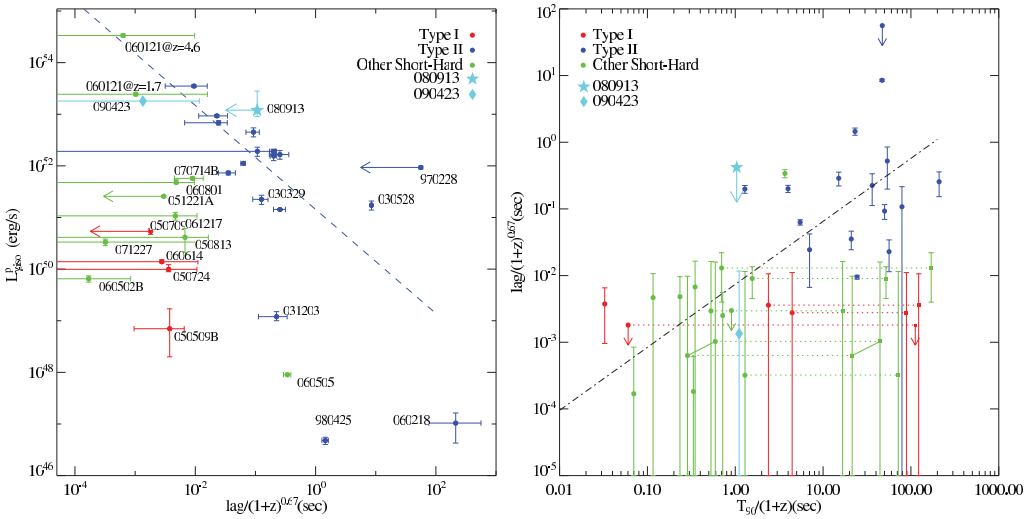

Figure 61 (a) The $L^p_{\gamma,iso}-$lag diagram. Same convention as Fig.3 is adopted. GRB 080913 and GRB 090423 satisfy both the correlation defined by Type II GRBs and the "zero lag" trend defined by Type I and Other SGRB Samples. Two possible redshifts $z = 4.6, 1.7$ for the short GRB 060121 are adopted, which satisfies the correlation well (unlike other short/hard GRBs). (b) the lag $- T_{90}$ (intrinsic) diagram of the three samples. The same GRBs with/without extended emission is connected by dotted lines. The spectral lags of these GRBs are for the short/hard spikes only. A positive correlation between duration and spectral lag is derived (dashed line). See text for details.

only the upper limit of spectral lag is derived) and 090423 are consistent with satisfying the $L^p_{\gamma,iso}-$ lag correlation of Type II, but are also consistent with the zero-lag trend of Type I/Other SGRB.

As discussed above, the luminosity lag relation may be related to the variability-luminosity relation, and may be more relevant to Type II GRBs. On the other hand, the physical origin of the relation is not clearly understood and is based on many assumptions. Although the correlation may be taken as a reference, it may not be taken as the definite criterion for judging the physical origin of a GRB.

Based on the high-latitude-effect interpretation of spectral lag , one expects that short spectral lags should be related to short angular spreading times. The latter corresponds to the width of individual pulses. If the number of pulses do not fluctuate significantly among bursts, one would also expect a rough correlation between spectral lags and durations. In Fig.61b we display the $T_{90}/(1+z) - \mathrm{lag}/(1+z)^{2/3}$ diagram of the three samples

of bursts. Again points of the same burst with and without extended emission are connected by lines. We investigate a possible correlation between duration and spectral lag. Since the spectral lags are defined for the short/hard spikes only for those GRBs with extended emission, we use T_{90} excluding the extended emission for those bursts. A positive correlation between T_{90} and lag with slope 0.94 ± 0.14 is obtained, with the Spearman's rank correlation coefficient $r = 0.735$, corresponding to a chance probability $P < 10^{-4}$. This is consistent with our naive expectation, suggesting that spectral lags are closely related to durations, and may not carry additional information in defining the categories of GRBs.

Luminosity And Redshift Distributions

Figure 62(a) and (b) display the observed 2-dimensional luminosity-redshift ($L^p_{\gamma,iso}-z$) and energy-redshift ($E_{\gamma,iso} - z$) distributions of the three samples. GRBs in the Type I Gold Sample are all at $z < 0.5$. Including the Other SGRB Sample, the upper boundary of z reaches ~ 1 (except GRB 060121). The Type II GRBs have a wider span of redshift distribution, with the peak around $z \sim 1$. In terms of luminosity distribution, the Type II GRBs on average are ~ 2 orders of magnitude more luminous than the Type I GRBs. Type I GRBs can at least reach a luminosity of $L^p_{\gamma,iso} \sim 2.5 \times 10^{51}$ erg s^{-1} (for the Type I Gold GRB 061006). Including the Other SGRB Sample, several short GRBs (070714B, probably 060313, and especially the latest GRB 090510) can reach $L^p_{\gamma,iso} \sim 10^{52}$ erg s^{-1}. GRB 060121 even reaches $L^p_{\gamma,iso} \sim 10^{53} - 10^{54}$ erg s^{-1} for the two fiducial redshifts in discussion. This luminosity is high even for Type II GRBs. GRB 080913 has $L^p_{\gamma,iso} \sim 1.2 \times 10^{53}$ erg s^{-1}. GRB 090423 has $L^p_{\gamma,iso} \sim 1.88 \times 10^{53}$ erg s^{-1} (Nava et al. 2009). Both are moderate to high luminosities for Type II GRBs, and are very high when compared with the Type I and Other SGRB Samples (except for GRB 060121). In the $E_{\gamma,iso} - z$ diagram, the separation between Type II and Type I is more distinct, with most SGRB sample bursts lying below the Type II distribution. But GRB 080913

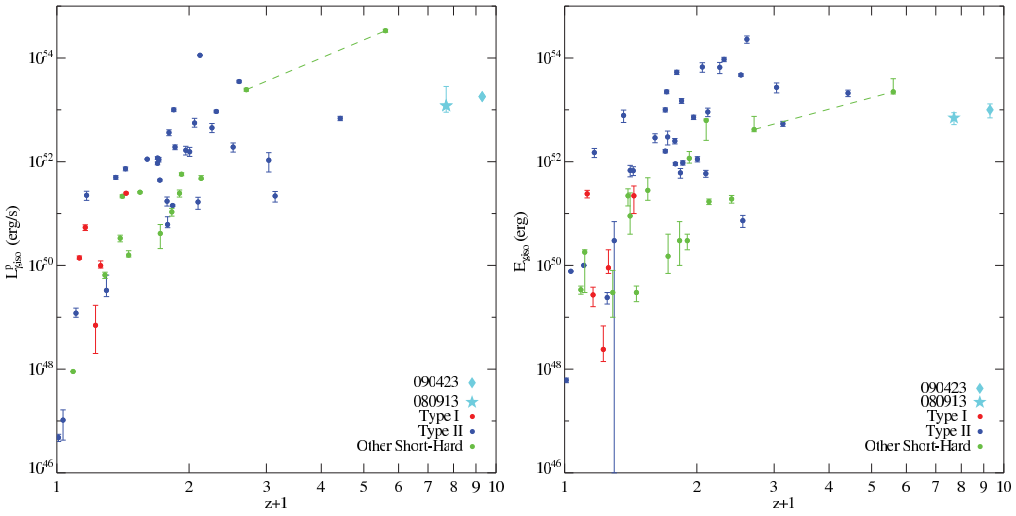

Figure 62 (a) The $L^p_{\gamma,iso} - z$ diagram, and (b) the $E_{\gamma,iso} - z$ diagram of the three samples.

and GRB 090423 become moderate in the Type II Sample due to their intrinsically short durations. The clearer separation between Type II and Type I/Other SGRB Samples is mainly due to the short duration of the SGRB sample, which makes them less energetic. However, GRB 060121 is still as energetic as the average Type II GRBs.

Afterglow Properties

Figures 63 and 64 present the intrinsic afterglow light curves in the X-ray and optical bands for the three samples. Figure 63 presents the rest-frame 2 keV specific luminosity light curves. Since many Type II Gold Sample GRBs are pre-Swift, we do not have many Type II X-ray light curves. The ones that are plotted include two low luminosity GRBs (060218 and 050826) and two intermediate-to-high luminosity GRBs (080520 and 050525A). These do not fully represent the Type II GRB X-ray afterglow properties. In order to compensate for this weakness of sample selection, we also overplot the X-ray light curves of a group of early Swift long GRBs in the sample of Nousek et al. (2006). Since we already demonstrated that the Type II Gold Sample represents the BATSE long GRBs well, we assume that the Nousek Sample represents the Type II GRB X-ray afterglows well. We can see that these bursts occupy the upper portion of the light curve

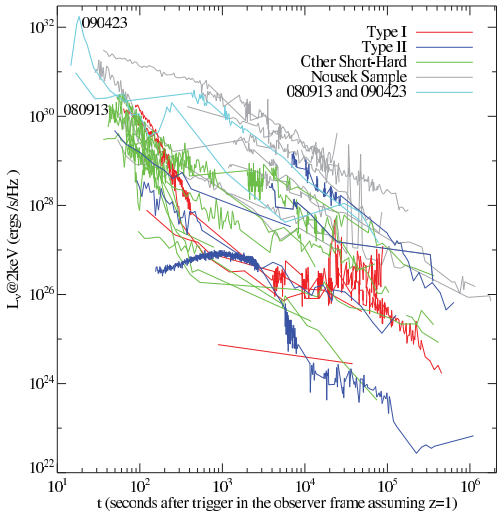

Figure 63 The rest frame 2 keV X-ray afterglow luminosity light curves of GRB 080913, GRB 090423, and the three samples. All bursts are placed at $z = 1$. The color scheme is the same as in the other figures. Since most Type II Gold Sample bursts are pre-Swift ones and have no X-ray light curves, we also add the z-known long GRBs in the sample of Nousek et al. (2006) (grey), which are generally believed to be Type II GRBs. GRB 080913 and GRB 090423 (cyan) both have bright X-ray afterglows typical of Type II GRBs.

space in Fig. 63. By contrast, the Type I Gold Sample occupy the lower portion, and the Other SGRB Sample populate in between with much overlap with both Gold Samples. Low luminosity Type II GRBs have luminosities comparable to Type I Gold Sample GRBs.

Figure 64 presents the optical light curves with corrected R_c-magnitude by moving all GRBs to $z = 1$. One big difference between these optical light curves and the X-ray light curves (Fig. 63) is that most Type II GRBs are represented, exceptions being those GRBs that had negligible optical afterglows but strong supernovae signatures (GRBs 980425, 031203, and XRF 060218), dark GRBs, where the optical emission was probably totally supressed by line-of-sight extinction in the host galaxy (GRBs 990506, 000210, 020819B, 051022), and some with very sparse optical data (XRF 020903, GRBs 030528, 050826, 060602A, 080520). Most data have been taken from Kann et al. (2007, 2008), where the methods of creating the intrinsic light curves are also presented. Similar to the

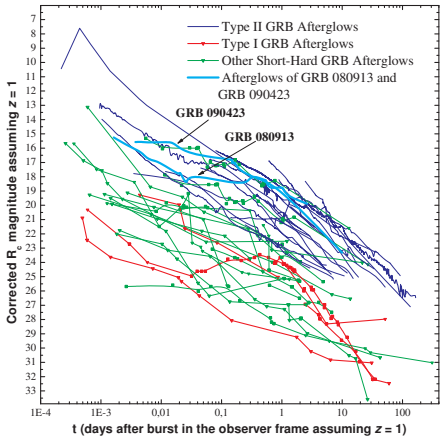

Figure 64 The rest frame optical light curves of GRB 080913, GRB 090423, and the three samples. The color scheme is the same as in the other figures. Similar to Kann et al. (2008, 2010), they are plotted at a common redshift of $z = 1$. As with the X-ray light curves (Fig. 63), the optical afterglows of the Type II Gold Sample GRBs are clearly more luminous than those of the Type I Gold Sample and the Other Short-Hard Sample. The latter two populations are in good agreement with each other. GRB 060121 is the single short-hard GRB which is optically highly luminous. GRB 080913 and GRB 090423 both have bright optical afterglows typical of Type II GRBs.

X-ray light curves, the Type II GRB afterglows form a much more luminous group than the Type I GRB afterglows (Kann et al. 2008).. The light curves of Type I Gold GRBs and those of most Other SGRBs overlap, indicating that they are likely drawn from the same population. The most prominent exception is again GRB 060121 with an optically luminous afterglow which is comparable to the afterglows of Type II GRBs.

For both X-ray and optical afterglows, GRB 080913 and GRB 090423 have a luminosity comparable to or higher than the average luminosity of the Type II GRB afterglowss (Greiner et al. 2009b; Salvaterra et al. 2009; Tanvir et al. 2009).

Summary

Prompted by the interesting question whether the $z = 6.7$ GRB 080913 and $z = 8.3$ GRB 090423 are intrinsically short GRBs associated with the Type II physical model category or high-z GRBs associated with the Type I physical model category. we performed a more thorough investigation on the two physically distinct categories of GRB

models and their predicted observational characteristics. We further developed the "Type I/II" concept proposed in Zhang et al. (2007b) in the following directions. (1) We have reviewed and expanded the possible multiple observational criteria, and discussed their physical origins from the theoretical point of view. By doing so, we are able to differentiate those criteria that are more closely related to the progenitor types and those that are more directly related to radiation physics. In particular, we argue that SN association, host galaxy properties (type and SSFR), and the offset of the GRB location in the host galaxy are more directly related to the progenitor types. The gamma-ray properties, such as duration, hardness, spectral lag, empirical correlations, are more related to jet dissipation and radiation processes in the emission region, and can only be related to progenitors indirectly. Afterglow and statistical properties can be used to diagnose GRB progenitor, but theoretical modeling is needed. Gravitational wave signals may be the best criterion to directly probe the progenitor system, but they are too faint for the current detectors to detect. (2) We use several key observational criteria that are directly related to GRB progenitors to define the Gold Samples for Type I and Type II, respectively. These criteria do not involve GRB gamma-ray emission properties such as duration, hardness, spectral lag, etc. We then use these samples to investigate their statistical properties, especially their distribution in the duration-hardness space. We found that the Type II Gold Sample represent the BATSE long/soft population well. The Type I Gold Sample, on the other hand, is not very representative of the short/hard population. The Type I Gold Sample GRBs are typically "long" and not particularly "hard". (3) Although some short/hard GRBs detected in the Swift era may share a similar origin as the Type I Gold Sample, we suggest that *some (maybe most) high-L short GRBs may be instead associated with Type II, namely, of a massive star origin.* (3) We summarized the multiple observational criteria needed to discern the physical origin of a GRB in Table 14, with various issues laid out. We emphasize that it is not always straightforward to judge the physical model category a particular GRB is associated with, and we cautiously proposed

an operational procedure to discern the physical origin of GRBs (Fig.59). (4) According to this procedure, GRB 080913 and GRB 090423 are Type II candidates. Although a specific Type I scenario invoking the Blandford-Znajek mechanism of a BH-NS merger system is not completely ruled out, the fact that two such GRBs are detected at high-z indeed suggest that a Type I association of these bursts is essentially impossible.

The proposed procedure to associate a particular GRB to a particular physical model category is subject to further test with new observational data[3]. More detailed analyses may allow more quantative criteria to discern the physical origin of GRBs. Based on past experience, the chances are high that new observations will bring surprises that continuously call for modifications of the criteria, which would further our understanding of the physical origins of cosmological GRBs.

[3]For example, the recent observed two bursts, GRB 101225A (Xu et al., 2011, Science, submitted, see also Chapter 12) and GRB 110328A probably do not belong any type of GRBs we have proposed.

PART V

CASE STUDY OF SOME SPECIAL BURSTS

CHAPTER 12

CASE STUDY ON SOME SPECIAL GRBS

During my Ph.D study, I've also involved in several projects that focus on particular GRBs. In most cases, I mainly contributed on the data analysis parts in these projects. In the following I only briefly summarize the results of those projects. Some sections below are reproduced from the corresponding paper.

XRF 060218:

Extremely Long Pulse Duration and Spectral Lag

This work has been published asr:

Liang, E.-W., Zhang, B.-B.. et al., The Astrophysical Journal Letters, 653, L81.

XRF 060218 was detected with the *Swift*/BAT on 2006 February 18.149 UT. It is a long burst, with a duration $T_{90} \sim 2000$ seconds in the 15-150 keV band. This makes it possible to measure its temporal structure.

We investigated the non-thermal emission of XRF 060218. The early SED of this event from 0.3-150 keV observed by BAT and XRT suggests that the non-thermal emission detected by the two instruments are the same component. By subtracting the contribution of the thermal emission we derive the light curves of the non-thermal emission. They are composed of a broad single pulse, and the energy dependences of the widths and the rising-to-decaying-time ratio of the pulses are roughly consistent with those derived in typical GRBs (Fig. 65). The light curves show significant spectral lags, with a well-defined peak time sequence from high energy band to low energy bands, i.e. $t_{\rm peak} \propto E^{-0.25\pm0.05}$. We infer the spectral lag in the BATSE bands and find that the hypothesis that this event complies with the $L_{\rm iso} - \tau$ relation with typical GRBs cannot be ruled out at the 2σ significance level (Fig. 66).

These intriguing facts, along with its compliance with the Amati-relation, strongly suggest that GRB 060218 is a "standard" burst at the very faint, long, and soft end

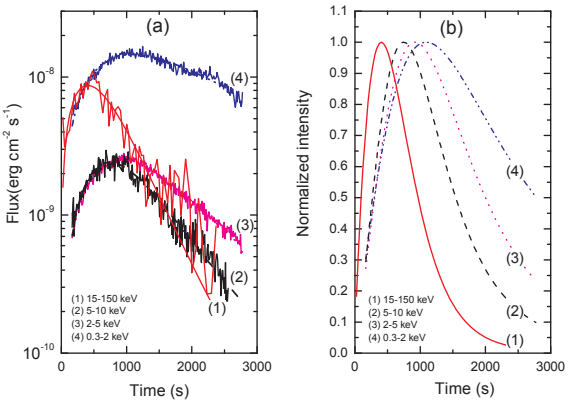

Figure 65 (a) XRF 060218 unabsorbed light curves of the non-thermal gamma-rays/X-rays in the energy bands of 15-150 keV, 5-10 keV, 2-5 keV, and 0.3-2 keV, respectively. (b) Normalized light curves from the empirical model fitting, see Liang et al 2007 for details.

of the GRB distribution (Fig. 67). Since all these relations concern the temporal and spectral properties of emission, they are likely related to the radiation mechanisms. The results therefore imply that XRF 060218 and other XRFs may share the similar radiation physics (e.g. synchrotron or inverse Compton scattering in internal shocks ; Zhang & Mészáros 2004; Piran 2005) with harder GRBs.

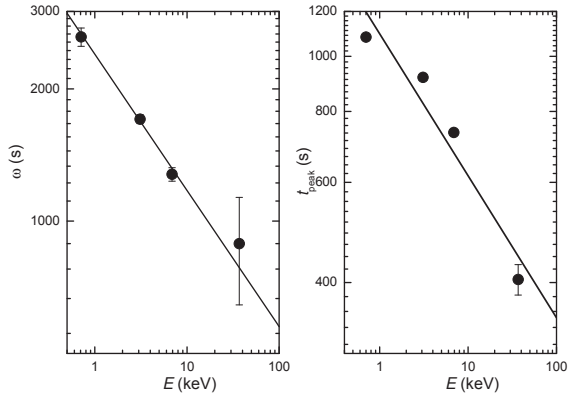

Figure 66 The pulse duration (panel a) and the peak time (panel b) as a function of the average photon energy of the non-thermal emission. The solid lines in both panels are the best fits.

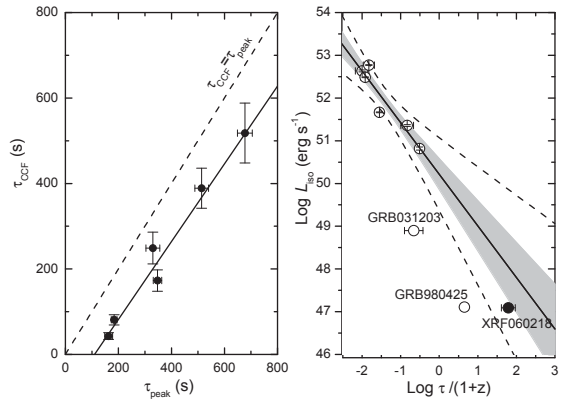

Figure 67 Panel (a): Comparison of the spectral lags derived from the peak times and from the CCF method for XRF 060218. The solid line is the best fit. Panel (b): Isotropic gamma-ray luminosity as a function of spectral lag. The spectral lags of typical GRBs and GRB 980425 are calculated with the light curves in the 25-50 keV and 100-300 keV bands observed by CGRO/BATSE. The lag of GRB 031203 is calculated with the light curves in the 20-50 keV and 100-200 keV bands. The grey band and the two dashed lines mark the best fits at the 1σ and 2σ confidence level, respectively, and the solid line is the regression line for the six typical GRBs presented in Norris et al. (2000).

GRB 070110:

An Extraordinary X-Ray Afterglow Powered by the Central Engine

This work has been published as:

Troja, E., et al. 2007, The Astrophysical Journal , 665, 599

The most intriguing feature of GRB 070110 is a very steep decay in the X-ray flux at ∼24 s after the burst, ending an apparent plateau (Fig. 68). The abrupt drop of the X-ray light curve rules out an external shock as the origin of the plateau in this burst and implies long-lasting activity of the central engine. The temporal and spectral properties of the plateau phase point towards a continuous central engine emission rather than the episodic emission of X-ray flares. We suggest that the observed X-ray plateau is powered by a spinning down central engine, possibly a millisecond pulsar, which dissipates energy at an internal radius before depositing energy into the external shock. For details please see Troja et al 2007.

GRBs 080913 & 090423 :

Two Highest Resdshift GRBS

These works have been published as

Greiner, J., et al. 2009, The Astrophysical Journal , 693, 1610

and

Zhang, B., Zhang, B.-B. et al. 2009, The Astrophysical Journal, 703, 1696

GRBs 080913 & 090423 are top two highest bursts with redshift z=6.7 and z=8.3, respectively. I joined in the discovery paper of GRB 080913 (Greiner et al. 2009a). Motivated by their amazingly similarity, we proposed a more physical scheme (Type I/II)to classify GRBs and suggest that GRB 080913 and GRB 090423 are more likely Type II events. For details see Chapter 11

GRB 090902B:

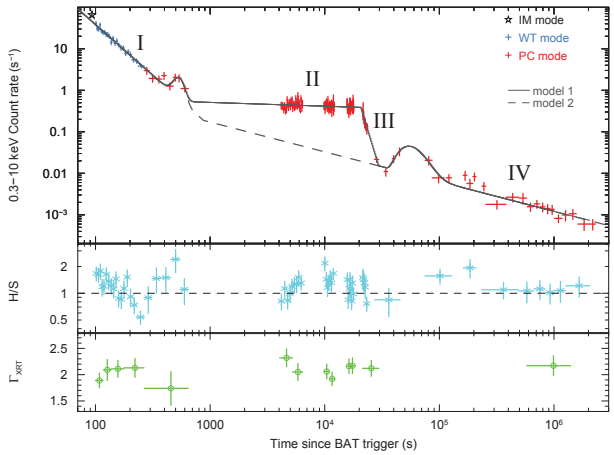

Figure 68 *Upper panel:* XRT light curve of GRB070110 in the 0.3-10 keV band. The two models described in the text are shown: power law segments with three temporal breaks (*solid line*) and a simple broken power law (*dashed line*). The bump at t∼530 s is modeled with a Gaussian function, the late one at t∼54s with a FRED profile. The four phases of the X-ray light curve are marked: (I) an early decay, (II) an apparent plateau followed by (III) a rapid drop, and (IV) a final shallow decay. *Middle panel:* Hardness ratio (H/S) light curve. It compares source counts in the hard band (H: 1-10 keV) and in the soft band (S: 0.3-1 keV). *Lower panel:* Photon index $\Gamma_{\rm XRT}$ temporal variations. These values were derived fitting the X-ray spectra with an absorbed power law model.

Thermal Emission vs Non-Thermal Emission

One of These works have been published as

Ryde, F., et al. 2010 The Astrophysical Journal Letters, 709, L172.

T he other is submitted to The Astrophysical Journal (Pe'er Asaf , Zhang, B.-B, et al arXiv:1007.2228)

GRB 090902B is identified with spectral type II+III (i.e, Blackbody+Power-Law, see Chapter 7). Besides then comprehensive data analysis work (Zhang, B.-B. et al 2011, see also Chapter 7), I also involved two theoretical projects to model the two different spectral components in details. In Ryde et al 2010, we proposed that GRB photosphere gives rise to a strong quasi-blackbody spectrum which indeed fits to the data (Fig. 69). In Pe'er et al 2010, we studied the connection between thermal and non-thermal emission for this burst and proposed that (Fig. 12) the non-thermal emission can be a combination of Synchrotron emission (dominated in low energy) and SSC and Comptonization of thermal photons (dominated in high energy).

GRB 090926A : AN BRIGHT FERMI/LAT GRB WITH LONG-LIVED SWIFT AFTERGLOWS

This work has been published as:

Swenson, C. A., et al. 2010, The Astrophysical Journal , 718, L14

GRB 090926A was detected by both the GBM and LAT instruments on board the Fermi Gamma-ray Space Telescope. Swift follow-up observations began ~ 13 hr after the initial trigger. The optical afterglow was detected for nearly 23 days post trigger, placing it in the long-lived category. The afterglow is of particular interest due to its brightness at late times, as well as the presence of optical flares at $T_0 + 10^5$ s and later, which may indicate late-time central engine activity. In Swensen et al 2010, we have compared this burst to other LAT- and BAT-detected bursts in an attempt to show whether the GRBs detected by LAT are simply brighter than the average BAT-triggered GRB or whether

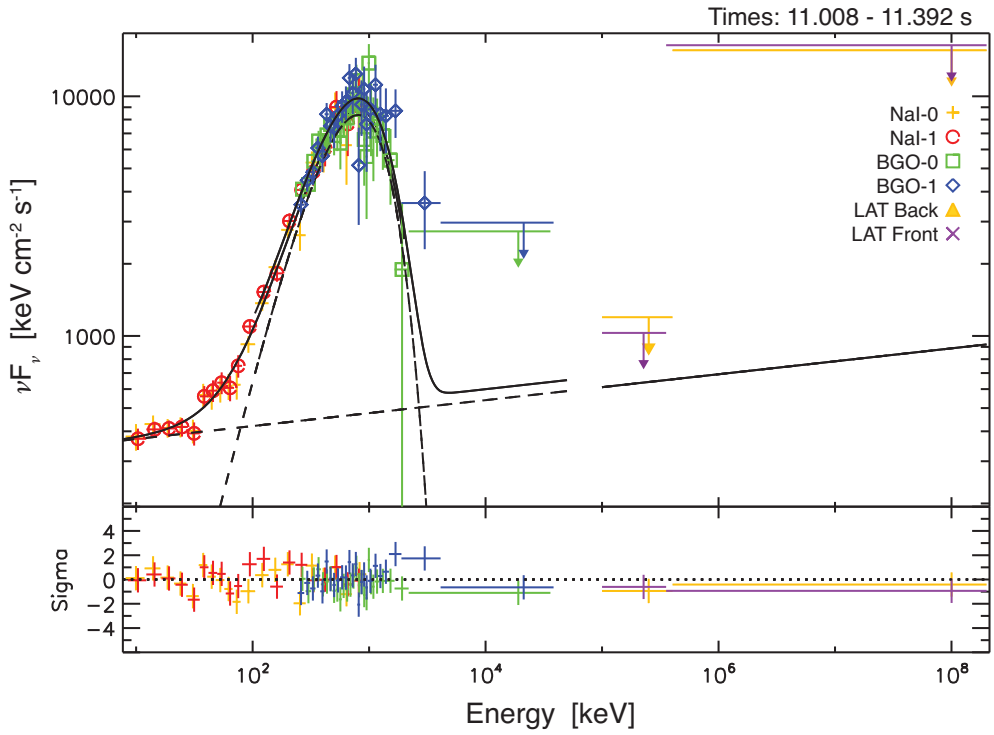

Figure 69 νF_ν spectrum of GRB 090902B for the interval $t = 11.008 - 11.392$ s

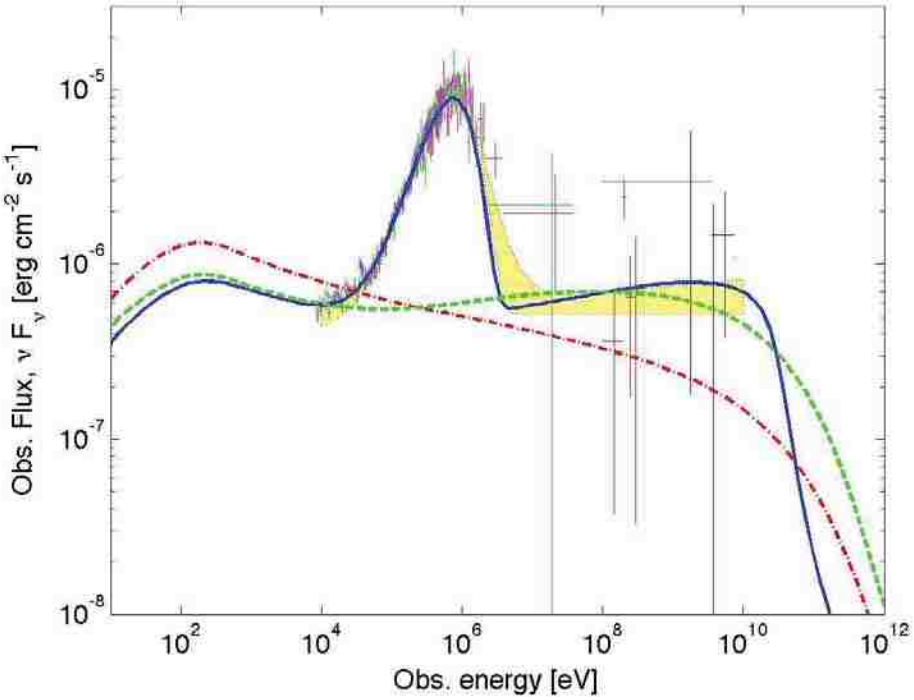

Figure 70 Demonstration of spectral decomposition into basic physical ingredients. The dash-dotted (red) curve show the spectrum that would have obtained if synchrotron radiation was the only source of emission. The dashed (green) curve) show the resulting spectrum from synchrotron and SSC, and the solid (blue) curve show the spectrum with the full radiative ingredients (synchrotron, SSC and Comptonization of the thermal photons). Dissipation radius $r_\gamma = 10^{16}$, , $\epsilon_e = 0.5$, $\epsilon_B = 0.33$, $p = 2.2$ and all other parameter values same as in Figure 1 are chosen. The low energy spectral slope (below the thermal peak) is mainly due to synchrotron emission, and is thus sensitive to the power law index of the accelerated electrons. However, the high energy part (above the thermal peak) results from all of the radiative processes, and therefore cannot be used directly to constrain the values of the free model parameters.

they represent a new type of GRB that commonly exhibits bright, long-duration optical afterglows due to some form of energy injection. We find that LAT-detected bursts are generally brighter than their BAT-triggered counterparts. We find that their fluence is consistently higher than the "average" BAT burst and that their X-ray and UV/optical afterglows are brighter than $\sim 80\%$ of BAT GRBs.

XRF 100316D/SN 2010BH : CLUE TO THE DIVERSE ORIGIN OF NEARBY SUPERNOVA-ASSOCIATED GAMMA-RAY BURSTS

his work has been published as:

Fan, Y.-Z., Zhang, B.-B., Xu, D., Liang, E.-W., & Zhang, B. 2011, The Astrophysical Journal, 726, 32

X-ray Flash (XRF) 100316D, a nearby super-long under-luminous burst with a peak energy $E_{\rm p} \sim 20$ keV, was detected by *Swift* and was found to be associated with an energetic supernova SN 2010bh. Both the spectral and the temporal behavior are rather similar to XRF 060218, except that the latter was associated with a "less energetic" SN 2006aj (Fig. 71), and had a prominent soft thermal emission component in the spectrum. We analyze the spectral and temporal properties of this burst (Fig. 72), and interpret the prompt gamma-ray emission and the early X-ray plateau emission as synchrotron emission from a dissipating Poynting flux dominated outflow, probably powered by a magnetar with a spin period of $P \sim 10$ ms and the polar cap magnetic field $B_{\rm p} \sim 3 \times 10^{15}$ G. The energetic supernova SN 2010bh associated with this burst is however difficult to interpret within the slow magnetar model, and we suspect that the nascent magnetar may spin much faster with an initial rotation period ~ 1 ms. It suggests a delay between the core collapse and the emergence of the relativistic magnetar wind from the star. one may envision a unified picture to understand the diversity of GRB/SN associations, by invoking a variety of initial powers and the delay times between the core collapse and

the emergence of the relativistic jet from the star. The speculation is the following:

- To produce an energetic SN/luminous GRB (e.g. GRB 030329/SN 2003dh), the central engine is powerful (a black hole with an accretion disk or a rapidly spinning magnetar) and the relativistic outflow can break out the progenitor soon enough when the engine is still working effectively.

- To produce an energetic SN/underluminous GRB (e.g. GRB 980425/SN 1998bw, GRB 031203/SN 2003lw, and XRF 100316D/SN 2010bh), the central engine is initially powerful, but it takes time for the relativistic wind to emerge from the star. As it breaks out the star, the central engine already fades down with a decreased power. The longer, softer XRFs are probably powered by a magnetar, while the shorter, harder GRBs are probably powered by a black hole.

- To produce a less-energetic SN/underluminous GRB (e.g. XRF 060218/SN 2006aj), the central engine is a slow magnetar with an initial rotation energy less than 10^{51} ergs. The emergence of the relativistic outflow can be prompt or somewhat (but not significantly) delayed.

GRB 101225A:
A Novel Long GRB without a Host Galaxy

This work is led by Dong Xu and is to be submitted to Nature.

GRB 101225A is an image triggered Swift GRB with duration longer than 1000 seconds. The BAT and XRT lightcurve are shown in Fig. 12 and 74. The lacking host galaxy feature of this burst and it X-ray and optical afterglow properties may suggest it of local origin, which is totally different progenitor type from type I or type II GRBs.

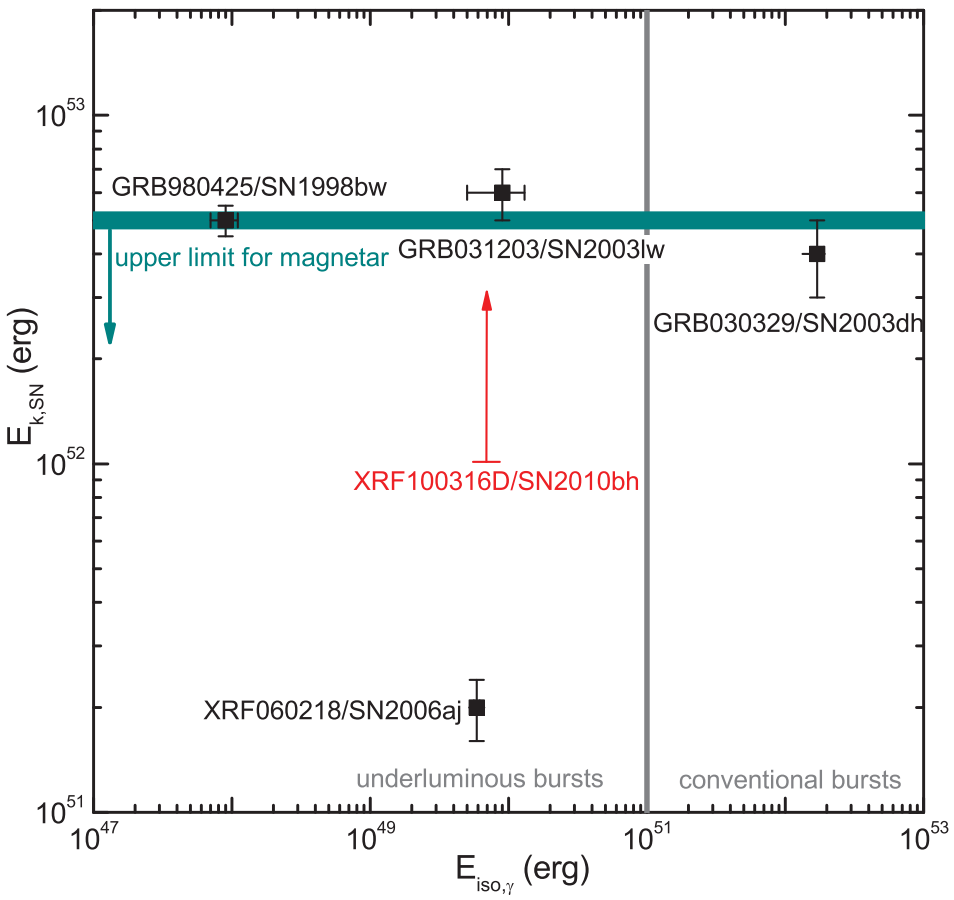

Figure 71 The isotropic energy of the prompt emission vs. the kinetic energy of the supernova outflow. The kinetic energy of SN 2010bh is estimated to be larger than $\sim 10^{52}$ erg. The possible maximum energy $\sim 5 \times 10^{52}$ erg that can be provided by a pulsar with $P \lesssim 1$ ms and $I \sim 2 \times 10^{45}$ g cm^2 is also plotted.

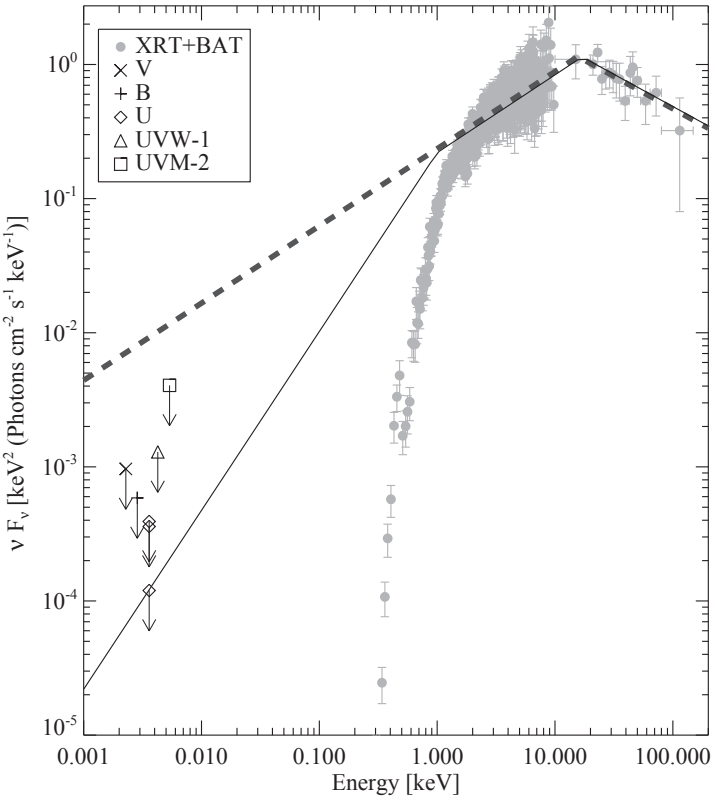

Figure 72 Broadband SED from UVOT, XRT, and BAT data for 100316D.

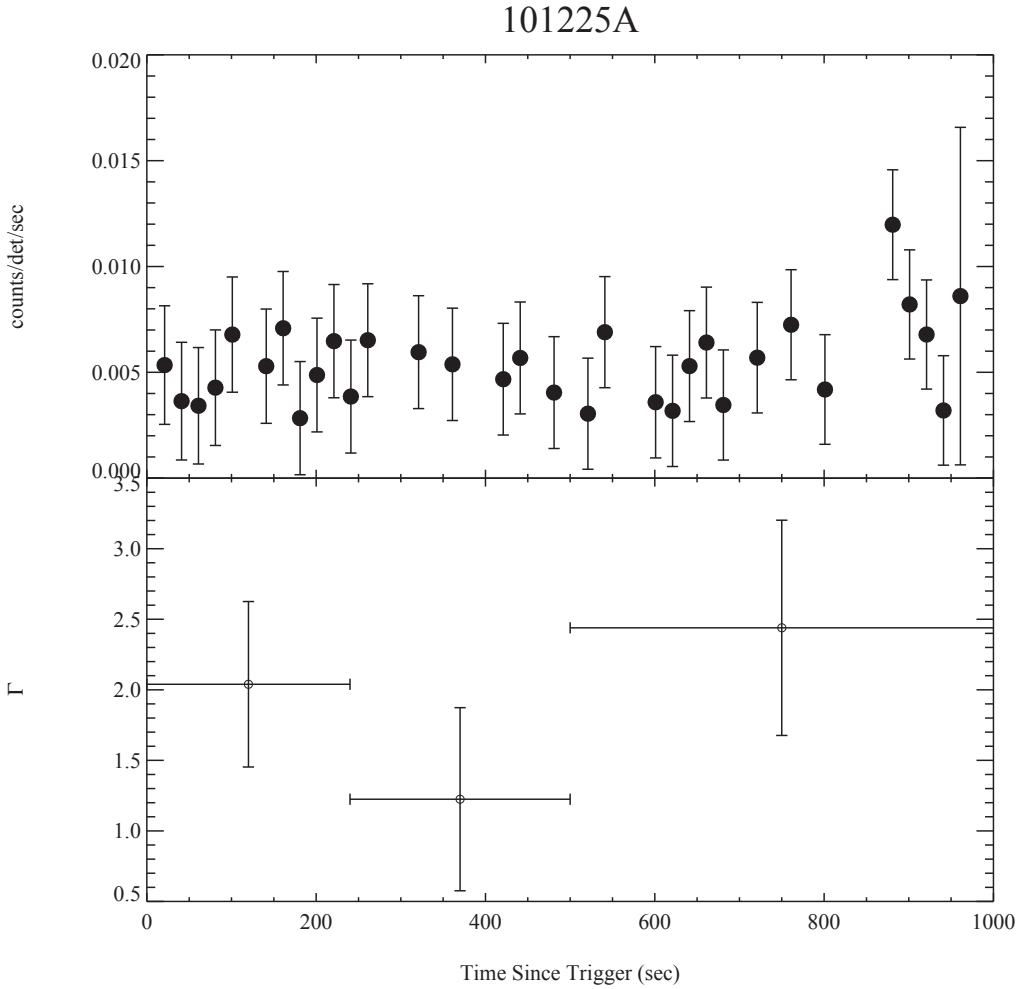

Figure 73 BAT light curve and spectral evolution of GRB 101225A.

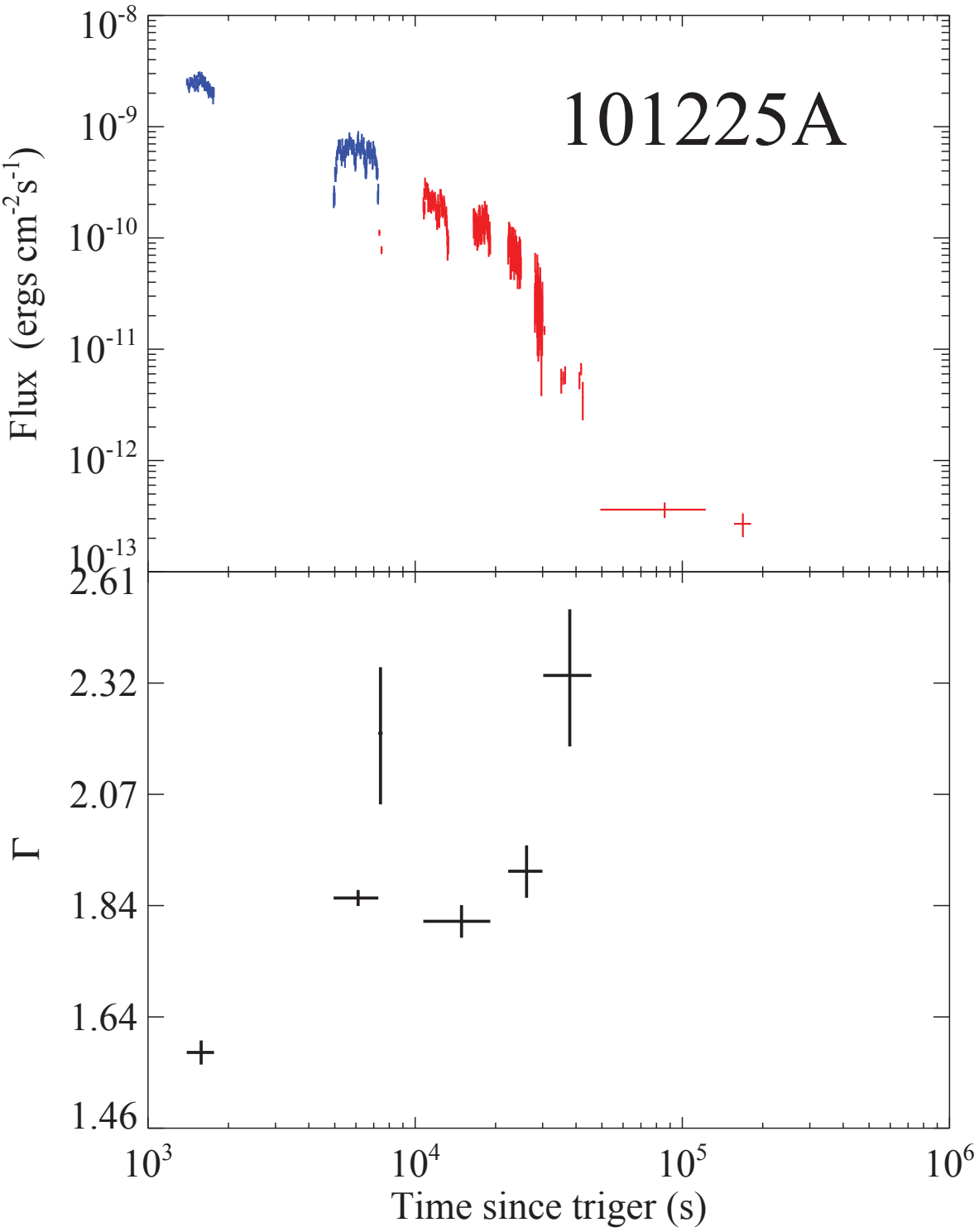

Figure 74 XRT light curve and spectral evolution of GRB 101225A.

REFERENCES

[1] Abdo, A. A., et al. 2009a, Science, 323, 1688

[2] Abdo, A. A., et al. 2009b, Nature, 462, 331

[3] Abdo, A. A., et al. 2009c, The Astrophysical Journal, 706, L138

[4] Abdo, A. A., et al. 2010d, The Astrophysical Journal, 712, 558

[5] Akerlof, C., et al. 1999, Nature, 398, 400

[6] Ackermann, M., et al. 2010, The Astrophysical Journal, 716, 1178

[7] Akaike, H. 1974, IEEE Transactions on Automatic Control, 19, 716

[8] Amati, L., et al. 2002, Astronomy and Astrophysics, 390, 81

[9] Amati, L. 2006, , 372, 233

[10] Ando, S., Nakar, E., & Sari, R. 2008, The Astrophysical Journal, 689, 1150

[11] Arnaud, K. A. 1996, Astronomical Data Analysis Software and Systems V, 101, 17

[12] Asano, K., & Terasawa, T. 2009, The Astrophysical Journal, 705, 1714

[13] Atwood, W. B., et al. 2009, The Astrophysical Journal, 697, 1071

[14] Band, D., et al. 1993, The Astrophysical Journal, 413, 281

[15] Barniol Duran, R., & Kumar, P. 2009, Monthly Notices of the Royal Astronomical Society, 395, 955

[16] Barthelmy, S. D., et al. 2005a, The Astrophysical Journal, 635, L133

[17] Barthelmy, S. D., et al. 2005b, Nature, 438, 994

[18] Belczynski, K., Holz, D. E., Fryer, C. L., Berger, E., Hartmann, D. H., & O'Shea, B. 2010, The Astrophysical Journal, 708, 117

[19] Belczynski, K., Perna, R., Bulik, T., Kalogera, V., Ivanova, N., & Lamb, D. Q. 2006, The Astrophysical Journal, 648, 1110

[20] Beloborodov, A. M. 2010, Monthly Notices of the Royal Astronomical Society, 407, 1033

[21] Berger, E., et al. 2001, The Astrophysical Journal, 556, 556

[22] Berger, E., Kulkarni, S. R., & Frail, D. A. 2003, The Astrophysical Journal, 590, 379

[23] Berger, E., et al. 2005, Nature, 438, 988

[24] Blandford, R. D., & Znajek, R. L. 1977, Monthly Notices of the Royal Astronomical Society, 179, 433

[25] Blinnikov, S. I., Kozyreva, A. V., & Panchenko, I. E. 1999, Astronomy Reports, 43, 739

[26] Bloom, J. S., Foley, R. J., Koceveki, D., & Perley, D. 2006, GRB Coordinates Network, 5217, 1

[27] Bloom, J. S., Frail, D. A., & Kulkarni, S. R. 2003, The Astrophysical Journal, 594, 674

[28] Bloom, J. S., et al. 2006, The Astrophysical Journal, 638, 354

[29] Burrows, D. N., et al. 2005a, Space Science Reviews, 120, 165

[30] Burrows, D. N., et al. 2005b, Science, 309, 1833

[31] Burrows, D. N., & Racusin, J. 2006, Nuovo Cimento B Serie, 121, 1273

[32] Burrows, D. N., et al. 2006, The Astrophysical Journal, 653, 468

[33] Butler, N. R., & Kocevski, D. 2007, The Astrophysical Journal, 668, 400

[34] Butler, N. R., Kocevski, D., Bloom, J. S., & Curtis, J. L. 2007, The Astrophysical Journal, 671, 656

[Campana et al.(2005)] Campana, S., et al. 2005, Astrophysical Journal Letters, 625, L23

[35] Campana, S., et al. 2006a, Astronomy and Astrophysics, 454, 113

[36] Campana, S., et al. 2006b, Nature, 442, 1008

[37] Chevalier, R. A., & Li, Z.-Y. 2000, The Astrophysical Journal, 536, 195

[38] Chincarini, G., et al. 2007, The Astrophysical Journal, 671, 1903

[39] Connaughton, V. 2002, The Astrophysical Journal, 567, 1028

[40] Corsi, A., Guetta, D., & Piro, L. 2010, The Astrophysical Journal, 720, 1008

[41] Covino, S., et al. 2006, Nuovo Cimento B Serie, 121, 1171

[42] Cui, X.-H., Liang, E.-W., & Lu, R.-J. 2005, Chinese Journal of Astronomy and Astrophysics, 5, 151

[43] Dado, S., Dar, A., & De Rújula, A. 2008, The Astrophysical Journal, 681, 1408

[44] Dai, Z. G., & Cheng, K. S. 2001, The Astrophysical Journal, 558, L109

[45] Dai, Z. G., & Lu, T. 1998a, Physical Review Letters, 81, 4301

[46] Dai, Z. G., & Lu, T. 1998b, Astronomy and Astrophysics, 333, L87

[47] Dai, Z. G., Wang, X. Y., Wu, X. F., & Zhang, B. 2006, Science, 311, 1127

[48] Daigne, F., & Mochkovitch, R. 2002, Monthly Notices of the Royal Astronomical Society, 336, 1271

[49] Daigne, F., & Mochkovitch, R. 2003, MNRAS, 342, 587

[50] De Pasquale, M., et al. 2006, Monthly Notices of the Royal Astronomical Society, 365, 1031

[51] de Ugarte Postigo, A., et al. 2006, The Astrophysical Journal, 648, L83

[52] Della Valle, M., et al. 2006, Nature, 444, 1050

[53] Dermer, C. D. 2007, The Astrophysical Journal, 664, 384

[54] Dermer, C. D. 2004, The Astrophysical Journal, 614, 284

[55] Dermer, C. D., Chiang, J., & Mitman, K. E. 2000, The Astrophysical Journal, 537, 785

[56] Djorgovski, S. G., Kulkarni, S. R., Bloom, J. S., Goodrich, R., Frail, D. A., Piro, L., & Palazzi, E. 1998, The Astrophysical Journal, 508, L17

[57] Donaghy, T. Q., et al. 2006, ArXiv Astrophysics e-prints, arXiv:astro-ph/0605570

[58] Dyks, J., Zhang, B., & Fan, Y. Z. 2005, ArXiv Astrophysics e-prints, arXiv:astro-ph/0511699

[59] Eichler, D., & Granot, J. 2006, The Astrophysical Journal, 641, L5

[60] Eichler, D., Livio, M., Piran, T., & Schramm, D. N. 1989, Nature, 340, 126

[61] Faber, J. A., Baumgarte, T. W., Shapiro, S. L., & Taniguchi, K. 2006, The Astrophysical Journal, 641, L93

[62] Falcone, A. D., et al. 2006, The Astrophysical Journal, 641, 1010

[63] Falcone, A. D., et al. 2007, The Astrophysical Journal, 671, 1921

[64] Fan, Y. Z., & Wei, D. M. 2005, Monthly Notices of the Royal Astronomical Society, 364, L42

[65] Fan, Y.-Z. 2010, Monthly Notices of the Royal Astronomical Society, 403, 483

[66] Fan, Y.-Z. 2009, Monthly Notices of the Royal Astronomical Society, 397, 1539

[67] Fan, Y.-Z., Piran, T., Narayan, R., & Wei, D.-M. 2008, Monthly Notices of the Royal Astronomical Society, 384, 1483

[68] Fan, Y.-Z., Piran, T., & Xu, D. 2006, Journal of Cosmology and Astro-Particle Physics, 9, 13

[69] Fan, Y., & Piran, T. 2006, Monthly Notices of the Royal Astronomical Society, 369, 197

[70] Fan, Y.-Z., Zhang, B.-B., Xu, D., Liang, E.-W., & Zhang, B. 2011, The Astrophysical Journal, 726, 32

[71] Fenimore, E. E., in 't Zand, J. J. M., Norris, J. P., Bonnell, J. T., & Nemiroff, R. J. 1995, The Astrophysical Journal, 448, L101

[72] Fenimore, E. E., Madras, C. D., & Nayakshin, S. 1996, The Astrophysical Journal, 473, 998

[73] Ford, L. A., et al. 1995, The Astrophysical Journal, 439, 307

[Fox et al.(2003)] Fox, D. W., et al. 2003a, Nature, 422, 284

[Fox et al.(2003)] Fox, D. W., et al. 2003b, The Astrophysical Journal Letters, 586, L5

[74] Fox, D. B., et al. 2005, Nature, 437, 845

[75] Frail, D. A., et al. 2001, The Astrophysical Journal, 562, L55

[76] Frail, D. A., Waxman, E., & Kulkarni, S. R. 2000, The Astrophysical Journal, 537, 191

[77] Frontera, F., et al. 1998, The Astrophysical Journal, 493, L67

[78] Fruchter, A. S., et al. 2006, Nature, 441, 463

[79] Fryer, C. L., et al. 2007, Publications of the Astronomical Society of the Pacific, 119, 1211

[80] Fryer, C. L., Woosley, S. E., Herant, M., & Davies, M. B. 1999, The Astrophysical Journal, 520, 650

[81] Fynbo, J. P. U., et al. 2006, Nature, 444, 1047

[82] Gal-Yam, A., et al. 2006, Nature, 444, 1053

[83] Galli, A., & Piro, L. 2007, Astronomy and Astrophysics, 475, 421

[84] Gao, W.-H., Mao, J., Xu, D., & Fan, Y.-Z. 2009, The Astrophysical Journal, 706, L33

[85] Gao, H., Zhang, B.-B., & Zhang, B. 2011, arXiv:1103.0074

[86] Gehrels, N. 1986, The Astrophysical Journal, 303, 336

[87] Gehrels, N., et al. 2004, The Astrophysical Journal, 611, 1005

[88] Gehrels, N., et al. 2006, Nature, 444, 1044

[89] Gehrels, N., et al. 2005, Nature, 437, 851

[90] Genet, F., Daigne, F., & Mochkovitch, R. 2007, Monthly Notices of the Royal Astronomical Society, 381, 732

[91] Ghirlanda, G., Nava, L., Ghisellini, G., Celotti, A., & Firmani, C. 2009, Astronomy and Astrophysics, 496, 585

[92] Ghisellini, G., Ghirlanda, G., Mereghetti, S., Bosnjak, Z., Tavecchio, F., & Firmani, C. 2006, Monthly Notices of the Royal Astronomical Society, 372, 1699

[93] Ghisellini, G., Ghirlanda, G., Nava, L., & Celotti, A. 2010, Monthly Notices of the Royal Astronomical Society, 403, 926

[94] Ghisellini, G., Ghirlanda, G., Nava, L., & Firmani, C. 2007a, The Astrophysical Journal, 658, L75

[95] Giannios, D., & Spruit, H. C. 2007, Astronomy and Astrophysics, 469, 1

[96] Giblin, T. W., Connaughton, V., van Paradijs, J., Preece, R. D., Briggs, M. S., Kouveliotou, C., Wijers, R. A. M. J., & Fishman, G. J. 2002, The Astrophysical Journal, 570, 573

[97] González, M. M., Dingus, B. L., Kaneko, Y., Preece, R. D., Dermer, C. D., & Briggs, M. S. 2003, Nature, 424, 749

[98] Goodman, J. 1986, The Astrophysical Journal, 308, L47

[99] Gou, L.-J., & Mészáros, P. 2007, The Astrophysical Journal, 668, 392

[100] Granot, J., Königl, A., & Piran, T. 2006, Monthly Notices of the Royal Astronomical Society, 370, 1946

[101] Greiner, J., et al. 2009, Astronomy and Astrophysics, 498, 89

[102] Greiner, J., et al. 2009a, The Astrophysical Journal, 693, 1610

[103] Greiner, J., et al. 2009b, The Astrophysical Journal, 693, 1912

[104] Grupe, D., Burrows, D. N., Patel, S. K., Kouveliotou, C., Zhang, B., Mészáros, P., Wijers, R. A. M., & Gehrels, N. 2006, The Astrophysical Journal, 653, 462

[105] Gupta, N., & Zhang, B. 2007, Monthly Notices of the Royal Astronomical Society, 380, 78

[106] Harrison, F. A., et al. 1999, The Astrophysical Journal, 523, L121

[107] He, H.-N., Wu, X.-F., Toma, K., Wang, X.-Y., & Meszaros, P. 2010, ArXiv e-prints, arXiv:1009.1432

[108] Heise, J., in't Zand, J., Kippen, R. M., & Woods, P. M. 2001, Gamma-ray Bursts in the Afterglow Era, 16

[109] Hjorth, J., et al. 2003, Nature, 423, 847

[110] Hjorth, J., et al. 2005a, Nature, 437, 859

[111] Hjorth, J., et al. 2005b, The Astrophysical Journal, 630, L117

[112] Horváth, I. 1998, The Astrophysical Journal, 508, 757

[113] Huang, Y. F., Dai, Z. G., & Lu, T. 2002, Monthly Notices of the Royal Astronomical Society, 332, 735

[114] Huang, Y. F., Gou, L. J., Dai, Z. G., & Lu, T. 2000, The Astrophysical Journal, 543, 90

[115] Ioka, K. 2010, Progress of Theoretical Physics, 124, 667

[116] Ioka, K., Toma, K., Yamazaki, R., & Nakamura, T. 2006, Astronomy and Astrophysics, 458, 7

[117] Jin, Z. P., Yan, T., Fan, Y. Z., & Wei, D. M. 2007, The Astrophysical Journal, 656, L57

[118] Kaneko, Y., Preece, R. D., Briggs, M. S., Paciesas, W. S., Meegan, C. A., & Band, D. L. 2006, The Astrophysical Journal Supplement Series, 166, 298

[119] Kann, D. A., et al. 2008, ArXiv e-prints, arXiv:0804.1959

[120] Kann, D. A., et al. 2010, The Astrophysical Journal, 720, 1513

[121] King, A., Olsson, E., & Davies, M. B. 2007, Monthly Notices of the Royal Astronomical Society, 374, L34

[Klebesadel et al.(1973)] Klebesadel, R. W., Strong, I. B., & Olson, R. A. 1973, The Astrophysical Journal Letters, 182, L85

[122] Kobayashi, S., Piran, T., & Sari, R. 1997, The Astrophysical Journal, 490, 92

[123] Kobayashi, S., & Zhang, B. 2007, The Astrophysical Journal, 655, 973

[124] Kocevski, D., & Butler, N. 2008, The Astrophysical Journal, 680, 531

[125] Kouveliotou, C., Meegan, C. A., Fishman, G. J., Bhat, N. P., Briggs, M. S., Koshut, T. M., Paciesas, W. S., & Pendleton, G. N. 1993, The Astrophysical Journal, 413, L101

[126] Kulkarni, S. R., et al. 1998, Nature, 393, 35

[127] Kumar, P., & Panaitescu, A. 2000a, The Astrophysical Journal, 541, L9

[128] Kumar, P., & Panaitescu, A. 2000b, The Astrophysical Journal, 541, L51

[129] Kumar, P., & Barniol Duran, R. 2010, Monthly Notices of the Royal Astronomical Society, 409, 226

[130] Kumar, P., & Barniol Duran, R. 2009, Monthly Notices of the Royal Astronomical Society, 400, L75

[131] Kumar, P., & Narayan, R. 2009, Monthly Notices of the Royal Astronomical Society, 395, 472

[132] Lamb, D. Q., Donaghy, T. Q., & Graziani, C. 2005, The Astrophysical Journal, 620, 355

[133] Lazzati, D., & Begelman, M. C. 2006, The Astrophysical Journal, 641, 972

[134] Lazzati, D., Morsony, B. J., & Begelman, M. C. 2009, The Astrophysical Journal, 700, L47

[135] Lazzati, D., & Perna, R. 2007, Monthly Notices of the Royal Astronomical Society, 375, L46

[136] Lazzati, D., & Begelman, M. C. 2010, The Astrophysical Journal, 725, 1137

[137] Lee, W. H., & Ramirez-Ruiz, E. 2007, New Journal of Physics, 9, 17

[138] Li, Z. 2010a, ArXiv e-prints, arXiv:1004.0791

[139] Li, Z. 2010b, The Astrophysical Journal, 709, 525

[140] Liang, E. W., Dai, Z. G., & Wu, X. F. 2004, The Astrophysical Journal, 606, L29

[141] Liang, E. W., et al. 2006a, The Astrophysical Journal, 646, 351

[142] Liang, E.-W., Zhang, B.-B., Stamatikos, M., Zhang, B., Norris, J., Gehrels, N., Zhang, J., & Dai, Z. G. 2006b, The Astrophysical Journal, 653, L81

[143] Liang, E., & Kargatis, V. 1996, Nature, 381, 49

[144] Liang, E.-W., Lü, H.-J., Hou, S.-J., Zhang, B.-B., & Zhang, B. 2009, The Astrophysical Journal, 707, 328

[145] Liang, E.-W., Racusin, J. L., Zhang, B., Zhang, B.-B., & Burrows, D. N. 2008, The Astrophysical Journal, 675, 528

[146] Liang, E.-W., Zhang, B.-B., & Zhang, B. 2007, The Astrophysical Journal, 670, 565

[147] Liang, E., & Zhang, B. 2005, The Astrophysical Journal, 633, 611

[148] Liang, E., Zhang, B., Virgili, F., & Dai, Z. G. 2007, The Astrophysical Journal, 662, 1111

[149] Liu, R.-Y., & Wang, X.-Y. 2011, The Astrophysical Journal, 730, 1

[150] Lu, R.-J., Hou, S.-J., & Liang, E.-W. 2010, The Astrophysical Journal, 720, 1146

[151] Lyutikov, M., & Blandford, R. 2003, ArXiv Astrophysics e-prints, arXiv:astro-ph/0312347

[152] Meszaros, P., & Rees, M. J. 1993, The Astrophysical Journal, 405, 278

[153] Meszaros, P., & Rees, M. J. 1994, MNRAS, 269, L41

[Meszaros & Rees(1997)] Meszaros, P., & Rees, M. J. 1997, The Astrophysical Journal, 476, 232

[154] Mészáros, P., & Rees, M. J. 2000, The Astrophysical Journal, 530, 292

[155] Mészáros, P. 2002, Annual Review of Astronomy and Astrophysics, 40, 137

[156] Mészáros, P., Ramirez-Ruiz, E., Rees, M. J., & Zhang, B. 2002, The Astrophysical Journal, 578, 812

[157] Mészáros, P. 2006, Reports on Progress in Physics, 69, 2259

[158] Meszaros, P., & Rees, M. J. 1997a, The Astrophysical Journal, 482, L29

[159] Meszaros, P., & Rees, M. J. 1997b, The Astrophysical Journal, 476, 232

[160] Meszaros, P., & Rees, M. J. 1994, Monthly Notices of the Royal Astronomical Society, 269, L41

[161] Meszaros, P., Rees, M. J., & Papathanassiou, H. 1994, The Astrophysical Journal, 432, 181

[162] MacFadyen, A. I., & Woosley, S. E. 1999, The Astrophysical Journal, 524, 262

[163] Mangano, V., et al. 2007, Astronomy and Astrophysics, 470, 105

[164] Maxham, A., Zhang, B.-B., & Zhang, B. 2010, ArXiv e-prints, arXiv:1101.0144

[165] Maxham, A., & Zhang, B. 2009, The Astrophysical Journal, 707, 1623

[166] Meegan, C., Fishman, G., Wilson, R., Brock, M., Horack, J., Paciesas, W., Pendleton, G., & Kouveliotou, C. 1993, American Institute of Physics Conference Series, 280, 681

[167] McBreen, S., et al. 2008, The Astrophysical Journal, 677, L85

[168] Meegan, C., et al. 2009, The Astrophysical Journal, 702, 791

[169] Mizuta, A., Nagataki, S., & Aoi, J. 2010, ArXiv e-prints, arXiv:1006.2440

[170] Monfardini, A., et al. 2006, The Astrophysical Journal, 648, 1125

[171] Mukherjee, S., Feigelson, E. D., Jogesh Babu, G., Murtagh, F., Fraley, C., & Raftery, A. 1998, The Astrophysical Journal, 508, 314

[172] Nakar, E., & Piran, T. 2002, Monthly Notices of the Royal Astronomical Society, 330, 920

[173] Narayan, R., & Kumar, P. 2009, Monthly Notices of the Royal Astronomical Society, 394, L117

[174] Narayan, R., Paczynski, B., & Piran, T. 1992, The Astrophysical Journal, 395, L83

[175] Narayan, R., Piran, T., & Kumar, P. 2001, The Astrophysical Journal, 557, 949

[176] Nava, L., Ghisellini, G., Ghirlanda, G., Cabrera, J. I., Firmani, C., & Avila-Reese, V. 2007, Monthly Notices of the Royal Astronomical Society, 377, 1464

[177] Nemiroff, R. J. 1994, Comments on Astrophysics, 17, 189

[178] Norris, J. P., & Bonnell, J. T. 2006, The Astrophysical Journal, 643, 266

[179] Norris, J. P., Bonnell, J. T., Kazanas, D., Scargle, J. D., Hakkila, J., & Giblin, T. W. 2005, The Astrophysical Journal, 627, 324

[180] Norris, J. P., Marani, G. F., & Bonnell, J. T. 2000, The Astrophysical Journal, 534, 248

[181] Nousek, J. A., et al. 2006, The Astrophysical Journal, 642, 389

[182] O'Brien, P. T., et al. 2006, The Astrophysical Journal, 647, 1213

[183] Ofek, E. O., et al. 2007, The Astrophysical Journal, 662, 1129

[184] Paczynski, B. 1986, The Astrophysical Journal, 308, L43

[185] Paczynski, B. 1998, The Astrophysical Journal, 494, L45

[186] Paczynski, B. 1991, Acta Astronomica, 41, 257

[187] Page, K. L., et al. 2007, The Astrophysical Journal, 663, 1125

[188] Pal'Shin, V., et al. 2008, GRB Coordinates Network, 8256, 1

[189] Panaitescu, A., Mészáros, P., Burrows, D., Nousek, J., Gehrels, N., O'Brien, P., & Willingale, R. 2006a, Monthly Notices of the Royal Astronomical Society, 369, 2059

[190] Panaitescu, A., Mészáros, P., Gehrels, N., Burrows, D., & Nousek, J. 2006b, Monthly Notices of the Royal Astronomical Society, 366, 1357

[191] Panaitescu, A. 2007a, Monthly Notices of the Royal Astronomical Society, 380, 374

[192] Panaitescu, A. 2007b, Monthly Notices of the Royal Astronomical Society, 379, 331

[193] Pe'er, A., Mészáros, P., & Rees, M. J. 2006, The Astrophysical Journal, 642a, 995

[194] Pe'er, A., Mészáros, P., & Rees, M. J. 2006, The Astrophysical Journal, 652b, 482

[195] Pe'er, A., & Ryde, F. 2010, ArXiv e-prints, arXiv:1008.4590

[196] Pe'er, A., & Waxman, E. 2004a, The Astrophysical Journal, 613, 448

[197] Pe'er, A., & Waxman, E. 2004b, The Astrophysical Journal, 603, L1

[198] Pe'er, A., Zhang, B.-B., Ryde, F., McGlynn, S., Zhang, B., Preece, R. D., & Kouveliotou, C. 2010, ArXiv e-prints, arXiv:1007.2228

[199] Pérez-Ramírez, D., et al. 2010, Astronomy and Astrophysics, 510, A105

[200] Perna, R., Armitage, P. J., & Zhang, B. 2006, The Astrophysical Journal, 636, L29

[201] Pian, E., et al. 2006, Nature, 442, 1011

[202] Pilla, R. P., & Loeb, A. 1998, The Astrophysical Journal, 494, L167

[203] Piran, T. 2005, Reviews of Modern Physics, 76, 1143

[204] Piran, T., & Nakar, E. 2010, The Astrophysical Journal, 718, L63

[205] Preece, R. D., Briggs, M. S., Mallozzi, R. S., Pendleton, G. N., Paciesas, W. S., & Band, D. L. 2000, The Astrophysical Journal Supplement Series, 126, 19

[206] Preece, R. D., Briggs, M. S., Pendleton, G. N., Paciesas, W. S., Matteson, J. L., Band, D. L., Skelton, R. T., & Meegan, C. A. 1996, The Astrophysical Journal, 473, 310

[207] Price, P. A., Berger, E., & Fox, D. B. 2006, GRB Coordinates Network, 5275, 1

[208] Proga, D., & Zhang, B. 2006, Monthly Notices of the Royal Astronomical Society, 370, L61

[209] Qin, Y.-P. 2008, The Astrophysical Journal, 683, 900

[210] Qin, Y.-P., Zhang, Z.-B., Zhang, F.-W., & Cui, X.-H. 2004, The Astrophysical Journal, 617, 439

[211] Razzaque, S., Dermer, C. D., & Finke, J. D. 2010, The Open Astronomy Journal, 3, 150

[212] Razzaque, S., Mészáros, P., & Zhang, B. 2004, The Astrophysical Journal, 613, 1072

[213] Rees, M. J., & Mészáros, P. 2005, The Astrophysical Journal, 628, 847

[214] Rees, M. J., & Meszaros, P. 1998, The Astrophysical Journal, 496, L1

[215] Rees, M. J., & Meszaros, P. 1994, The Astrophysical Journal, 430, L93

[216] Rees, M. J., & Meszaros, P. 1992, Monthly Notices of the Royal Astronomical Society, 258, 41P

[217] Rhoads, J. E. 1999, The Astrophysical Journal, 525, 737

[218] Romano, P., et al. 2006, Astronomy and Astrophysics, 456, 917

[219] Roming, P. W. A., et al. 2005, Space Science Reviews, 120, 95

[220] Roming, P. W. A., et al. 2006, The Astrophysical Journal, 651, 985

[221] Roming, P. W. A., et al. 2009, The Astrophysical Journal, 690, 163

[222] Rossi, E., Lazzati, D., & Rees, M. J. 2002, Monthly Notices of the Royal Astronomical Society, 332, 945

[223] Rosswog, S. 2007, Monthly Notices of the Royal Astronomical Society, 376, L48

[224] Rosswog, S., Ramirez-Ruiz, E., & Davies, M. B. 2003, Monthly Notices of the Royal Astronomical Society, 345, 1077

[225] Ryde, F., et al. 2010, The Astrophysical Journal, 709, L172

[226] Ryde, F., et al. 2011, arXiv:1103.0708

[227] Ryde, F., & Svensson, R. 2002, The Astrophysical Journal, 566, 210

[228] Sakamoto, T., et al. 2006, The Astrophysical Journal, 636, L73

[229] Sakamoto, T., et al. 2008, The Astrophysical Journal Supplement Series, 175, 179

[230] Sakamoto, T., et al. 2009, The Astrophysical Journal, 693, 922

[231] Salmonson, J. D. 2000, The Astrophysical Journal, 544, L115

[232] Sari, R., & Mészáros, P. 2000, The Astrophysical Journal, 535, L33

[233] Sari, R., Piran, T., & Halpern, J. P. 1999, The Astrophysical Journal, 519, L17

[234] Sari, R., Piran, T., & Narayan, R. 1998, The Astrophysical Journal, 497, L17

[235] Sari, R., & Piran, T. 1997, MNRAS, 287, 110

[236] Savaglio, S., Glazebrook, K., & Le Borgne, D. 2009, The Astrophysical Journal, 691, 182

[237] Shao, L., & Dai, Z. G. 2007, The Astrophysical Journal, 660, 1319

[238] Shirasaki, Y., et al. 2008, Publications of the Astronomical Society of Japan, 60, 919

[239] Soderberg, A. M., et al. 2006, Nature, 442, 1014

[240] Stanek, K. Z., et al. 2003, The Astrophysical Journal, 591, L17

[241] Strong, I. B., & Klebesadel, R. W. 1974, Nature, 251, 396

[242] Swenson, C. A., et al. 2010, , 718, L14

[243] Tagliaferri, G., et al. 2005, Nature, 436, 985

[244] Tanvir, N. R., et al. 2009, Nature, 461, 1254

[245] Thompson, C. 1994, Monthly Notices of the Royal Astronomical Society, 270, 480

[246] Thompson, C., Mészáros, P., & Rees, M. J. 2007, The Astrophysical Journal, 666, 1012

[247] Toma, K., Ioka, K., Sakamoto, T., & Nakamura, T. 2007, The Astrophysical Journal, 659, 1420

[248] Toma, K., Wu, X.-F., & Mészáros, P. 2009, The Astrophysical Journal, 707, 1404

[249] Toma, K., Wu, X.-F., & Meszaros, P. 2010, ArXiv e-prints, arXiv:1002.2634

[250] Troja, E., et al. 2007, The Astrophysical Journal, 665, 599

[251] Troja, E., King, A. R., O'Brien, P. T., Lyons, N., & Cusumano, G. 2008, Monthly Notices of the Royal Astronomical Society, 385, L10

[252] Uhm, Z. L., & Beloborodov, A. M. 2007, The Astrophysical Journal, 665, L93

[253] van Paradijs, J., et al. 1997, Nature, 386, 686

[254] Vaughan, S., et al. 2006, The Astrophysical Journal, 638, 920

[255] Villasenor, J. S., et al. 2005, Nature, 437, 855

[256] Virgili, F. J., Liang, E.-W., & Zhang, B. 2009, Monthly Notices of the Royal Astronomical Society, 392, 91

[257] Wang, X. Y., Dai, Z. G., & Lu, T. 2001, The Astrophysical Journal, 556, 1010

[258] Wang, X.-Y., He, H.-N., Li, Z., Wu, X.-F., & Dai, Z.-G. 2010, The Astrophysical Journal, 712, 1232

[259] Wei, D. M., & Gao, W. H. 2003, Monthly Notices of the Royal Astronomical Society, 345, 743

[260] Wei, D.-M., & Fan, Y.-Z. 2007, Chinese Journal of Astronomy and Astrophysics, 7, 509

[261] Willingale, R., et al. 2007, The Astrophysical Journal, 662, 1093

[262] Woosley, S. E. 1993, The Astrophysical Journal, 405, 273

[263] Wu, X. F., Dai, Z. G., Wang, X. Y., Huang, Y. F., Feng, L. L., & Lu, T. 2006, 36th COSPAR Scientific Assembly, 36, 731

[264] Yamazaki, R., Toma, K., Ioka, K., & Nakamura, T. 2006, Monthly Notices of the Royal Astronomical Society, 369, 311

[265] Yamazaki, R., Yonetoku, D., & Nakamura, T. 2004, Gamma-Ray Bursts: 30 Years of Discovery, 727, 416

[266] Yi, T., Liang, E., Qin, Y., & Lu, R. 2006, Monthly Notices of the Royal Astronomical Society, 367, 1751

[267] Yonetoku, D., Murakami, T., Nakamura, T., Yamazaki, R., Inoue, A. K., & Ioka, K. 2004, The Astrophysical Journal, 609, 935

[268] Yonetoku, D., et al. 2008, Publications of the Astronomical Society of Japan, 60, 352

[269] Yu, Y. W., & Dai, Z. G. 2007, Astronomy and Astrophysics, 470, 119

[270] Yu, Y. W., Liu, X. W., & Dai, Z. G. 2007, The Astrophysical Journal, 671, 637

[271] Zhang, B.-B., Liang, E.-W., & Zhang, B. 2007, The Astrophysical Journal, 666, 1002

[272] Zhang, B.-B., et al. 2011, The Astrophysical Journal, 730, 141

[273] Zhang, B.-B., Zhang, B., Liang, E.-W., & Wang, X.-Y. 2009, The Astrophysical Journal, 690, L10

[274] Zhang, B. 2007, Chinese Journal of Astronomy and Astrophysics, 7, 1

[275] Zhang, B. 2006, Nature, 444, 1010

[276] Zhang, B., Fan, Y. Z., Dyks, J., Kobayashi, S., Mészáros, P., Burrows, D. N., Nousek, J. A., & Gehrels, N. 2006, The Astrophysical Journal, 642, 354

[277] Zhang, B., et al. 2007a, The Astrophysical Journal, 655, 989

[278] Zhang, B., Zhang, B.-B., Liang, E.-W., Gehrels, N., Burrows, D. N., & Mészáros, P. 2007b, The Astrophysical Journal, 655, L25

[279] Zhang, B., & Mészáros, P. 2004, International Journal of Modern Physics A, 19, 2385

[280] Zhang, B., & Mészáros, P. 2002a, The Astrophysical Journal, 571, 876

[281] Zhang, B., & Mészáros, P. 2002b, The Astrophysical Journal, 581, 1236

[282] Zhang, B., & Mészáros, P. 2001a, The Astrophysical Journal, 552, L35

[283] Zhang, B., d & Mészáros, P. 2001b, The Astrophysical Journal, 559, 110

[284] Zhang, B., & Pe'er, A. 2009, The Astrophysical Journal, 700, L65

[285] Zhang, B., & Yan, H. 2011, The Astrophysical Journal, 726, 90

[286] Zhang, B., et al. 2009, The Astrophysical Journal, 703, 1696 Network, 4429, 1

[287] Zou, Y.-C., Fan, Y.-Z., & Piran, T. 2009, Monthly Notices of the Royal Astronomical Society, 396, 1163

VITA

Graduate College
University of Nevada, Las Vegas

Binbin Zhang

Degrees:

Bachelors of Science, Physics, 2003
Hebei Normal University, Hebei, China

Special Honors and Awards:

2008-2009: UNLV President's Graduate Fellowship

Publications:

Zhang, B.-B., Zhang, B., Liang, E.-W., Fan, Y.-Z., Wu, X.-F., Pe'er, A., Maxham, A., Gao, H., & Dong, Y.-M., *A Comprehensive Analysis of Fermi Gamma-ray Burst Data. I. Spectral Components and the Possible Physical Origins of LAT/GBM GRBs*, The Astrophysical Journal, 730, 141 (2011)

Gao, H., **Zhang, B.-B.**, & Zhang, B., *Evidence Of Superposed Variability Components In GRB Prompt Emission Lightcurves*, ArXiv e-prints, arXiv:1103.0074 (2011)

Fan, Y.-Z., **Zhang, B.-B.**, Xu, D., Liang, E.-W., & Zhang, B., *XRF 100316D/SN 2010bh: Clue to the Diverse Origin of Nearby Supernova-associated Gamma-ray Bursts*, The Astrophysical Journal, 726, 32 (2011)

Maxham, A., **Zhang, B.-B.**, & Zhang, B., *Is GeV Emission from Gamma-Ray Bursts of External Shock Origin?*, ArXiv e-prints, arXiv:1101.0144 (2010)

Liang, E.-W., Yi, S.-X., Zhang, J., Lü, H.-J., **Zhang, B.-B.**, & Zhang, B., *Constraining Gamma-ray Burst Initial Lorentz Factor with the Afterglow Onset Feature and Discovery of a Tight* $\Gamma_0 - E_{\gamma,iso}$ *Correlation*, The Astrophysical Journal, 725, 2209 (2010)

Lü, H.-J., Liang, E.-W., **Zhang, B.-B.**, & Zhang, B., *A New Classification Method for Gamma-ray Bursts*, The Astrophysical Journal, 725, 1965 (2010)

Pe'er, A., **Zhang, B.-B.**, Ryde, F., McGlynn, S., Zhang, B., Preece, R. D., & Kouveliotou, C., *The Connection Between Thermal and Non-Thermal Emission in Gamma-ray Bursts: General Considerations and GRB090902B as a Case Study*, ArXiv e-prints, arXiv:1007.2228 (2010)

Swenson, C. A., Maxham, A., Roming, P. W. A., Schady, P., Vetere, L., **Zhang, B. B.**, Zhang, B., Holland, S. T., Kennea, J. A., Kuin, N. P. M., Oates, S. R., Page, K. L., & De Pasquale, M., *GRB 090926A and Bright Late-time Fermi Large Area Telescope Gamma-ray Burst Afterglows*, The Astrophysical Journal, 718, L14 (2010)

Ryde, F., Axelsson, M., **Zhang, B. B.**, McGlynn, S., Pe'er, A., Lundman, C., Larsson, S., Battelino, M., Zhang, B., Bissaldi, E., Bregeon, J., Briggs, M. S., Chiang, J., de Palma, F., Guiriec, S., Larsson, J., Longo, F., McBreen, S., Omodei, N., Petrosian, V., Preece, R., & van der Horst, A. J., *Identification and Properties of the Photospheric Emission in GRB090902B*, The Astrophysical Journal, 709, L172 (2010)

Cui, X.-H., Liang, E.-W., Lv, H.-J., **Zhang, B.-B.**, & Xu, R.-X., *Towards the properties of long gamma-ray burst progenitors with Swift data*, Monthly Notices of the Royal Astronomical Society, 401, 1465 (2010)

Liang, E.-W., Lü, H.-J., Hou, S.-J., **Zhang, B.-B.**, & Zhang, B., *A Comprehensive Analysis of Swift/X-Ray Telescope Data. IV. Single Power-Law Decaying Light Curves Versus Canonical Light Curves and Implications for a Unified Origin of X-Rays*, The Astrophysical Journal, 707, 328 (2009)

Zhang, B., **Zhang, B.-B.**, Virgili, F. J., Liang, E.-W., Kann, D. A., Wu, X.-F., Proga, D., Lv, H.-J., Toma, K., Mészáros, P., Burrows, D. N., Roming, P. W. A., & Gehrels, N., *Discerning the Physical Origins of Cosmological Gamma-ray Bursts Based on Multiple Observational Criteria: The Cases of z = 6.7 GRB 080913, z = 8.2 GRB 090423, and Some Short/Hard GRBs*, The Astrophysical Journal, 703, 1696 (2009)

Racusin, J. L., Liang, E. W., Burrows, D. N., Falcone, A., Sakamoto, T., **Zhang, B. B.**, Zhang, B., Evans, P., & Osborne, J., *Jet Breaks and Energetics of Swift Gamma-Ray Burst X-Ray Afterglows*, The Astrophysical Journal, 698, 43 (2009)

Greiner, J., Krühler, T., Fynbo, J. P. U., Rossi, A., Schwarz, R., Klose, S., Savaglio, S., Tanvir, N. R., McBreen, S., Totani, T., **Zhang, B. B.**, Wu, X. F., Watson, D., Barthelmy, S. D., Beardmore, A. P., Ferrero, P., Gehrels, N., Kann, D. A., Kawai, N., Yoldaş, A. K., Mészáros, P., Milvang-Jensen, B., Oates, S. R., Pierini, D., Schady, P., Toma, K., Vreeswijk, P. M., Yoldaş, A., Zhang, B., Afonso, P., Aoki, K., Burrows, D. N., Clemens, C., Filgas, R., Haiman, Z., Hartmann, D. H., Hasinger, G., Hjorth, J., Jehin, E., Levan, A. J., Liang, E. W., Malesani, D., Pyo, T.-S., Schulze, S., Szokoly, G., Terada, K., & Wiersema, K., *GRB 080913 at Redshift 6.7*, The Astrophysical Journal, 693, 1610 (2009)

Zhang, B.-B., Zhang, B., Liang, E.-W., & Wang, X.-Y., *Curvature Effect of a Non-Power-Law Spectrum and Spectral Evolution of GRB X-Ray Tails*, The Astrophysical Journal, 690, L10 (2009)

Liang, E.-W., Racusin, J. L., Zhang, B., **Zhang, B.-B.**, & Burrows, D. N., *A Comprehensive Analysis of Swift XRT Data. III. Jet Break Candidates in X-Ray and Optical Afterglow Light Curves*, The Astrophysical Journal, 675, 528 (2008)

Liang, E.-W., **Zhang, B.-B.**, & Zhang, B., *A Comprehensive Analysis of Swift XRT Data. II. Diverse Physical Origins of the Shallow Decay Segment*, The Astrophysical Journal, 670, 565 (2007)

Zhang, B.-B., Liang, E.-W., & Zhang, B., *A Comprehensive Analysis of Swift XRT Data. I. Apparent Spectral Evolution of Gamma-Ray Burst X-Ray Tails*, The Astrophysical Journal, 666, 1002 (2007)

Troja, E., Cusumano, G., O'Brien, P. T., Zhang, B., Sbarufatti, B., Mangano, V., Willingale, R., Chincarini, G., Osborne, J. P., Marshall, F. E., Burrows, D. N., Campana, S., Gehrels, N., Guidorzi, C., Krimm, H. A., La Parola, V., Liang, E. W., Mineo, T., Moretti, A., Page, K. L., Romano, P., Tagliaferri, G., **Zhang, B. B.**, Page, M. J., & Schady, P., *Swift Observations of GRB 070110: An Extraordinary X-Ray Afterglow Powered by the Central Engine*, The Astrophysical Journal, 665, 599 (2007)

Zhang, B., Liang, E., Page, K. L., Grupe, D., **Zhang, B.-B.**, Barthelmy, S. D., Burrows, D. N., Campana, S., Chincarini, G., Gehrels, N., Kobayashi, S., Mészáros, P., Moretti, A., Nousek, J. A., O'Brien, P. T., Osborne, J. P., Roming, P. W. A., Sakamoto, T., Schady, P., & Willingale, R., *GRB Radiative Efficiencies Derived from the Swift Data: GRBs versus XRFs, Long versus Short*, The Astrophysical Journal, 655, 989 (2007)

Zhang, B., **Zhang, B.-B.**, Liang, E.-W., Gehrels, N., Burrows, D. N., & Mészáros, P., *Making a Short Gamma-Ray Burst from a Long One: Implications for the Nature of GRB 060614*, The Astrophysical Journal, 655, L25 (2007)

Liang, E.-W., **Zhang, B.-B.**, Stamatikos, M., Zhang, B., Norris, J., Gehrels, N., Zhang, J., & Dai, Z. G., *Temporal Profiles and Spectral Lags of XRF 060218*, The Astrophysical Journal, 653, L81 (2006)

Dissertation Title: A Multi-wavelength Study on Gamma-Ray Bursts and Their Afterglows

Dissertation Committee:

Committee Chairperson: Bing Zhang, Ph.D.
Committee Memeber: Kentaro Nagamine, Ph.D.
Committee Memeber: Daniel Proga, Ph.D.
Committee Memeber: David Burrows, Ph.D.
Committee Memeber: Paul O'Brien, Ph.D.
Graduate Faculty Representative: Pengtao Sun, Ph.D.